Title

Electronic and Structural Dynamics in Solids with Attosecond Transient Absorption Spectroscopy

Author

Chang, Hung-Tzu

Publication Date

2021

Peer reviewed|Thesis/dissertation

Electronic and Structural Dynamics in Solids with Attosecond Transient Absorption Spectroscopy

by

Hung-Tzu Chang

A dissertation submitted in partial satisfaction of the

requirements for the degree of

Doctor of Philosophy

in

Chemistry

in the

Graduate Division

of the

University of California, Berkeley

Committee in charge:

Professor Stephen R. Leone, Chair
Professor Daniel M. Neumark
Professor Steven G. Louie

Spring 2021

Electronic and Structural Dynamics in Solids with Attosecond Transient Absorption Spectroscopy

Abstract

Electronic and Structural Dynamics in Solids with Attosecond Transient Absorption Spectroscopy

by

Hung-Tzu Chang

Doctor of Philosophy in Chemistry

University of California, Berkeley

Professor Stephen R. Leone, Chair

Exploring photoinduced dynamics in solids is crucial to the understanding and development of opto-electronics, photovoltaics, and photocatalytic cells. Core-level transient absorption spectroscopy is a powerful tool to probe the electronic and structural dynamics in atoms, molecules, and condensed matter. After photoexcitation with a sub-5 femtosecond optical pulse, time-delayed broadband subfemtosecond extreme ultraviolet (XUV, 10-200 eV) pulses produced by high harmonic generation excite core-level electrons in the photoexcited sample. The change of absorption spectrum in the XUV provides snapshots of electronic and vibrational states of the system, enabling real-time tracking of electronic and structural dynamics with subfemtosecond resolution. This technique, termed attosecond transient absorption spectroscopy, is utilized througout this work to investigate dynamics of photoexcited semiconductors, metals, and insulators.

In semiconducting 2H-$MoTe_2$, attosecond transient absorption spectroscopy tracks the relaxation and recombination of carriers and coherent lattice displacement by probing the core-level absorption at the Te $N_{4,5}$ edge (40 eV). Here transient absorption signal below the Te N_5 edge can be directly mapped to the energy distribution of photoexcited holes, and a 15 ± 5 fs thermalization time, a 380 ± 90 fs hole relaxation time, and a 1.5 ± 0.1 ps carrier recombination time are experimentally obtained. Coherent phonon excitations causes periodic shifts of the core-level absorption edge and an oscillatory XUV transient absorption feature. Fourier transform of the oscillations in the XUV transient absorption signal reveals the excitations of out-of-plane A_{1g} (5.1 THz) and in-plane E_{1g} (3.7 THz) phonons. By comparison to Bethe-Salpeter equation simulations, the spectral changes are mapped to real-space excited-state displacements of the lattice along the dominant A_{1g} coordinate.

While in semiconducting 2H-$MoTe_2$ the core-level absorption spectrum can be directly mapped to the density of states in the valence shell, core-level absorption in semiconducting WS_2 exhibits both direct core-to-band transitions at the W O_3 edge (40 eV) and discrete core-exciton transitions at the W $N_{6,7}$ edge. Here the dynamics of photoexcited carriers and carrier-induced modifications of core-excitons are probed when the XUV pulse arrives after the optical pulse. When the pulse sequence is reversed, core-excitons are excited with the XUV pulse and the optical pulse perturbs

the transition dipole of the core-excitons by carrier photoexcitation and field-induced coupling to high-lying core-exciton states or the continuum. Global fitting of the transient absorption signal at the W $N_{6,7}$ edge yields $\sim$ 10 fs coherence lifetimes of core-exciton states and reveals that the photoexcited carriers, which alter the electronic screening and band filling, are the dominant contributor to the spectral modifications of core-excitons and that direct field-induced changes play a minor role. A 1.2 ± 0.3 ps hole-phonon relaxation time and a 3.1 ± 0.4 ps carrier recombination time are also extracted from the XUV transient absorption spectra from the core-to-conduction band transitions at the W O_3 edge.

Unlike many semiconductors, core-level absorption in metals cannot be generally described by single-particle core-to-band transitions due to electron scattering at the Fermi surface mediated by the core hole potential, which strongly renormalizes the core-level absorption spectrum beyond the single-particle picture. By studying the dynamics of photoexcited electrons in nickel with attosecond transient absorption spectroscopy, it is observed that the core-level absorption lineshape of photoexcited nickel can be described by a Gaussian broadening (σ) and a red shift (ω_s) of the ground state absorption spectrum. Theory predicts, and the experimental results verify, that after initial rapid carrier thermalization, the electron temperature increase (ΔT) is linearly proportional to the Gaussian broadening factor σ, providing quantitative real-time tracking of the relaxation of the electron temperature. During and after photoexcitation, rapid electron thermalization via carrier-carrier scattering accompanies and follows the nominal 4 fs photoexcitation pulse until the carriers reach a quasi-thermal equilibrium. Entwined with a <6 fs instrument response function, carrier thermalization times ranging from 34 fs to 13 fs are estimated from experimental data acquired at different pump fluences, and it is observed that the electron thermalization time decreases with increasing pump fluence, which is consistent with predictions with Fermi liquid theory. Measurements also reveal an electron cooling time of 640±80 fs. With hot thermalized carriers, the spectral red shift exhibits a power-law relationship with the change in electron temperature of $\omega_s \propto \Delta T^{1.5}$.

For insulators, we outline the experimental results of the decay of core-excitons in NaCl probed by attosecond transient absorption spectroscopy at the Na $L_{2,3}$ edge (32-48 eV). Here, core-excitonic transitions span an energy range over 15 eV. Coherence lifetimes up to 11 fs are observed for core-exciton states below the core-to-conduction band transition onset (36 eV), while the coherence lifetimes of core-exciton states above the core-to-conduction band onset are well within the duration of the optical pulse (<5 fs).

Lastly, we report an experimental technique to simultaneously generate sub-5 fs pulses centered at 400 nm and 800 nm, enabling direct optical excitation of wide band gap semiconductors to probe their dynamics after photoexcitation. By using a dichroic beamsplitter to separate spectral components of a supercontinuum below and above 500 nm and separately compressing each arm with a set of chriped mirrors, laser pulses centered at 400 nm and 800 nm with <4.5 fs pulse duration are simultaneously obtained.

This work summarizes four prototypical experiments of attosecond transient absorption spec-

troscopy in solids, including a metal, two different semiconductors, and an insulator. The methodologies for the experiments and analyses can be extended and generalized to study electronic and structural dynamics in more complex systems, such as alloys, multilayers, heterostructures, and superlattices.

To my parents

Contents

List of Figures

List of Tables

Acknowledgments

This work would not be possible without the help and effort from many people. First and foremost, I would like to thank my two advisors, Prof. Stephen Leone and Prof. Daniel Neumark, who supported me throughout my time as a PhD student despite many hiccups in my experimental work; Prof. Michael Zürch, then supervising me as a postdoc, taught me a lot about the knowledge on lasers and optics. I would like to thank Prof. David Attwood and Prof. Steven Louie; the former broadened my view on X-ray and extreme ultraviolet (XUV) techniques and the concepts of solid state physics taught by the latter is the basis of many analysis techniques developed in this work. I would also like to thank the Leone and Neumark group members, including but not limited to, Dr. Alexander Guggenmos, Dr. Juwon Oh, Dr. Lauren Borja, Dr. Andrew Attar, Dr. Marieke Jager, Dr. Christian Ott, Prof. Peter Kraus, Dr. Christopher Kaplan, Dr. Romain Géneaux, Dr. Mihai Vaida, Dr. Lou Barreau, Dr. James Gaynor, Dr. Chang-Ming Jiang, Dr. Lucas Carneiro, Dr. Valeriu Scultenic, Dr. Tymur Parpiiev, Dr. Sonia Marggi Poullain, Dr. Yuki Kobayashi, Dr. Ashley Fidler, Kristina Chang, Andrew Ross, Ilana Porter, for creating an inclusive learning and working environment and making the life in the lab enjoyable. In particular, I have to thank Dr. Alexander Guggenmos, Dr. Romain Géneaux, and Dr. Juwon Oh for their help in working with me in the lab.

Secondly, I would like to thank our collaborators. Dr. Uwe Bergmann and Dr. Ming-Fu Lin have reached out to us to form a successful collaboration on the study of $MoTe_2$ with groups led by Prof. Pulickel Ajayan and Prof. Priya Vashishta, and graciously allowed me to participate in their experiment on soft X-ray absorption spectroscopy at the free electron laser at Pohang Accelerator Laboratory. Here I have to thank Dr. Andrew Attar (again) and Dr. Alexander Britz for helping and including me in the ultrafast electron diffraction experiments on 2D materials at the SLAC national laboratory. Additionaly, Dr. Eric Gullikson and Dr. Yi-De Chuang have helped me acquiring many XUV spectra of 2D materials at the Advanced Light Source. The synthesis of 2D materials in this work was conducted at the Molecular Foundry under the supervision of Dr. Adam Schwartzberg, who taught me about the use of the Raman microscope and the atomic layer deposition in the clean room, Dr. Christopher Chen, who taught me about the use of tube furnace, various 2D material synthesis and transfer techniques, and running the grazing incidence wide angle X-ray scattering experiment at the Advanced Light Source, Dr. Shaul Aloni, who helped me acquiring transmission electron microscope images of the 2D thin films, and Liana Klivansky, who helped us acquiring X-ray photoemission spectra to characterize our samples. The study on 2D materials in this work has largely benefited from the discussion and help from the group led by Prof. Vincent Tung at KAUST, whose members Dr. Areej Aljarb, Xuan Wei, and Jui-Han Fu have provided us various samples for testing and helped us with characterizations. I would also like to thank our theory collaborators Dr. David Prendergast, who provided a lot of insights in our discussions on the experimental results, and Prof. Volodymyr Turkowski, who taught me a lot on time-dependent density functional theory calculations. In addition, I would like to thank Prof. Felipe da Jornada and Prof. Diana Qiu for helping us on many-body GW-Bethe-Salpeter equation calculations, Dr. Angel Garcia Esparza and Dr. John Vinson for providing guidance on calculating core-level absorption spectra, Dr. Aravind Krishnamoorthy and Tom Linker on the study of $MoTe_2$,

and Naseem Ud Din and Shree Ram Archaya for helping us calculating optical transition dipole moments in nickel.

I would like to thank our university and department staff, in particular, Kathleen Buckley, Michelle Haskins, Lynn Keithlin, Ellen Levitan, Joel Adlen, and Erin Skelly, for guiding me through all the administrative matters. I would also like to thank Philip Simon and Eric Granlund for helping me build the experimental apparatus and teaching me about machining.

Last but not least, I would like to thank my parents and my aunt and uncle. Without their help and care (even it's from remote), my life as a student in Berkeley would have been more difficult and their mental support and care are fundamental to the completion of this work.

Chapter 1

Introduction

The observation and measurement of the dynamics in physical and chemical processes are fundamental to the understanding of their mechanism and further applications. The recording of dynamics of physical objects started from chronophotography in the second half of the 19^{th} century.[1] Using a rolling shutter, the motion of an object could be recorded with resolution down to milliseconds. The invention of flash lamp technology enabled photorecording of high-speed projectiles with time resolution down to microseconds and gave birth to one of the most important pillars in the contemporary ultrafast science — pump-probe spectroscopy. With flash lamp technology, a physical or chemical system can be impulsively excited and the dynamics following the photoexcitation are synchronized by the short duration of the excitation pulse. Next, the evolution of the system can be interrogated by the second flash of light which is time-delayed with respect to the photoexcitation pulse [2]. The pump-probe technique allows the investigation of mechanisms of chemical reactions. For example, Kok et al. utilized the flash lamp technique to determine the number of intermediate steps in the oxygen evolution reaction in photosynthetic complexes before the advent of ultrafast lasers [3].

Dynamics in condensed matter spans a wide range of timescales. The translational motion of molecules, such as molecular diffusion and reorganization of protein structures, occurs at microsecond to millisecond timescales. Molecular rotation typically takes place at nanosecond to picosecond timescales, whereas electronic and vibrational motion occur at picoseconds to below 1 fs [2]. The time resolution of pump-probe spectroscopy using light sources controlled by electronic gating technology, such as flash lamps and Q-switched laser sources, is limited to nanoseconds or hundreds of picoseconds due to the limitation in the electronic switching speed. The observation of electronic and vibrational dynamics in real-time thus requires a different light source that provides femtosecond time resolution.

With the development femtosecond laser sources [4], in particular, the Ti:sapphire laser [5], which provides sufficient gain bandwidth to allow generation of sub-10 fs pulses, femtosecond dynamics of atoms, molecules, and solids can be directly visualized. With nonlinear optical techniques for wavelength conversion, such as sum-frequency generation and optical parametric

[1] e.g. see references in Ref. [1]

amplification [6], ultrafast pump-probe spectroscopy ranging from terahertz to vacuum ultraviolet regimes has become a widespread tool to investigate photophysical and photochemical phenomena [2]. The scheme of optical pump-probe spectroscopy is depicted in Fig. 1.1. After pump-pulse excitation, the probe pulse detects the decrease of ground state population from a negative change of absorbance (ΔA), termed ground state bleaching, and the new absorption pathways from the pump-induced population in the excited state manifold, namely, excited state absorption. However, as the electronic excited states in condensed matter are highly congested, and in particular, the band-to-band transitions in solids are continuous rather than discreet, the signal of ground state bleaching and excited state absorption may have significant overlap that encumbers the interpretation of the transient absorption results.

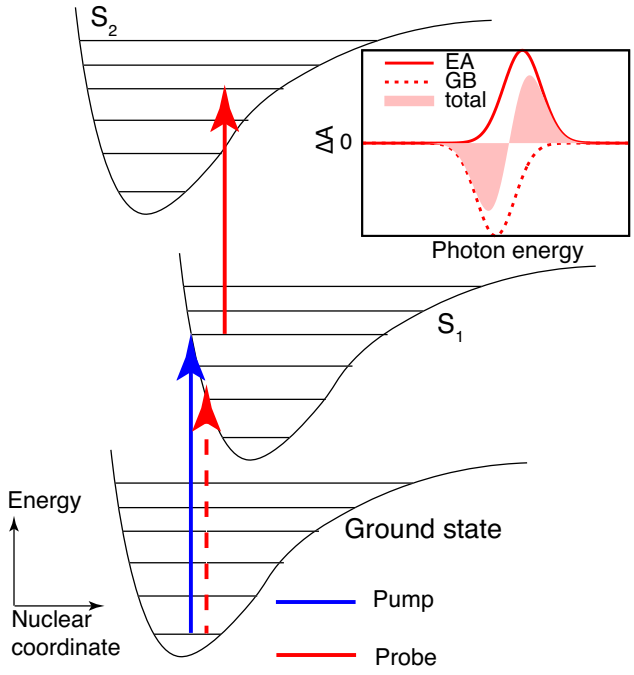

Figure 1.1: Scheme of optical pump-probe spectroscopy. The pump pulse is designated in blue and the probe in red. The ground state bleach (dashed line) and excited state absorption (solid line) are denoted as GB and EA respectively.

To resolve the excited state dynamics in condensed matter, nonlinear spectroscopies beyond optical transient absorption have been developed [7]. For example, multi-dimensional optical spectroscopies can resolve different excitation mechanisms and electronic and vibrational relaxation pathways. The highly congested optical excited states also prevent state-specific probing of dynamics such as electron scattering. For example, the visible spectrum spanning 400-700 nm can already harbor a large number of vibronic states or valence to conduction band transitions. However, the bandwidth of the visible spectrum ($\sim$ 1.3 eV) has a transform-limited pulse duration of 3.2 fs, indicating that any pulse shorter than 3 fs requires a larger bandwidth than the visible spectrum.

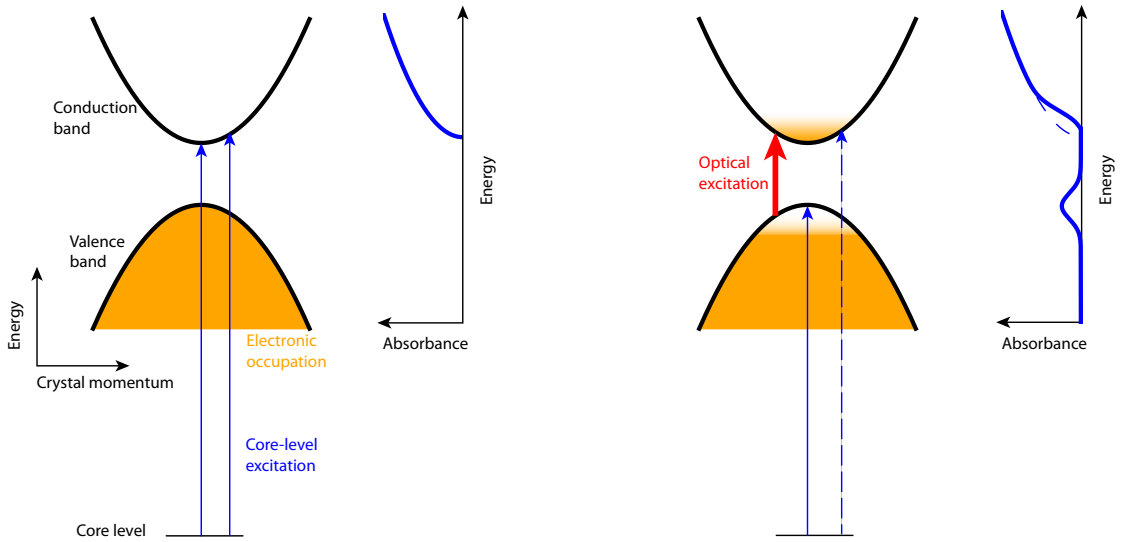

Figure 1.2: A simplified scheme of core-level transient absorption. The left panel shows the core-level absorption before optical excitation (static) and the right panel exhibits the changes of core-level absorption after optical excitation. The static absorption spectrum is displayed in dashed blue line in the right panel as a reference.

Therefore, it is important to develop a method that provides femtosecond to subfemtosecond time resolution and is capable of resolving electronic and structural dynamics after photoexcitation.

Core-level transient absorption spectroscopy involving an optical pulse and an extreme ultraviolet (XUV) or X-ray pulse provides an alternative route to directly resolve the electronic and structural dynamics in the valence shell [8]. Figure 1.2 presents a highly simplified scheme of core-level transient absorption spectroscopy in solids. An optical laser pulse first illuminates the sample to create photoexcited electron-hole pairs, and the sample is subsequently probed by an XUV or X-ray pulse that excites the core electrons to the empty orbitals in the valence shell. As the optical excitation changes the occupancy of the orbitals in the valence shell, the photoexcited carrier distribution can be extracted from the difference between the core-level absorption with (on) and without (off) the optical pulse:

$$\Delta A = \Delta A_{on} - \Delta A_{off}. \tag{1.1}$$

Similarly, the changes of the valence energy levels due to changes of electronic screening, phonon heating, and lattice displacement can also be visualized via core-level absorption. It is thus possible to visualize and resolve both electronic and structural dynamics using core-level transient absorption spectroscopy.

Unlike broadband optical transient absorption in solids where electrons in the valence band with a range of different energies can be excited due to band dispersion, core-levels are nearly dispersionless across the whole Brillouin zone. Therefore, in the single particle mean-field picture,

the energies of core-level excitations are solely due to the energy of the valence orbitals the electrons are excited to and in core-level transient absorption spectroscopy, the signal from carriers at different energies can be separated [9].

In addition, the core-levels of different atomic species are typically separated by several to hundreds of electronvolts, enabling element specific probing of valence electronic structure. The large energy separation between core-levels and valence excitations further allows the use of ultra-broadband XUV or X-ray pulses spanning tens to hundreds of electronvolts as a probe, whose large bandwidths support femtosecond to attosecond pulse durations [10].

Core-level spectroscopy was pioneered with the development of bremsstrahlung X-ray sources in the first half of the 20^{th} century [11]. X-ray photons are emitted with accelerated charged particles such as high energy electron beams impinging on a metal target, or relativistic electron bunches traveling in magnetic fields [12]. Synchrotron light sources, where electrons traveling at velocities near the speed of light traverse a series of magnets termed "undulators", generate X-ray photons with brilliance up to 10^{22} photons/sec/mrad^2/mm^2/[0.1% BW] and facilitate a wide range of studies including X-ray absorption and photoemission spectroscopy, X-ray scattering and diffraction, and X-ray microscopy and tomography [13]. However, the duration of the X-ray pulses produced with a synchrotron is limited by the length of electron bunches, which are difficult to compress due to the Coulomb repulsion of electrons, and it is highly challenging to generate <1 ps X-ray pulses with synchrotrons [14].

The generation of tens to a hundred femtosecond long coherent X-ray pulses has been achieved with the advent of free electron lasers [15]. As relativistic electron bunches travel through a long undulator, the electrons can interact with the electric field of the emitted radiation and form "microbunches" that produce short, coherent X-ray pulses [13]. Although free electron lasers produce X-ray pulses with improved pulse duration and coherence compared to synchrotrons, performing pump-probe experiments with free electron lasers is nontrivial. First, the construction and operation of free electron lasers require large facilities and are thus not available at a lab-based table-top scale. In addition, the long distance required for electron acceleration in a free electron laser makes it difficult to phase-lock the pump and probe pulses [16].

With the development of high power laser amplifiers using chirped pulse amplification [17], direct generation of XUV and X-ray pulses via nonlinear laser optics has been achieved by focusing laser pulses with $> 10^{13}$ W/cm^2 peak intensity in rare gas media [18]. The process, termed "high harmonic generation", produces photons with tens to hundreds of times the frequency of the fundamental driving field [19]. For example, using laser pulses produced by a Ti:sapphire laser amplifier centered around 800 nm, it is possible to generate XUV and soft X-ray photons with >120 eV energy, capable of exciting core electrons in many different atoms [20]. The XUV and soft X-ray field produced via high harmonic generation is intrinsically phase-locked with the fundamental driving field. The setup only requires a laser with high peak power and can be fit on an optical table in a single laboratory.

The high harmonic generation process is purely optical and can be controlled by the shaping of the fundamental driving field and the generation media. Using near single-cycle driving fields whose pulse duration is smaller than two periods of the field oscillation, XUV and X-ray pulses with less than 0.1 fs (=100 as) duration have been generated [10, 21]. The subfemtosecond XUV

and X-ray pulses provides unprecedented time resolution for investigating ultrafast electronic and structural dynamics.

Pump-probe experiments utilizing an optical pulse and a subfemtosecond XUV or X-ray pulse, termed "attosecond transient absorption spectroscopy", have been utilized to explore the decoherence in strong-field ionized atoms [22], decay of atomic autoionizing states [10, 23, 24], ponderomotive effects on transition dipoles of autoionization states [25], and vibrational wave packet dynamics in molecules [26]. In solids, attosecond transient absorption spectroscopy (ATAS) has been used to investigate the AC Stark shift of core-excited states [27], tunneling and field-enhanced excitation of carriers [28, 29], carrier relaxation and recombination in semiconductors [9, 30], decay of core-excitons [31–33], changes of electronic screening in photoexcited metals [34], dynamical Franz-Keldysh effect via inner valence excitations [35], and femtosecond photoinduced demagnetization [36].

In this work, I present the experimental findings in electronic and structural dynamics in solids with attosecond transient absorption spectroscopy. Chapter 2 outlines the experimental technique — near single-cycle optical pulse generation, high harmonic generation, and detection and characterization of the optical and XUV beam — along with details of the table-top experimental setup. Chapter 3 presents the real-time observation of hole relaxation, carrier recombination, and coherent phonon oscillations in photoexcited 2H-$MoTe_2$, a layered semiconductor. In Chapter 4, I discuss the hole relaxation dynamics in WS_2 along with the observation of carrier-induced modifications on core-exciton transitions. Chapter 5 presents our investigations on the sub-40 fs electron thermalization and relaxation dynamics in photoexcited nickel; in Chapter 6, I discuss the dynamics of core-excitons and their decay in NaCl, and in Chapter 7, an experimental technique to simultaneously generate sub-5 fs laser pulses centered at 800 nm and 400 nm (3 eV) is presented, enabling the investigation of photoinduced dynamics in wide band gap semiconductors. The work presents a comprehensive methodological study on the interpretation of core-level transient absorption spectra and unraveling the underlying electronic and structural dynamics. Starting from an electronically screened semiconductor where core-level excitations can be understood in a single-particle picture (Fig. 1.2), I advance to semiconductors and insulators where the attraction between the electron and the core hole, namely, the core-excitonic effect, is not negligible. Further, I discuss the interpretation of core-level transient absorption spectra of metals, where the scattering between the electrons at the Fermi surface mediated by the core hole potential is so strong that the core-level absorption spectra is strongly renormalized [37]. By studying photoexcited metals, semiconductors, and insulators with ATAS, this work paves the way for real-time observation and extraction of electronic and structural dynamics in more complex materials such as heterostructures, superlattices, and alloys, where the element specificity of core-level spectroscopy can be exploited to enable domain-selective detection of electronic and structural dynamics.

Chapter 2

Experimental Techniques

The measurements in this work were conducted on an optical-XUV pump-probe setup, where a broadband optical pulse and an XUV pulse both illuminate the sample and the absorbance of the XUV is recorded as a function of time delays between the optical and XUV pulse. A schematic of the experiment is illustrated in Fig. 2.1. The optical pulse is time-delayed with respect to the XUV pulse via a retroreflector and focused onto the sample by a concave mirror (focal length f=1.25 m). In general, the time delay t between the two pulses is defined such that positive t indicates that the optical pulse arrives before the XUV pulse. The optical and XUV beam are combined collinearly by a motorized annular mirror. A motorized stage is positioned at the focus of both optical and XUV beam. A sample holder for thin film samples and a cylindrical gas cell with 2 mm diameter are placed on the stage to enable optical-XUV pump-probe studies on both solid-state and gaseous media. After the sample stage, a sub-micron thick metal filter is used to block the optical pump beam whereas the XUV beam transmits through the filter and is dispersed by a rotatable toroidal flat-field grating (Hitachi 001-0437) onto an XUV CCD camera (Princeton Instruments PIXIS 400B).

The XUV beam is produced by high harmonic generation of the driving laser pulse in a noble gas medium. Figure 2.2 outlines the instrumentation for XUV light generation and propagation. The XUV beamline is enclosed in high vacuum chambers with a base pressure of approximately 10^{-6} torr. The high harmonic generation process takes place in a finite gas cell with a path length of 4 mm.[1] Metallic filters are placed on a push-pull mount after the gas cell to block the optical driving beam. When the spectral region of interest is between 20-73 eV, 0.1-0.2 μm thick aluminum filters are used and 0.15 μm thick Zr filters are used for XUV light between 70-150 eV. The XUV beam is focused onto the sample with an off-axis toroidal mirror with incidence angle of 80°and focal length of 1 m.

Figure 2.3 depicts the optical beamline for generation of broadband, $\leq$ 4 fs optical pulses for the optical arm and the high harmonic generation arm. In brief, laser pulses centered at 790 nm with 1.4-1.8 mJ pulse energy and nominal pulse duration of approximately 30 fs are produced by a laser amplifier operating at 1 kHz. The laser beam is focused into a neon-filled hollow core fiber to

[1] Stainless steel and machinable ceramic (Macor) gas cells have been used. The gas cells made of machinable ceramic have much higher damage threshold and are more durable.

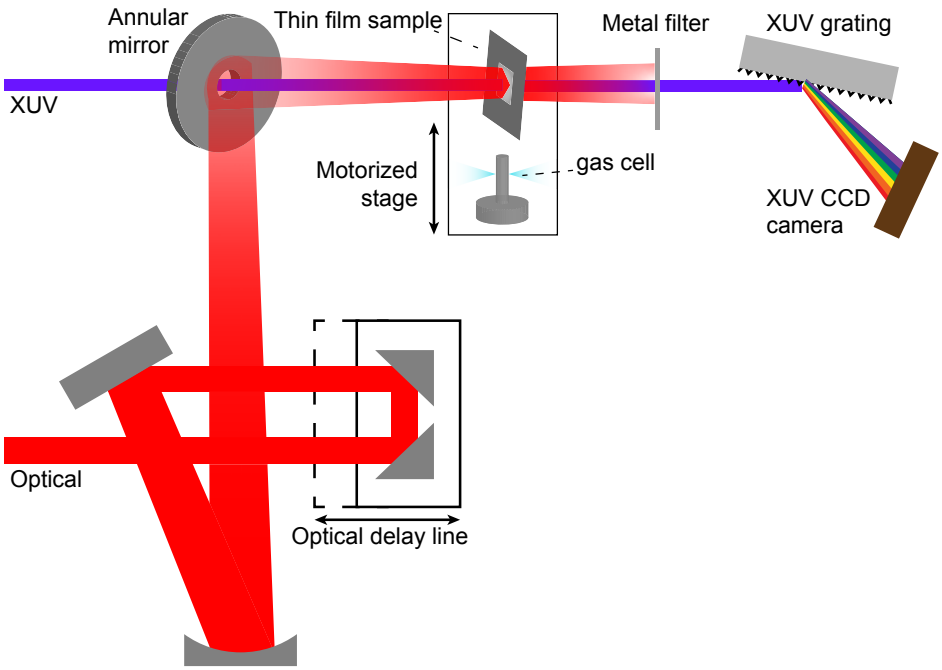

Figure 2.1: Scheme of the optical-XUV pump-probe experiment.

achieve spectral broadening via self-phase modulation. A mechanical chopper is placed after the fiber outlet to lower the pulse repetition rate in the experiments so as to prevent sample damage. The laser beam is subsequently recollimated into a chirped mirror compressor to compensate the dispersion accumulated during beam propagation, and the beam is split into two arms via a beamsplitter, where the majority of the photons transmit through the beamsplitter and are sent into the high harmonic generation gas cell (Fig. 2.2). Photons in the other arm are sent along the optical delay line and recombine with the generated XUV via an annular mirror (Fig. 2.1). Detailed descriptions of the instrumentation and principles of operating the setup are recounted in the following sections.

2.1 Short Laser Pulse Generation

2.1.1 The Laser Source

The light source in the experimental apparatus is a Ti:sapphire multipass chriped pulse amplifier (Femtopower Compact Pro) seeded by a broadband femtosecond Ti:sapphire oscillator (Femtolaser Rainbow). Laser pulses centered at 790 nm wavelength with <30 fs duration and 1 kHz repetition rate are generated by the amplifier. Figure 2.4 displays the typical spectrum and measured auto-correlation trace of the amplifier output. The output pulse energy of the amplifier ranges between 1.2–1.8 mJ depending on conditions of operation. The output spectrum of the amplifier is controlled

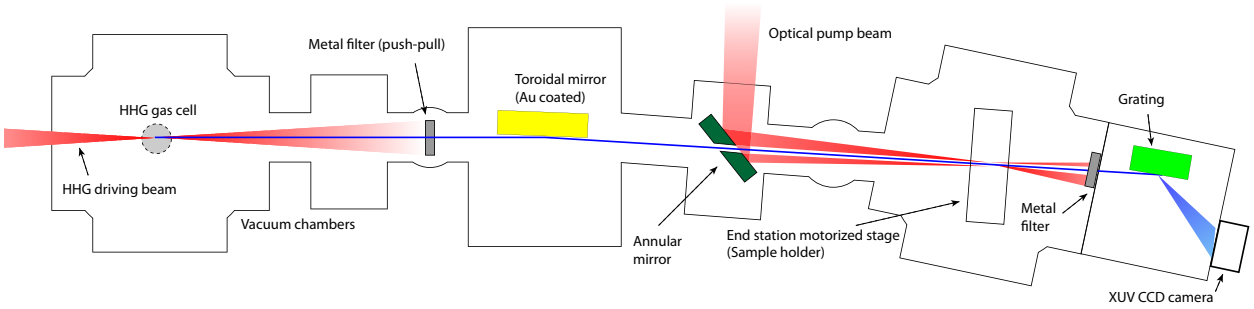

Figure 2.2: Layout of the optical beamline including the high harmonic generation stage and the endstation.

by an acousto-optic pulse shaper (Fastlite DAZZLER) located after the 4^{th} pass in the amplifier. In combination with a pair of transmission gratings as the pulse compressor, the acousto-optic pulse shaper also controls the dispersion of the output pulse. The laser pulses are carrier-envelope-phase stabilized by two separate devices in the oscillator and the amplifier.

The carrier envelope phase (CEP) ϕ for a Gaussian pulse $\mathcal{E}(t) = \mathcal{E}_0(t)\cos(\omega t + \phi)$ defines the relative phase between the field oscillation and the center of the pulse envelope $\mathcal{E}_0(t)$.[2] CEP can be measured in an f-$2f$ interferometer, where the spectrum of the fundamental is broadened to span more than an octave and the interference between the fundamental and its second harmonic is recorded. Interference between the overlapped second harmonic and the fundamental produces a frequency comb, and the CEP is retrieved from the phase of the Fourier transform of the frequency comb [38]. On the other hand, for the laser oscillator, the CEP is measured by interference between the fundamental and the field produced by difference frequency generation (DFG) between the high and low frequency end of the spectrum of the fundamental. The interference between the fundamental and the DFG signal produces a microwave frequency beating signal that can be locked to an external local oscillator. The frequency of the beat signal f_b is related to the CEP by $f_b = nf_r \pm \phi f_r/(2\pi)$ [39, 40], where f_r is the repetition rate and n is an integer.[3]

In the laser oscillator, the CEP is controlled by an acousto-optic modulator, which modulates the intensity of the pump laser beam, and a pair of movable fused silica wedges in the cavity that compensates the slow drift of the CEP. The CEP is measured by simultaneous self-phase modulation (SPM) and DFG of the laser pulses in a periodically-poled lithium niobate (PPLN) crystal [41, 42]. A long-pass dichroic mirror with cut-on wavelength at 1250 nm is placed after the PPLN crystal to

[2]Here we assume $-\pi \leq \phi \leq \pi$.

[3]The principle of CEP detection through second harmonic generation (SHG) and DFG can be briefly described as the following. Considering a laser field $\mathcal{E}(t) = \mathcal{E}_0(t)\cos(\omega t + \phi)$, the field of the SHG signal can be written as $\mathcal{E}_{SHG} \sim \cos(2\omega t + 2\phi)$ and the field of the DFG signal $\mathcal{E}_{SHG} \sim \cos((\omega_1 - \omega_2)t)$ where ω_1 and ω_2 belong to the high and low frequency edge of the spectrum of the fundamental. The CEP ϕ can thus be retrieved by interfering the SHG or DFG signal with the fundamental, where the interference signal $\mathcal{E}_{if} = |\mathcal{E}_{SHG/DFG} + \mathcal{E}|^2$. The cross term $\mathcal{E}\mathcal{E}_{SHG/DFG} \sim \cos(\omega_{if}t \pm \phi)$, and ω_{if} is the frequency of spectral overlap between the fundamental and SHG/DFG field.

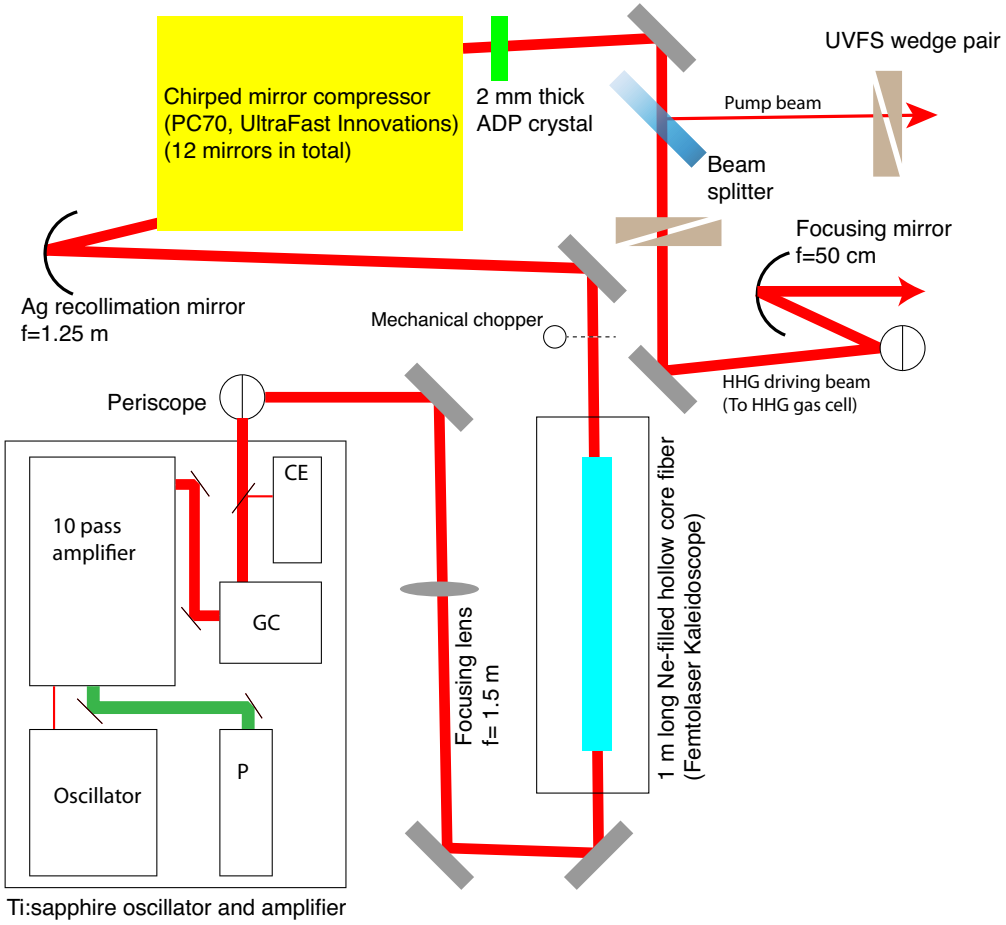

Figure 2.3: Layout of the optical beamline including the light source, supercontinuum generation, and pulse compression stage. P: pump laser for the amplifier (Photonics Industries DM30). GC: transmission grating compressor. CE: f-$2f$ interferometer for carrier envelope phase detection (Menlosystems APS 800).

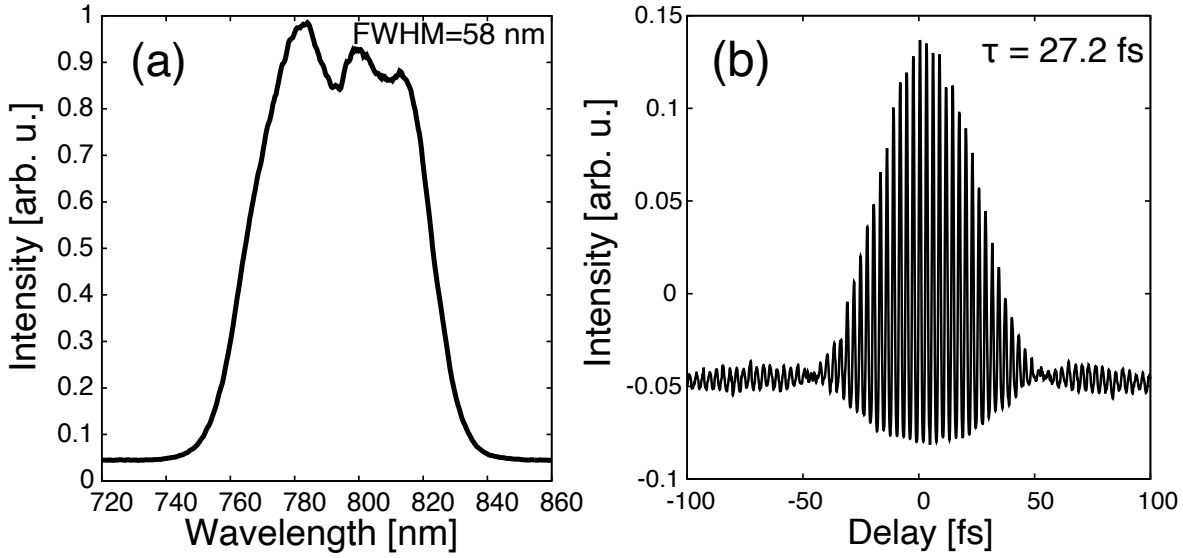

Figure 2.4: (a) A spectral sample of the output pulse from the laser amplifier. (b) shows a typical autocorrelation trace of the laser pulses produced by the amplifier.

separate the long-wavelength interference signal from the main beam. The long-wavelength beam containing the interference between the fundamental and the DFG signal passes through another long-pass filter to clean up the remnants of short-wavelength light. The beat signal is detected by an InGaAs avalanche photodiode. To stabilize the CEP, the beat signal is locked to an external local oscillator with frequency at $f_r/4 \approx 20$ MHz.

In the laser amplifier, an f-$2f$ interferometer (Menlosystems APS 800) is placed after the grating compressor to measure the CEP. The amplifier output beam is split off by a beamsplitter and the split-off beam is first broadened by SPM in a sapphire plate and frequency-doubled in a β-barium borate (BBO) crystal. A polarizer is used to project the electric field of the fundamental and the second harmonic onto the same plane. The interference-generated frequency comb is measured in a high-speed UV-Vis spectrometer. The extracted CEP is transmitted into a proportional–integral–derivative (PID) controller that controls the piezo-mounted prism pulse stretcher modulating the CEP.

2.1.2 Supercontinuum Generation

The millijoule pulses from the laser amplifier are focused into a 1 m long neon-filled hollow core fiber (HCF) by a fused silica lens to generate a supercontinuum spanning 500-1000 nm wavelength via self-phase modulation (SPM) [43]. The spectrum of the input pulse and the generated supercontinuum are presented in Fig. 2.5. The focal length of the fused silica lens is specifically chosen to match the diameter of the focal spot to the inner diameter of the HCF [44]. Coupling of the laser beam into the HCF is facilitated by mounting the focusing lens onto a linear

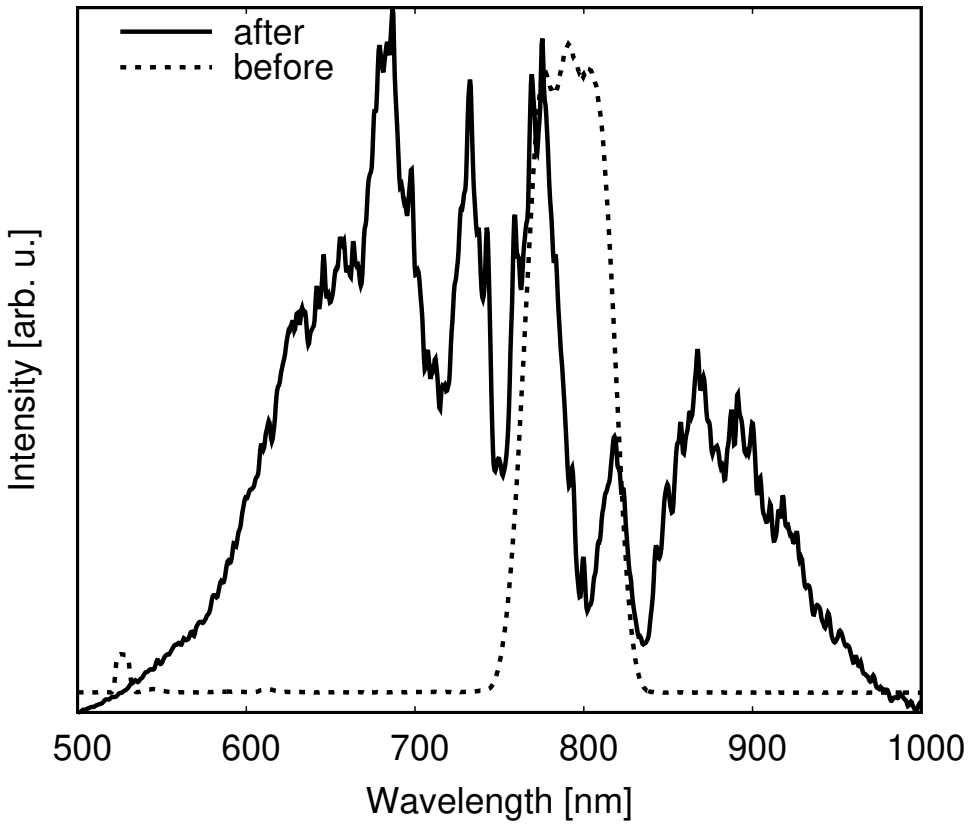

Figure 2.5: Typical spectrum of the laser pulses before and after supercontinuum generation in the hollow-core fiber.

stage that moves along the beam axis. An iris is mounted between the focusing lens and the inlet of the HCF to fine tune the focal spot size and clean up the laser mode. One-point active beam pointing stabilization is installed to ensure long-term pointing stability at the inlet of the HCF.

The pulse energy and spectrum out of the HCF are controlled by the Ne gas pressure inside the HCF, the dispersion of the incoming beam, and the quality of the beam coupling into the fiber. Maximum transmission of the HCF (approximately 73%) [44] is achieved when the HCF is fully evacuated. With an increase of Ne pressure, the transmission decreases to between 40-50%. The spectral broadening increases with Ne pressure. However, at high Ne pressures or high input pulse energies, the mode of the output becomes fragmented. Therefore, the Ne pressure and the input pulse energy, which can be controlled by the iris before the HCF entrance, should always be balanced. Note that instead of using SPM in the Ne gas, white light can also be generated when the laser beam clips into the glass fiber wall. Clipping the beam by the glass fiber wall can damage the fiber and thus care should be taken when optimizing the output spectrum of the HCF. Clipping the beam with glass can be avoided by observing the output mode and the inlet of the fiber. When the

laser beam clips into the fiber wall, bright white light scattering can be observed at the inlet of the fiber and higher order modes will become more prominent in the fiber output.

Fibers with diameters of 320 μm and 250 μm have been used in the course of the experiments. While the fiber with larger diameter typically has higher transmission, the stability of the output mode is degraded. This is because the transmission of higher order laser modes increases with increasing fiber diameter. For the HCF with 320 μm, the required Ne pressure for spectral broadening typically ranges from 2-2.8 bar and the typical transmission is 50%. The Ne pressure required to generate a supercontinuum in the 250 μm diameter fiber is between 0.9-1.7 bar and the typical transmission of the HCF is 40%. Despite the higher transmission of the 320 μm fiber, the output mode cannot be maintained for more than 12 hrs, whereas the output mode of the 250 μm fiber can typically be maintained for longer than 18 hrs.

2.1.3 Dispersion compensation

The dispersion of the laser pulse is compensated by a set of broadband double-angle chirped mirrors (PC70, UltraFast Innovations) [45]. A 2 mm thick ammonium dihydrogen phosphate crystal is inserted after the chirped mirror compressor to compensate third order dispersion [46]. After the beamsplitter that separates the pump and probe arm, each arm is equipped with a pair of UV-grade fused silica wedges mounted on a linear stage to allow fine tuning of the dispersion. The wedge pair in the probe arm can also be used to control the CEP of the laser pulse for high harmonic generation.

Fine tuning of dispersion compensation for the pump arm is achieved by placing a BBO crystal in front of the sample position inside the chamber for frequency doubling and maximizing the intensity of the second harmonic generation (SHG) signal.[4] A sample SHG spectrum of the pump pulse is shown in Fig. 2.6. Dispersion of the probe arm is tuned by maximizing the cut-off energy and flux of the XUV photons produced via high harmonic generation. The relation between the cut-off energy in high harmonic generation and the driving pulse is discussed in Sec. 2.2.

2.1.4 Pulse Characterization

The temporal profile of the broadband optical pulse is characterized by dispersion scan (D-scan, Sphere Photonics) [47]. The device comprises a pair of motorized glass wedges, a set of chirped mirrors for dispersion compensation, a 5 μm thick BBO crystal for second harmonic generation (SHG), and a broadband spectrometer covering 200-1100 nm wavelengths (Fig. 2.7). To unravel the temporal profile of the optical pulse, SHG spectra of the optical pulse with varying position of the glass wedges, which controls the dispersion of the pulse, are measured, and the spectral phase of the optical pulse is retrieved by minimizing the error of the simulated SHG spectra based on the spectrum of the optical pulse using the downhill simplex algorithm [48] with multiple basis sets [49].

[4] Note that white light can also be generated in the BBO via self-phase modulation (SPM). The SPM signal typically occurs below 450 nm and the SHG signal occurs between 350-450 nm and thus the two can be separated.

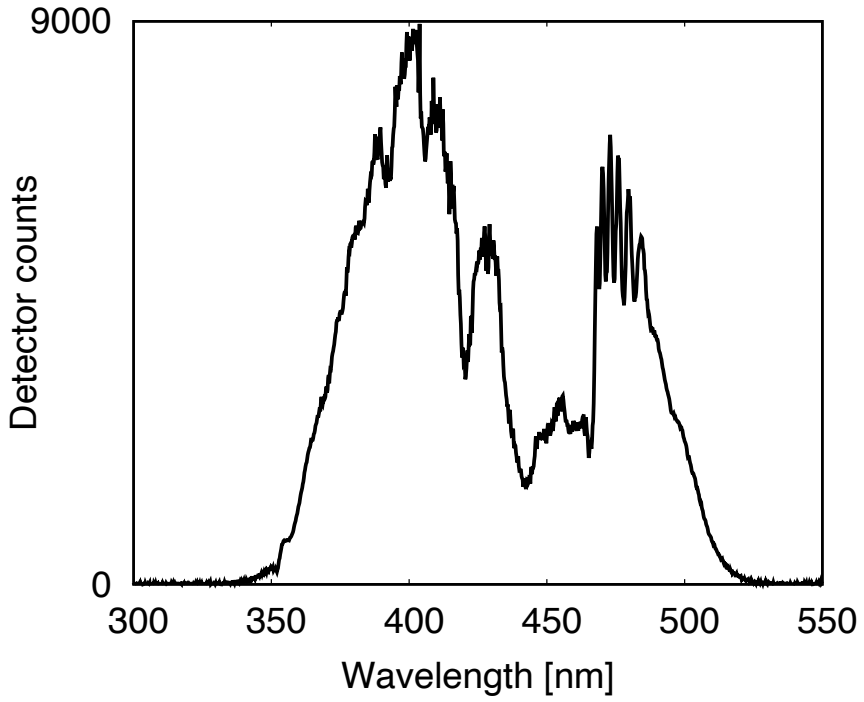

Figure 2.6: Sample spectrum produced by second harmonic generation of the pump pulse.

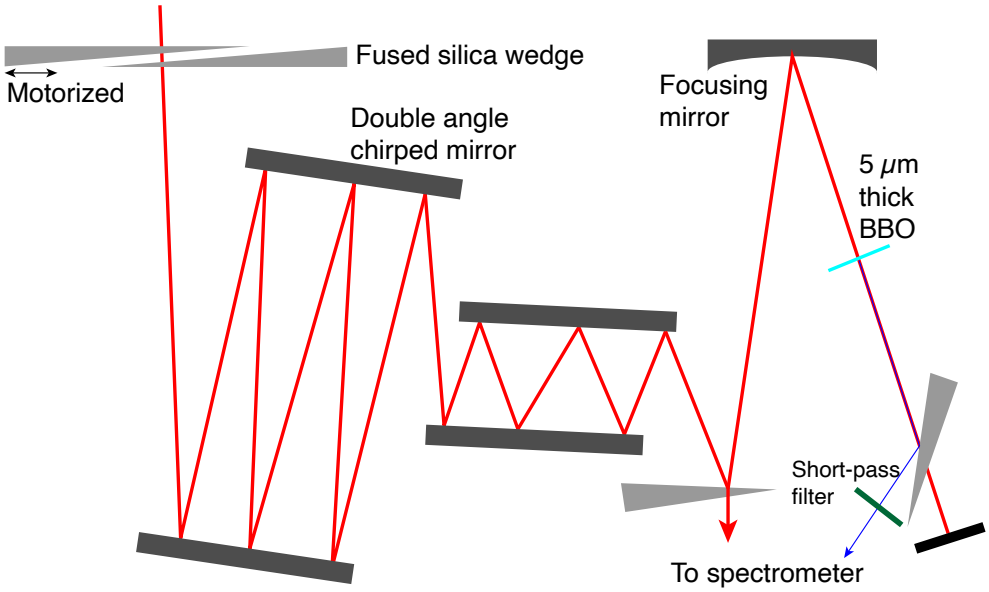

Figure 2.7: The optical layout scheme of dispersion scan.

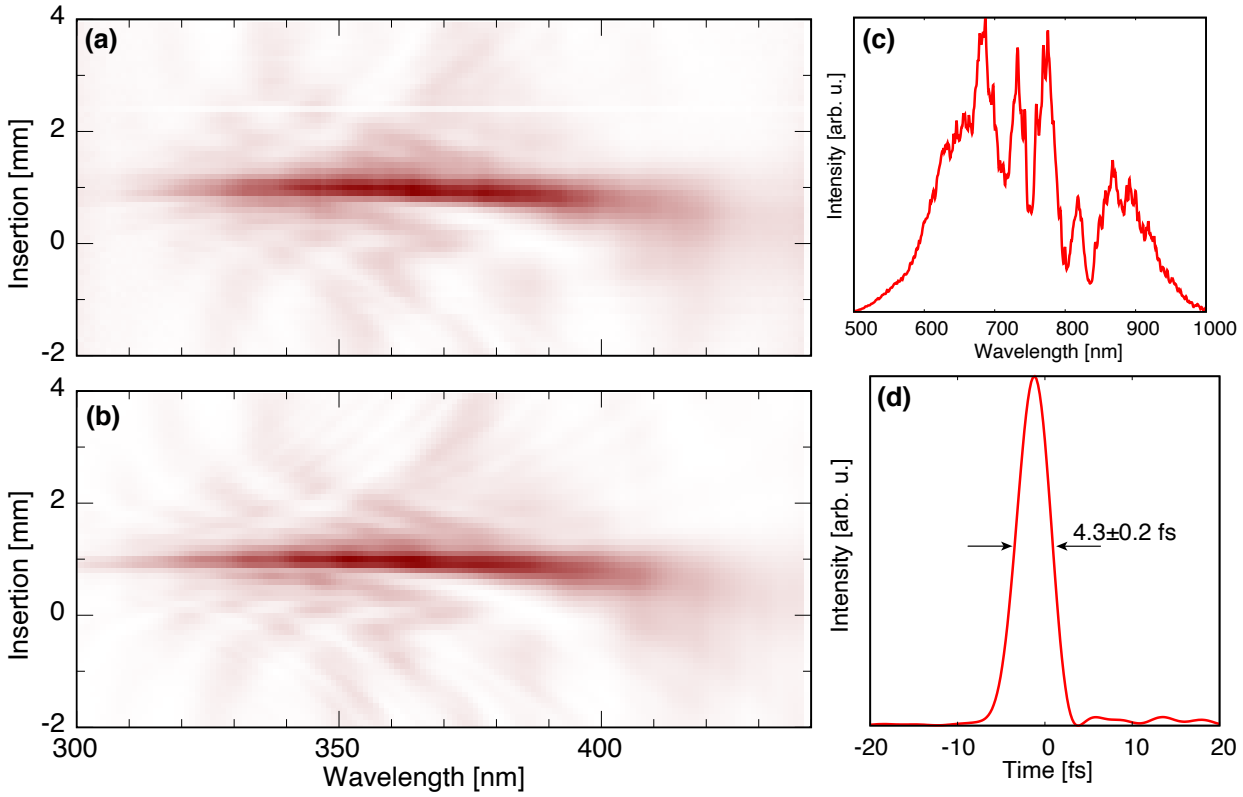

Figure 2.8: (a) Measured and (b) simulated SHG spectra as a function of glass wedge insertion in dispersion scan. (c) shows the measured spectrum of the optical pulse and (d) the retrieved temporal profile.

Figures 2.8(a) and (b) show the measured and simulated results of the dispersion scan. The strongest SHG signal occurs at 1 mm glass insertion, matching the thickness of the laser window on the vacuum chamber for the pump beam. Non-zero higher order dispersion in the laser beam introduces a wavelength dependence on the maximum SHG signal as a function of glass insertion. The dispersion scan result in Fig. 2.8 exhibiting maximum SHG signal at a single glass insertion position for all wavelength indicates that higher order dispersion is minimized.

2.2 Broadband XUV Pulse Generation and Characterization

2.2.1 Introduction to High Harmonic Generation

High harmonic generation is a nonlinear optical process in which an electromagnetic wave with frequency ω is up-converted by interacting with a medium to generate photons with frequencies of $N\omega, (N \gg 2)$ [50]. The high harmonic generation (HHG) process can be described in a

semiclassical *three-step model* [51, 52] and the scheme of HHG in noble gases is illustrated in Fig. 2.9. First, near the peak of the laser field, the atomic Coulomb potential is strongly modified such that the electrons tunnel out and the atoms become ionized. Secondly, the tunneling electrons are accelerated by the driving electric field and gain kinetic energy. As the electric field changes sign, the electrons are driven back to the parent atoms. During recombination with the atoms, the energy of the electrons are emitted as high energy photons. As the tunnel ionization event occurs when the electric field magnitude reaches its maximum, a "burst" of high energy photons occurs at every half-cycle of the driving field. If the duration of the driving pulse is much longer than the period of the field oscillations ($2\pi/\omega$), an XUV pulse train will be generated within the envelope of the driving field (Fig. 2.9, upper panel). While the spectrum of each individual XUV "burst" is continuous, the spectrum of the pulse train is composed of discrete peaks separated by 2ω due to the half-cycle periodicity in the pulse train. Therefore, the generation of attosecond, broadband XUV pulses requires limiting the electron-atom recombination event to only once per driving pulse. Techniques to achieve attosecond pulse generation are listed as follows.

Amplitude gating. The amplitude gating technique limits the number of recombination events by allowing only a single cycle of the driving pulse to have sufficient amplitude to tunnel-ionize the atom [53]. This requires reducing the width of the pulse envelope to near single cycle. For a driving pulse with spectrum centered near 800 nm wavelength, a pulse duration of approximately 3 fs is required.

Polarization gating. The prevention of multiple recombination events can be achieved by introducing opposite circular polarization to the leading edge and trailing edge of the driving pulse [20, 54–57]. The circularly polarized electric field prevents recombination events by directing the ionized electron away from the atom [54] and the opposite circular polarization between the leading and trailing edge of the pulse results in linear polarization of the field at the center of the pulse envelope, which is able to facilitate recombination. Polarization gating can be further combined with two-color gating, where the driving pulse is modified by its second harmonic, to enable single isolated attosecond pulse generation from driving pulses with duration up to 12 fs [58]. Although the polarization gating technique is able to generate single isolated attosecond pulses [20, 56, 57], the fluence of the generated XUV light is typically much lower and the technique is not used in the experiments described in this work.

Ionization gating. Single isolated XUV pulses can be obtained by destroying phase-matching of the HHG process except at the leading edge of the driving pulse [59, 60].[5] As an intense laser pulse interacts with a noble gas medium, the time-dependent ionization rate increases with the electric field strength. When the density of ionized atoms exceed the critical ionization threshold, the negative dispersion of the electron-ion plasma can no longer be compensated by the positive dispersion of the neutral gas, thereby destroying the phase-matching of the HHG process [61].

[5] Description of phase-matching in HHG will be discussed in the following.

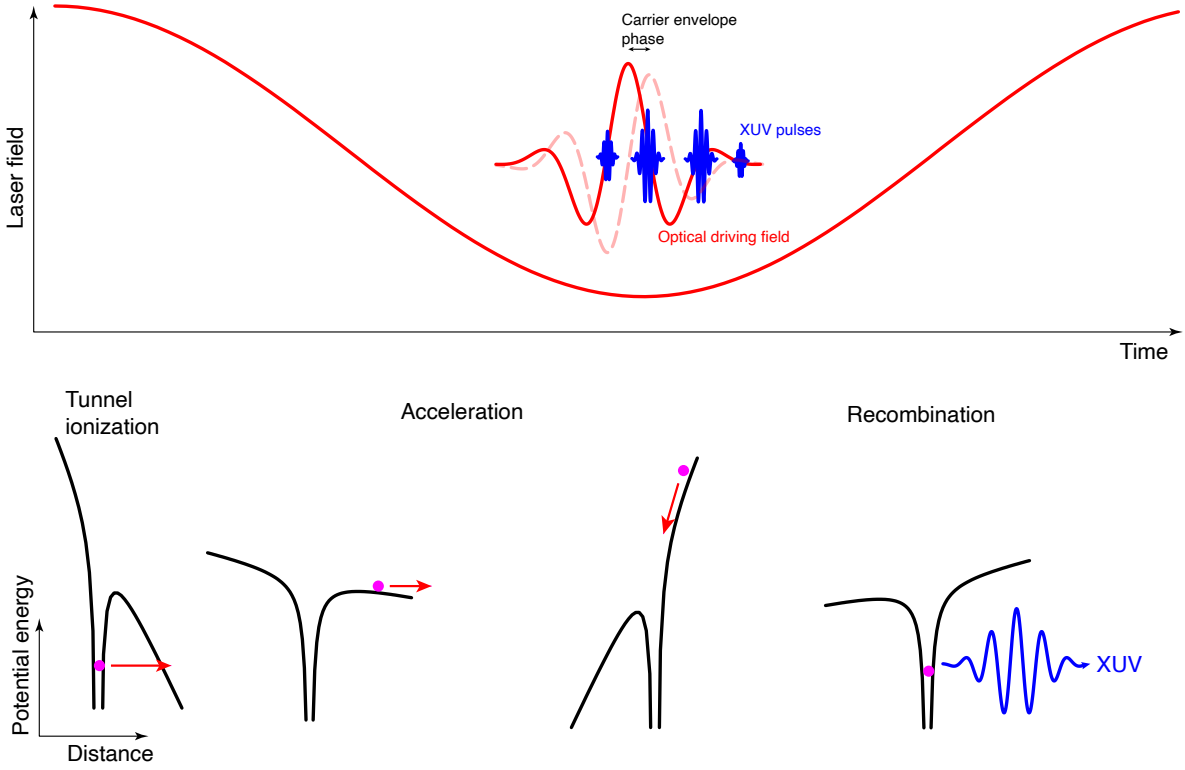

Figure 2.9: Scheme of high harmonic generation in a gaseous medium. The driving field is marked in red and the high harmonic XUV field is marked in blue. The electron moving according to the combined potential (black in the lower panel) due to atomic Coulomb interaction and the driving field is denoted by a magenta dot.

Ionization gating is particularly effective for gases with low ioinization potentials such as Xe, Kr, and Ar.

The experiments described in this work use a combination of amplitude and ionization gating to generate broadband XUV pulses with continuous spectra.

2.2.2 Tuning of XUV Spectra

Theoretical background

The XUV spectra produced through HHG can be controlled by the the gas medium, the peak intensity, pulse duration, and the wavelength of the driving field, and the phase matching of the driving field and the generated XUV light [62]. To understand the effects of those parameters, we focus on the three-step model. Although the three-step model treats the electron accelerating in the laser field as a classical point particle, many predictions on the HHG spectra based on the model

are highly accurate and useful and conform to the quantum mechanical simulations under strong field approximation [63].

In the three-step model, the electron first tunnel-ionizes through the modified atomic Coulomb potential by the laser field. To overcome the atomic Coulomb potential, an electric field on the order of 1-10 V/Å is required and this indicates that the peak intensity of the laser pulse has to be on the order of 10^{14}-10^{15} W/cm^2. The tunnel-ionization rates can be calculated by Ammosov-Delone-Krainov (ADK) theory [19, 64–66].

After tunnel-ionization at time t_0, the electrons are accelerated in the electric field. Considering an alternating electric field $\mathcal{E}(t) = \mathcal{E}_0 \cos(\omega t)$, the classical equation of motion for the electron on coordinate $\hat{x}$ can be written as

$$\ddot{x}(t) = -\frac{e}{m_e}\mathcal{E}(t).$$

Here e is the elementary charge and m_e the electron mass. While electrons may have nonzero velocities immediately after tunnel-ionization, quantum mechanical calculations have shown that the electrons with zero initial velocity are the dominant contributor to HHG [63]. Henceforth, the equations for the velocity (v) and position of the electron as a function of time can be described as

$$v(t) = -\frac{e\mathcal{E}_0}{m_e\omega}(\sin(\omega t) - \sin(\omega t_0))$$
$$x(t) = \frac{e\mathcal{E}_0}{m_e\omega^2}(\cos(\omega t) - \cos(\omega t_0)) + \frac{e\mathcal{E}_0}{m_e\omega}(t - t_0)\sin(\omega t_0).$$

The time of electron recombination t_r can be obtained by numerically solving the equation

$$x(t_r) = 0 = \cos(\omega t_r) - \cos(\omega t_0) + \omega(t_r - t_0)\sin(\omega t_0),$$

and the electron kinetic energy is expressed as

$$E_{KE}(t) = \frac{m_e v^2}{2} = \frac{(e\mathcal{E}_0)^2}{2m_e\omega^2}(\sin(\omega t) - \sin(\omega t_0))^2,$$

which can be further simplified as

$$E_{KE} = 2U_p(\sin(\omega t) - \sin(\omega t_0))^2.$$

The term U_p is the ponderomotive energy with

$$U_p = \frac{(e\mathcal{E}_0)^2}{4m_e\omega^2} \propto I\lambda^2,$$

where I is the intensity and λ the wavelength. Therefore, the electron kinetic energy gained through acceleration in the laser field is proportional to the laser intensity and the square of the wavelength of the driving field.

In the semiclassical model, the energy released during electron recombination E_{photon} is the sum of the electron kinetic energy at time t_r and the ionization potential I_p of the atom:

$$E_{photon} \approx I_p + E_{KE}(t_r).$$

Figure 2.10(a) exhibits electron trajectories $x(t)$ with different ionization times t_0 within the first quarter of the field cycle ($0 \leq \omega t_0 \leq \pi/2$) and electron kinetic energies during the electron motion. It is observed that the electron travels the farthest at $\omega t_0 = 0$ and the trajectories shorten as ωt_0 reaches $\pi/2$. However, the relation between the electron kinetic energy released during recombination and the trajectory length is not monotonic. While the trajectory starting at $t_0 = 0$ is the longest, the electron recombines with the atom with zero kinetic energy. It is observed in Fig. 2.10(a) that the majority of high energy recombination events occur at $\omega t_r \approx 3\pi/2$, and Fig. 2.10(b) shows that the ionization time t_0 that results in highest kinetic energy release at recombination is at $\omega t_0^{max} \approx \pi/10$. Numerical solution of maximum $E_{KE}(t_r)$ yields the relation

$$\max\ E_{photon} \approx I_p + 3.17U_p,$$

which conforms with the experimentally observed maximum photon energy, termed "cutoff'," in HHG [52, 67].

The non-monotonic relation between the electron kinetic energy at recombination and the trajectory length indicates that except at the cutoff energy, at least two different electron trajectories contribute to the generation of photons. The electron trajectories with $0 \leq t_0 \leq t_0^{max}$ are termed "long trajectories" and the trajectories with $t_0^{max} \leq t_0 \leq \pi/(2\omega)$ "short trajectories". Compared to short trajectories, the ionization event of long trajectories occurs closer to the peak of the electric field. Thus in HHG with few-cycle pulses, while both long and short trajectories contribute to HHG near the center of the field envelope, long trajectory emissions are more likely to also occur from field satellites. In addition, the short and long trajectories have different dispersion relations. For short trajectories, $E_{KE}(t_r)$ and thus the emitted photon energies increase with t_r while long trajectories follow an opposite trend. Macroscopically, this can potentially lead to generation of two different bursts of XUV from the two sets of trajectories, lengthen the overall pulse duration of the XUV, and cause modulations in the XUV spectrum [68]. Therefore, to generate single isolated attosecond XUV pulses, long trajectory emission needs to be suppressed. This can be achieved by exploiting the opposite dispersion relation of the two sets of trajectories, which is discussed next.

Phase matching. The macroscopic phase matching of the driving field and the XUV field produced through HHG in a gas jet involves the positive dispersion of the neutral gas medium, the negative dispersion from the electron-ion plasma generated from the strong driving field, the Gouy phase from the Gaussian laser beam, and the phase, or dispersion of the harmonic photons (XUV) due to different electron trajectories, which is termed "dipole phase" [62].

The selection of a specific set of electron trajectories can be achieved by tuning the focal point of the driving field with respect to the gas jet. As the Gouy phase has positive sign before the focal point and becomes negative after the focus,[6] phase matching of short trajectory recombination events can be achieved by positioning the laser focus before the gas target, thereby canceling the positive phase of short trajectory emissions with the negative Gouy phase [62]. The different dispersion of short and long trajectory emissions enables the enhancement of a specific set of trajectory emissions by

[6]The Gouy phase shift near focal point ($z = 0$) is $-\arctan\frac{z}{z_R}$ with z_R denoting the Rayleigh range.

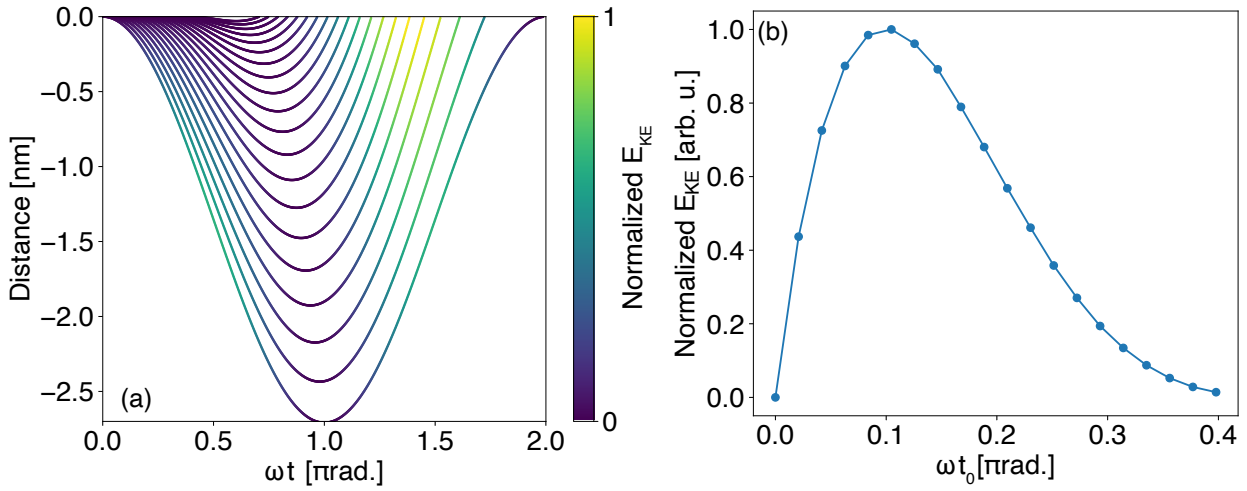

Figure 2.10: (a) Electron trajectories at different ionization times in electric field $\mathcal{E}(t) \sim \cos(\omega t)$. The line color represents the electron kinetic energy E_{KE}. (b) shows $E_{KE}(t_r)$ with different ionization time ωt_0. In the simulation, $\omega \approx 1.7$ eV and the electric field amplitude $\mathcal{E}_0 \approx 0.5$ V/Å.

selecting the position of the laser focus with respect to the gas target. However, if the difference between the optimal phase matching position of the gas target for short and long trajectories is small, residual emission from long trajectory recombinations can still be observed when the gas target position is optimized for short trajectory emissions. Figure 2.11 displays a sample spectral image of XUV produced by HHG in argon. Alongside the strong and continuous on-axis emission, weak discrete harmonic emissions due to long trajectory recombinations are observed. For gas media such as argon or krypton, residual long trajectory emissions are difficult to eliminate due to the small difference of optimal phase matching position between short and long trajectories. To further suppress the discrete harmonic emissions, ionization gating is used by exploiting the time-dependent plasma density with respect to the pulse envelope and destroying the phase matching after the leading edge of the pulse through excessive plasma dispersion.

Carrier envelope phase. For HHG with few-cycle pulses, the carrier envelope phase (CEP) plays a significant role in the XUV spectra because for few-cycle pulses, the number of XUV bursts is strongly dependent on the CEP. Figures 2.12 and 2.13 show the CEP dependence of XUV spectra produced by HHG in krypton and argon with a nominal 3.5 fs pulse centered at 690 nm wavelength. When the CEP is at $\pm\pi/2$, distinct "valleys" appear in the spectra and the spectra become more discrete than when the CEP is around 0 or $\pm\pi$. This is due to the change in number of XUV bursts that interfere with each other, causing the spectral profile to alternate between discrete and continuous. In addition, the change in CEP also modulates the overall intensity of the XUV spectrum. In Fig. 2.12(b), the intensity of the spectra is maximized at CEP $\approx 0, \pm\pi$. The strong CEP dependence of the produced XUV spectra is a signature of HHG in few- to near-single-cycle

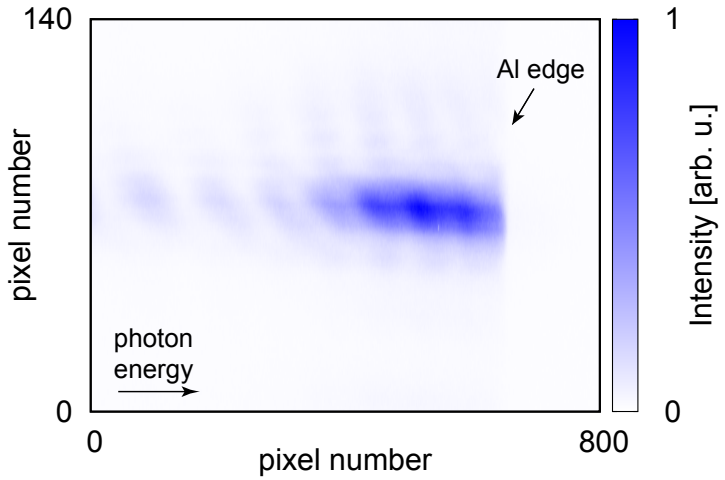

Figure 2.11: Sample spectral image of XUV produced by HHG in argon. The white region on the right of the image is due to absorption from the $L_{2,3}$ edge of aluminum, which is used to filter out the driving optical pulse.

pulses. In such a regime, the stability of CEP is important because the intensity and spectral shape fluctuation due to CEP drift can contribute significantly to the noise in the measurement.

Experimental

The mechanism of high harmonic generation indicates that the energy range of the photons produced by such a process can be largely determined by the ionization potential of the interacting gas medium. The larger the ionization potential, the more energy can be gained during recombination, and the higher the cutoff photon energy becomes. In addition, gas media with high ionization potentials allow driving beams with higher peak intensity without reaching the critical ionization threshold that destroys phase matching. Using laser pulses centered around 700 nm with 10^{14}-10^{15} W/cm^2 peak intensity and pulse duration of approximately 3.5 fs, XUV photons spanning 30-60 eV, 35-80 eV, and 70-110 eV are generated with Kr, Ar, and Ne gases (Fig. 2.14).

Phase matching of short trajectory emissions is achieved by tuning the focal spot of the driving beam with respect to the HHG gas cell, and the focal spot size and laser intensity with an iris aperture.[7] The instrumentation for phase matching is illustrated in Fig. 2.15. The optical driving beam passes through an iris aperture and is reflected by a focusing mirror on a linear mechanical stage. The linear stage is used to fine-tune the distance between the laser focus and the gas cell.

To optimize the XUV spectrum in terms of photon flux, cutoff energy, and spectral "continuity", harmonic spectra are first generated with low gas density, where laser-induced plasma density is low. By changing the neon pressure in the HCF and moving the glass wedge after the beamsplitter (Fig.

[7]Note that for a Gaussian beam the diffraction-limited focal spot diameter $2w_0$ is inversely proportional to the beam diameter on the focusing element D: $2w_0 = (4\lambda f)/(\pi D)$, where f is the focal length and λ the wavelength.

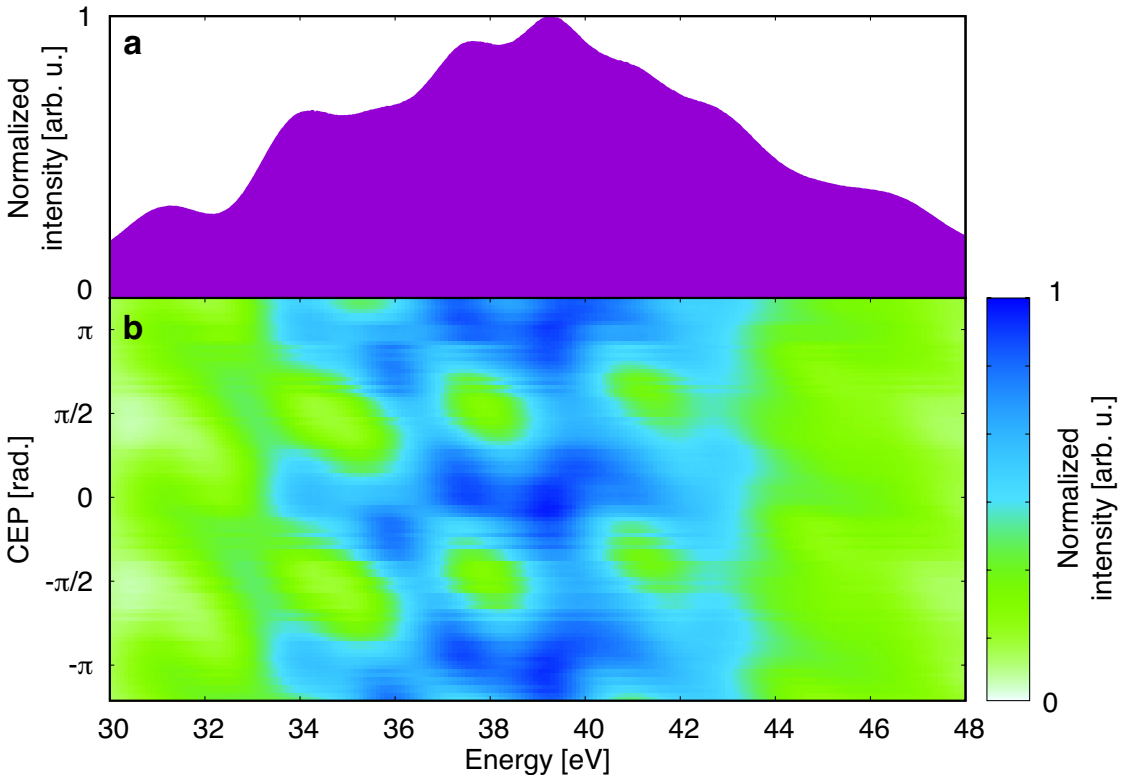

Figure 2.12: (a) A sample spectrum of XUV produced by HHG in krypton. (b) shows the XUV spectra as a function of CEP.

2.3), the spectral bandwidth and dispersion are respectively fine-tuned for highest cutoff energy of the generated XUV. At low plasma density, destruction of phase matching due to ionization is reduced and harmonics generated by the peak of the pulse are not suppressed. The cutoff energy, which scales with the peak laser intensity here, is thus a suitable indicator for amplitude gating. To enhance short trajectory emission, the iris aperture before the HHG gas cell (Fig. 2.15) is first opened up so that the laser intensity reaches right below the critical ionization threshold.[8] Subsequently, the position of the focusing mirror before the HHG gas cell is moved by the linear stage to maximize the cutoff energy and minimize the width of the XUV beam. Afterwards, the gas density in the HHG gas cell is increased to increase the XUV photon flux and the iris aperture shown in Fig. 2.15 is used to fine-tune the cutoff energy and shape of the XUV spectrum. The carrier envelope phase, which can be changed by the glass wedge after the beamsplitter and the prism stretch in the laser amplifier, is also used for fine-tuning of spectral continuity.

[8] When critical ionization threshold is reached, the XUV beam becomes defocused and unstable due to the plasma.

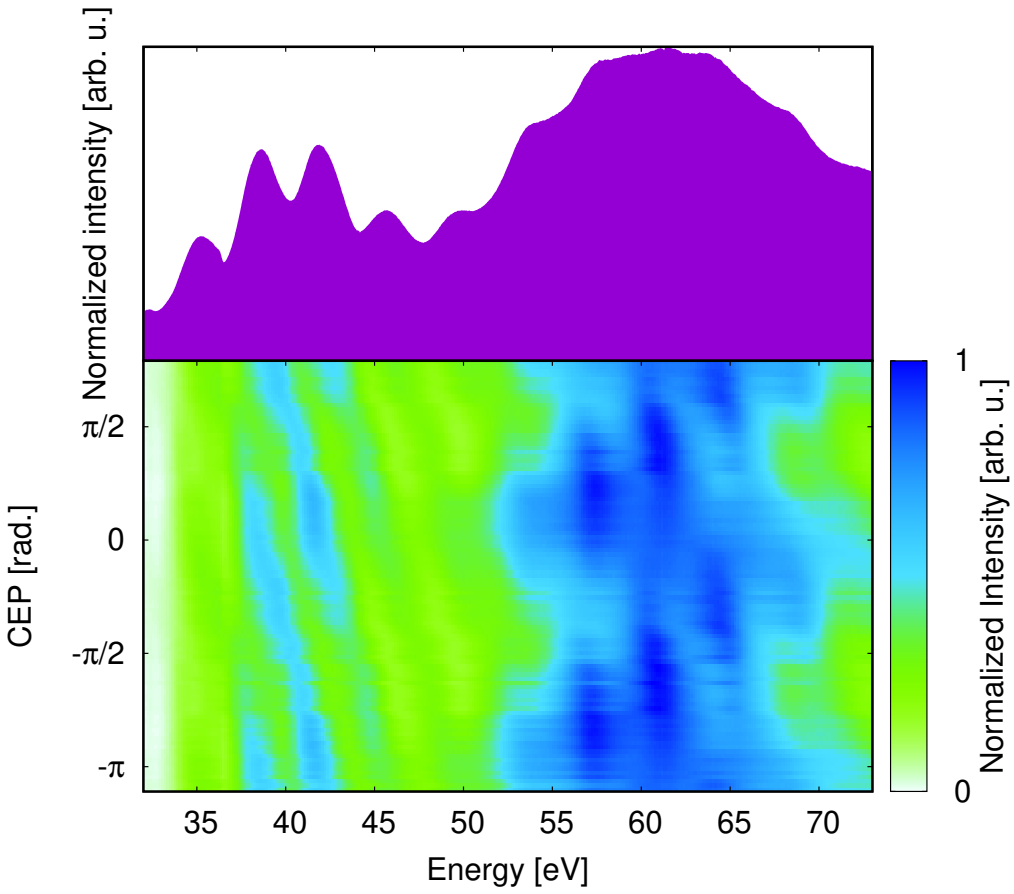

Figure 2.13: Sample XUV spectrum of HHG in argon (upper panel) and XUV spectra as a function of CEP (lower panel).

2.2.3 Energy Calibration

The XUV spectra are measured by dispersing the XUV light with a flat-field toroidal grating onto an XUV CCD chip. The calibration of XUV spectrometer is conducted by measuring line spectra of atomic autoionization states and well-defined core-level absorption edges of elemental solids. Autoionization lines of He (60 – 64 eV) [69, 70], Ne (44 – 47 eV) [71], Ar (25 – 35 eV) [72], Kr (90 – 95 eV) [73], and the sharp absorption of Al $L_{2,3}$ (~73 eV) and Si $L_{2,3}$ edges (~99 eV) are utilized to calibrate the acquired XUV spectra [74]. The pixel (N) of the peaks (edge) in measured line (edge) spectra are fitted to the corresponding wavelength (λ) in literature using the grating equation [75]:

$$\lambda = \frac{d}{m}(\sin(\theta_0) + \sin(\theta)).$$

Here the pixel number is proportional to the diffraction angle θ and θ_0 is the fixed incident angle; d is the spacing of the grating grooves and m is the diffraction order. In practice, the small angle

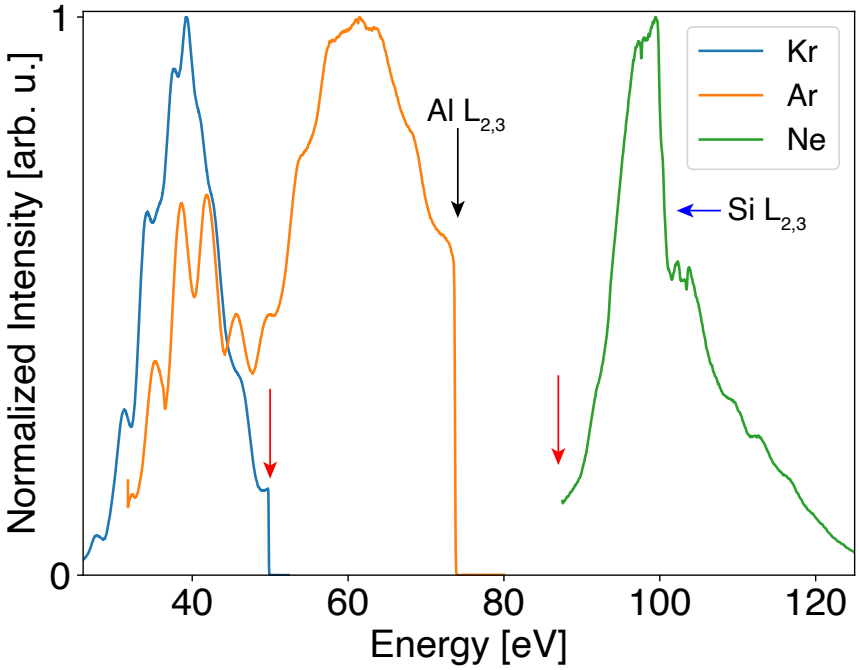

Figure 2.14: Typical XUV spectra obtained through HHG in different gas media using the experimental setup. Note that the spectra for HHG in Kr and Ne are cut off due to limited XUV CCD chip size (black arrows). The XUV spectrum of HHG in Ar is cut off by the Al filter used to block the optical driving beam (red arrow). The sharp drop in measured intensity in the spectrum of HHG in Ne near 100 eV is due to absorption at the Si $L_{2,3}$ edge of the XUV CCD chip.

approximation is invoked such that the sine function is expanded into a polynomial and the fitting equation is simplified to

$$\lambda = c_1 + c_2 N + c_3 N^2.$$

Here N is the pixel number and c_n are fitting coefficients.

2.3 Spatial, Temporal Overlap and Stabilization

To establish spatial and temporal overlap of the pump and probe beam, a CMOS camera is installed beside the sample holder to enable *in situ* beam diagnostics (Fig. 2.16). To spatially overlap the pump and probe beam, a neutral density filter (OD=3) is first placed before the beamsplitter that separates the pump and probe arm (Fig. 2.3). After removing the metal filter, the two attenuated optical beams are overlapped on the CMOS camera with the motorized annular mirror (Fig. 2.1). A stack of neutral density filters (OD=5) is placed in front of the camera to further attenuate the beam

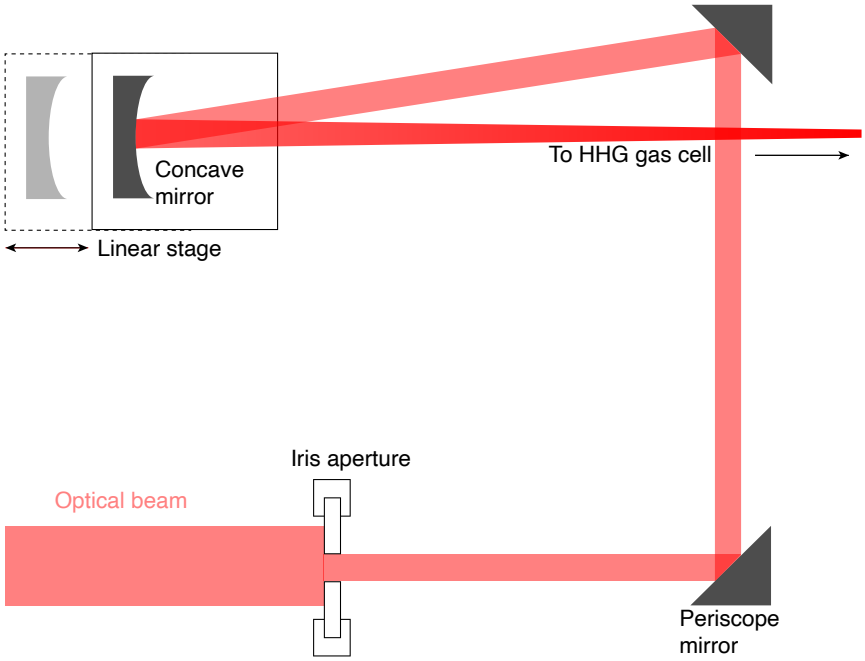

Figure 2.15: Instrumentation for phase matching and trajectory selection for HHG.

and prevent pixel damage.[9] In addition to the spatial overlap of the two beams, the CMOS camera captures the optical beam profile that is used to calculate the fluence of the beam and the number of excited electrons in the experiments. A sample image of the time-delayed optical beam (pump) is displayed in Fig. 2.17. To prevent drift of beam pointing during experiments and the subsequent loss of spatial overlap, the beam pointing of each arm is detected by a quadrant photodiode and actively stabilized by a motorized mirror.

Temporal overlap of the pump and probe beam is achieved by tuning the motorized stages in the optical delay line (Fig. 2.1) and detecting spatial and spectral interference of the beams. The optical delay line consists of a long-traveling stage (10 cm travel range) for picosecond delay experiments and a piezo-motorized stage for < 200 fs time delay experiments. To observe the spectral interference, the beams are picked up by a concave recollimation mirror on the motorized sample stage (Fig. 2.16) and sent out of the vacuum chamber and focused into an optical spectrometer. The spatial interference of the two beams are captured by the CMOS camera on the motorized sample stage.

The typical duration of an attosecond transient absorption experiment on solid thin films is 12-24 hrs. Changes of optical path length at micrometer scale due to temperature and humidity fluctuation in the lab can occur within this timescale and subsequently cause the time zero of the attosecond transient absorption experiment to drift. To measure the drift of time zero in

[9]The neutral density filter in front of the camera can be replaced by a laser line filter centered at a wavelength in the leading edge of the optical beam spectrum.

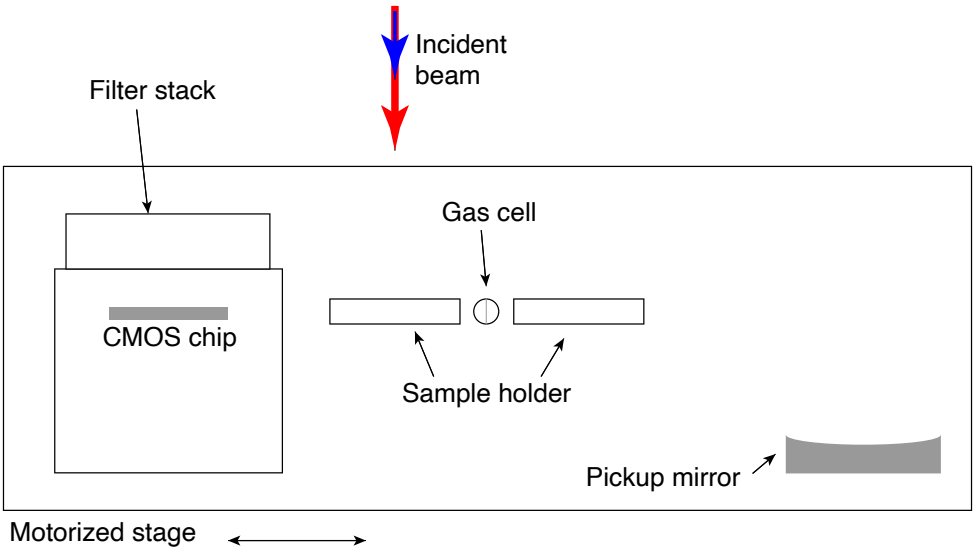

Figure 2.16: Scheme of sample stage assembly including a CMOS camera, two sample stages, a gas cell, and a pickup mirror for beam diagnostics.

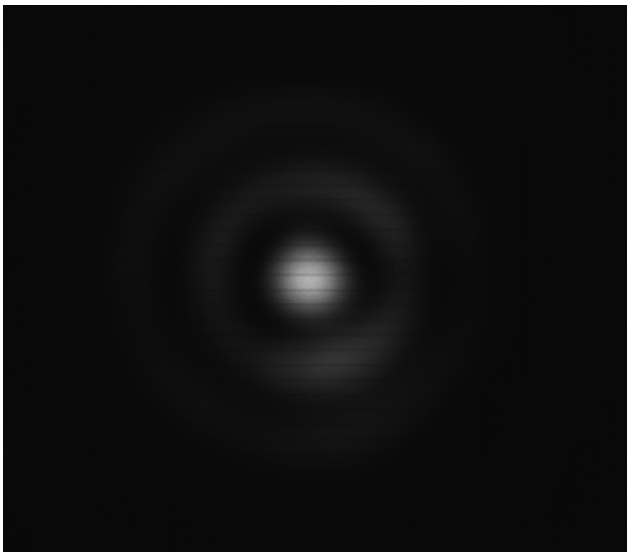

Figure 2.17: A typical profile of the optical (pump) beam taken by the CMOS camera (Fig. 2.16). The rings are due to beam diffraction on the annular mirror.

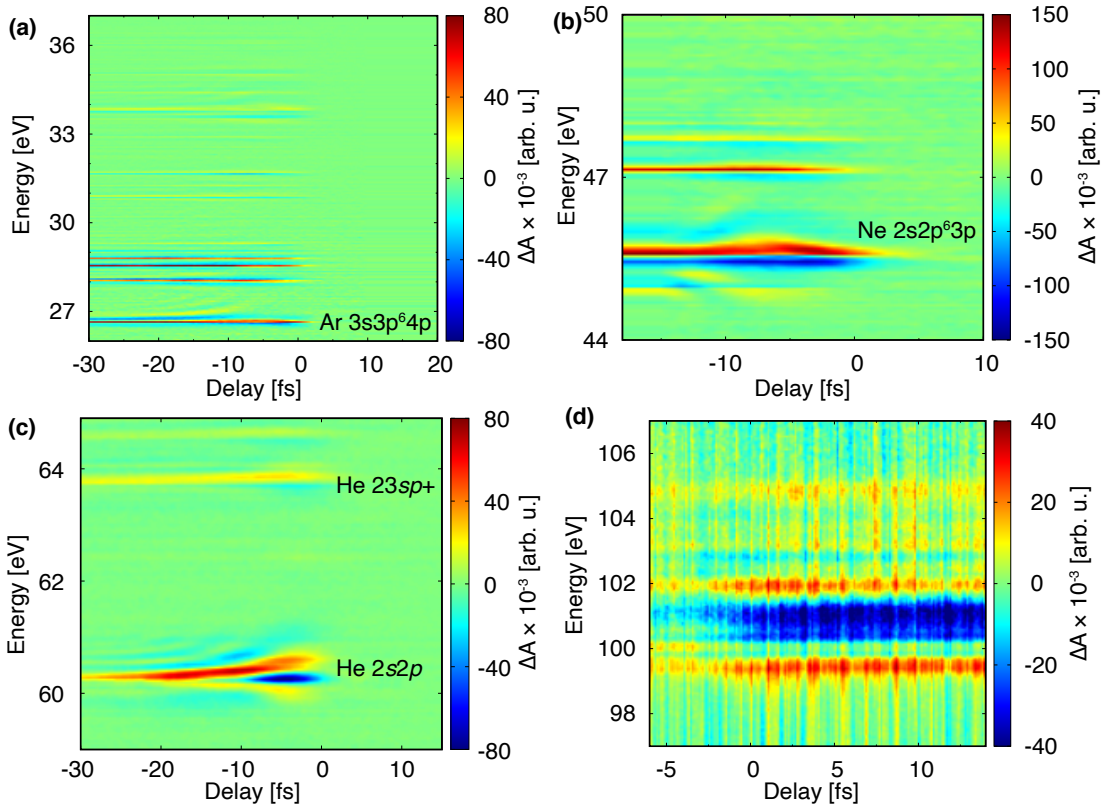

Figure 2.18: XUV TA spectra of autoionizing states of (a) Ar, (b) Ne, and (c) He. (d) shows the core-level TA absorption spectra of Si at the Si $L_{2,3}$ edge.

the attosecond transient absorption scans, we ran one transient absorption measurement on the autoionizing states of noble gases after each scan through all time delay points on the solid sample [10, 23, 24]. Typical transient absorption traces on the autoionizing states of Ar, Ne, and He are shown in Figs. 2.18(a-c), respectively. For measurements in the 25-50 eV energy region, the transient absorption signal at Ar $3s3p^6np$ states and Ne $2s2p^6np$ states can be used as reference for time zero. For experiments within the 50-73 eV energy region, XUV transient absorption of He $2snp$ states can be used. And for energies between 80-120 eV, the transient absorption signal of the Si $L_{2,3}$ edge is sufficiently strong to be used as a time zero reference (Fig. 2.18(d)). Otherwise, XUV transient absorption of Kr $M_{4,5}$ edge ($\sim$ 90 eV) can also be used.

To compensate the time zero drift during the experiments, the transient absorption signal of the reference scans with noble gases or Si near time zero are fit to an error function to determine the exact zero time overlap between the XUV and optical pulses. With the calibrated time zero of each scan, the changes of absorbance for each solid sample scan are interpolated onto a gridline and averaged together [9]. A sample time zero drift trace over the course of an XUV TA measurement is presented in Fig. 2.19, showing an overall time zero drift of approximately 5 fs over 14 hrs.

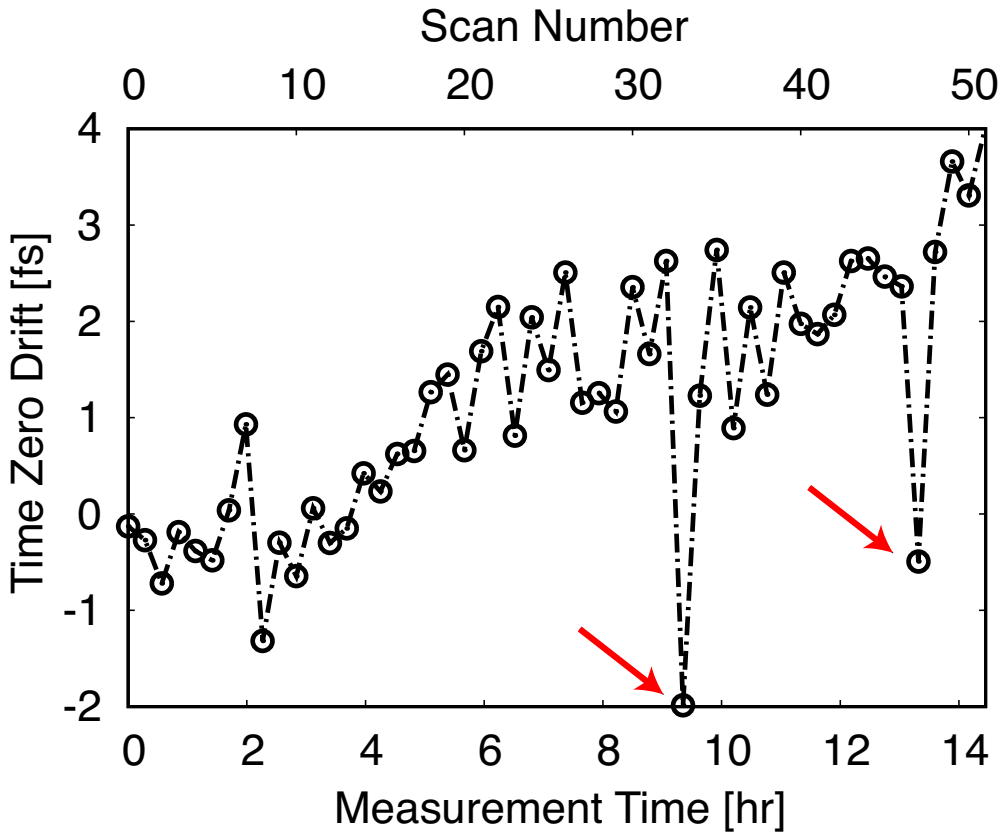

Figure 2.19: A sample of time zero measurements in an experiment of over 14 hrs.

In addition, there are large time zero jumps (red arrows) of over 4 fs between the scans. As the experiments for short time dynamics typically have a time delay range of 30-40 fs, a > 3 fs time zero difference between neighboring time zero measurements indicates that on average, the time delay axis of the scan is stretched or compressed by $\sim 3/30 = 0.1$ fs. To avoid compromising the time resolution of the experiments, scans with neighboring time zero difference larger than 3 fs are therefore discarded.

Chapter 3

Electronic and Structural Dynamics in 2H-$MoTe_2$[1]

3.1 Introduction

In this chapter, we discuss the observation of carrier and phonon dynamics with core-level transient absorption spectroscopy in a well-screened semiconductor, where the core-level absorption spectra can be largely interpreted using a single-particle, band-to-band transition picture. $MoTe_2$ is a two-dimensional (2D) layered transition metal dichalcogenide (TMDC) whose atomically thin layers are separated by weakly bound van der Waals interactions [77–79]. Two different stable phases of $MoTe_2$ exist at room temperature: the semiconducting hexagonal 2H phase and the semimetallic monoclinic 1T' phase. The semiconducting 2H-phase $MoTe_2$ has a bandgap of 0.9 eV in bulk and 1.1 eV in the monolayer and is viewed as a silicon equivalent in the 2D form [80, 81]. Recent investigations have shown the potential for integrating both monolayer and multilayer TMDC semiconductors into devices, including transistors [82, 83], photonic logic gates [84], photodetectors [85], and nonvolatile memory cells [86]. While the typical device application involves stacking different subcomponent thin-film materials into heterostructures to extend functionality [84, 86, 87], the overall performance of TMDC-based devices can be dominated by the individual subcomponent's carrier dynamics [88]. For devices involving multilayer thin-films of 2H-$MoTe_2$, the carrier transport properties within the $MoTe_2$ subcomponent can dictate their functionality [84, 89]. In addition to the carrier dynamics, there is a growing interest in the light-induced structural responses of TMDC's including $MoTe_2$ and WTe_2, especially for applications in optically controlled phase transitions [90–92].

Recent studies have therefore aimed at characterizing the carrier relaxation and associated structural dynamics of few-layer and bulk 2H-$MoTe_2$ [91, 93–95]. Although the understanding of carrier-specific dynamics of holes and electrons is critical for designing ambipolar semiconductor

[1]The content and figures of this chapter are adapted or reprinted with permission from A. R. Attar et al., "Simultaneous Observation of Carrier-Specific Redistribution and Coherent Lattice Dynamics in 2H-$MoTe_2$ with Femtosecond Core-Level Spectroscopy", ACS Nano **14**, 15829–15840 (2020).

devices [89, 96, 97], separating the different contributions of the charge carriers by traditional time-resolved optical/IR and THz spectroscopies is challenging due to overlapping spectral features. This is exemplified by the studies of 2H-$MoTe_2$ by Li et al. [93] and Chi et al. [94], where THz and optical experiments were used to measure the carrier lifetime, but without carrier specificity and without sensitivity to hot carrier intraband dynamics.

As a possible solution to these challenges, recent investigations have shown the potential of using ultrafast core-level spectroscopy such as XUV transient absorption to disentangle the intraband hole and electron dynamics in semiconductors [9, 28–30, 98]. In XUV transient absorption experiments, an optical pump pulse excites carriers across the bandgap at time zero and, at a series of controlled time delays, the energy-dependent change in carrier population is probed by core-level transitions to the partially occupied valence band (VB) and conduction band (CB). In some cases, photoexcited holes and electrons can be separately and simultaneously attributed to changes in spectrally distinct transitions from atomic core levels to the transiently empty states in the VB (holes) and reduced absorption in the transiently filled CB (electrons). These phenomena are collectively referred to here as "state-filling." It is possible not only to distinguish the hole and electron distributions, but to also gain energy-dependent dynamics of the specific hot carriers within the VB and CB [30, 99]. The element-specificity inherent to core-level spectroscopy offers the additional capability to distinguish the individual subcomponent materials in heterostructures [100, 101]. Finally, the sensitivity of core-level spectroscopy to bonding, bond distances, and symmetry provides simultaneous structural information of photoexcited materials [102–107].

In the present study, we apply sub-5 fs XUV transient absorption spectroscopy on a 2H-$MoTe_2$ semiconductor thin film (~50 nm/70 layers) to probe the dynamics of intraband carrier-specific relaxation, interband electron-hole recombination, and excited-state coherent lattice displacement. We obtain element-specific information by simultaneously measuring the spectral range around the Te $N_{4,5}$ absorption edge (39-46 eV) and the Mo $N_{2,3}$ edge (35-38 eV), as a function of delay time after optical excitation. The XUV absorption captures the same total density of states information at both edges. This enables us to analyze the hole distribution dynamics in the VB, distinguishing between thermalization of the holes by carrier-carrier scattering, subsequent cooling by carrier-phonon scattering, and the much slower electron-hole recombination process. We also report on the observation of light-induced coherent lattice vibrations in the out-of-plane A_{1g} and the in-plane E_{1g} modes of 2H-$MoTe_2$, which are captured via high-frequency oscillations (THz) in the XUV spectra. By comparison to ab initio Bethe-Salpeter equation simulations of the core-level absorption spectrum with different 2H-$MoTe_2$ lattice geometries, the excited-state displacement of the lattice that drives the coherent motion is extracted. Using this approach, we are able to capture the real-space lattice displacement simultaneously with the carrier-carrier thermalization of the holes, cooling (hole-phonon), and electron-hole recombination, leading to a cohesive picture of carrier and structural dynamics in a layered semiconductor nanomaterial.

3.2 Results and Discussion

3.2.1 Experimental Scheme and Static Absorption of 2H-$MoTe_2$

The experimental apparatus and methodology of the XUV transient absorption spectroscopy measurements performed here have been previously described [9] and a detailed description is provided in Chapter 2. The experiment is performed on a thin-film (50 nm thick, i.e. 70 layers) polycrystalline sample of 2H-phase $MoTe_2$, which is synthesized by chemical vapor deposition (CVD) onto a Si_3N_4 susbtrate of 30 nm thickness and 3×3 mm lateral size. The sample is characterized by Raman spectroscopy to confirm the 2H-phase structure (see Appendix for sample preparation and detailed characterization) [79]. In the XUV transient absorption experiments, this sample is photoexcited by a sub-5 fs, visible-to-near infrared (Vis-NIR) pump pulse spanning 1.2-2.2 eV with an average photon energy of 1.65 eV. The initial photoexcited carrier density is $\sim 1 \times 10^{20}$ cm^{-3} (i.e. $\sim 7 \times 10^{12}$ cm^{-2} in each layer, given the ~0.7 nm thickness per layer), which corresponds to a 0.1% excitation fraction of the total valence electrons (see Appendix for details). The photoexcited sample is then probed at a controlled time delay τ, by the arrival of a broadband (30-50 eV), sub-5 fs XUV pulse produced by high-harmonic generation. The transmitted XUV intensity through the sample is measured as a function of photon energy, $I(E)$, by a spectrometer. The transient absorption signal, $\Delta\mathrm{OD}(E,t) = \mathrm{OD}_{pumpon}(E,t) - \mathrm{OD}_{pumpoff}(E)$, is determined by the difference between the XUV absorbance, or optical density (OD), of the photoexcited sample at time and the static XUV absorbance in the absence of pump excitation.

The broadband XUV pulse allows for the simultaneous absorption measurement covering the Mo $N_{2,3}$ edges (~35-38 eV, referred to as the "Mo window") and the Te $N_{4,5}$ edges (39-46 eV, referred to as the "Te window"). The transmission of the broadband XUV spectrum is referenced to the transmission of a blank Si_3N_4 substrate to obtain the static absorption spectrum of the thin-film 2H-$MoTe_2$ sample: i.e. Absorbance = $\log(I_{blank}/I_{sample})$, which is shown in Figure 3.1a. XUV transitions in the Mo and Te windows occur by promotion of Mo $4p_{3/2,1/2}$ and Te $4d_{5/2,3/2}$ core electrons to the CB, respectively. The onset of the transitions from each observed core level is labeled 1-3 in Figure 3.1a and the corresponding transition is shown schematically in Figure 3.1b. Note that the arrows in Figure 3.1b only show the onset of the core-level absorption edge. As the XUV energy is increased above each onset, carriers are promoted from the corresponding core level to higher valleys in the CB at different k-space positions throughout the Brillouin zone. In the Mo window, the onset of transitions from the Mo $4p_{1/2}$ core level is too weak to observe in the static spectrum and is omitted from the analysis. The onset of Mo $4p_{3/2} \rightarrow$ CB absorption is measured at 36.1 eV and labeled edge 1. In the Te window, the onset of the Te $4d_{5/2} \rightarrow$ CB (edge 2) is measured at 40.7 eV and the onset of the Te $4d_{3/2} \rightarrow$ CB (edge 3) is at 42.2 eV. The 1.5 eV separation of edges 2 and 3 matches the Te $4d_{5/2,3/2}$ spin-orbit splitting in $MoTe_2$ confirmed by XPS spectra (Figure 3.7). When the Vis-NIR pulse excites the material, additional transitions become accessible from the core levels to the VB and transitions to the CB can be reduced due to state-filling, as discussed below.

Considering more closely the Te window (Figure 3.1c), the relatively sharp features allow for a detailed mapping of the CB density of states (DOS) from the Te 4d core levels. First, DOS

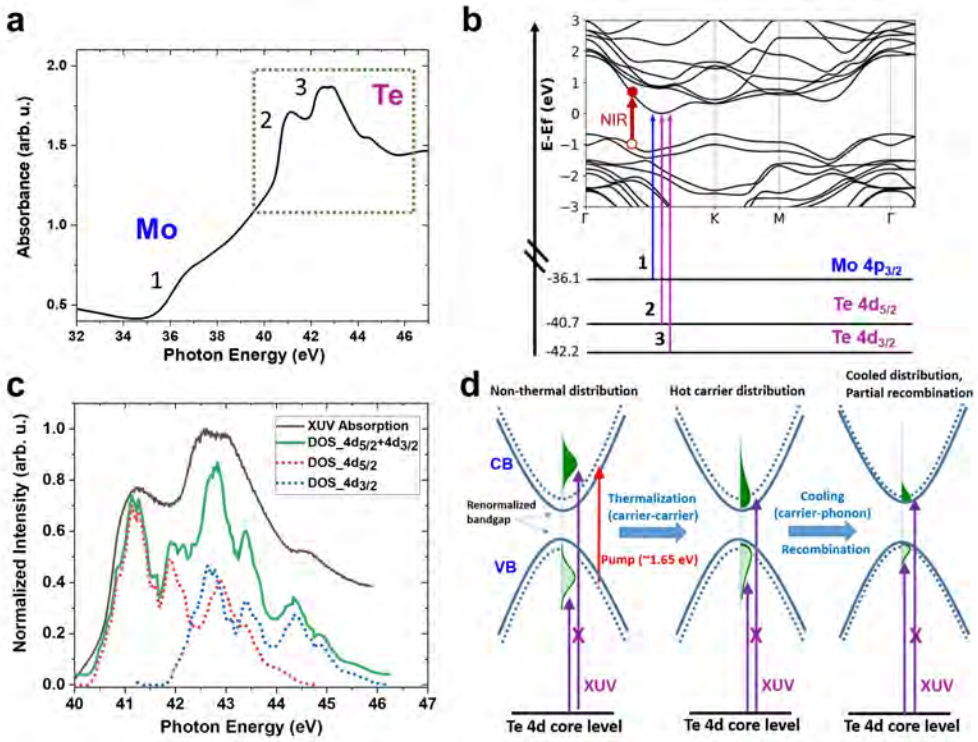

Figure 3.1: (a) Static XUV absorption spectrum of 2H-MoTe$_2$ with Mo $4p_{3/2} \rightarrow$ CB and Te $4d_{5/2,3/2} \rightarrow$ CB absorption edges labeled 1-3. The Mo $4p_{1/2} \rightarrow$ CB edge is too weak to observe and is omitted. (b) Band structure of 2H-MoTe$_2$ along the path. The corresponding core-level transitions for the three absorption edges labeled in (a) are shown by vertical blue and purple arrows and labeled 1-3 accordingly. Note that the arrows only show the onset of the core-level absorption edge for the case of the material without Vis-NIR excitation. As the XUV energy is increased above each onset, carriers are promoted to higher energies in the CB at different positions throughout k-space. One representative VB→CB transition induced by the Vis-NIR pump pulse (of the range of transitions possible from the broad bandwidth pump) is shown as a red arrow. (c) An expanded plot of the normalized XUV absorption spectrum in the Te window (black line). The red-dotted and the blue-dotted lines are plots of the calculated normalized CB DOS relative to the Te $4d_{5/2}$ core level (labeled DOS_4d$_{5/2}$) and $4d_{3/2}$ core level labeled DOS_4d$_{3/2}$), respectively. The difference in the relative amplitudes of DOS_4d$_{5/2}$ and DOS_4d$_{3/2}$ is described in the text. The sum of DOS_4d$_{5/2}$ and DOS_4d$_{3/2}$ is plotted (green solid line). (d) Model of the XUV transient absorption probing scheme for 2H-MoTe$_2$. The VB and CB are shown as parabolic bands. The solid (dashed) parabolas represent the bands with (without) band-gap renormalization. The photoexcited holes and electrons are represented by the shaded light-green and dark-green areas, respectively. Representative XUV transitions from the Te $4d$ core levels are shown with and without an X to represent a decrease or increase in absorption relative to the static spectrum, respectively, due to state-filling.

calculations are performed. In Figure 3.1c, the calculated CB density of states (DOS) is plotted relative to the $4d_{5/2}$ core level (red dashed line, labeled DOS_4d$_{5/2}$) and to the $4d_{3/2}$ core level (blue dashed line, labeled DOS_4d$_{3/2}$). The relative amplitudes between DOS_4d$_{5/2}$ and DOS_4d$_{3/2}$ is set according to the expected degeneracies of the core-hole total angular momentum J states ($J = 5/2$ vs $J = 3/2$), which, to first approximation, predicts a 3:2 ratio for $4d_{5/2} \rightarrow$ CB versus $4d_{3/2} \rightarrow$ CB amplitudes. The resulting core-hole-mapped DOS (green solid line) is compared to the experimental XUV absorption spectrum (black solid line). The close agreement between the calculated CB DOS and the XUV absorption spectrum in Figure 3.1c demonstrates that the core hole of the Te $N_{4,5}$ absorption is well screened such that the core-level absorption spectrum can be regarded as a map of the CB unoccupied DOS in the valence shell.

Within this picture, the probing scheme for measuring the carrier dynamics following optical excitation can be understood by the model illustrated in Figure 3.1d. In the leftmost panel, above-bandgap photoexcitation produces a non-thermalized distribution of carriers corresponding to a convolution of the excitation spectrum and the VB/CB DOS. The broad bandwidth excitation in the present experiment produces carriers over a large range of momentum values in k-space. Moving from left to right in Figure 3.1d, the initial non-thermal carrier distribution is expected to undergo carrier-carrier thermalization, carrier-phonon cooling, and recombination in accordance with known carrier-carrier and carrier-phonon scattering processes in semiconductors [108]. These carrier dynamics lead to energy- and time-dependent changes in the unoccupied DOS within the VB and CB, as shown in the schematic. For example, the peak of the hot hole distribution is expected to shift upwards toward the VB maximum due to both thermalization and cooling, which can occur from tens to hundreds of femtoseconds [108–111]. The corresponding changes to the XUV absorption (OD) due to state-filling effects [9, 30, 98, 99] are schematically illustrated by vertical arrows from the representative Te 4d core-level. In the following sections, the time-resolved OD of the spectrally dispersed XUV probe is used to extract both the carrier distribution and population dynamics in 2H-$MoTe_2$, revealing the individual steps depicted in Figure 3.1d. Due to the sharper XUV absorption edge observed in the Te window as compared to the Mo window, we focus primarily on the Te N-edge to report on the carrier and structural dynamics in this work. However, as shown in Figure 3.9 and Figure 3.4 in Appendix, respectively, the Mo $4p_{3/2}$ core-level can also be used to capture the hole population dynamics and the coherent phonon dynamics.

3.2.2 XUV Transient Absorption Following Broadband Photoexcitation

In Figure 3.2a, the change in the XUV absorbance, $\Delta\mathrm{OD}(E, t)$, following Vis-NIR excitation is plotted in a false-color map as a function of time delay and photon energy. Changes are observed in both the Mo and Te windows near 33-37 eV and 38-46 eV, respectively. The ground-state absorbance spectrum of 2H-$MoTe_2$ is shown here again in Figure 3.2b to emphasize where the major pump-induced absorption changes appear relative to the static spectrum. The dotted vertical lines in Figure 3.2b at 36.1 eV and 40.7 eV show the energies of the Mo $4p_{3/2} \rightarrow$ CB minimum and the Te $4d_{5/2} \rightarrow$ CB minimum, respectively. With a bulk bandgap of 0.9 eV in 2H-$MoTe_2$, the dash-dotted vertical lines at 35.2 eV and 39.8 eV correspond to the derived VB maximum energy relative to the Mo $4p_{3/2}$ and Te $4d_{5/2}$ core levels, respectively. Clear OD signals are observed

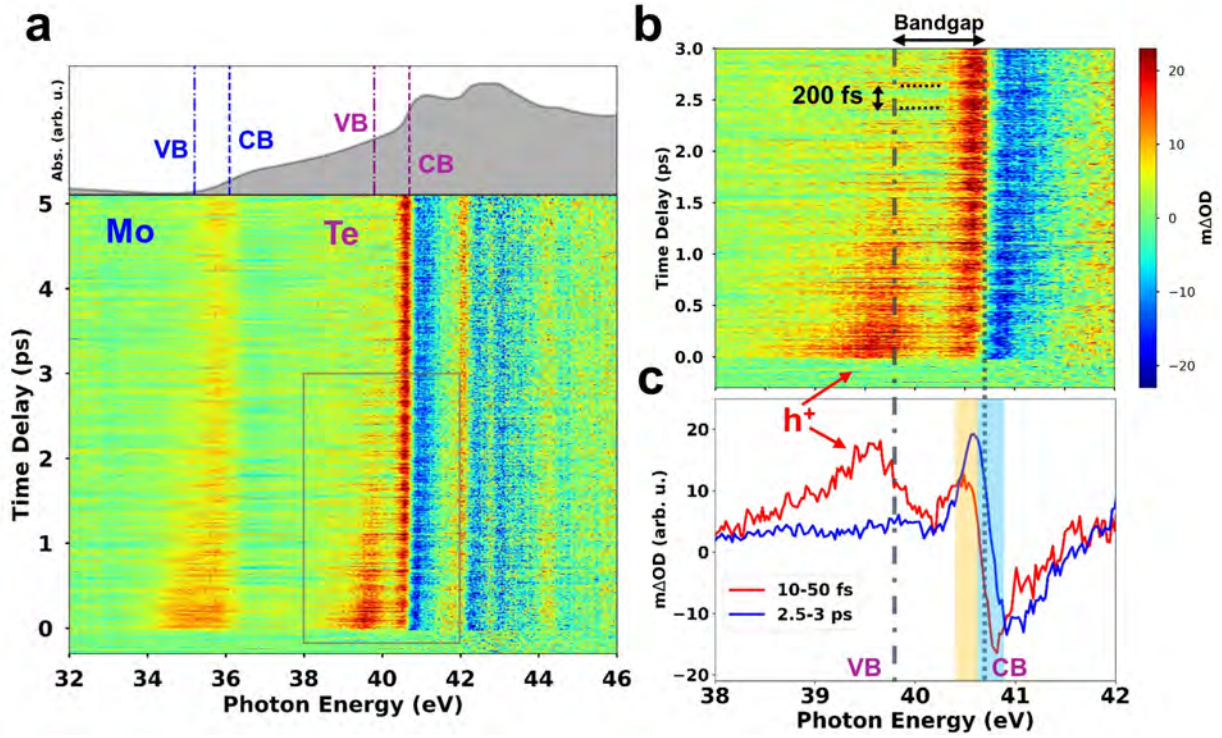

Figure 3.2: (a) XUV transient absorbance in a false-color plot versus time shown in the bottom panel and compared to the static absorbance spectrum in the top panel. The vertical dotted and dash-dotted lines in the upper panel are drawn at the energies corresponding to the CB minimum and VB maximum, respectively, from both the Mo $4p_{3/2}$ and Te $4d_{5/2}$ core levels. (b) Transient absorbance in a false color plot versus time, expanded from the grey box region in the lower panel of (a). The indicated 200 fs oscillations in the differential absorbance is discussed further in Sec. 3.2.6. (c) Differential absorbance lineouts averaged over early time delays (10-50 fs) and long time delays (2.5-3ps). Orange and blue shaded regions indicate the energy windows used for temporal lineouts in Figure 3.5.

near these energies in the photoexcited sample, as shown in Figure 3.2a. We focus first on the Te window in the grey box region of Figure 3.2a, which is blown up for clarity in Figure 3.2c. At energies above 42 eV within the Te window, the XUV absorption spectrum involves overlapping transitions from both the Te $4d_{5/2}$ and the Te $4d_{3/2}$ core levels, as shown in Figure 3.1c. Below 42 eV (i.e. 38-42 eV), however, the spectrum is characterized by resonant transitions involving only the Te $4d_{5/2}$ core level, which is why we focus on this energy region. Two ΔOD spectral lineouts in this energy window are shown in Figure 3.2d, averaged over short (10-50 fs) and long delay times (2.5-3 ps). Within this energy range (38-42 eV), the resonant transitions correspond to promotion of an electron primarily from the Te $4d_{5/2}$ core level into the unoccupied DOS of the VB and CB.

Two main features are observed in the differential spectra at early delay times (10-50 fs window):

a positive peak appearing near 39.5 eV and a derivative-shaped feature centered at the onset of the ground-state $4d_{5/2} \rightarrow$ CB absorption edge at 40.7 eV. The positive feature centered at 39.5 eV appears 0.3 eV below the derived $4d_{5/2} \rightarrow$ VB maximum (shown as dash-dotted vertical line). This feature is therefore assigned to transitions from the $4d_{5/2}$ core level to 'hot' holes in the VB produced by the above-bandgap photoexcitation (schematically represented by the left panel in Figure 3.1d). In the later time window (2.5-3 ps), the $4d_{5/2} \rightarrow$ VB hole feature has disappeared and the derivative feature is characterized by a slight blue shift relative to the early delay times and a significant increase in absorption at energies between 40.6 and 40.9 eV. Several effects contribute to the derivative feature, including state-filling by the electrons in the CB and bandgap renormalization (BGR), as schematically illustrated in Figure 3.1d [9, 98, 103]. These overlapping effects, which are discussed in detail below, make the electron state-filling signal less straightforward as compared to the hole signal. In the following, we therefore concentrate first on extracting the hole distribution and population dynamics from the temporal evolution of the $4d_{5/2} \rightarrow$ VB signal centered near 39.5 eV.

3.2.3 Hole Distribution and Population Dynamics in the Valence Band

In order to track the detailed dynamics of both the population and distribution of the holes in the VB, we measure the time-dependent amplitude (population) and the central energy (distribution) of the $4d_{5/2} \rightarrow$ VB peak. In Figure 3.3a, the hole population measured via the integrated $4d_{5/2} \rightarrow$ VB absorption amplitude near the VB maximum (39.7-39.9 eV) is plotted as a function of delay time. The population decay is fit to a single exponential with a time constant of $\tau_{pop} = 1.5 \pm 0.1$ ps, which is assigned to electron-hole recombination. The fit to an exponential decay is chosen to provide a direct comparison to recent mid-IR and THz transient absorption measurements of the carrier lifetime in 2H-$MoTe_2$ [93, 94]. In the THz study [93], the carrier lifetime is found to be dominated by a phonon-mediated trapping/recombination mechanism, accelerated by Auger scattering, which can be reduced to a single exponential decay constant of ~2 ps. This is consistent with our result of $\tau_{pop} = 1.5 \pm 0.1$ ps, but here we can explicitly assign this time constant to electron-hole recombination with minimal contributions from long-lived carrier traps. Any long-lived trapped holes would still be visible in the XUV transient absorption spectrum, if present in sufficient densities [30], but no evidence for these long-lived hole states is evident after a few ps. The population dynamics of the holes can also be independently extracted from the Mo edge by measuring the decay of the integrated Mo $4d_{3/2} \rightarrow$ VB signal at 35.1-35.3 eV (Figure 3.9). A time constant of $\tau_{pop} = 1.4 \pm 0.1$ ps is extracted, which matches the measurement in the Te window within the error bars.

Turning now to the distribution dynamics of the holes within the VB, we first examine more closely the Te $4d_{5/2} \rightarrow$ VB hole feature at three representative time slices of 0-10 fs, 60-80 fs, and 700-800 fs plotted in Figure 3.3b-d. The spectrum of the hole feature is interpreted in accordance with the one-particle picture to directly record the hole energy distribution within the VB. In each time slice, the Te $4d_{5/2} \rightarrow$ VB peak is fit by a Voigt function to take into account the photoexcitation bandwidth, which produces a broad hole distribution approximated by a Gaussian function, and the convolved Lorentzian core-hole lifetime broadening. In the first time slice (0-10 fs), the $4d_{5/2} \rightarrow$

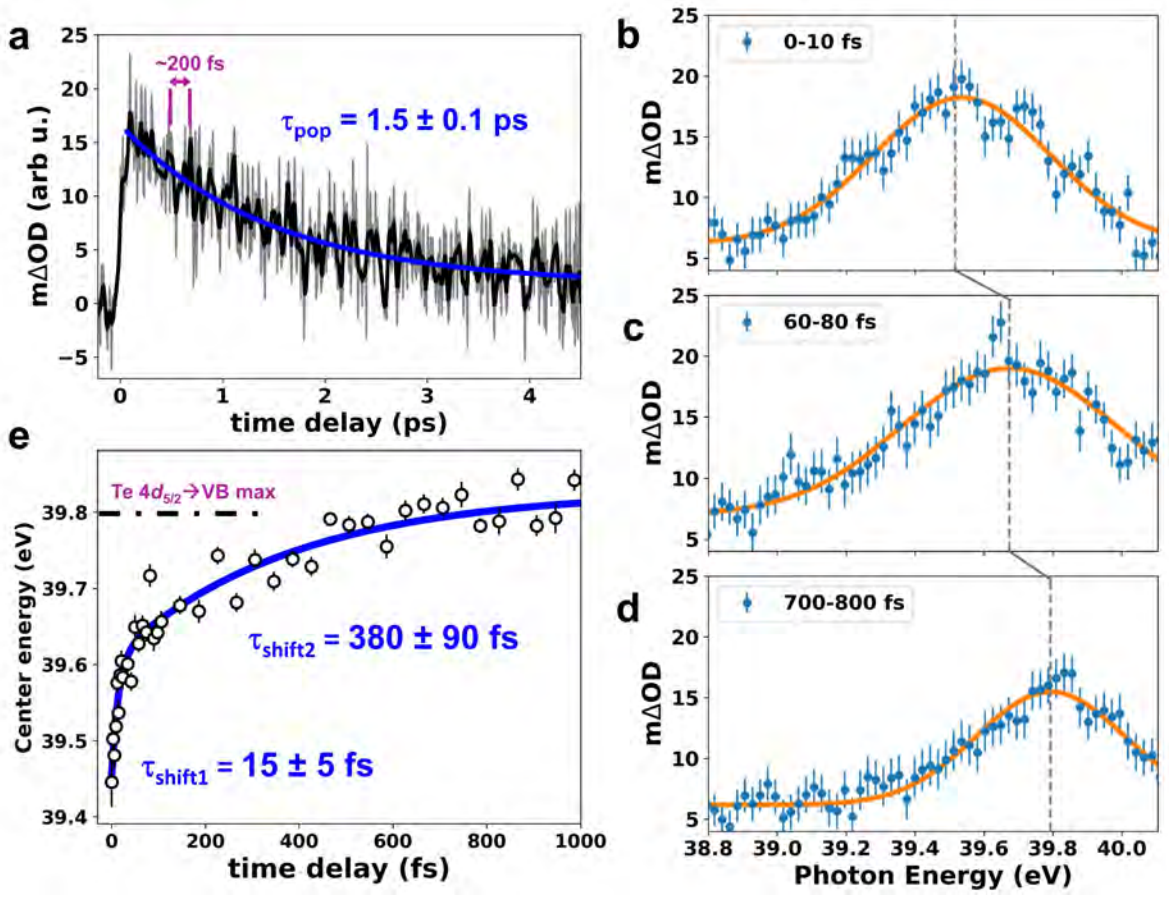

Figure 3.3: (a) Hole population dynamics measured as the integrated ΔOD amplitude at 39.7-39.9 eV versus time delay. The grey solid line is the experimental absorption data and the black solid line is a rolling average over 7 delay points. A single exponential decay is fit to the data (blue solid line) with a time constant of 1.5 ± 0.1 ps (b)-(d) Differential absorption of the Te $4d_{5/2} \rightarrow$ VB hole signal at time delays of 0-10 fs, 60-80 fs, and 700-800 fs. The closed circles are the experimental absorption data and the solid orange lines are Voigt fits. The grey dashed vertical lines show the center energy of the Voigt fit in each time slice. Blue arrows show the energy shift observed between time slices. Each differential absorption spectrum is an average over 10 time points within the designated time window. At each time point, 36 ΔOD spectra are averaged and the error bars are calculated as the standard error of the mean. The error for each time point is then propagated in the average of the 10 time points for each window and plotted with the data. (e) Hole distribution dynamics determined by extracting the center energy of the Te $4d_{5/2} \rightarrow$ VB hole signal using a Voigt fit at each time delay. The open circles are the extracted center energies and the error bars represent the standard error of the center energy fitting parameter in each Voigt fit. A biexponential decay function is fit (solid blue line) to the data with time constants of 15 ± 5 fs and 380 ± 90 fs.

VB signal is centered at 39.5 eV, which is 0.3 eV below the $4d_{5/2} \rightarrow$ VB maximum. This peak is assigned to $4d_{5/2}$ core transitions to the nascent, non-thermal hole distribution in the VB, which is represented by the schematic illustration in the left panel of Figure 3.1d. In the 60-80 fs time slice in Figure 3.3c, the $4d_{5/2} \rightarrow$ VB hole feature has blue shifted from 39.5 eV to 39.65 eV. This shift of the holes to higher energies is interpreted as a combination of carrier-carrier (i.e. hole-hole or hole-electron) thermalization and partial hole-phonon cooling of the nascent hole distribution, which correlates to the middle and right panels of the schematic model in Figure 3.1d. While thermalization by carrier-carrier scattering does not lead to a change in the total energy of the carrier distribution, the peak of the hole distribution still shifts toward the VB maximum by thermalization to a Fermi-Dirac distribution. A slight asymmetry is observed in the feature at 60-80 fs (Figure 3.3c), which could be an indication of the formation of a Fermi-Dirac distribution, but the peak is still fit well by a broad Voigt distribution. In the 700-800 fs time slice in Figure 3.3d, the hole feature is blue shifted further to the VB maximum at 39.8 eV and the overall amplitude of the peak is decreased. This 700-800 fs time slice is interpreted in accordance with the rightmost panel of Figure 3.1d. The blue shift toward the VB maximum represents near-complete cooling of the holes and the decay of the integrated area of the signal is caused by partial loss of hole population due to electron-hole recombination.

To map the full evolution of the hole distribution, the Voigt fitting procedure of the $4d_{5/2} \rightarrow$ VB peak is repeated for each time delay within the lifetime of the hole population and the extracted Voigt center energies are plotted as a function of delay time in Figure 3e. This allows us to trace the entire hole relaxation process using a single time-dependent parameter. The observed hole energy distribution dynamics can be described by a biexponential energy shift with a fast time constant (τ_{shift1} = 15 ± 5 fs) and a slower component (τ_{shift2} = 380 ± 90 fs). A monoexponential fit was also attempted, but did not result in a good agreement with our data (see Figure 3.10). The initial energy redistribution timescale (τ_{shift1} = 15 ± 5 fs) from the biexponential fit is very similar to the <20 fs time constant measured by Nie et al in MoS_2 for carrier-carrier scattering using optical transient absorption spectroscopy [110]. In the experiment by Nie et al, the hole and electron dynamics are not distinguished and the optical spectrum is blind to the distinct energy distributions of the carriers. However, the <20 fs time constant is assigned to thermalization by carrier-carrier scattering, which is supported by *ab initio* calculations. In our experiment, the τ_{shift1} = 15 ± 5 fs measured in the peak of the carrier-specific hole distribution energy in 2H-$MoTe_2$ is assigned to a similar thermalization step via hole carrier-carrier scattering, as schematically represented in Figure 3.1d (left to middle panels). This assignment is consistent with a recent calculation of carrier-carrier scattering in monolayer 2H-$MoTe_2$ at similar carrier densities (per layer), which predicts a thermalization time of sub-20 fs [112]. This is also consistent with carrier-carrier thermalization timescales measured in other semiconductors including lead iodide perovskite [109] and other layered materials including graphite [113]. Additionally, intra- or intervalley scattering processes involving carrier-phonon interactions may also contribute. An intervalley scattering time of 70 fs was measured, for example, in another TMDC semiconductor, WSe_2, via ultrafast angle-resolved photoemission spectroscopy at similar excitation fluences [114]. However, the hole distribution in 2H-$MoTe_2$ measured here does not reach the global maximum of the VB, which is localized at the point (Figure 3.1b), until after the slower time constant of τ_{shift2} = 380 ± 90 fs.

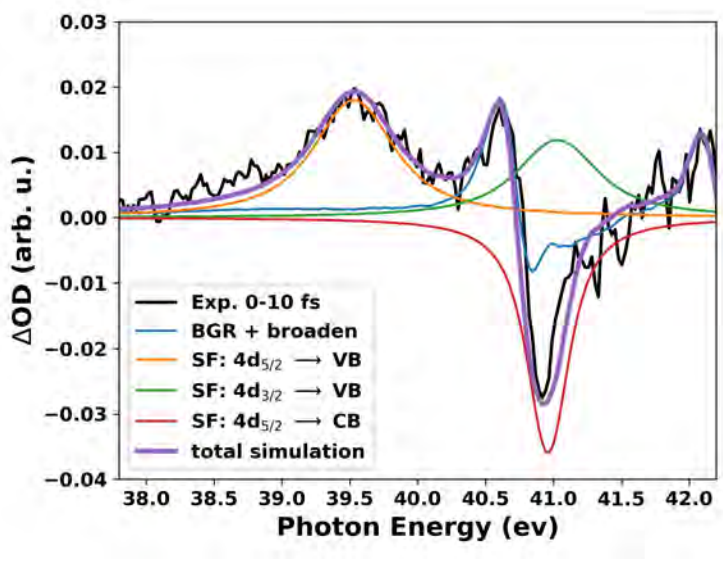

Figure 3.4: The solid black line is the experimental transient absorption data at a time delay of 0-10 fs. The colored solid lines are the manually decomposed contributions from the state-filling (SF), broadening, and bandgap renormalization (BGR). The total sum of the decomposed contributions is shown as the solid purple line.

The hole distribution energy then remains constant near the VB maximum over the remaining hole population lifetime of $\tau_{pop} = 1.5 \pm 0.1$ ps. The slower hole redistribution time of $\tau_{shift2} = 380 \pm 90$ fs is therefore assigned to hole-phonon cooling via intra- or intervalley scattering in the VB to the point, allowing the carriers and lattice to come into thermal equilibrium before electron-hole recombination takes place.

3.2.4 Spectral Decomposition of Conduction Band Transients

We now discuss the derivative feature in the transient spectra near the onset of the Te $4d_{5/2} \rightarrow$ CB absorption (~40.7 eV). Several effects contribute to this feature including bandgap renormalization (BGR) and state-filling by the electrons in the CB (illustrated in Figure 3.1d), excited-state broadening, and local modifications to the structural environment due to phonon excitations [9, 98, 103]. In Figure 3.4, the Te window OD spectrum in the time slice immediately following photoexcitation (0-10 fs) is plotted along with a manual decomposition of the broadening, BGR, and state-filling contributions in this energy window (further details in Appendix). The decomposition is performed using a similar procedure to that used by Zürch *et al.* on germanium [9].

The BGR and broadening contributions are calculated starting from the measured static XUV absorption spectrum by applying a linear energy shift and convolving the spectrum with a Gaussian filter, respectively. The state-filling effects are modeled by Voigt functions with a positive (negative) ΔOD sign for holes (electrons) and by taking into account the known spin-orbit splitting of the

Te $4d_{5/2}$ and Te $4d_{3/2}$ core levels. The unknown parameters of the shift, broadening, and state-filling contributions are manually adjusted to find a qualitative match with the spectrum in Figure 3.4. The resulting decomposition shows that the Te $4d_{5/2} \rightarrow$ VB hole signal is clearly isolated from the other transient effects, which makes the interpretation of this feature straightforward (as exploited in the previous section). The situation is less straightforward for the electron signal (state-filling: Te $4d_{5/2} \rightarrow$ CB), which overlaps with the Te $4d_{3/2} \rightarrow$ VB hole signal and the BGR and broadening contributions of the Te $4d_{5/2} \rightarrow$ CB edge. Nonetheless, the negative ΔOD signal contribution is dominated by the Te $4d_{5/2} \rightarrow$ CB electron signal. Therefore, we now analyze the time-dependent ΔOD observed near these energies (40.65 to 40.9 eV) in terms of the decay in this electron state-filling contribution and the overlapping evolution of the broadening and BGR related to recombination.

3.2.5 Electron Population Dynamics and Recombination-Induced Lattice Heating

In Figure 3.5a, the integrated differential absorption amplitude at energies near the onset of the Te $4d_{5/2} \rightarrow$ CB edge (40.65 to 40.9 eV, marked as blue shaded region in Figure 3.2d) is plotted as a function of delay time. The initial decrease in absorption at $t = 0$ is followed by a slow increase, leading to an overall positive differential absorption after ~2 ps. The slowly evolving increase is fit to a single exponential growth and a time-constant of 1.6 ± 0.1 ps is extracted. This time constant matches well with the decay of the hole signal shown in Figure 3.3a. Two overlapping effects can contribute to the increase in absorption between 40.6 to 40.9 eV, both of which are caused by electron-hole recombination. The first is the electron kinetics in the CB. As illustrated schematically in Figure 3.1d and demonstrated by the spectral decomposition in Figure 3.4, the initial state-filling effect in the CB leads to a decrease in absorption at these energies immediately following photoexcitation. When electron-hole recombination occurs, this causes the re-opening of these states with a corresponding increase in the Te $4d_{5/2} \rightarrow$ CB absorption. Second, non-radiative electron-hole recombination leads to a concomitant increase in the lattice thermal energy. Structural modifications caused by lattice heat can lead to a corresponding increase in the $4d_{5/2}$ core-level transitions at energies just below the CB minimum due to shifting and broadening effects [98, 115]. This is evidenced by the increase in differential absorption at these photon energies in a continuously heated sample compared to the room temperature sample (details in Appendix Figure 3.8). Since both of these recombination-induced effects can lead to the observed increase in the XUV absorption at 40.65-40.9 eV, we assign this time-dependent increase as a signature of the electron population decay and corresponding non-radiative lattice heating.

3.2.6 Coherent Lattice Displacement Dynamics

Superimposed on the slowly-varying ΔOD signal described in the previous section, high-frequency oscillations in ΔOD are evident near the derivative feature. In Figure 3.5b, the ΔOD at XUV energies where the largest-amplitude oscillations are observed (40.45 – 40.65 eV, marked as orange shaded region in Figure 3.2c) is plotted as a function of delay time. The inset in Figure 3.5b shows

the high-frequency oscillations at 40.45 – 40.65 eV after subtraction of the slowly varying signal. In Figure 3.5c, the Fourier transform (FT) spectrum of the time-domain oscillations in the Figure 3.5b inset is plotted, showing the presence of two clear vibrational frequencies at 169 cm^{-1} (5.1 THz) and 122 cm^{-1} (3.7 THz). These frequencies match closely to the A_{1g} out-of-plane and E_{1g} in-plane optical phonon modes of 2H-$MoTe_2$, respectively, as observed by Raman scattering (Figure 3.6) [116]. The phonon motions associated with these modes are shown schematically in Figure 5c.

From the FT spectrum in Figure 3.5c, the amplitude of the coherent oscillations in the XUV spectra is dominated by the A_{1g} mode, which is similar to the observation of coherent phonons through transient optical transmission measurements in MoS_2 and WSe_2 [117, 118]. We note that the E^1_{2g} mode is not observed in the FT spectrum at the characteristic frequency seen in the Raman spectrum (232 cm^{-1}), however, there may be evidence for a small contribution by this mode, which we describe in the Appendix (Figure 3.11). Also, while the largest-amplitude oscillations are observed near the Te $4d_{5/2} \rightarrow$ CB edge (40.45-40.65 eV), oscillations at the dominant A_{1g} frequency are also seen in other spectral regions, including near the hole signal in the Te window and near the Mo edge (see Figure 3.12). Focusing on the 40.45-40.65 eV region, the oscillating signal plotted in the inset of Figure 3.5b can be fit (blue line) using the following function:

$$\Delta\mathrm{OD}(t) = \alpha_1 \cos(2\pi t\omega_1 + \phi_1) + \alpha_2 \cos(2\pi t\omega_2 + \phi_2),$$

where α_n, ω_n, and ϕ_n correspond to the amplitude, frequency, and phase of the nth vibrational component. The fitted frequencies are $\omega_1 = 5.08 \pm 0.01$ THz and $\omega_2 = 3.69 \pm 0.02$ THz, in agreement with what we observe in the FT spectrum in Figure 5c, and the fitted phases are $\phi_1 = 0.95 \pm 0.07$ and $\phi_2 = 0.1 \pm 0.2$.

There are two possible mechanisms for the observed coherent phonon generation when the optical pump pulse is resonant with the electronic excitations of the material. First, the electronic excitation can lead to a direct change in the charge density of the electronic excited state and drive the nuclei to the new minimum of the potential energy surface. This mechanism is referred to as "displacive excitation of coherent phonons" (DECP) [119]. On the other hand, the optical pump pulse can couple the ground-state electronic wavefunction to the potential energy surfaces of electronic excited states through resonant impulsive stimulated Raman scattering (ISRS), resulting in a force driving coherent vibrations of the lattice [120]. As mentioned by Trovatello et al. [121], a consensus as to the dominant mechanism in the absorptive regime has not been established in the literature. Both mechanisms can produce displacive coherent phonons with cosine phases of 0 or π [122, 123]. For this reason, the Raman scattering mechanism is also termed "transient stimulated Raman scattering" (TSRS) in the absorptive regime, to account for the possibility of inducing a displacive force by this mechanism [122]. However, while the DECP mechanism favors coherent phonon excitations of totally symmetric modes (A_{1g}) [119, 124], the Raman scattering mechanism allows excitation of all Raman-active modes. Therefore, the excitation of both A_{1g} and E_{1g} modes (Figure 3.5c) indicates that TSRS contributes to the coherent phonon excitation in 2H-$MoTe_2$. Regardless of the mechanism, the force induced by interaction with the ultrashort resonant excitation pulse in 2H-$MoTe_2$ is clearly displacive, as determined by the extracted phases ($\phi_1 = 0.95 \pm 0.07$ and $\phi_2 = 0.1 \pm 0.2$). With this information, our aim is to extract the real-space lattice displacement involved.

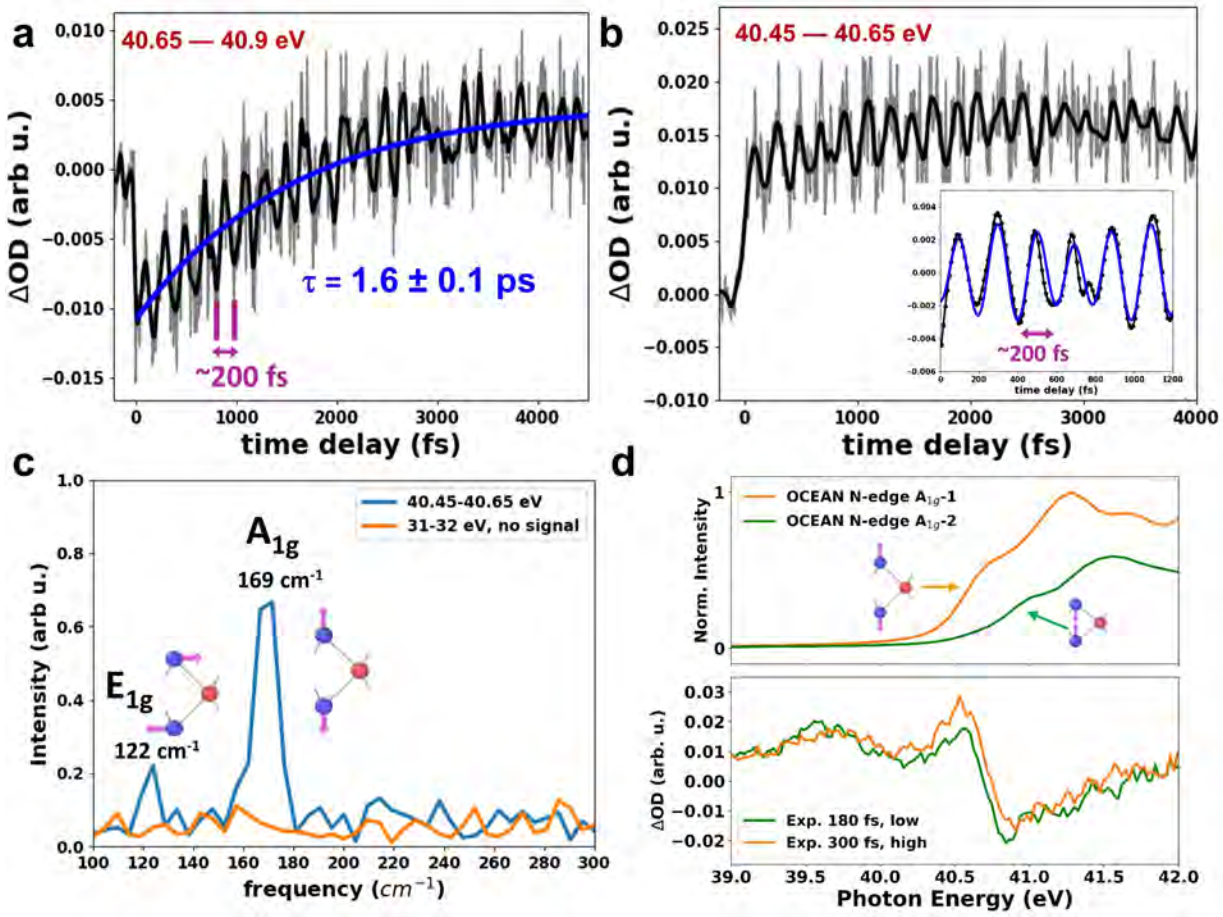

Figure 3.5: (a) The time evolution of the integrated ΔOD at photon energies just above the Te $4d_{5/2} \rightarrow$ CB edge (40.65-40.9 eV). This energy range is indicated by the blue shaded region in Figure 3.2c. The grey line is the experimental data and the black line is a 7-point rolling average over delay time. The blue line is a single exponential fit to the data with a time constant of 1.6 ± 0.1 ps. (b) Time evolution of the ΔOD just below the onset of the Te $4d_{5/2} \rightarrow$ CB edge (40.45-40.65 eV). This energy range is indicated by the orange shaded region in Figure 3.2c. The grey solid line is the experimental absorption data and the black line shows a 7-point rolling average (smoothed) over delay time. The inset shows a cosine fit to the smoothed data as described in the text (c) The Fourier transform (FT) spectrum of the time-dependent ΔOD signal in (b) is shown as a solid blue line, revealing peaks at 169 cm^{-1} (5.1 THz) and 122 cm^{-1} (3.7 THz). The orange line is the FT spectrum of the time-dependent ΔOD integrated over 31-32 eV (i.e. where no transient absorption signal is observed) to illustrate the noise floor. The inset shows a schematic of the displacive excitation mechanism, as described in the text. (d) The upper panel shows the simulated displacement-induced change in the XUV spectrum calculated by OCEAN for each A_{1g} distortion direction. The bottom panel shows the experimental ΔOD data at a time slices of 180 fs and 300 fs, respectively, demonstrating the uniform increase/decrease of the absorption near these energies at the two extremes of the coherent oscillation.

To understand the XUV ΔOD oscillations in terms of real-space lattice displacements, we first calculate distorted 2H-$MoTe_2$ structures along the dominant A_{1g} displacement coordinate. This is achieved by displacing each atom i, with mass m_i located at r_i in the $MoTe_2$ unit cell by a distance Δr_i along the real part of the eigenvector e, corresponding to the dominant A_{1g} vibration mode ($q = \Gamma$), computed as $\Delta r_i = \alpha/\sqrt{m_i}\mathrm{Re}[e \cdot \exp(q \cdot r_i)]$. The amplitude of the displacement, α, is chosen such that the maximum real-space displacement of any atom in the simulation cell is less than 0.3 Å. Next, Bethe-Salpeter equation calculations of the A_{1g}-distortion-dependent Te $4d \rightarrow$ CB transitions are performed using the OCEAN (Obtaining Core-level Excitations using *ab initio* methods and the NIST BSE solver) software package [125, 126]. The results are plotted in Figure 3.5d (upper panel). The calculations reveal that the XUV absorption amplitude at the $4d_{5/2} \rightarrow$ CB onset reaches a maximum when the Te atoms are moved outwardly in the direction away from the plane of Mo atoms. In the opposite direction, corresponding to the Te atoms moving inwardly toward the plane of Mo atoms, the XUV absorption amplitude decreases and slightly blue shifts near the Te $4d_{5/2} \rightarrow$ CB onset. This uniform decrease/increase over the $4d_{5/2} \rightarrow$ CB spectral region qualitatively matches the observed ΔOD oscillations in the experiment, as shown in the bottom panel of Figure 3.5d. From the phase of the A_{1g} oscillation (π) extracted from the experimental data in Figure 5b, the displacement at $t = 0$ begins with increasing absorption near the $4d_{5/2} \rightarrow$ CB onset. This shows that photoexcitation leads to a displacement along the A_{1g} mode in the outward direction. This ultrafast lattice expansion along the specific A_{1g} phonon mode in the excited state provides a key experimental benchmark for understanding how light-induced changes in electronic structure can drive non-thermal structural changes in layered materials.

3.3 Conclusions

In a single optical pump, XUV transient absorption probe experiment, we simultaneously uncover the detailed dynamics of intraband hole relaxation, electron-hole recombination, and excited-state coherent lattice displacement in 2H-$MoTe_2$. In contrast to optical transient absorption spectroscopy where the signals correspond to convolutions of electrons and holes at various energies within the VB and CB, here we directly map the time evolution of the hole energy distribution specifically in the VB. Taking advantage of the straightforward, one-particle interpretation of the N-edge core-level absorption, especially through the Te XUV edge, the intraband hole relaxation timescales are separated from the interband electron-hole recombination. The holes are found to redistribute within the VB on two distinct timescales of 15 ± 5 fs and 380 ± 90 fs. The former time constant is assigned to a thermalization process by carrier-carrier scattering, which leads to a shift in the peak of the hole energies closer toward the VB maximum. The slower hole redistribution time constant of 380 ± 90 fs is assigned to carrier-phonon cooling by intra- or intervalley scattering to the VB maximum, which is localized at the critical point. These dynamics provide key insight regarding energy loss mechanisms following above bandgap excitation of 2H-$MoTe_2$ thin films, which is important for designing next-generation photovoltaic or other optoelectronic devices using this layered semiconductor nanomaterial.

The present work furthermore reveals light-induced coherent lattice displacement dynamics

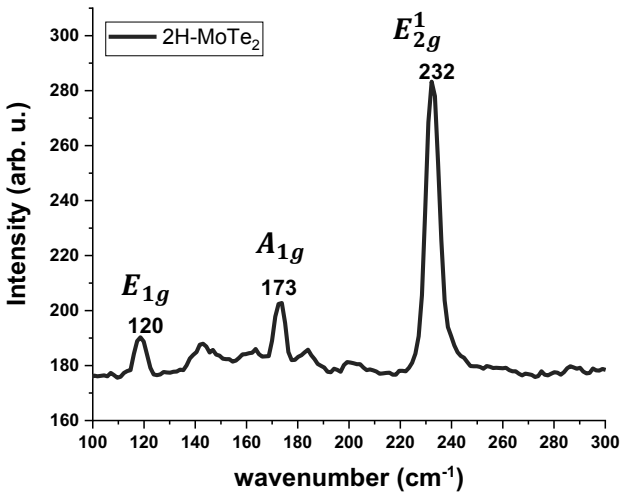

Figure 3.6: Raman Spectrum of 2H-$MoTe_2$ samples

along the out-of-plane A_{1g} and the in-plane E_{1g} phonon coordinates of 2H-$MoTe_2$. These structural dynamics show that the A_{1g} mode in particular is strongly coupled to the electronic excitation. The strong electron-phonon coupling in this out-of-plane mode leads to a new equilibrium structure in the excited state reached by expansion of the Te atoms away from the Mo plane. By extracting the real-space displacement of the 2H-$MoTe_2$ lattice following optical excitation, the measurements presented here provide a benchmark for understanding how structural changes in these materials are coupled to excited-state electronic structure. Our findings and experimental approach will be of benefit to the larger community that has a growing interest in light-induced lattice displacements in layered materials for applications toward optically controlled phase transitions [90, 92].

3.A Appendix

3.A.1 Sample preparation.

The $MoTe_2$ thin film was synthesized by tellurizing a Mo film at 700 °C for 2 hours in a tube furnace directly on a 30 nm thick, 3×3 mm square Si_3N_4 window. The Mo film was first deposited onto the Si3N4 window by sputtering previous to the reaction with Te powders. The synthesized $MoTe_2$ film was characterized by Raman spectroscopy and X-ray photoelectron spectroscopy (XPS). The Raman spectrum in the Figure 3.6 shows several modes including E_{1g}, A_{1g}, E^1_{2g}, indicating that the $MoTe_2$ film forms the 2H phase. Figure 3.7 shows the XPS spectrum of the 2H-$MoTe_2$ sample studied in this work. The relative peak spacing gives the spin-orbit splitting of the $4d_{5/2}$ and the $4d_{3/2}$ core levels of 1.5 eV. The detailed sample preparation and characterization can be found in Ref. [79]. Note that the synthesized $MoTe_2$ is a large area and continuous polycrystalline thin film.

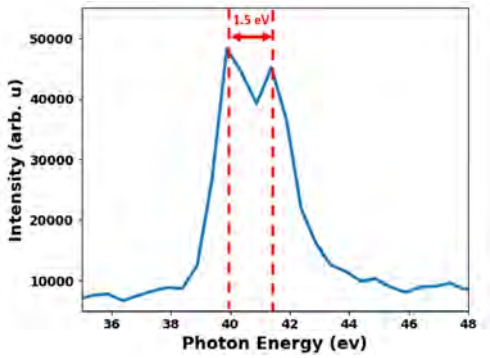

Figure 3.7: XPS spectrum of 2H-$MoTe_2$ near the Te 4d binding energies. The binding energies of the $4d_{5/2}$ and $4d_{3/2}$ core levels are spin-orbit split by 1.5 eV.

3.A.2 Experimental methods

The detailed experimental methods are described in Chapter 2. In the XUV transient absorption experiment, compressed broadband laser pulses spanning 500-1000 nm were split into the probe and pump arm by a broadband beam splitter with 9:1 intensity ratio. The laser repetition rate was reduced to 100 Hz by a mechanical chopper to prevent sample damage. With dispersion scan [47], the pulse duration of the pump and the probe were characterized to be below 5 fs. The laser beam in the probe arm was focused into a 4 mm long cell filled with Kr to generate broadband XUV light. The driving field in the probe arm was filtered by a 100 nm thick Al filter and the XUV light subsequently focused into the sample chamber by an Au coated toroidal mirror in a 2f-2f geometry. The pump light was optically delayed and recombined with the probe by an annular mirror with a hole at 45 degree with respect to the mirror surface. To eliminate time delay drift, a transient absorption measurement on Ar $3s3p6np$ autoionizing states was run after each time-delay scan on the $MoTe_2$ sample [10].

3.A.3 OCEAN and density functional theory calculations

Density functional theory (DFT) with the projector augmented wave (PAW) method [127] implemented in the Vienna ab initio Simulation Package (VASP) [128, 129] was used to compute the ground-state density of states for bulk $MoTe_2$ crystals. Exchange and correlation effects are calculated using the Perdew-Burke-Ernzerhof form of generalized gradient approximation [130]. Wave functions are constructed using a plane wave basis set with components up to kinetic energy of 400 eV and the reciprocal space is sampled using a $3 \times 3 \times 3$ Gamma-centered mesh with a 0.05 eV Gaussian smearing of orbital occupancies. DFT simulations of lateral interfaces were performed on a bilayer $MoTe_2$ supercell containing 216 atoms, measuring $21.09 \times 21.09 \times 13.97$ Å^3 along the a-, b- and c-directions. Calculations were performed till each self-consistency cycle is converged in energy to within 10^{-7} eV/atom and forces on ions are under 10^{-4} eV/Å.

The calculation of core-level absorption spectra at the Te $M_{4,5}$ edge was accomplished with

DFT and Bethe-Salpeter equation (BSE) calculations using Quantum ESPRESSO and the OCEAN software package [125, 126, 131, 132]. The DFT-BSE calculation was conducted using norm-conserving scalar-relativistic Perdew-Burke-Ernzerhof pseudopotentials with nonlinear core correction under generalized gradient approximation and a $6 \times 6 \times 1$ k-point meshgrid [130, 133–135]. In the calculation, the number of bands is set to 40 and the dielectric constant is set to 12.9. Convergence was achieved with an energy cutoff of 80 Ryd and cutoff radius of 4 Bohr.

3.A.4 Excited carrier density

The carrier density is determined by estimating the total photon absorption per pump excitation pulse, assuming each absorbed photon produces one excited electron-hole pair. In the measurements presented here, the pulse energy is 1.2 μJ and the spot size of the pump pulse at the sample is 190 μm. We use the equations described in chapters 4(119) and 4(120) in Ref [136], which take into account the complex refractive indices of air, the 2H-$MoTe_2$ sample (50 nm thick), and the Si_3N_4 substrate (30 nm thick) to calculate the percent absorption, reflection, and transmission. This gives a total percent absorption of the incoming excitation light of 26.5% in 2H-$MoTe_2$ before taking into account the saturable absorber effect. In the next step, a correction due to the saturable absorber effect is calculated using:

$$\alpha = \alpha_0/(1 + I/I_s),$$

where α and α_0 are the absorption coefficients with and without the saturable absorber effect, respectively. I is the peak intensity used in the experiment and I_s is the saturation peak intensity. With $I = 1700$ GW/cm^2 and $I_s = 217$ GW/cm^2 [137], we find $\alpha/\alpha_0 = 0.113$, which gives a final absorption percent of 26.5%. The carrier density is therefore estimated to be 1.02×10^{20} cm^{-3}. Considering 2H-$MoTe_2$ has a unit cell volume of $1.7395416 \times 10^{-22}$ cm^3, with 18 valence electrons per unit cell, the total valence electron density is 1.034755×10^{23} cm^{-3}. This gives the excitation percent in the present experiment of 0.1%.

3.A.5 Comparison of residual heat signal at 1 kHz and 100 Hz with the transient spectrum at 4-5 ps

As discussed briefly in experimental methods section above, the repetition rate of the laser is reduced to 100 Hz in the data presented in this main text in order to allow the photoexcited sample to recover close to room temperature conditions between every laser pulse (10 ms separation). Without the chopper, the 1 ms temporal spacing between the 1 kHz pulses at 1 kHz is not sufficient to allow lateral cooling of the sample to the sample holder. In this 1 kHz mode, the heat deposited from each laser pulse therefore accumulates in the sample [9]. From previous analysis of this heat deposition effect in germanium thin films of similar thickness and thermal conductivity [9], it was found that a thermal equilibrium is reached after only a few laser pulses. Therefore, the two datasets shown in Figure 3.8 labeled in the legend as “heat”, which are collected by averaging 32 cycles of 1,000 pulse integrations at negative time delays, is a measurement of the differential absorption between this thermally equilibrated sample at an elevated temperature versus the room

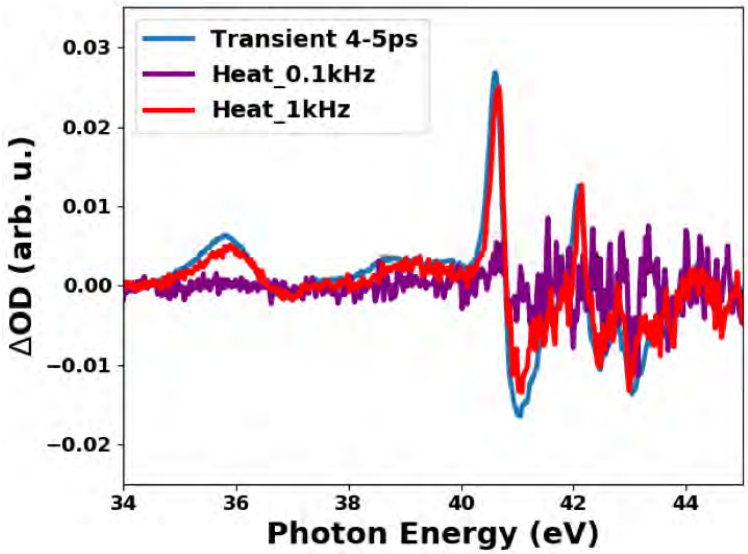

Figure 3.8: Transient spectrum in the long delay time limit compared to residual heat signal. The purple and red lines are differential absorption spectra averaged over negative time delays of -1 to -0.5 ps, taken on the same sample, but with different repetition rates of 100 Hz and 1 kHz, respectively. As discussed in Sec. 3.A.5, the negative-time-delay spectrum represents the residual changes in XUV absorption persisting from the previous pump pulse excitation (delay of 10 ms and 1 ms for 100 Hz and 1 kHz repetition rates, respectively). The residual change is due to heat that has not been sufficiently conducted away from the sample before the next pulse arrives and therefore the purple/red lines represent the difference between the XUV spectrum of this residually heated sample and the spectrum in the absence of heating (pump beam blocked). The residual heat signal is significantly reduced at 100 Hz. The blue line is the normalized differential absorption spectrum averaged over time delays of 4-5 ps from the data in Fig. 3.2(a) (100 Hz, 8 mJ/cm^2)

temperature sample in the absence of the pump. Comparison between the negative-time-delay spectrum at 100 Hz repetition rate versus the 1 kHz experiment shows the significant reduction in heat accumulated in the sample due to the 10 ms delay between pulses at 100 Hz. Comparison of the purely heat-induced change in the XUV absorption at 1 kHz (shown as the red line in Figure 3.8) and the transient spectrum at 4-5 ps (blue line) indicates that the carrier relaxation process is completed by 4-5 ps and the remaining signal after this delay time is characterized dominantly by heat-induced effects. Therefore, any contribution of long-lived hole traps in the carrier relaxation process observed here must be minimal and is below our detection limit.

3.A.6 Mo edge hole population dynamics

In Figure 3.9a, differential absorption lineouts averaged over early time delays (10-50 fs) and later time delays (2.5-3 ps) are plotted. These lineouts are identical to the lineouts in Figure 3.2d, except

now the plot range is expanded to show both Mo and Te windows from 33-42 eV. Signatures of the photoexcited holes at early time delays are observed via Mo $4p_{3/2}$ →VB transitions near 35 eV and via Te $4d_{5/2}$ →VB transitions near 39.6 eV. Due to the sharp XUV absorption edge observed in the Te window, there is a clear separation of the Te $4d_{5/2}$ →VB absorption compared to the Te $4d_{5/2}$ →CB onset. The situation is different in the Mo window where the broad onset of the Mo N edge leads to overlapping Mo $4p_{3/2}$ →VB and Mo $4p_{3/2}$ →CB signals. For this reason, we focus primarily on the Te $4d$ core-level absorption to report on the carrier and structural dynamics in Results and Discussion (i.e. hole relaxation extracted in Figure 3.3a). However, the population dynamics of the photoexcited holes can be independently extracted using both the Mo and Te elements as reporter atoms. In Figure 3.9b, the hole population measured via the integrated Mo $4p_{3/2}$ →VB signal near the Mo $4p_{3/2}$ →VB maximum (35.1-35.3 eV) is plotted as a function of delay time. A time constant of $\tau_{pop} = 1.4 \pm 0.1$ ps is extracted, which matches the measurement in the Te window (Figure 3.3a) within the error bars.

3.A.7 Comparison of monoexponential and biexponential fits to the time-dependent energy shift of the Te $4d_{5/2}$ →VB hole signal

As discussed in Sec. 3.2.3, the time-dependent energy distribution of the holes is extracted via a Voigt fit to the $4d_{5/2}$ →VB peak at each time delay within the hole population lifetime. The extracted center energies are plotted in Figure 3.10 with the blue line in the left panel corresponding to a biexponential fit to the shifting energy, as shown in Figure 3.3e. In the right panel of Figure 3.10, the time evolution of the hole distribution is fit to a monoexponential function, shown as the red line. The insets of both panels show an expanded view of the early time delays up to 200 fs. The poor fit in the right panel, especially at early time delays shown in the inset, indicates that the monoexponential function is not sufficient to describe the data. A correct fit is achieved at using the biexponential function in the left panel.

3.A.8 Decomposition of transient spectrum (0-10 fs)

In Figure 3.4, a lineout of the ΔOD spectrum near the Te N_4 edge averaged over delay times of 0-10 fs is plotted along with a manual decomposition of broadening, band-gap renormalization (BGR), and state-filling contributions. The decomposition is determined using the following procedure. First, state-filling (SF) by the new Te $4d_{5/2}$ →VB hole transitions is manually fit to a Voigt function. The Te $4d_{3/2}$ →VB hole contribution is then produced by blue-shifting the $4d_{5/2}$ →VB peak by the known 1.5 eV spin-orbit splitting and by scaling down the area by the 3:2 ratio for $d_{5/2}$:$d_{3/2}$ core-hole state degeneracies. The $4d_{5/2}$ →CB SF contribution (negative differential absorption) from the electrons is assumed to have the same integrated area as the $4d_{5/2}$ →VB peak (i.e. same number of photoexcited electrons as holes) and the width of the Gaussian and center energy of the Voigt function are adjustable. The blue line shows the broadening and BGR contributions, which are manually produced by red-shifting and broadening the experimental static absorption spectrum, iterating with the adjustable parameters of the $4d_{5/2}$ →CB electrons contribution, until the total

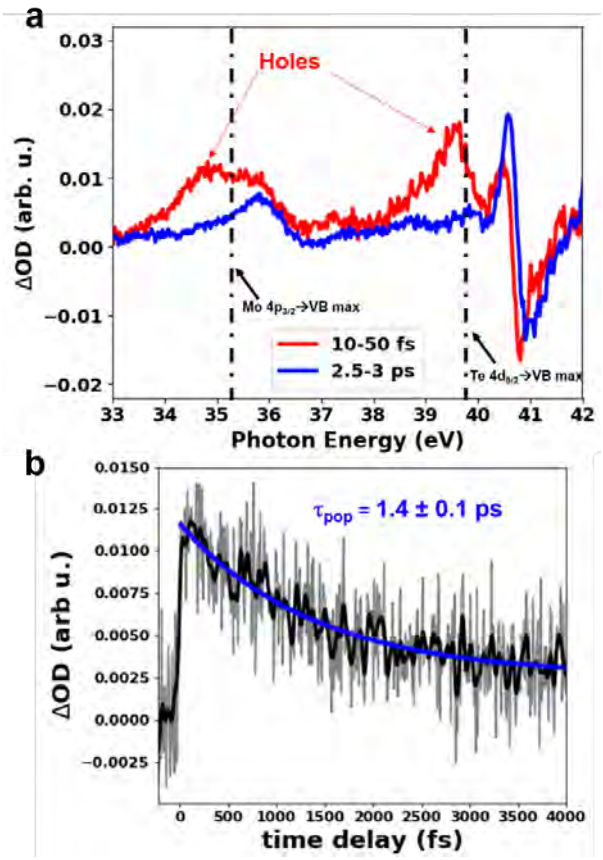

Figure 3.9: Hole population dynamics measured in the Mo window. (a) Differential absorption lineouts averaged over 10-50 fs and 2.5-3 ps. Signatures of the photoexcited holes are observed in both the Mo window and the Te window. (b) Hole population dynamics measured as the integrated OD amplitude in the Mo window at 35.0 -35.2 eV as a function of time delay. The grey solid line is the experimental absorption data and the black solid line is a rolling average over 7 delay points. A single exponential decay is fit to the data (blue solid line) with a time constant of 1.4 ± 0.1 ps.

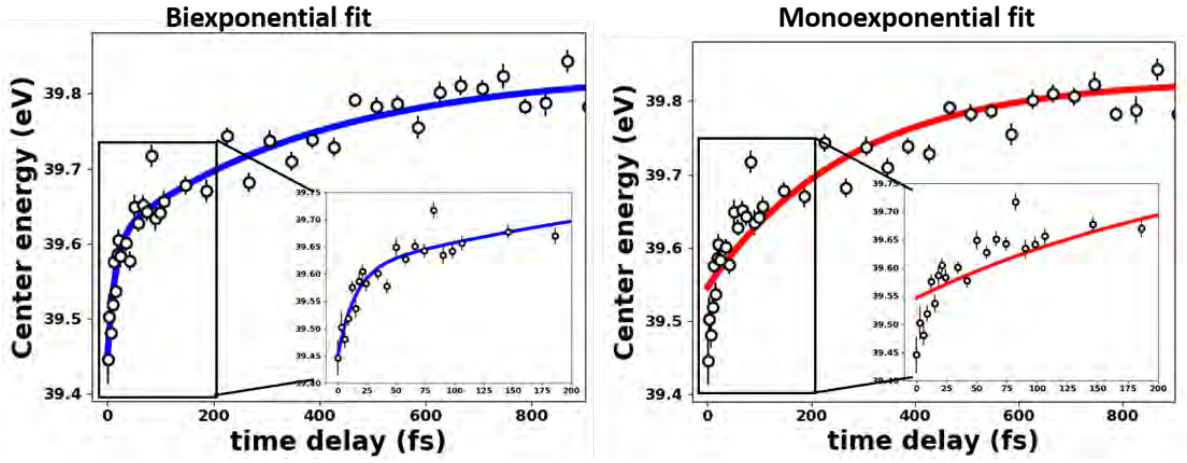

Figure 3.10: Temporal evolution of the hole distribution energy and fit to a biexponential function (left) and monoexponential function (right). The left panel is the same as in Figure 3.3e with the addition of an inset showing an expanded view of the early time delays up to 200 fs. An expanded view of these early time delays is also shown in the right panel with the monoexponential fit. The poor fit at early time delays using the monoexponential function indicates that an additional decay component needs to be taken into account.

simulation matches the experimental transient absorption. The resulting red shift used to simulate the BGR is 9 meV and the broadening is achieved with a Gaussian filter of $\sigma = 0.1$ eV.

3.A.9 Possible coherent phonon motion in the E^1_{2g} mode

As noted in Sec. 3.2.6, the E^1_{2g} mode is not observed at the expected frequency (~232 cm^{-1}) in the FT spectrum of the coherent spectral oscillations near the Te $4d_{5/2}$ →CB edge. One potential reason for this is that the motion along this mode could lead to an energy shift in the XUV spectrum in the same direction for each turning point of the vibrational motion (i.e. at and 2 phases). This possibility is justified by OCEAN calculations of the XUV absorption spectrum of the distorted structures along the E^1_{2g} coordinate, shown in Figure 3.11a. At both extremes of the E^1_{2g} distortion, the XUV absorption spectrum displays the same shift relative to the equilibrium structure. This may lead to an oscillation in the XUV spectrum at double the frequency of the E^1_{2g} phonon. As seen in Figure 3.11b, which shows the extension of the Fourier Transform (FT) spectrum in Figure 3.5c out to 500 cm^{-1}, an additional peak is observed near ~460 cm^{-1}, which is close to double the frequency of the E^1_{2g} mode. However, this peak is near the noise level of the measurement and we feel that this does not provide conclusive evidence that the E^1_{2g} mode is coherently excited. Therefore, we do not make this assignment in the present work and do not include it in our model in Sec. 3.2.6.

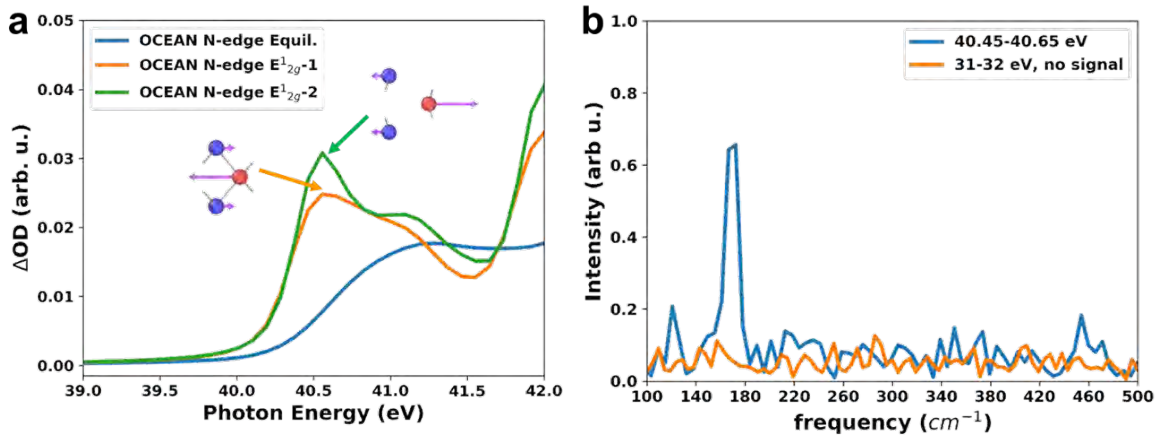

Figure 3.11: (a) The simulated displacement-induced change in the XUV spectrum calculated by OCEAN for each E^1_{2g} distortion direction, compared to the OCEAN-simulated XUV spectrum of the equilibrium structure. (b) The extended FT spectrum plotted in Fig. 5c, out to 500 cm^{-1}. A peak is observed near ~460 cm^{-1}, which is nearly double the expected frequency of the E^1_{2g} mode (232 cm^{-1}).

3.A.10 Coherent phonon motion observed in "hole" signal and in Mo window

In Figure 3.12a, the false-color map of ΔOD from Figure 3.2a is reproduced. Thin grey lines are drawn at two energy regions, labeled (I): 35.7-36.1 eV and (II):39.7-39.9 eV. Energy (I) represents the energy region near the Mo $4p_{3/2}$ →CB edge and energy (II) represents the energy region near the Te $4d_{5/2}$ →VB maximum. Time-domain oscillations are observed at both energy regions (I) and (II), similar to those seen near the Te $4d_{5/2}$ →CB minimum, which is described in detail in Sec. 3.2.6. In Figure 3.12b-c, Fourier transform (FT) spectra of the ΔOD oscillations at energies (I) and (II) are shown, respectively. Both FT spectra show the presence of a vibrational frequency at 167 cm^{-1}, which matches the 169 cm^{-1} A_{1g} mode observed at the Te $4d_{5/2}$ →CB edge in Figure 3.5b. This indicates that the dominant A_{1g} coherent motion launched upon photoexcitation affects multiple regions of the XUV spectrum and is not specific to the Te $4d_{5/2}$ →CB edge.

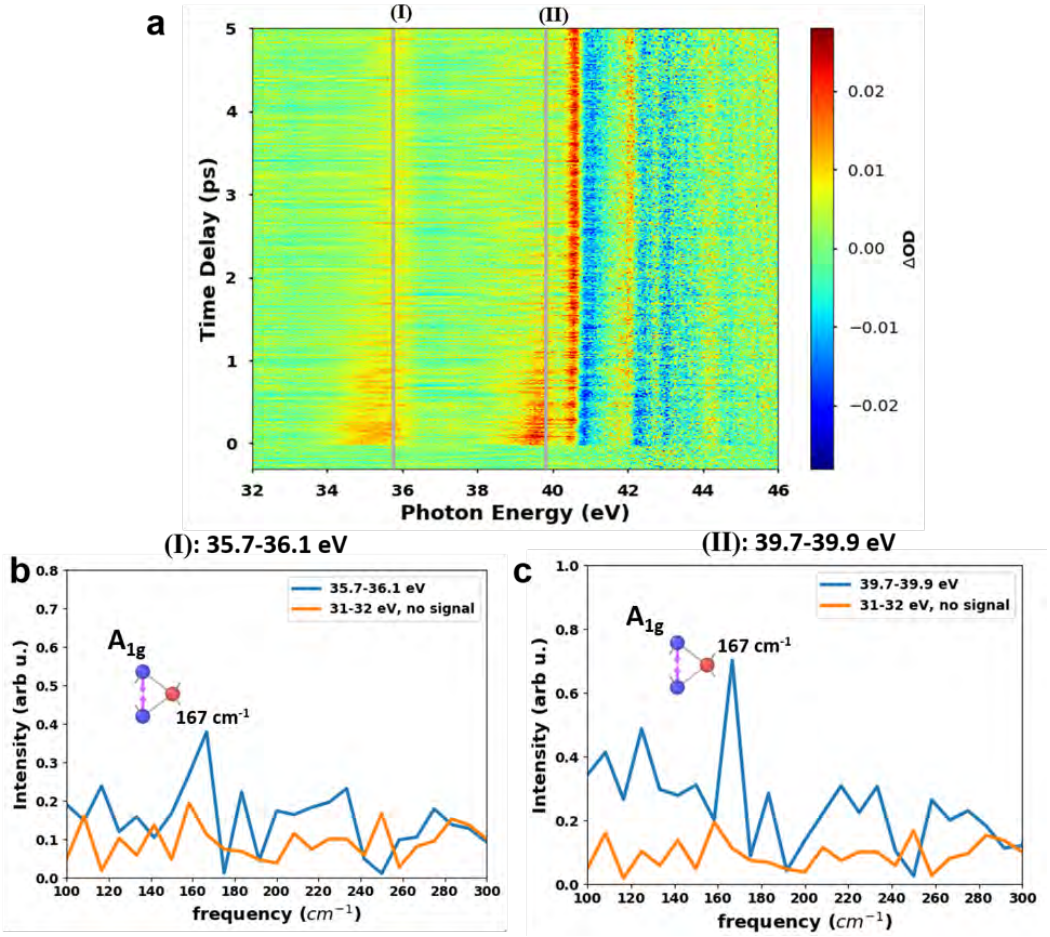

Figure 3.12: (a) XUV transient absorption false-color plot reproduced from Figure 3.2a. Vertical grey lines are drawn, labeled (I) and (II), which indicate the energies at which time-domain lineouts are taken. (b),(c) Fourier transform spectra of the time-domain lineouts taken at energy range (I):35.7-36.1 eV and (II):39.7-39.9eV. Energy (I) is taken at the onset of the Mo $4p_{3/2}$ →CB edge and energy range (II) is taken at the Te $4d_{5/2}$ →VB maximum (hole signal). Both FT spectra at these two energy regions show a peak at 167 cm^{-1}, consistent with the A_{1g} phonon mode.

Chapter 4

Dynamics of Core-Excitons and Free Carriers in Bulk WS_2[1]

4.1 Introduction

Studying the dynamics of elementary excitations in semiconductors such as photoexcited carriers, phonons, and excitons has been crucial to the success of electronic devices [108, 139]. While most measurements on the photophysical and photochemical properties of semiconductors are performed within the optical domain, core-level transient absorption (TA) and transient reflectivity spectroscopy have recently been utilized to investigate carrier dynamics in semiconductors and two-dimensional materials [9, 28, 29, 76, 98, 99, 140, 141] and the decay of core-excitons in insulators [31–33]. Core-level TA spectroscopy in semiconductors typically consists of an optical pulse to excite the carriers in the sample and an extreme ultraviolet (XUV) or X-ray pulse to record the changes in the core-level absorption spectra. In many semiconductors, the core-level absorption spectra can be mapped onto the conduction band (CB) density of states (DOS) due to significant dielectric screening [142], and the core-level TA spectra directly reflects the carrier distributions as a function of energy, thereby providing real-time tracking of carrier dynamics [9, 76, 98, 99].

In contrast, the core-level absorption spectra of many insulators, in particular ionic solids with poor dielectric screening, exhibit sharp peaks below the onset of core-to-CB edges [143–153]. These discrete transitions are termed "core-excitons", which are formed by the Coulomb attraction between the excited electron and the core hole [145, 147]. The electron-hole binding results in longer lifetimes of the core-excitons compared to the typical <1 fs decay time of core-to-CB transitions [148, 154]. The observation of the decay of core-excitons is enabled through attosecond transient absorption spectroscopy in the extreme ultraviolet, a core-level TA spectroscopy utilizing sub-femtosecond XUV pulses in combination with <5 fs long optical pulses. As opposed to the typical attosecond TA measurement in semiconductors where the XUV pulse probes the valence

[1]The content and figures of this chapter are adapted or reprinted with permission from Ref. H.-T. Chang et al., "Coupled Valence Carrier and Core-Exciton Dynamics in WS_2 Probed by Attosecond Transient Absorption Spectroscopy", ArXiv Prepr., 2103.09965 (2021).

electronic state after optical excitation [28], experiments to probe core-exciton states use the sub-femtosecond XUV pulse to excite the core-excitons and the core-exciton transition dipoles are subsequently perturbed with the optical pulse [31–33]. Due to the large band gap in insulators, which exceeds the photon energy of available visible and ultraviolet light pulses, the observation of the effect of carrier dynamics on a core-excitonic system via core-level TA spectroscopy has not been achieved and the effect of valence electron-hole pairs on core-exciton transitions and their dynamics remains elusive.

In this work, we report the observation of core-exciton transitions within the W $N_{6,7}$ edge (32-37 eV) of WS_2 and the nearby W O_3 edge (37-45 eV), a smooth core-level absorption edge consisting of core-to-CB transitions that can be understood within the single-particle mean field picture. The proximity of the two different types of core-level absorption edges presents an excellent opportunity in simultaneously observing the dynamics of carriers in the valence shell and their influence on the dynamics of core-excitons. A single experiment thus probes the carriers at the W O_3 edge and the discrete core-exciton transitions at the W $N_{6,7}$ edge. Tungsten disulfide is a Group VI transition metal dichalcogenide and a semiconducting two-dimensional (2D) layered material. In its mono- and bilayer form, the electronic structure and photophysics of WS_2 have been extensively studied for potential applications in optoelectronics, 2D valleytronics and spintronics [155–167]. Recently, interlayer charge transfer excitations and novel elementary excitations such as moiré excitons were observed in heterostructures containing WS_2 layers [168–171].

Here, by conducting attosecond core-level transient absorption spectroscopy in the XUV on WS_2 thin films, picosecond hole relaxation and carrier recombination times are obtained from the core-level TA spectra at the W O_3 edge. A $\sim$ 10 fs coherence lifetime of core-excitons at the W $N_{6,7}$ edge is also measured. In contrast to the attosecond TA studies on insulators where the observed dynamics are dominated by coupling of core-exciton states with the optical field [31–33], here the core-exciton lineshape is primarily influenced by the change of electronic screening and band filling due to carriers excited by the optical pulse. The optical-XUV transient absorption study at the W O_3 and $N_{6,7}$ edges provides a prototypical example for measuring the carrier-induced modification of core-excitons and paves the way for exploring carrier dynamics in 2D heterostructures and superlattices involving transition metal dichalcogenides, where the element specificity of core-level TA spectroscopy can be employed to enable layer-selective probing of photophysical and photochemical phenomena.

4.2 Experimental Scheme

The details of sample preparation and the scheme of the attosecond TA spectroscopy experiment are provided in Appendix 4.A and 4.B, respectively. In brief, 40 nm thick WS_2 films were synthesized on 30 nm thick silicon nitride windows by atomic layer deposition (ALD) of WO_3 thin films and subsequent sulfurization with H_2S [172]. In the attosecond TA experiments, the samples were irradiated with a broadband optical pulse (500-1000 nm) with nominal duration of 4 fs and a time-delayed broadband XUV pulse (30-50 eV) produced by high harmonic generation using a near single cycle optical pulse in a Kr gas jet.

4.3 Results and Discussion

The core-level absorption spectrum of the 40 nm thick WS_2 film is displayed in Fig. 4.1(a) (red line). The static spectrum below 37 eV (marked with dashed cyan line) exhibits four distinct peaks labeled as A-D. Peaks A and B occur on top of the absorption edges between 33 eV and 34 eV. Peak C exhibits a Fano-type asymmetric lineshape at approximately 35.5 eV with fine structure peak D occurring at approximately 36.6 eV [173]. A smooth absorption feature extends from 38.5 eV to beyond 45 eV. By comparing the measured spectrum with the calculated imaginary part of the dielectric function using all-electron full-potential linearized augmented plane wave (FP-LAPW) method (Appendix 4.C) with random phase approximation [174, 175], the smooth absorption feature above 38.5 eV is assigned to the transition between the W $5p_{3/2}$ core bands and the CB (W O_3 edge). Peaks A and B are assigned to the W $4f_{7/2}$ transitions (W N_7 edge), and peaks C and D to the transitions from W $4f_{5/2}$ core-levels to the CB (W N_6 edge). The comparison between the measured W $5p_{3/2}$ absorption edge and the calculated dielectric function (Fig. 4.1(a), dashed line) indicates significant lifetime broadening of the W $5p_{3/2}$-to-CB transitions. In addition, the peaks measured at the absorption edges between 32 eV and 37 eV are clearly different from the smooth onset of the $4f$-to-CB transitions (Fig. 4.1(a), dash-dotted line) calculated with mean field approximation, suggesting that many-body interactions between the electron and the core hole contribute to the measured discrete lineshape. Note that the broadband XUV pulse (30-50 eV) covers the core-level transitions from both the W $4f$ and $5p$ orbitals, enabling simultaneous observation of dynamics at the two different edges.

Typical core-level TA spectra between -40 fs to 2.6 ps time delay are displayed in Fig. 4.1(b). In this article, the time delay is defined as the arrival time of the XUV pulse subtracted from the time of the optical pulse and positive time delay indicates the samples are probed by the XUV pulse "after" optical excitation. The change of absorbance $\Delta A(t)$ at a specific time delay t is defined as $\Delta A(t) = A(t) - A(t = -40\text{ fs})$ with A denoting absorbance. The pump-excited carrier density is estimated to be 2×10^{20} cm^{-3} or 1×10^{13} /(layer·cm^2) (Appendix 4.D). Between 37-40 eV below the W O_3 edge, two weak, broad positive features are observed (Fig. 4.1 (b)). Although the difference of static absorbance below and above the W $N_{6,7}$ edge, or "edge jump", is much smaller than the W O_3 edge (Fig. 4.1(a)), the XUV TA signal occurring near transitions A, B, and C is narrow and much stronger than the TA signal above 37 eV (Fig. 4.1(b)). Clearly, the nature of the W $N_{6,7}$ edge (peaks A-D) and the W O_3 edge transitions are different and separate treatment is needed to understand their corresponding XUV TA spectra.

When a core electron is excited into the CB, the excited electron can interact with the core hole via Coulomb attraction. In many semiconductors, the electronic screening reduces the Coulomb interaction such that the core-level transitions can still be understood in a single-particle picture [142]. As the core bands are dispersionless, the core-level transitions maps the CB density of states and, with optically excited carriers in the VB and CB, core-level transitions probe the electronic occupation in the valence shell and the energy shifts of the VB and CB due to carrier and phonon excitations (Fig. 4.1(c)) [9, 76, 98, 99]. This scheme corresponds to the smooth W O_3 edge transitions above 37 eV but cannot describe the transitions at W $N_{6,7}$ edge.

Discrete peaks form in core-level absorption spectra when the Coulomb attraction between the

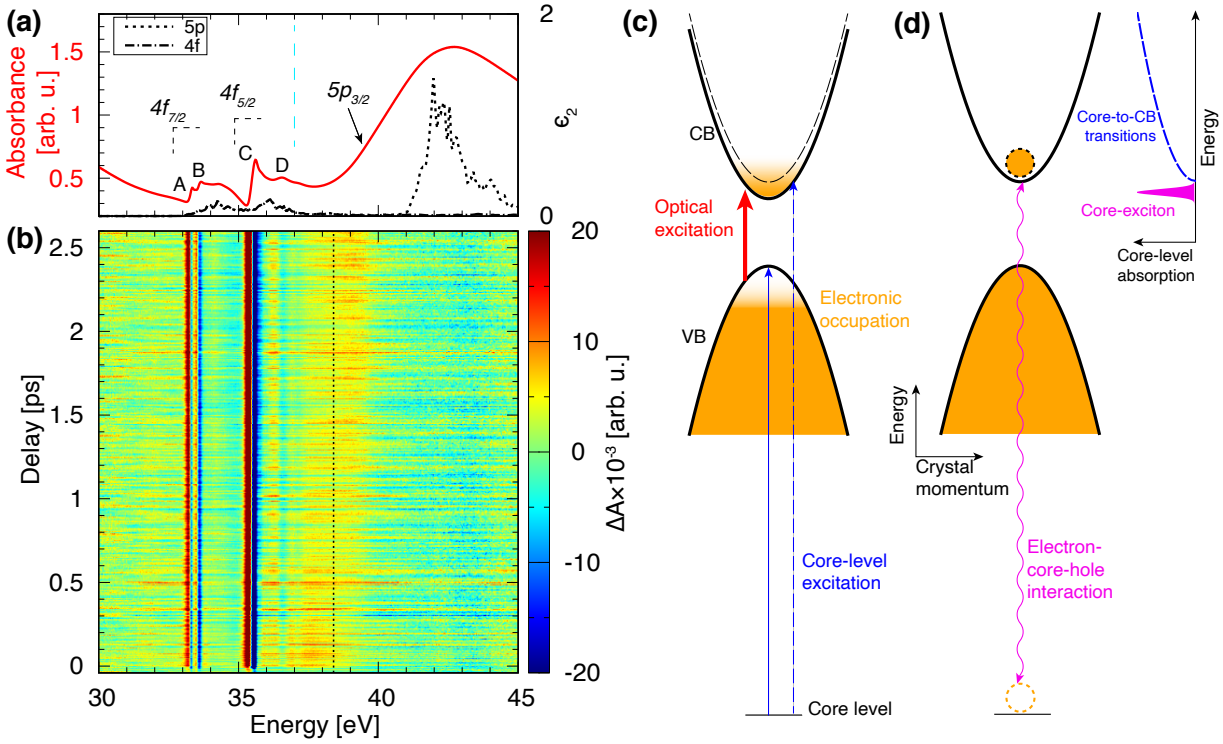

Figure 4.1: (a) Static core-level absorption spectrum of a 40 nm thick WS_2 film (magenta). The dashed and dash-dotted lines show the computed imaginary part of the dielectric function ($\epsilon_2(\omega)$) from the $5p$ and $4f$ core bands, respectively. (b) exhibits the XUV TA spectra between -40 fs and 2.6 ps delay. A dashed cyan line and a dotted black line is plotted at 37 eV in (a) and 38.4 eV in (b), respectively, to serve as a reference (see text). The scheme for typical core-level TA measurement in highly screened semiconductors is shown in (c), where the core-level excitation probes the electronic occupation in the VB and CB plus the energy shift of the bands. (d) illustrates the formation of core-exciton through electron-core-hole attraction and its corresponding absorption spectrum.

electron and the core hole is non-negligible. The interaction between the electron and the core hole renormalizes the core-level absorption and discrete "core-exciton" peaks can form near the critical points of the core-to-CB transitions (Fig. 4.1(d)) [145]. Note that excitonic interactions between the excited electron and the core hole are present for all core-to-CB absorption. Therefore, the renormalization of the core-level absorption spectra is not limited to the near-edge transitions, but may extend several eV above the edge [153, 176]. The behavior of transitions at the W $N_{6,7}$ edge below 37 eV is consistent with the description of core-excitons. To verify this, we compare the XUV TA spectra of the W $N_{6,7}$ and W O_3 edges near zero time delay.

Figure 4.2(a) displays the XUV TA spectra between -25 fs and +25 fs time delay; lineouts of the XUV TA spectra at 5 different time delays between -20 fs and +7 fs are plotted in Fig. 4.2(b). At positive delays, the XUV light probes the changes due to photoexcitations in the valence shell, while at negative time delays, the optical pulse perturbs the core-level transition dipole before its decay by both carrier photoexcitation and the direct coupling of the core-excitonic transitions with the optical field [31–33]. The distinction between the transitions at the W $N_{6,7}$ edge and the W O_3 edge can be visualized in the XUV TA signal at negative delays. While the TA signal at the W O_3 edge (37-40 eV) diminishes to zero at < -4 fs time delays, TA signals near peaks A, B, and C are still visible at ≤ -10 fs time delays. The experimental results thus indicate that the transitions A, B, and C are more long-lived than the transitions below the W O_3 edge. The comparison of core-level transition lifetimes corroborates the assignment that the peaks within the W $N_{6,7}$ edge (Fig. 4.1(a)) are core-excitons because the electron-core-hole attraction of the core-exciton stabilizes the core-excited state and enables a longer lifetime [148]. The broad positive feature above 37 eV at positive time delays can then be interpreted as photoexcited holes in the VB. In the following, we first focus on the measured dynamics induced by photoexcited carriers at the W O_3 edge. Next, we discuss the measured TA spectra of core-exciton transitions at the W $N_{6,7}$ edge at both positive and negative time delays.

4.3.1 Carrier dynamics at the W O_3 edge

To understand the XUV TA signal at the W O_3 edge, XUV TA spectra at 5 different time delays between +7 fs and +2 ps are presented in Fig. 4.3(a). At energies above the edge (41-45 eV), the XUV TA spectra exhibit a weak decrease in absorbance (negative ΔA) throughout the entire range of delays, whereas two positive features with different dynamical behavior are observed between 37-40 eV below the edge. The feature spanning 37-38.4 eV decays with time, while the feature between 38.4 eV and 39.5 eV, which is barely observable near time zero, increases in magnitude with the time delay.

The positive and negative ΔA below and above the edge might initially suggest that the positive feature is due to holes in the VB, which open up new excitation pathways from the core, and the negative feature is due to electrons in the CB, which blocks the core-level excitations into the CB. The different dynamical behavior between 37-38.4 eV and 38.4-39.5 eV could then be assigned to relaxation of photoexcited hot hole to the VB edge. However, such an assignment implies that the transition from the core to the VB edge is at approximately 39.5 eV and the initially photoexcited holes are located approximately 2 eV below the VB maximum. Given the approximately 2 eV direct

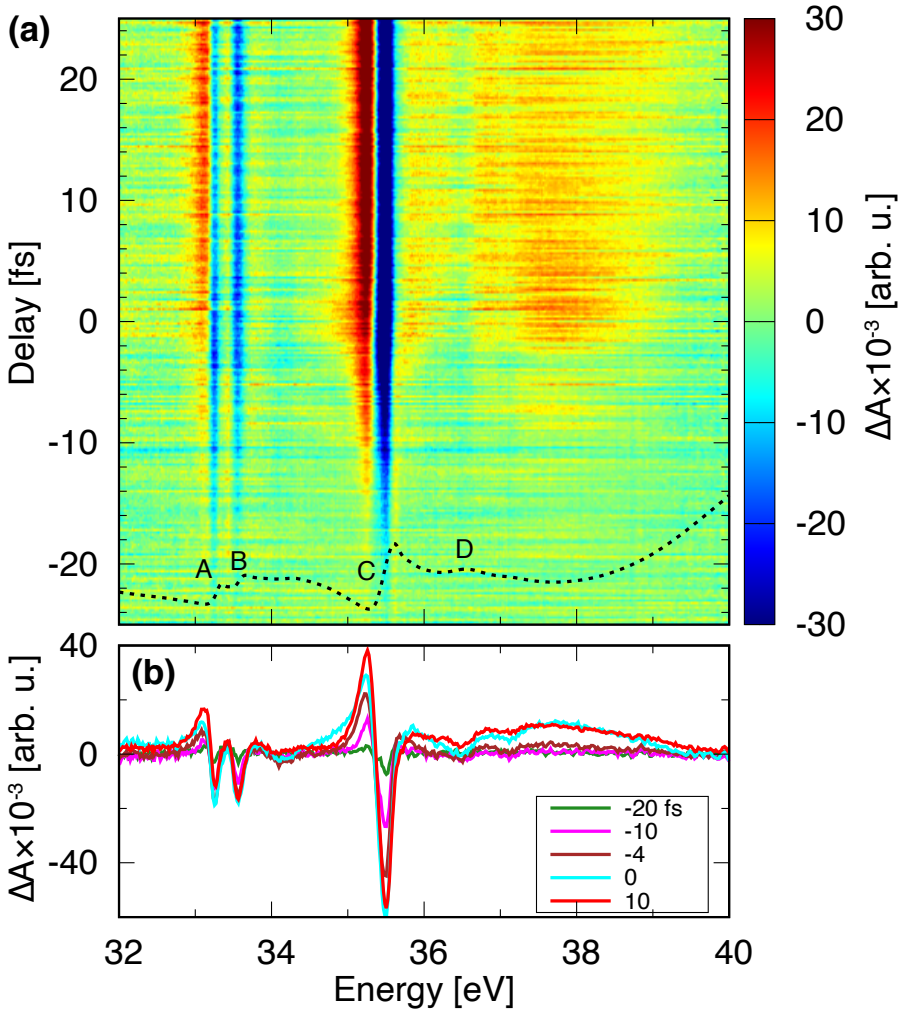

Figure 4.2: (a) XUV TA signal between -25 fs and +25 fs time delay. The static spectrum is plotted in dotted black line as reference. (b) shows the XUV TA lineouts at 5 different time delays between -20 fs and 10 fs.

band gap of bulk WS_2 [155], this suggests an optical transition energy of approximately 4 eV, far exceeding the maximum photon energy at 2.5 eV of the optical pulse. Therefore, the positive feature between 38.4-39.5 eV cannot be assigned to holes in the VB. Instead, it can be interpreted as a red shift of the W O_3 edge due to band gap renormalization. Both the change in electronic screening and phonon heating due to photoexcited electrons and holes can lead to band gap renormalization, resulting in the lowering of CB edge and therefore a red shift of the core-to-CB transition energies [9]. As energy dissipates from the electronic domain, the increase in phonon temperature and the heat-induced lattice expansion can further enhance band gap renormalization and lowering of the CB [177], which causes the positive features to grow with time delay. In addtion, with the assignment of the positive feature spanning 38.4-39.5 eV as due to the phonon-induced edge shift, the feature between 37-38.4 eV, which diminishes with increasing time delay, can then be assigned to holes.

To track the hole relaxation process, the median energy of the hole signal $E_{h,med} = \frac{\int E\Delta A dE}{\int \Delta A dE}$ is plotted in the inset of Fig. 4.3(b). The median energy $E_{h,med}(t)$ shifts from 37.7 eV to 37.9 eV with respect to time and can be fitted by a single exponential with a time constant of 1.2 ± 0.3 ps. In addition, as holes relax to the VB edge at the long time limit, the core-to-VB edge transition energy can be determined from $E_{h,med}(t \rightarrow \infty)$. The extracted transition energy from the core to the VB edge from the exponential fitting is 37.9 eV. The proximity between the hole feature and the positive feature due to band gap renormalization leads us to assign the core-to-VB edge transition with the median energy of the hole feature at the long time limit rather than use the maximum energy cutoff of the hole feature as in the core-level TA studies of germanium and 2H-$MoTe_2$ [9, 76].

Consulting the band structure diagram of WS_2 (Fig. 4.4(b)) and the initial photoexcited carrier distribution that is proportional to the number of photons available for excitation as a function of crystal momentum (Fig. 4.4(a)), the initial carrier distribution is characterized as residing mainly within the K valley and the carriers in the Γ valley near the VB maximum are barely excited. The results suggest that the 1.2 ps timescale of hole relaxation is related to the intervalley redistribution of holes between the K valley and the Γ valley (VB maximum) mediated by hole-phonon interactions.

In addition, Fig. 4.4(b) shows that the orbital character near the top of VB and bottom of CB is dominated by W $5d$ orbitals, indicating that the core-level transitions from W $4f$ and $5p$ states are both sensitive to carrier dynamics near the band edges. This excludes the possibility that the diminishing TA signal ranging from 37-38.4 eV is due to carriers reaching band regions where core-level transitions from W $4f$ and $5p$ orbitals are forbidden. The loss of holes in the VB due to recombination is characterized by the integrated TA signal $\Delta A_{int} = \int \Delta A dE$ over the 37-38.4 eV range (Fig. 4.3(c)). The magnitude of ΔA_{int} as a function of time can be fitted by a single exponential with a decay constant of 3.1 ± 0.4 ps convoluted by the instrument response function. The 3.1 ps decay is therefore assigned to the carrier recombination time as the hole signal (37-38.4 eV) decays to zero at the long time limit.

The assignment of the VB maximum at 37.9 eV suggests that a negative TA feature due to excited electrons is expected at 39.9 eV (37.9 + 2 eV band gap). While a weak negative TA signal barely above the noise level is indeed observed spanning 41-45 eV, assigning this to the CB electrons plus the VB maximum at 37.9 eV would suggest an electron-hole energy separation of at least 3

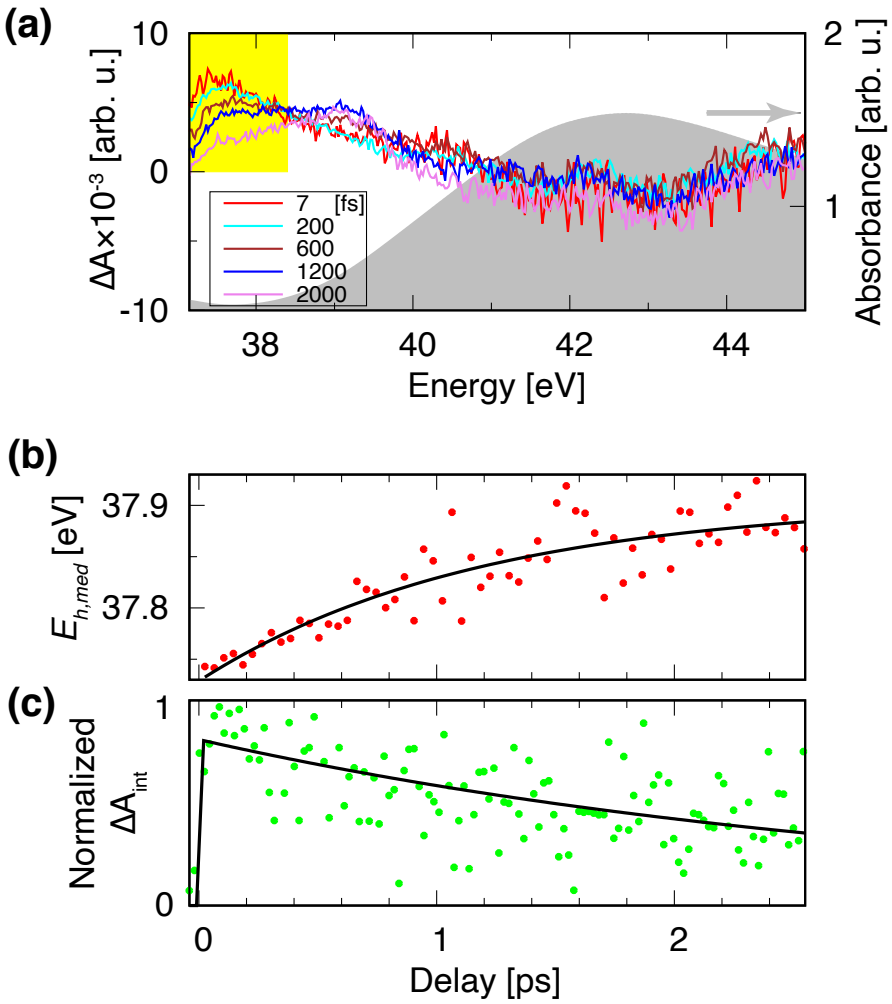

Figure 4.3: (a) XUV TA spectra at W O_3 edge at 5 different time delays. The static core-level absorption spectrum is plotted in gray as reference. (b) shows the median energy $E_{h,med}$ of the TA signal between 37.4–38.4 eV (yellow shaded area in (a)) and (c) shows the integrated XUV TA signal in the same energy region.

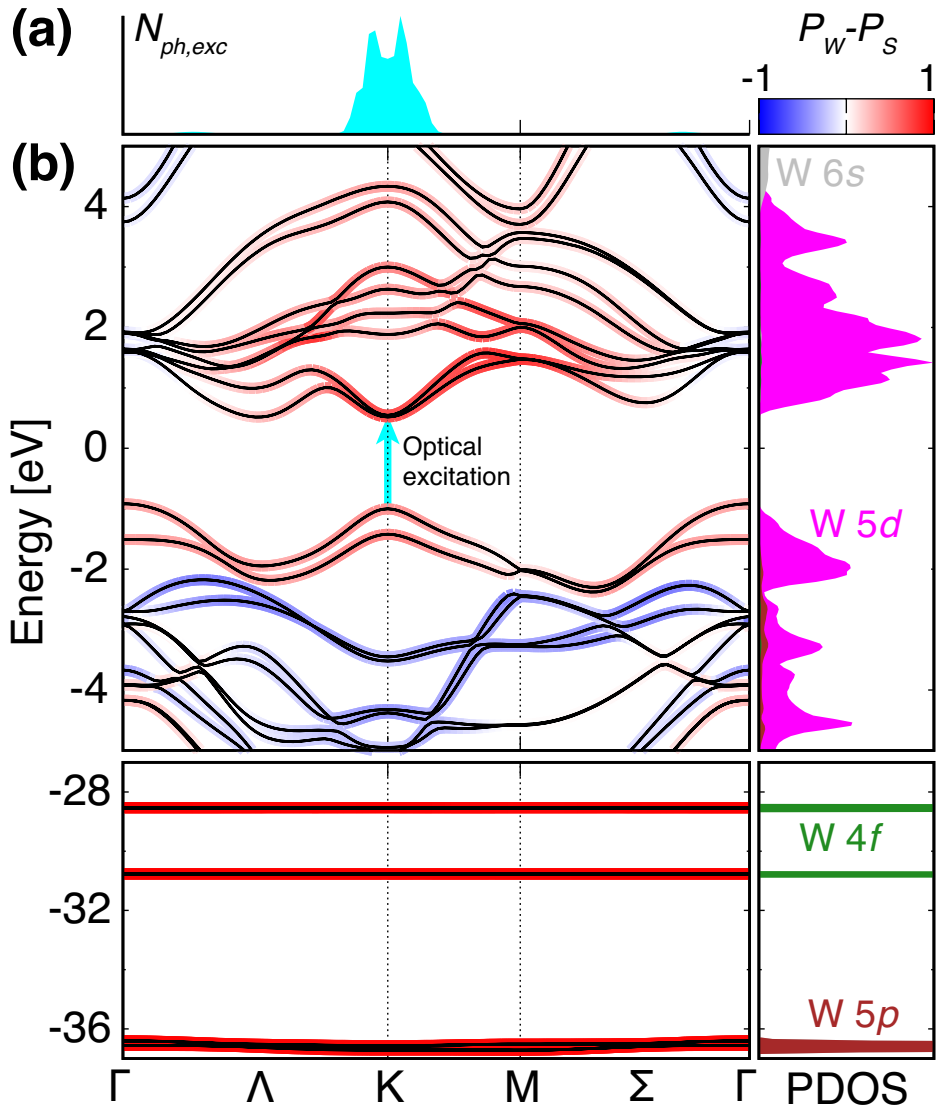

Figure 4.4: (a) Number of photons in the optical pulse available to excite carriers from the VB to the CB as a function of k-points. (b) shows the band structure and projected density of states (PDOS) of WS_2. The colors on the bands (left panel) reflects the difference between the atomic orbital projection on W and S ($P_W - P_S$). P_n is the sum of modulus square of wavefunction projections of atom n.

eV, which exceeds the maximum photon energy of 2.5 eV in the optical pulse. In addition, no significant dynamics are observed for the negative feature between 41-45 eV, whereas the electrons are expected to recombine with the holes within the observed 3.1 ps recombination time. This indicates that the weak signal at ≥41 eV may be caused by changes in core-hole lifetime, which affects the spectral broadening of the edge, or a decrease in oscillator strength of the W O_3 edge due to carrier and phonon excitations [76, 103], rather than directly due to the photoexcited electrons in the CB.

The absence of the XUV TA signal due to occupation of photoexcited electrons in the CB can be explained by the significant spectral broadening above the W O_3 edge, where the experimentally measured static spectrum is much wider and smoother than the calculated dielectric function according to the projected CB DOS (Fig. 4.1(a)). Here the fine structure in the projected CB DOS due to critical points in the CB is completely lost in the measured absorption edge. This is in contrast to the recently studied $L_{2,3}$ edge in Si and Te $N_{4,5}$ edge in 2H-$MoTe_2$ where the critical points in the CB can be directly mapped onto the core-level absorption spectrum [76, 115]. The broadening in the W O_3 edge increases the overlap between the expected negative XUV TA feature due to electron occupation in the CB and the positive feature due to CB red shift. The overlapping negative and positive features thus lead to the cancellation between the two and make extracting the electron distribution in the CB from core-level TA spectra here unreliable.

4.3.2 Dynamics and lifetimes of core-excitons at the W $N_{6,7}$ edge

While the core-level TA spectra at the W O_3 edge can be explained by the red shift of CB and electronic occupation in the VB and CB, XUV TA signals of core-exciton transitions within the W $N_{6,7}$ edge cannot be interpreted with the same approach. Note that unlike the insulators where core-exciton dynamics have only been observed when XUV light arrives first [31–33], here XUV TA signal at the core-exciton transitions extends throughout the entire range of positive time delays (Fig. 4.1(b) and Fig. 4.2(a)). This difference arises because in insulators, the band gap exceeds the photon energy range of the optical pulse, so electron-hole pairs in the VB and CB are not excited. Thus, the core-excitons can only be perturbed by optical field induced coupling of core-exciton states. Here, photoexcited carriers with picosecond lifetimes can instantaneously "dress" the XUV-excited core-excitons by the carrier-induced change of band filling and electronic screening [178, 179]. Therefore, carrier-induced modification of the core-exciton lineshape occurs at both negative and positive time delays.

In Fig. 4.2(a), the core-level TA signal at short (< 25 fs) positive delays is solely due to photoexcited carriers since dynamics caused by electron-phonon scattering occur on a timescale of 10^2 fs and can be ignored [110, 180, 181]. While photoexcited carriers are the sole contributor to the modification of core-excitons at short positive time delays, at negative delays direct field-induced changes can also modify the core-exciton lineshape. It has been shown that similar to atomic autoionizing states [10, 25, 182–184], the optical pulse can cause energy shifts of the core-exciton transitions through the AC Stark effect and resonant coupling between the core-exciton states or with the ionization continuum [31–33]. Formal treatment of the XUV TA spectra at negative time delays requires computation of the free induction decay of the core-exciton transition

dipoles by solving a time-dependent Schrödinger equation, including couplings of the core-level transitions with both the photoexcited carriers and the optical field [25, 31–33]. However, due to the complexity in including the many-body interactions between the core-level transitions and the photoexcited carriers, which is detailed in the next section, we propose an alternative method to separate the contribution from photoexcited carriers and the optical field by their different time behaviors.

Here we analyze the different contributions by applying global fitting to the XUV TA spectra ΔA through singular value decomposition (SVD) (Appendix 4.E): $\Delta A(t, E) = \sum_n s_n u_n(t) v_n(E)$. Functions $\{u_n(t)\}$ and $\{v_n(E)\}$ are singular vectors, or *components*, ranked by singular values $\{s_n\}$ in descending order. Transition D is excluded from the analysis due to poor signal in that spectral region. The XUV TA signal from the largest component at transitions A and B is shown in Fig. 4.5(a), showing good agreement with experimental data (Fig. 4.2(a)) and indicating the dynamics at transitions A and B can be described by a single component. The corresponding singular vector (Fig. 4.5(b)) directly reflects the TA signal measured at +10 fs time delay (Fig. 4.2(b)) and the dynamics of the component (Fig. 4.5(c)) exhibits an exponential decay at negative delay and becomes constant when $t > 0$. This indicates that transitions A and B have similar decay dynamics and lifetimes, and although the optical pulse can potentially affect the core-excitons directly through coupling the core-exciton transition dipoles with the optical field, the carriers excited in the valence shell remain the dominant influence on the core-excitons A and B.

Within their decay time, the core-excitons A and B are modulated by the valence electron-hole pairs. By fitting the decay dynamics with a single exponential (Fig. 4.5(c)), a core-exciton coherence lifetime (T_2) of 10.9 ± 0.4 fs is extracted. The decoherence in core-exciton transitions can be caused by population decay through Auger processes or by exciton-phonon coupling [31–33]. Previous studies on the decay of core-excitons in insulators show that when exciton-phonon coupling prevails over other decoherence channels, the free induction decay of core-exciton transition dipole moment exhibits a Gaussian decay [31–33] that leads to a Gaussian spectral profile [185, 186]. Here the decay of XUV TA signal at negative time delays is exponential rather than Gaussian (Fig. 4.5(c) and (f); comparison between Gaussian and exponential fitting is detailed in Appendix 4.E), suggesting that phonon-induced dephasing is insignificant and Auger processes are the dominant contributor to core-exciton decay. Thus, a population decay time ($T_1 \approx T_2/2$) at 5.5 ± 0.2 fs can be inferred.

To quantitatively reproduce the XUV TA spectra at transition C (Fig. 4.2(a)), the two largest components in the SVD are required (Fig. 4.5(d)). The dynamics of the two components (Fig. 4.5(f)) show that at >10 fs delays, the largest (1^{st}) component is constant whereas the second component is zero. In addition, the second component only becomes nonzero either at negative time delays or during pulse overlap. This indicates that the largest component represents the influence of carriers on the core-exciton and the second component originates from the direct coupling of the core-exciton to the optical field, because in contrast to the direct coupling to the optical field that can only occur when the field overlaps with the transition dipole before its decay, the carriers are much longer lived than the transient optical pulse and can cause spectral changes at >10 fs time delays. The field-induced TA component (Fig. 4.5(e), blue line) exhibits a negative amplitude below the edge and a positive amplitude above (cf. Fig. 4.6(b)). The asymmetry of

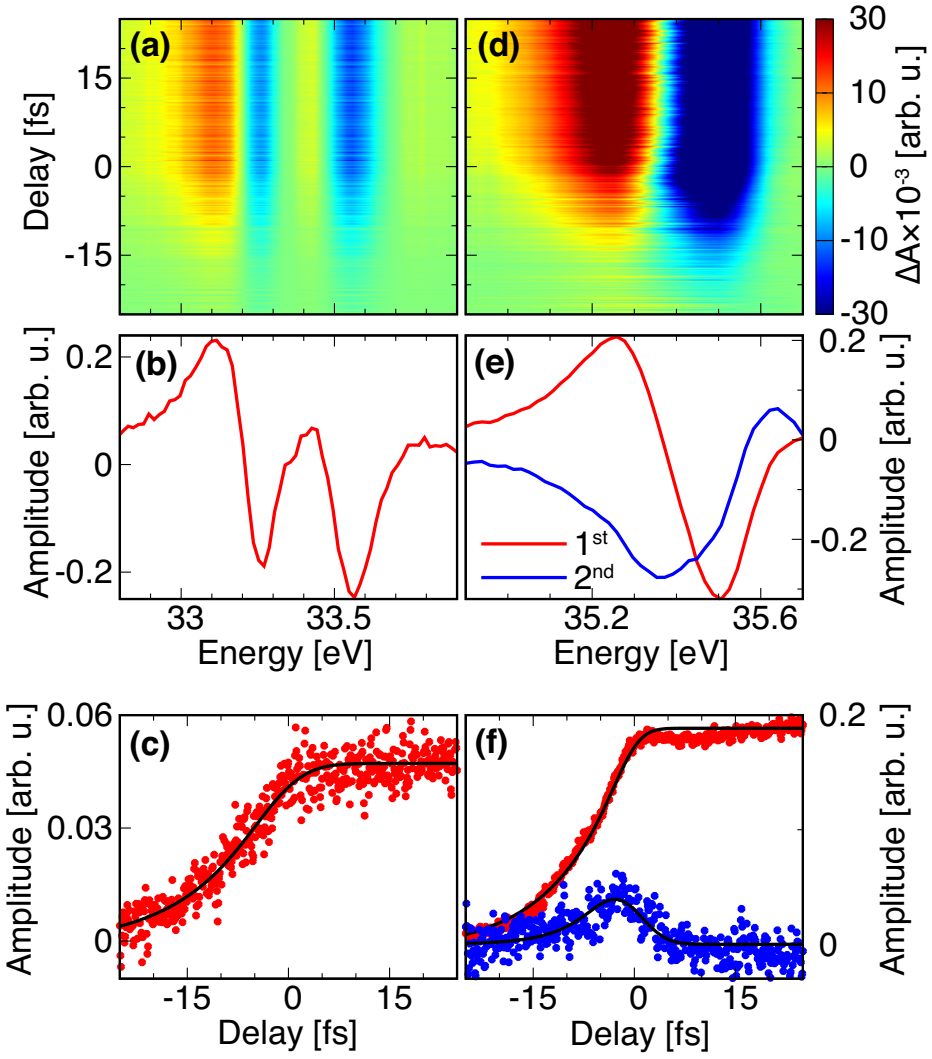

Figure 4.5: (a) XUV TA signal from the largest component in SVD for transitions A and B and the corresponding singular vector with respect to energy and time are shown in (b) and (c), respectively. (d) exhibits the XUV TA signal from the two highest ranked component in SVD for transition C and the corresponding singular vectors for the first and second largest singular values as a function of energy and time are shown in (e) and (f), respectively. The XUV TA signal from only the largest component in SVD for transition C is shown in Fig. 4.9 (Appendix 4.E). Note that the magnitude of the singular value of each component is included in the amplitude shown in (c) and (f).

XUV TA amplitude centered around the edge suggests that it may relate to the change in the Fano q-factor of the transition, which can be induced by the optical pulse through a ponderomotive phase shift [25], or direct coupling to neighboring core-excited states [182]. Fitting the dynamics of the largest component with a single exponential yields a core-exciton coherence lifetime of 9.6 ± 0.1 fs.

4.3.3 Carrier-induced modification of core-exciton transitions within W $N_{6,7}$ edge

In this section, we focus on the modification of core-exciton absorption lineshape by photoexcited carriers. First, we compare the effect of photoexcited carriers on core-exciton and core-to-band absorption at +10 fs time delay (Fig. 4.2(b)). In contrast to the broad, positive TA signal observed below the W O_3 edge, no positive signal is observed between 30-33 eV (Fig. 4.1(b)) and the majority of the TA signal occurs near the core-exciton transitions A-C. The lack of XUV TA signal directly from the electronic state blocking of carriers as at the W O_3 edge can be attributed to the renormalization of core-level absorption spectra due to core-exciton formation. The formation of core-excitons concentrates the oscillator strength of core-to-CB transitions to the bound core-excitonic states and the core-level absorption spectra no longer maps to the CB DOS. In addition, the oscillator strength at the W $N_{6,7}$ edge is lower than the W O_3 edge. Compared to the edge change (jump) of 1 OD (optical density) below and above the W O_3 edge, the W $N_{6,7}$ edge has an edge jump of $\leq$0.5 OD (Fig. 4.1(a)). This indicates that the signal of electronic state blocking, if present at the W $N_{6,7}$ edge, would be much lower than the signal below the W O_3 edge (37.4-38.4 eV), which is already close to the noise level.

To understand the effect of carriers on core-exciton transitions, the core-level absorption spectra at +10 fs time delay with 3 different optical pump fluences are displayed in Fig. 4.6. While transition D is broadened with increasing pump fluence, the carrier-induced changes at A, B, and C are much more complex. At transitions A, B, and C, the absorption edge shifts to higher energy with increasing pump fluence. However, the changes in absorbance below and above the edge are non-monotonic with increasing optical excitation. At fluences between 0-21 mJ/cm^2, the absorbance below the edges (Fig. 4.6, black arrows) increases while the absorbance above the edge (Fig. 4.6, magenta arrows) decreases with increasing fluence. At a fluence of 29 mJ/cm^2, the absorption above the edge increases rather than decreases compared to the absorbance at 21 mJ/cm^2 pump fluence. In addition, shoulders and ripples start appearing around transitions A, B, and C at a fluence of 29 mJ/cm^2. New small features appear below the edge of A and C and a dip appears below the absorption edge B. Clearly, the carrier-induced changes to the core-exciton transitions cannot be simply described by an energy shift or a broadening of the lineshape.

The behavior of the core-exciton spectral change at +10 fs delay with respect to increasing pump fluence is reminiscent of the changes in optical absorption of valence excitons in highly excited semiconductors [179]. For example, it has been observed that in highly excited GaAs, the absorption peak of bound excitons decreases in magnitude and new features below the onset of excitons appear in the optical absorption spectra [178]. Using a generalized Elliot formula

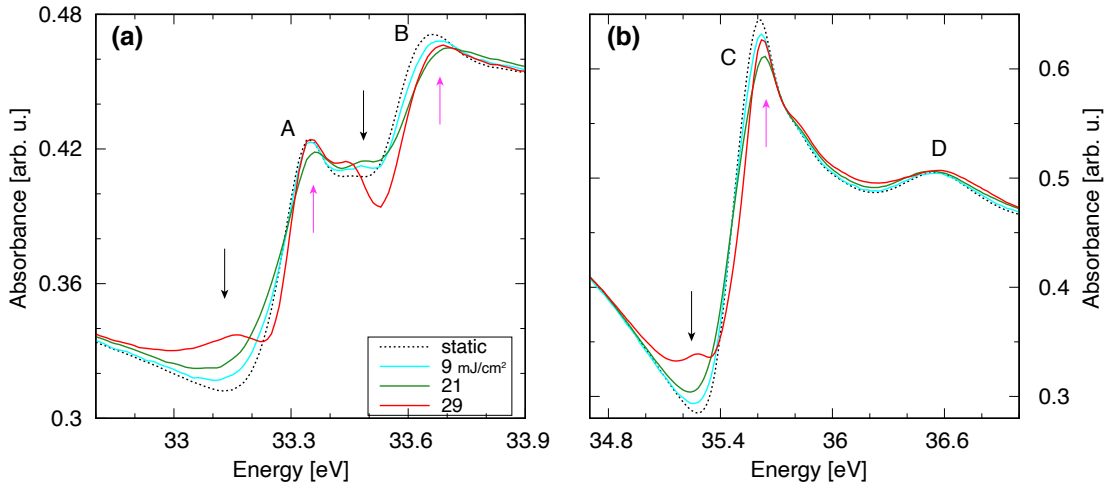

Figure 4.6: Fluence dependence measurement of core-level absorption spectra at transitions (a) A, B, and (b) C, D, at +10 fs time delay. The static spectrum is shown in black dashed line as a reference. The estimated excited carrier density (Appendix 4.D) at pump fluences 9, 21, 29 mJ/cm^2 are 1.4×10^{20}, 1.8×10^{20}, and 1.9×10^{20} cm^{-3}, respectively.

[187–189], Lee et al. showed that the contributions to the optical absorption spectra of highly excited semiconductors can be divided into three categories [178]. First, the ionization of bound excitons due to the screening of the photoexcited electron-hole plasma causes suppression of the bound exciton transitions and an overall blue shift of the absorption edge. Secondly, the increasing band filling causes ripples to appear around the exciton transitions, especially below the absorption onset. Thirdly, the carrier-induced band gap renormalization introduces a red shift of the CB edge that partially compensates the blue shift of absorption onset due to suppression of bound exciton transitions.

The phenomena observed for optical excitons can analogously explain the spectral changes of core-exciton transitions here. The increase of electronic screening due to electron-hole excitations in the VB and CB suppresses bound core-exciton transitions and contributes to the overall blue shift of the absorption onset. The changes of band filling in the valence shell modulates the core-excited states' energies, oscillator strengths, and the coupling to the continuum so that new absorption features appear.

The similar behavior between the carrier-dressed core-exciton lineshape and optical absorption in highly excited semiconductors, which can be simulated analytically, leads us to explore the possibility of extending the formalism [188] to quantitatively extract parameters such as core-exciton radii and binding energies. The generalized Elliot formula [187–189] is based on a parabolic two-band model that only incorporates a single CB minimum. As core-exciton feature B and D are clearly embedded in the core-to-CB continuum transitions, the parabolic two-band approximation is no longer applicable. In addition, due to the dispersionless core bands, core-excitons can form

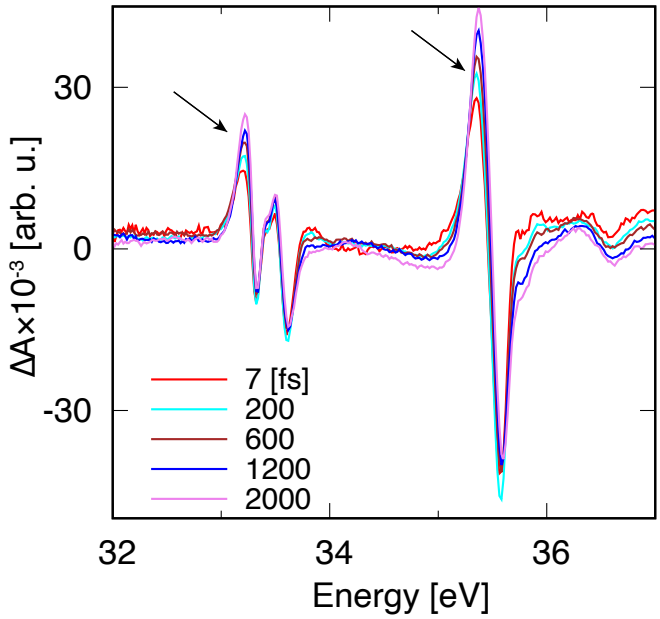

Figure 4.7: XUV TA spectra at 5 different positive time delays between 0-2 ps.

at multiple CB minima, e.g. at the K, Λ, and Σ valleys (Fig. 4.4), and the wavefunctions at those CB minima can further hybridize. Therefore, quantitative treatment of core-exciton transitions here, and by extension, their modification due to carriers, will require Bethe-Salpeter equation calculations including the full bandstructure of WS_2 [190–192], which is beyond the scope of this work.

4.3.4 Picosecond XUV transient absorption signal at the W $N_{6,7}$ edge

As photoexcited carriers are the major contributor to the modulations of the core-exciton spectra at negative and short positive time delays, we consider here the possibility of using the TA spectra of core-excitons to extract carrier dynamics. Although picosecond carrier relaxation and recombination would suggest a decay of TA signal at the core-exciton transitions, a growth of TA signal (Fig. 4.7, black arrows) is observed below the transitions A and C with increasing time delay and no significant TA change is measured above the edge at transitions A, B, and C throughout 0-2.6 ps. This indicates that in addition to photoexcited carriers, the excitation of phonons through electron-phonon interactions also contribute to the spectral changes of core-excitons at long time delays, as phonon induced band gap renormalization can induce a red shift of CB that is consistent with the positive TA signal observed below the transitions. Therefore, the core-exciton transitions at W $N_{6,7}$ edge here are poorly configured for extraction of carrier dynamics, because the spectral changes due to carriers and phonons at hundreds-of-femtoseconds to picosecond timescales cannot be easily separated.

4.3.5 Comparison between the core-exciton and core-to-conduction band transitions

The contrasting behavior of core-exciton transitions at the W $N_{6,7}$ edge and the core-to-band transitions at the W O_3 edge in the same energy range is highly unique and indicates that factors other than the macroscopic screening, which are experienced by transitions from both W $4f$ and $5p$ core-levels, are contributing to the core-exciton formation. As the CB minima are dominated by W $5d$ orbitals that are accessible from both W $4f$ and $5p$ through XUV photons, it is thus suggested that the contributor to the difference between the W $N_{6,7}$ edge and the W O_3 edge absorption lies in the properties of the core orbitals. The W $4f$ orbitals involved at the W $N_{6,7}$ edge are far more localized than the W $5p$ orbitals for the O_3 edge transitions. The localized core hole may then act as a point positive charge and modulate the electronic wavefunctions in the CB to form a core-exciton [147].

4.4 Conclusion

In summary, photoinduced dynamics at W $N_{6,7}$ and O_3 edges in WS_2 are simultaneously measured by attosecond core-level transient absorption spectroscopy. Picosecond hole relaxation and recombination dynamics in the valence band are extracted from the transient absorption spectra of the core-to-conduction band transitions at the W O_3 edge. Lifetimes of core-excited states at the W O_3 edge and the W $N_{6,7}$ edge are obtained from XUV transient absorption spectra at negative time delays. While the lifetimes of W O_3 edge transitions are well below the duration of the optical pulse ($\sim$ 4 fs), core-exciton coherence lifetimes up to 11 fs are observed at the W $N_{6,7}$ edge. Global fitting of the XUV transient absorption spectra at short time delays reveals that in contrast to the direct field-induced core-exciton dynamics observed in insulators [31–33], carrier-induced modulation of core-exciton states dominates the dynamics at the few-tens-of-femtosecond timescale.

The drastically different behavior between the absorption from the W $5p$ and $4f$ core orbitals in the same energy region suggests that in addition to macroscopic screening, the degree of localization of the core orbitals can contribute significantly to the core-level absorption lineshape and the formation of core-excitons. The observation of carrier-modulated core-exciton transitions can serve as an initial step in further understanding and manipulating the dynamics of core-excitons in condensed matter, and the extraction of hole dynamics at W O_3 edge further advances the use of core-level TA spectroscopy in measuring carrier dynamics in transition metal dichalcogenides and their heterostructures.

4.A Sample preparation

The WS_2 sample was synthesized by atomic layer deposition of WO_3 thin films on 30 nm thick silicon nitride membranes (Norcada Inc.). The tungsten oxide film was subsequently converted sulfide in a tube furnace with H_2S. Before atomic layer deposition, 16 nm thick silicon nitride films were deposited onto the Si frame of the silicon nitride windows using plasma-enhanced chemical

vapor deposition (PECVD) to prevent silicon sulfide formation during the reaction with H_2S [193]. The passivated windows were then coated with WO_3 using atomic layer deposition in an oxygen plasma [172]. The thickness of WO_3 was calculated from the required thickness of WS_2 using the ratio of the density between the two assuming no W loss in the reaction with H_2S. The thickness of the oxide film was characterized by *in situ* spectroscopic ellipsometry. After the oxide deposition, the windows were put in a quartz boat and transferred into a tube furnace which was heated up to 600 °C. H_2S (5 sccm) and Ar (100 sccm) as a buffer gas was flowed into the tube to react with WO_3. After 1 hr of reaction, the H_2S flow was turned off while maintaining the Ar flow to prevent contamination from outside air and the furnace is left to cool down. After the temperature reached below 200 °C, the Ar flow was switched to N_2 and the samples were taken out after the instrument reached room temperature. To verify that the absorption peaks below 37 eV are not due to defect-induced color centers, the XUV absorption spectrum of the synthesized film is compared with total electron yield (TEY) spectrum of single crystal WS_2 (2Dsemiconductors USA) measured at Beamline 4.0.3 at the Advanced Light Source (Appendix 4.F).

4.B Experimental setup

Detailed description of the light source of the experimental setup is listed in Chapter 2. In brief, compressed broadband laser pulses spanning 500-1000 nm operating at 100 Hz was separated into the probe and pump arm by a 9:1 broadband beamsplitter. The probe beam was subsequently focused into a Kr gas jet to produce broadband XUV pulses (30-50 eV) via high-harmonic generation (Fig. 2.12). The XUV beam then traveled through a 100 nm thick Al filter blocking the high-harmonic driving field and is focused onto the sample with a Au coated toroidal mirror. The pump beam was time-delayed with respect to the probe by a piezo-driven optical delay stage and was subsequently recombined with the probe arm by an annular mirror. A 200 nm thick Al filter is placed after the sample to prevent the pump beam reaching the XUV spectrometer. The XUV beam passing through the sample and the Al filter was dispersed by a flat-field grating onto an XUV CCD camera. The duration of the pump pulse was characterized by dispersion scan [47] to be 4.2 ± 0.1 fs and the spectrum and temporal profile of the pump pulse are shown in Fig. 4.8(a) and (b), respectively. The pulse energy of the pump beam was controlled by an iris and the beam profile of the pump pulses was imaged directly at the sample position with a CMOS camera to calculate the pump fluence. During the XUV transient absorption experiment, the sample was raster-scanned to prevent heat damage.

To avoid the drift of time delay during the experiments, an optical-XUV transient absorption measurement on Ar was conducted after each WS_2 transient absorption scan [9, 76]. The Ar gas cell was mounted alongside the WS_2 sample. The suppression of Ar $3s3p^6np$ autoionization lines by the optical pulse at 26-37 eV photon energies was measured (Fig. 4.8(c)) [10, 72] and the time reference of each scan was determined by fitting the integrated absolute value of transient absorption signal of the Ar $3s3p^64p$ state along the energy axis and fit it with a Gaussian error function [9]. The time axis of each WS_2 transient absorption scan was shifted according to its time zero reference and the transient absorption signal ΔA interpolated onto a uniform time delay grid.

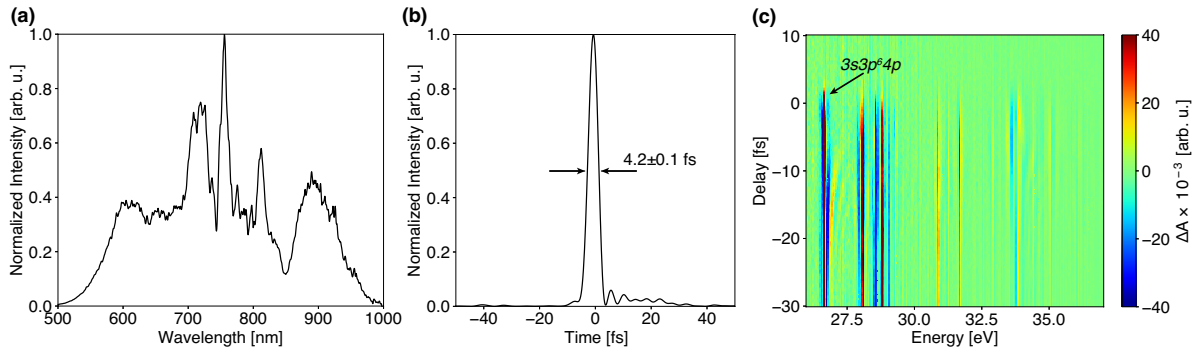

Figure 4.8: (a) Spectrum and (b) temporal profile of the pump pulse. (c) transient absorption spectra of Ar $3s3p^6np$ autoionization states for time zero calibration.

To provide a reference for future studies on carrier effects on core-excitons in solids that cannot be prepared as thin films, we performed attosecond transient reflectivity experiments on 40 nm thick WS_2 thin films deposited on silicon wafers, which were synthesized alongside the samples for attosecond transient absorption experiments (see Sample Preparation). The measurements were taken on an almost identical beamline as the one for attosecond transient absorption, except for the interaction geometry at the sample [194]. The optical pump and XUV probe pulses (p- and s-polarized, respectively) impinged on the sample surface with a 66° angle from the sample normal. The reflected XUV beam was directed into an identical spectrometer as the one used in absorption. A gold mirror was used as a reference to extract absolute reflectivity of the WS_2 sample [194] and because of the relatively weak change in reflectivity, the data was processed using edge-pixel referencing [195]. The results of the XUV reflectivity measurements are detailed in Appendix 4.G.

4.C Electronic structure calculations

The electronic structure of bulk WS_2 is computed with all-electron full-potential linearized augmented plane wave (FP-LAPW) method using the Elk code [174, 196]. The density functional theory (DFT) computation is conducted within local spin density approximation (LSDA) [197]. Spin-orbit coupling effects are included and the calculations are converged with a k-grid of 10×10×3 k-points. A 4 eV blue shift is added to the calculated dielectric function in Fig. 4.1(a) to compensate the underestimated gap between the core-levels and the CB in DFT calculations.

4.D Optically excited carrier density

The photoexcited carrier density ρ_{exc} is estimated by calculating the number of absorbed photons in the 40 nm thick WS_2 film per unit area σ_{abs} divided by the thickness of the film d: $\rho_{exc} = \sigma_{abs}/d$.

The number of photons absorbed per unit area can be calculated with the equation

$$\sigma_{abs} = \int d\omega\, \bar{\sigma}_{inc}(\omega) f_{abs}(\omega),$$

where $\bar{\sigma}_{inc}(\omega)$ is the number of incident photons per unit area with photon energy ω and f_{abs} is the fraction of photons absorbed in the film. $\bar{\sigma}_{inc}(\omega)$ can be calculated from the spectrum of the pump pulse and the measured fluence. The fraction of photons absorbed (f_{abs}) is calculated using the transfer matrix method including the 40 nm thick WS_2 film and the silicon nitride window [198]. The refractive indices of WS_2 and silicon nitride are taken from Ref. [199] and [200]. A correction due to saturable absorber effect is included with

$$\kappa = \frac{\kappa_0}{1 + \frac{I}{I_s}},$$

where κ/κ_0 is the ratio between the imaginary part of refractive indices with and without saturable absorption. I is the peak intensity of the pulse and $I_s = 0.471$ TW/cm^2 is the saturation intensity taken from Ref. [201]. We conducted the experiments with fluences ranging 6-30 mJ/cm^2, peak intensities ranging 0.7-3.3 TW/cm^2, and the resulting calculated excited carrier density ranges 1.3×10^{20}-1.9×10^{20} cm^{-3}. The much smaller range in carrier density compared to the excitation fluence is strongly due to saturable absorption. The carrier density per layer is calculated multiplying the carrier density by volume with the layer thickness of 6.2 Å [202].

4.E Singular value decomposition

The XUV TA spectra between -25 fs and 25 fs below 37.5 eV are analyzed with global fitting via singular value decomposition (SVD), where the TA signal $\Delta A(t, E)$ is written as a matrix with rows and columns indicating different time t and energy E, respectively. The TA matrix $\Delta A(t, E)$ is then decomposed with SVD into $\Delta A(t, E) = U(t)^T S V(E)$, where U and V are unitary matrices consisting of singular vectors $\{u_n(t)\}$ and $\{v_n(E)\}$, respectively. S is a rectangular diagonal matrix and the diagonal matrix elements $S_{nn} = s_n$ are singular values ranked in descending order. The reconstruction of TA signal $\Delta A_{rec}(t, E)$ by components up to the n^{th} rank is defined as $\Delta A_{rec}(t, E) = \sum_{m=1}^{n} s_m u_m(t) v_m(E)$.

To verify whether phonon-induced dephasing contributes significantly to the decay of core-excitons, we focus on the decay dynamics of the largest component in the SVD $u_1(t)$ (Fig. 4.5(c) and (f), red dots) at negative delays. The largest SVD component is plotted in logarithmic scale in Fig. 4.10 and the component $\log_{10} u_1(t)$ is fitted with a quadratic function $at^2 + bt + c$. The fitted coefficients of the quadratic function are listed in Table 4.1, showing that the quadratic term a is two orders of magnitude smaller than the linear term b. In addition, the fitted a are positive rather than negative as expected for a Gaussian function. This indicates that the decay of XUV TA signal at negative time delays is exponential rather than Gaussian and the effect of phonon-induced dephasing is insignificant.

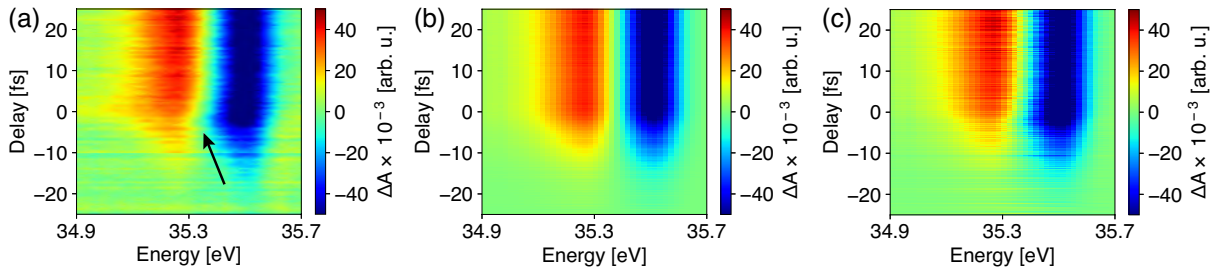

Figure 4.9: (a) Experimental short time XUV TA spectra at transition C. (b) shows the reconstruction of the XUV spectra with the first (largest) spectral component and (c) shows the reconstruction with the first and second component.

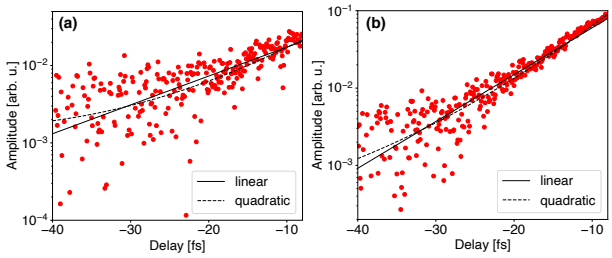

Figure 4.10: Quadratic fitting (dashed line) of the logarithm of the largest component in the SVD of XUV TA signal at (a) core-exciton transiton A and B and (b) core-exciton transition C. The data points from the SVD are shown as red dots. Results of linear fitting of the components are shown in black solid lines.

Table 4.1: Results of quadratic fitting of $\log_{10} u_1(t)$ for core-exciton A, B and core-exciton C (Fig. 4.10).

	A,B	C
a	$(6 \pm 2) \times 10^{-4}$	$(5 \pm 2) \times 10^{-4}$
b	0.061 ± 0.008	0.084 ± 0.007
c	-1.21 ± 0.06	-0.4 ± 0.07

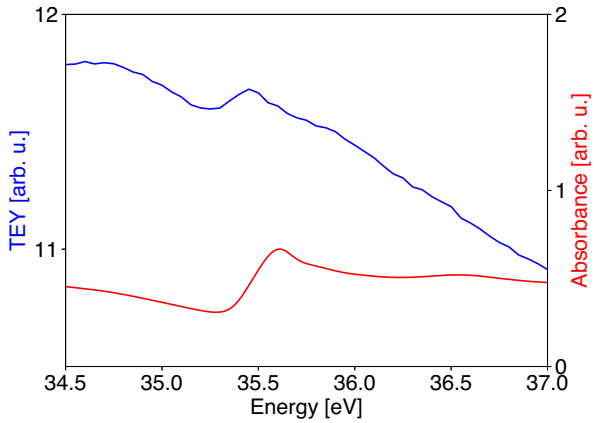

Figure 4.11: Normalized total electron yield spectrum of single crystal WS_2 measured at Beamline 4.0.3 at the Advanced Light Source (blue) and the XUV absorption spectrum of 40 nm thick WS_2 thin film used in the core-level transient absorption experiment (red).

4.F Comparison with XUV total electron yield of single crystal WS_2

To verify that the absorption peaks below 37 eV are not due to defect-induced color centers, the XUV absorption spectrum of the synthesized film is compared with total electron yield (TEY) spectrum of single crystal WS_2 (2Dsemiconductors USA) measured at Beamline 4.0.3 at the Advanced Light Source. The measured TEY of the single crystal sample is shown in Fig. 4.11. The spectrum is cut off at 34.5 eV due to the lack of XUV photons below 34.5 eV at the undulator beamline. The measured TEY of WS_2 shown in Fig. 4.11 is normalized by the measured TEY of a gold film: $TEY_{norm} = TEY_{sample}/TEY_{Au}$.

4.G Additional static and transient reflectivity measurements

Here we provide measurements of core-exciton dynamics in the presence of photoexcited carriers in reflectivity geometry. Certain materials are challenging to synthesize as thin films for XUV absorption measurements, yet the analysis of reflectivity data alone is challenging and often relying on Kramers-Kronig transforms. Therefore, the data presented below can serve as a useful reference point for future studies of materials other than WS_2.

The absolute static reflectivity of WS_2 deposited on a silicon wafer, taken at 66° from normal (Fig. 4.12(a)), shows that while core-exciton C is very visible, core-excitons A and B are difficult to resolve. Nevertheless, reflectivity changes are clearly observed (shown in Fig. 4.12(b) and (c) at +10 fs delay) for each peak and share the same shape: a reduced reflectivity at the center of the exciton lineshape, and a slight increase on each side of it. The comparison (Fig. 4.12(d)) with

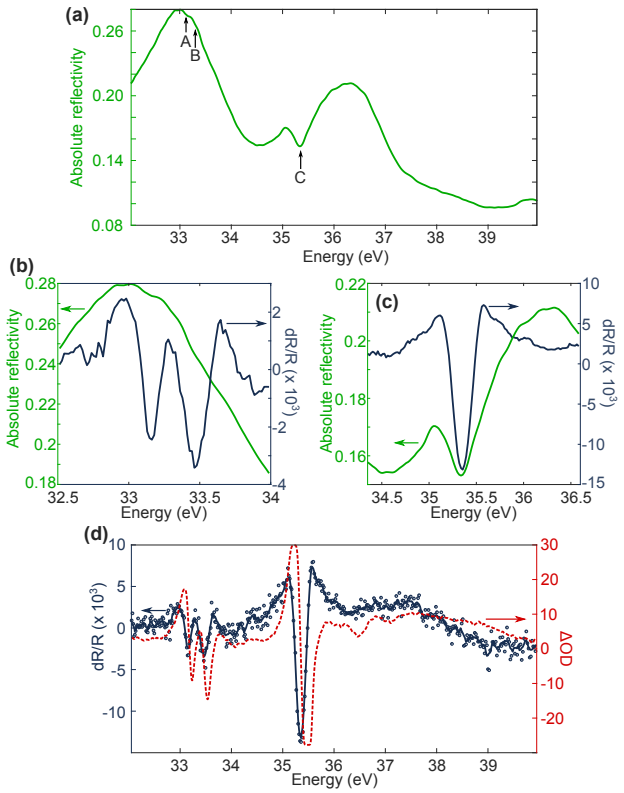

Figure 4.12: (a) Static XUV reflectivity (s-polarized) of WS_2. The core-exciton transitions A, B, and C are labeled. (b) and (c) present the transient reflectivity $dR/R = (R_{on} - R_{off})/R_{off}$ of core-exciton A, B, and C at +10 fs delay. (d) displays the changes in reflectivity at +10 fs (blue points), together with a 5-point moving average (blue full line), overlaid with the changes in optical density at the same pump-probe delay (red dashed line). The pump fluence used to obtain the transient reflectivity results is 25 mJ/cm^2. The reflectivity with and without optical pump is denoted as R_{on} and R_{off}, respectively.

the transient absorption reported in the main text shows that the two observables are consistent with each other. These results display how the core-excitonic lineshapes in reflection geometry are modified by the excitation of free carriers, which has not been reported thus far.

Chapter 5

Electron Thermalization and Relaxation in Nickel[1]

5.1 Introduction

Probing and harnessing the relaxation of hot carriers in metals and semiconductors are vital to the development and design of photovoltaics and photocatalysts [204–210], and to the understanding of mechanisms in various photoinduced phase transitions [211–214]. After photoexcitation, carriers driven out of equilibrium quickly form a thermalized hot carrier distribution within a few to tens of femtoseconds through carrier-carrier scattering, before further cooling takes place through carrier-phonon interactions at timescales ranging from hundreds of femtoseconds to picoseconds [108]. Although the carrier cooling process typically involves complex interactions between the electronic, phonon, and spin degrees of freedom, the dynamics can be successfully described phenomenologically by a "multi-temperature model" in a wide variety of systems [108, 204, 206, 208, 214–217]. In such a model, the electronic, vibrational, and spin degrees of freedom are regarded as individual heat reservoirs and the energy transfer between the reservoirs is governed by a set of "interaction coefficients". Each reservoir is presumed to be in quasi-thermal equilibrium with a particular "temperature", based on the assumption that the heat equilibration within each reservoir, e.g. due to electron-electron scattering within electronic reservoir and anharmonic interactions for phonon baths, is much faster than the inter-reservoir energy transfer [217]. The usefulness of multi-temperature models is widely evidenced in studies of energy transfer in heterostructures [218], hot electron cooling in two-dimensional materials and superconductors [219, 220], and photoinduced spin dynamics and phase transitions [211, 214, 221–230].

Despite the success of the multi-temperature model in elucidating a wide variety of photophysical phenomena, its applications are often limited to systems with an already thermalized carrier distribution. On the other hand, non-equilibrium hot carriers are known to facilitate charge

[1]The content and figures of this chapter are adapted or reprinted with permission from Ref. H.-T. Chang et al., "Electron thermalization and relaxation in laser-heated nickel by few-femtosecond core-level transient absorption spectroscopy", Phys. Rev. B **103**, 064305 (2021).

separation dynamics in organic heterojunctions [207] and play an important role in plasmon-induced photocatalysis [209, 210]. Studies of ultrafast demagnetization and all-optical magnetic state switching also demonstrate that the resulting spin dynamics can be coherently driven by non-thermal photoexcited carriers [36, 213, 231–236]. The importance of measuring the electron thermalization process is further outlined in a recent optical pump-probe study on copper, which shows that the electron thermalization timescale is strongly dependent on the excitation fluence and at the low fluence limit, the thermalization timescale can become comparable to the electron-phonon scattering time [237]. To measure the photoexcited carrier distributions, time-resolved photoemission methods for valence electrons probe energy and momentum resolved carrier distributions in real time. However, the photoemission methods are restricted to timescales greater than tens of femtoseconds, due to the relation between the energy bandwidth and the duration of the pulses that eject the photoelectrons, and thus have limited capacity in directly capturing carrier dynamics below 20 fs while maintaining <0.2 eV energy resolution that is typically required to resolve carrier distributions in condensed matter. In addition, as alloy and multilayer structures are intrinsic to the construction of photovoltaics and many magnetic materials exhibiting photoinduced changes in magnetization [36, 232–234, 238, 239], insight into the properties and performance of these materials can be obtained through understanding the carrier dynamics in each layer or sub-domain in the system. Therefore, it is important to develop a unified experimental approach that provides element specificity, and thus domain or layer selectivity, can interrogate the sub-10 fs dynamics of non-equilibrium carrier distributions, and is also capable of presenting key parameters such as carrier temperature after thermalization to facilitate the understanding of the interactions between the different degrees of freedom in photoexcited materials.

Core-level transient absorption (TA) spectroscopy in the extreme ultraviolet (XUV) has recently been developed and utilized to investigate carrier dynamics in semiconductors [9, 28–30, 98, 99, 101, 103, 115, 240, 241]. Exploiting the element specificity of this method, Cushing et al. investigated layer-specific carrier dynamics in a Si-TiO_2-Ni trilayer structure [101]. In studies on germanium [9], lead iodide [98], and lead halide perovskites [99], the energy distribution of the carriers and their relaxation can be directly extracted from XUV TA spectra. In addition, Volkov et al. utilized XUV TA spectroscopy to explore effects due to the change of electronic screening during photoexcitation of titanium [34]. However, despite numerous studies on electron dynamics in solids using core-level TA spectroscopy, the methodology to extract the energy distribution of photoexcited carriers or carrier temperature in metals from core-level TA spectra is still lacking. For many semiconductors with well-screened core holes, features of the core-level absorption spectra can be mapped onto the conduction band (CB) density of states (DOS) [9, 76, 98, 99, 103, 142], and carrier dynamics can therefore be directly extracted from core-level TA measurements. In metals, by contrast, many-body interactions of electrons at the Fermi surface with the core hole potential strongly renormalize the spectral lineshape of core-to-CB transitions [37], resulting in strong resonances at the absorption edge, termed “edge singularities” [242–246]. As many-body interactions drastically reshape the core-level absorption spectra beyond the CB DOS, it is thus highly challenging in metals to unravel the carrier distributions and extract important parameters such as carrier temperatures using core-level absorption spectroscopy.

Here we employ nickel as a prototypical system and study the core-level TA spectra at the nickel

$M_{2,3}$ edge around 67 eV to develop a framework to understand the core-level TA spectra of metals, extract the electron temperatures, investigate the carrier cooling dynamics, and explore electron thermalization. Nickel is a ferromagnetic material exhibiting sub-picosecond demagnetization when irradiated with a femtosecond laser pulse and has been extensively studied [36, 211, 221, 223, 232, 239, 247–253]. Time-resolved photoemission measurements indicate that the photoexcited electrons in nickel thermalize on a sub-30 fs timescale [253] and electron-phonon relaxation times ranging from 200 fs to 1 ps have been derived from optical transient reflectivity and time-resolved second harmonic generation measurements [221, 247–251]. On the other hand, ultrafast electron diffraction experiments show that a non-thermal phonon distribution persists over several picoseconds after optical excitation [254]. The many studies on photoexcited carrier dynamics in nickel thus provide suitable benchmarks for the methodology development here to reveal electron dynamics in metals using XUV core-level spectroscopy.

In this work, it is observed that the core-level absorption of laser-heated nickel can be described by a red-shifted and Gaussian broadened static absorption spectrum. In Sec. 5.2.1, the results of a set of power dependence measurements are shown and the resulting Gaussian broadening exhibits a linear dependence with respect to the electron temperature change. In addition, the fitted spectral shift exhibits a power-law relationship with the electron temperature change. A theory for the linear relation between the Gaussian broadening and electron temperature change is derived in Sec. 5.2.2 to complement the analyses, and Sec. 5.3 presents a conjecture based on analogy to the works on many-body interactions in the core-excited state after optical excitation [34] to explain the nonlinear relationship between the spectral shift and electron temperature. Section 5.2.3 displays the extraction of electron temperature from core-level TA spectra of photoexcited nickel according to the linear relationship between the spectral broadening and electron temperature rise, enabling real-time tracking of the carrier cooling process, and an electron cooling time of 640±80 fs is obtained. The measurement results indicate that the contribution to spectral changes from phonon heating is negligible and the cause of the spectral red shift in all measurements within this work is purely electronic. In Sec. 5.2.4, fluence dependence measurements reveal a decrease of XUV TA signal rise time from 35 fs to 15 fs as the final electron temperature, viz. the maximum electron temperature after thermalization, increases from 2100 K to 3100 K. The measured fluence-dependent electron thermalization times are in good agreement with theoretical predictions [255]. By comparing the <6 fs long instrument response function with the <40 fs growth dynamics of the spectral features that become the profile of thermalized carrier distributions in the fluence dependence measurements, a range of electron thermalization times between 34 fs and 13 fs is obtained.

5.2 Results

The core-level TA experiment on nickel was carried out with a table-top XUV source based on high-harmonic generation. The experiment is depicted in Fig. 2.1 and details of the experimental setup are described in Sec. 5.A. Briefly, 50 nm thick polycrystalline nickel thin films deposited on 30 nm thick silicon nitride windows (Sec. 5.B) were excited at normal incidence by a 4.3 ± 0.2

fs long (Gaussian FWHM), broadband optical pulse with a spectrum extending from 500 nm to 1000 nm and linear polarization. After optical excitation, the sample was probed by a time-delayed broadband linearly polarized XUV pulse, which is produced by high-harmonic generation in argon with a 3.6 ± 0.1 fs long laser pulse centered at 730 nm. The polarization of the XUV pulse is parallel to the optical pump and the XUV spectrum spans 40-73 eV (Fig. 2.13). The XUV spectrum covers the nickel $M_{2,3}$ edges located at 66.2 and 68.0 eV, consisting of excitations from nickel $3p$ levels to the conduction band [256]. The static absorption spectrum of nickel $M_{2,3}$ edges, shown in Fig. 5.1(a), exhibits a steep rising edge at approximately 66 eV due to absorption from the Ni $3p_{3/2}$ core level (M_3) and another small absorption feature at approximately 68.5 eV from the Ni $3p_{1/2}$ level excitation (M_2). Above 69 eV, the absorbance slowly decreases with increasing energy.

Dynamics following photoexcitation of nickel were probed by the change of core-level absorbance ΔA at variable time delays between the pump and probe pulses. A set of typical XUV TA spectra between -50 fs and 1.9 ps time delay is displayed in Fig. 5.1(b) alongside the static absorption spectrum in Fig. 5.1(a). Two positive features (increased absorption) are observed at 65.7 and 67.4 eV, below the nickel M_3 and M_2 edge, respectively. The two features decay within 1 ps, a duration conforming to the electron cooling time in nickel due to electron-phonon interactions [251]. To probe the electron thermalization dynamics, the XUV TA results ranging from -20 fs to +35 fs time delay with 0.33 fs time steps are plotted in Fig. 5.1(c). The XUV TA spectra show no significant changes between 15 fs and 35 fs time delay and no energetically shifting spectral features are observed. In the following, we analyze the results by first considering the interpretation of the core-level TA spectra and extraction of electron temperature. Details of the electron cooling and thermalization dynamics are discussed in Sec. 5.2.3 and 5.2.4, respectively.

To understand the core-level absorption spectra of optically excited nickel, we focus on the XUV TA profile right after photoexcitation. A core-level TA spectrum at 40 fs pump-probe delay is plotted in Fig. 5.2(a). Here, apart from the increase in absorption (positive ΔA) below the nickel M_3 and M_2 edge (<67.4 eV), a shallow negative feature occurs above the nickel M_2 edge (68 eV). Unlike the core-level TA spectra at the nickel $L_{2,3}$ edge, where the magnitude of absorption changes below and above the edge is highly symmetric [223, 224], in the M edge TA spectrum the positive features are much stronger than the the negative feature and the integrated area of the TA profile ($\int \Delta A(\omega) d\omega$) is clearly nonzero. The asymmetry of the TA profile indicates that it cannot be directly interpreted by electronic occupation below and above the Fermi level in contrast to the TA spectra at the nickel L edge [257]. While the cause of the asymmetric TA profile is beyond the scope of this work, it may stem from the asymmetric Fano broadening of the nickel $M_{2,3}$ edge due to Coster-Kronig decay of the core hole [**dietzLineShapeExcitation1974**, 256, 258], the many-body interactions between the electrons at the Fermi surface and the core hole [34], and the splitting of core-levels with different angular and magnetic quantum numbers [259].

As Tengdin et al. showed that the electron thermalization time in nickel is <30 fs,[2] a hot, thermalized electron distribution is expected to be established in the CB by 40 fs after photoexcitation,

[2]Tengdin et al. detected thermalized hot electron distribution with time-resolved angle-resolved photoemission 24 fs after photoexcitation by pulses centered at 780 nm with fluence of <6 mJ/cm^2 [253]. The reported pulse duration in Ref. [253] is 28 fs. As the rate of electron scattering increases with carrier temperature, the carrier thermalization time is expected to be <30 fs long at fluences used in this study (8 – 62 mJ/cm^2).

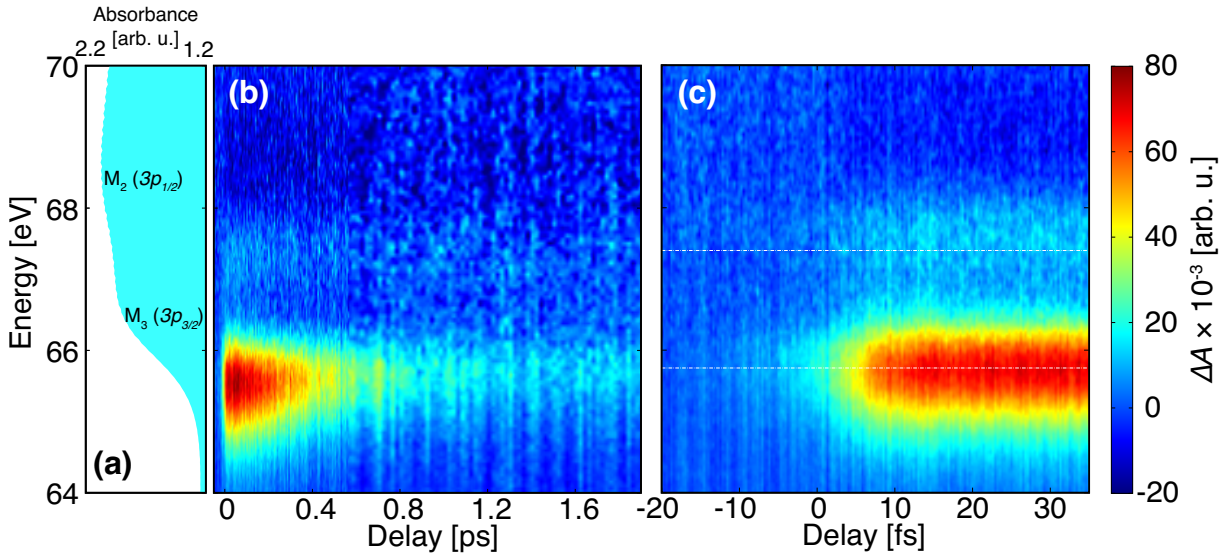

Figure 5.1: (a) Static absorption spectrum of nickel $M_{2,3}$ edge and (b), the measured XUV TA spectra of nickel between -50 fs and 1.9 ps time delay. (c) displays the experimental XUV TA spectra between -20 and 35 fs time delay. The experimental pump fluence of the results in (b) and (c) are 41 mJ/cm^2 and 33 mJ/cm^2, respectively.

and as the electron-phonon scattering time in nickel is on the order of a few hundred femtoseconds, energy loss to the phonon bath can be ignored. Almbladh and Minnhagen [260], Ohtaka and Tanabe [261–263], and Ortner and coworkers [264–266] have independently shown that the increase of electron temperature in metals can impose a broadening to the core-level absorption edge. In addition, the change of electronic screening in CB due to photoexcitation can cause an energy shift of the core-to-CB transitions [34, 223, 267]. Thus motivated, we consider a model where the core-level absorption of photoexcited nickel ($I(\omega)$) is simulated by a Gaussian broadening σ of the static absorption spectrum ($I_0(\omega)$) with an overall energy shift ω_s:

$$I(\omega, \omega_s, \sigma) = \int d\omega' \, I_0(\omega - \omega_s - \omega') f(\omega', \sigma), \tag{5.1}$$

$$f(\omega, \sigma) = \frac{1}{\sigma\sqrt{2\pi}} \exp(-\frac{\omega^2}{2\sigma^2}).$$

The fitting of the experimental TA spectrum (Fig. 5.2(a), blue line) with Eq. (5.1) (Fig. 5.2(a), red line) exhibits good agreement between the fitted and the experimental result.

5.2.1 Power Dependence Measurements

To quantify the effects of electron temperature on the core-level absorption spectra and extract the physical properties related to the broadening and shift, we performed power dependence mea-

surements at five different laser fluences (8 – 62 mJ/cm^2). The core-level TA spectra at 40 fs time delay and their fitting with Eq. (5.1) are displayed in Fig. 5.2(b). The magnitude of all TA features increases with increasing fluence and the fitting results show that Eq. (5.1) can accurately describe the measured spectral changes (Fig. 5.2(b), black lines). The spectral broadening and shift obtained from the fitting with the corresponding electron temperature change, calculated from the pump fluence and electron heat capacity of nickel (Sec. 5.C), are plotted in Figs. 5.2(c) and (d), respectively. Here it is observed that the spectral broadening σ and the corresponding calculated electron temperature change ΔT_{est} can be fitted by a formula $\sigma = a\Delta T_{est}$ (Fig. 5.2(c), black line), with $a = (5.7 \pm 0.8) \times 10^{-5}$ eV/K. The negative spectral shift ω_s indicates the absorption edge red-shifts with increasing electron temperature (Fig. 5.2(d)) and it exhibits a power-law relationship with electron temperature change ($\omega_s \propto \Delta T_{est}^{\alpha}$), with exponent $\alpha = 1.5 \pm 0.2$ (Fig. 5.2(d), inset). We defer discussion on the cause of the spectral shift to Sec. 5.3.1 and first consider a theoretical explanation of the observed relation between the electron temperature change and Gaussian broadening.

5.2.2 Relation between Gaussian Broadening and Electron Temperature Changes

The many-body theory of core-level absorption in metals at nonzero temperatures, pioneered by Almbladh and Minnhagen [260], Ohtaka and Tanabe [261–263], and Ortner and coworkers [264–266], shows that the core-level absorption spectra $I'(\omega)$ can be approximated by a simple formula (in atomic units):

$$I'(\omega) \propto \frac{1}{2}\mathrm{Re}\int_{-\infty}^{\infty} e^{i(\omega-\omega_0)t} I'(t)dt$$
$$I'(t) = \left(\frac{\pi T}{i\sinh(\pi T t)}\right)^{1-\zeta}. \tag{5.2}$$

Here, ω_0 represents the difference between the Fermi energy and the excited core-level, T is the electron temperature, and $\zeta < 1$ is a coefficient related to the phase shift of the scattered electrons from the core hole potential. Although the expression only includes the effect of electron temperature, assumes a slowly varying density of states near the Fermi level, and ignores several factors that can lead to spectral distortion and broadening such as Auger decay of core holes, phonon heating [268, 269], and sample crystallinity and inhomogeneity, it provides a clear mathematical representation of temperature effects on core-level absorption. Note that while the formula is derived from many-body theory, it is still valid for core-level absorption in metals when core-hole mediated electron scattering at the Fermi surface is negligible.

To derive an expression relating spectral changes and electron temperature rise ΔT, we consider an *ansatz* relating the absorption lineshape $I(\omega, T_0 + \Delta T)$ with electron temperature change ΔT with respect to the absorption spectrum of the sample at temperature T_0 before excitation:

$$I(\omega, T_0 + \Delta T) = \int d\omega'\, I(\omega - \omega', T_0) f(\omega', \Delta T), \tag{5.3}$$

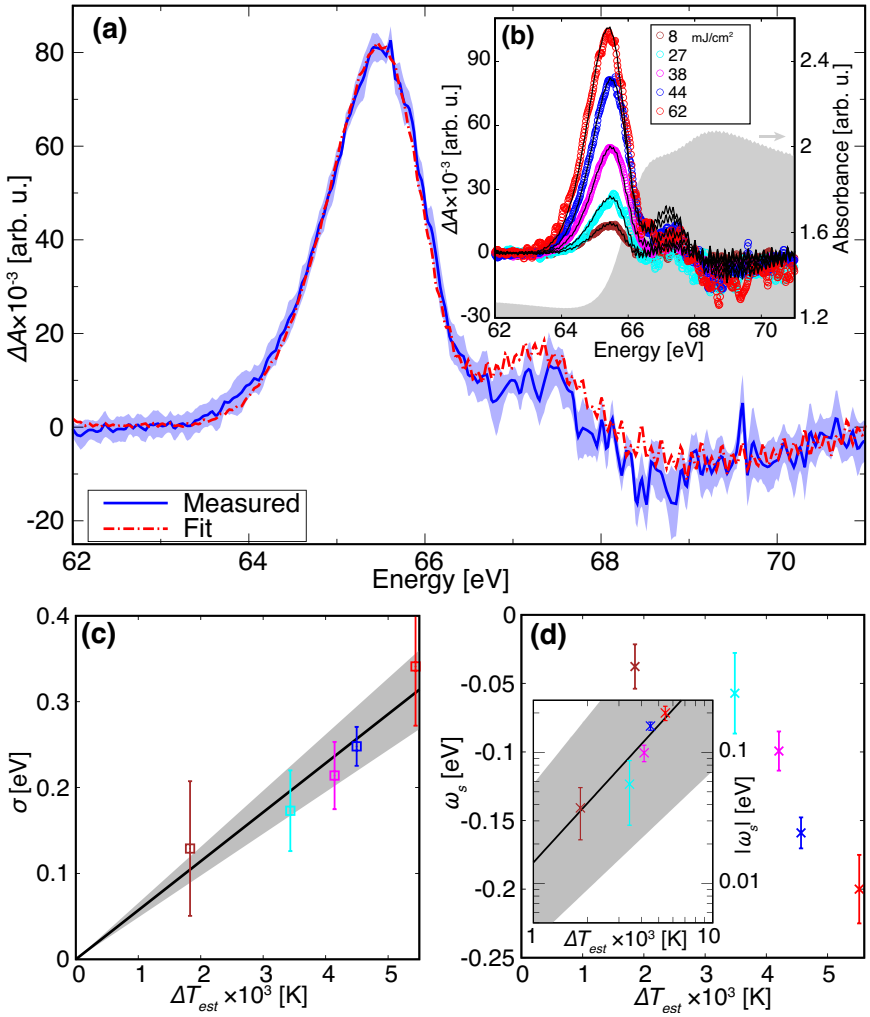

Figure 5.2: (a) A typical XUV TA spectrum of nickel at 40 fs time delay (blue line). ΔA denotes the change of XUV absorbance and the blue shade in (a) shows the uncertainty of the TA spectrum. The red line is the fitting result of Eq. (5.1) on the experimental data. The Gaussian broadening and shift obtained from the fitting are 0.25 ± 0.02 eV and -0.16 ± 0.01 eV, respectively. (b) Absorbance change ΔA (circles) after optical excitation at 40 fs time delay with 5 different laser fluences. The static absorption spectrum of nickel $M_{2,3}$ edge is displayed in gray as a reference. Results of the fitting of measured data with Eq. (5.1) are shown in black lines and the obtained σ and ω_s as a function of the simulated electron temperature rise ΔT_{est} are shown in (c) and (d), respectively. The results of linear fitting of σ versus ΔT_{est} is displayed as a black line in (c) and the inset in (d) exhibits the fitting of $|\omega_s|$ versus ΔT_{est} with a power function (black line) in a log-log plot. The uncertainties in the fitting are shown as gray areas in (c) and (d), respectively.

where the absorption lineshape at electron temperature T_0 is convoluted by a function $f(\omega, \Delta T)$. The choice of convolution in the expression is motivated from experimental observation (Fig. 5.2 and Eq. (5.1)) and theoretical results [263]. The combination of Eqs. (5.2) and (5.3) indicate that $f(\omega, \Delta T)$ can be found by approximating the component of free-induction decay $I'(t)$ in Eq. (5.2) by

$$\frac{\pi(T_0 + \Delta T)}{\sinh(\pi(T_0 + \Delta T)t)} \approx \frac{\pi T_0}{\sinh(\pi T_0 t)} \times e^{g(t,\Delta T)}, \tag{5.4}$$

with $f(\omega, \Delta T) = \frac{1}{2\pi}\int_{-\infty}^{\infty} e^{i\omega t} e^{(1-\zeta)g(t,\Delta T)} dt$. Using second order expansion of ΔT on both sides of Eq. (5.4), it is shown that the first order term in the expansion of $g(t, \Delta T)$ with respect to time t is zero and the coefficient of the second order term is proportional to $(\Delta T)^2$ when T is small compared to ΔT (Sec. 5.D). In other words, the term $e^{(1-\zeta)g(t,\Delta T)}$ can be approximated by the expression

$$e^{(1-\zeta)g(t,\Delta T)} \propto \exp\left(-\frac{(\sigma t)^2}{2}\right),$$

with $\sigma = a\Delta T$, where a is a proportionality constant. This suggests that the core-level absorption spectrum after laser heating $I(\omega, T_0 + \Delta T)$ can be described by the convolution of the spectrum before heating $I(\omega, T_0)$ with a Gaussian function $f(\omega, \sigma) = \frac{1}{\sigma\sqrt{2\pi}} \exp\left(-\frac{\omega^2}{2\sigma^2}\right)$ and the broadening factor σ is directly proportional to the temperature rise ΔT.

Comparing Eq. (5.4) with Eq. (5.1), it is observed that the reference spectrum at temperature T_0 in Eq. (5.4) is represented by the static spectrum in Eq. (5.1). The two expressions merely differ by the spectral shift ω_s, which is not present in the derivation above because the overall energy shift of the core-excited state is not included in either the many-body theory of core-level absorption [263, 266] or our proposed ansatz (Eq. (5.3)). The mathematical derivation thus justifies the fitting of TA profiles with a Gaussian broadened static spectrum and suggests that this approach can be extended to other metallic systems. In addition, the robustness of the method (Eq. (5.1)) is ensured by limiting the fitting parameters to only the shift and broadening. This is because the major factors that contribute to spectral distortions and broadenings are implicitly included in the formalism. The reference spectrum $I(\omega, T_0)$ in Eq. (5.3) and the static absorption spectrum in Eq. (5.1) automatically incorporate the spectral contribution from the intrinsic core hole lifetime as well as sample geometry and crystallinity, which remain unchanged throughout the measurement. The effects of interaction between the core hole and laser-heated CB electrons are included in Eq. (5.2), the starting point of the derivation of $f(\omega, \Delta T)$. Note, however, the mathematical derivation only considers the spectral changes due to variation in electron temperature; other contributions from processes that would follow photoexcitation, such as phonon dynamics, are not included. In addition, the derivation of $f(\omega, \Delta T)$ involves truncation in a series expansion and is not analytically exact. Therefore, the application of this method (Eq. (5.1)) and the extraction of electron temperature from the broadening always require verification that the relation between the electron temperature and the broadening is linear and dynamics in the electronic domain are the dominant contributor to the TA lineshape. The relationship between projected electron temperature and the fitted spectral broadening in power dependence measurements, and the correspondence

between the fitted spectral shift and broadening, can both serve as checkpoints to examine the adequacy of this analysis approach.

5.2.3 Electron Cooling Dynamics

Equipped with the formalism to understand the spectral change in core-level excitations in nickel with hot thermalized electrons at a short 40 fs pump-probe delay (Eq. (5.1)), we consider here the electron cooling dynamics at >40 fs timescales (Fig. 5.1(b)). To analyze the measured dynamics, we first apply Eq. (5.1) to fit the TA spectrum at each time delay. The fitted spectra are shown in Fig. 5.3(a), displaying good agreement with the experimental results (Fig. 5.1(b)). Note that phonon heating is expected to occur from electron-phonon scattering processes during the cooling of the electron bath [251] and the adequacy of relating electron temperature with spectral broadening requires verification. It has been shown that the rise of non-thermal phonon occupation persists over timescales above 2 ps [254] and the electronic reservoir cools down below 1 ps [251]. If phonon dynamics contribute significantly to the XUV TA spectra, it is expected that at >1 ps timescales the contribution from phonons would dominate and the magnitude of the XUV TA signal would rise with increasing time delay. Contrary to the expectations, however, the experimental TA signal diminishes to zero with increasing time delay and its magnitude at 1.9 ps delay is barely above noise level (Fig. 5.1(b)). This suggests that the contribution from heated phonons to the observed core-level TA signal is negligible compared to the dynamics in the electronic domain.[3] As such, the obtained spectral broadening σ can still be connected with ΔT in the analysis of XUV TA spectra at hundreds of femtoseconds to picoseconds.

Figure 5.3(b) shows the fitted spectral shift (blue dots) and electron temperature ($\Delta T = \sigma/a$, red dots) derived from the fitted spectral broadening at different time delays. Both the spectral shift and electron temperature as a function of time delay can be fitted by a single exponential decay convoluted with the instrument response function (Fig. 5.3(b), lines) and the time constants for electron temperature decay $\tau_\sigma = 640 \pm 80$ fs and spectral shift $\tau_s = 380 \pm 30$ fs are obtained, respectively. Note that the shift ω_s and broadening σ are the only variables in the fitting procedure (Eq. (5.1)), and no additional parameters are introduced. The 640 ± 80 fs cooling time is consistent with the reported values from optical pump-probe measurements [247, 248, 250]. The discrepancy between τ_σ and τ_s also agrees with the observed relationship between the electron temperature and the spectral shift in the power dependence measurements (Fig. 5.2(d)). As the spectral shift is related to the electron temperature change by a power law ($\omega_s \propto \Delta T^\alpha$), it is expected that the decay dynamics of spectral shift to follow the relation $\omega_s(t) \propto \Delta T(t)^\alpha \propto e^{-\alpha t/\tau_\sigma}$,with $\alpha = \tau_\sigma/\tau_s$. Here, the obtained τ_σ/τ_s is approximately 1.7, agreeing with the $\alpha = 1.5 \pm 0.2$ obtained from the power dependence measurements (Fig. 5.2(d), inset). It is thus observed that the relation between the spectral shift and broadening is maintained between 40 fs and 1.9 ps time delay. At 40 fs delay, the effect of electron-phonon interaction is negligible because the timescale is well below the electron-phonon scattering time [251], whereas at picosecond timescales, non-equilibrium phonon

[3]Note that the results only indicate that the TA signal is not sensitive to the particular phonon heating dynamics in the experiment. It does not imply that core-level absorption spectroscopy is insensitive to phonon dynamics overall and depending on the system measured, lattice dynamics can contribute to core-level TA signals (e.g. Ref. [270]).

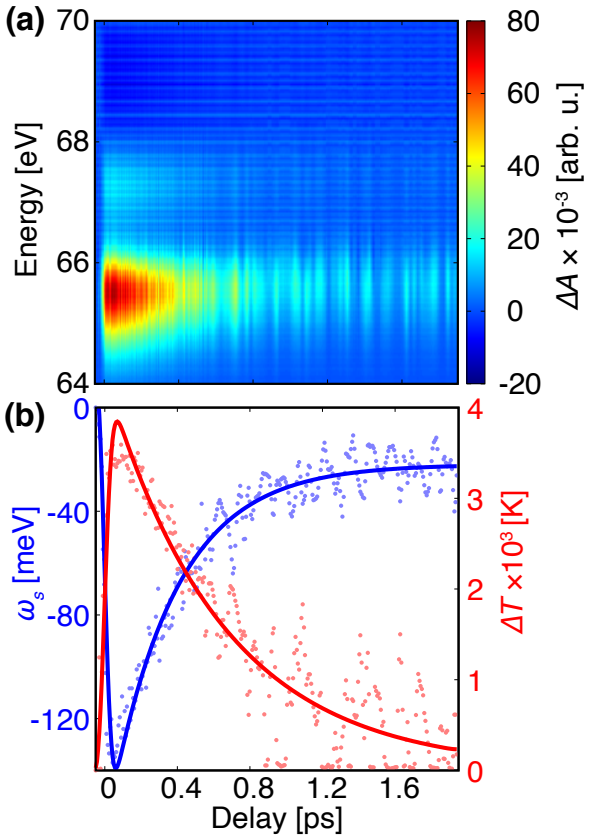

Figure 5.3: (a) Results of fitting the TA spectra in Fig. 5.1(b) with Eq. (5.1) and the fitting parameters ω_s and ΔT at different time delays are shown as dots in (b). The fitting of the changes of ω_s and ΔT as a function of time delay with single exponential decay convoluted with a Gaussian instrument response function are shown as the blue and red line, respectively.

dynamics are paramount [251, 254, 271]. The consistency of the behavior between the spectral shift and broadening from 40 fs to picosecond time delays further corroborate that the fitted spectral broadening and shift are related to physical properties in the electronic domain because the relation between the two persists regardless of the generation of phonons out of thermal equilibrium.

5.2.4 Electron Thermalization Dynamics

In this section, we focus on the few-femtosecond dynamics of carrier photoexcitation and thermalization. The XUV TA spectra between -20 and 35 fs pump-probe delay with optical pump fluence at 33 mJ/cm^2 are plotted in Fig. 5.1(c), which exhibits two positive features at 65.75 eV and 67.4 eV that increase in magnitude within -10 fs to +15 fs time delay and reach a plateau at >15 fs. The lack of changes in the TA signal between 15 fs and 35 fs suggests that the electrons thermalize within 15

fs.[4] The absence of energetically shifting spectral features within -10 fs to +15 fs time delay, which could be used to directly signify the scattering and decay of the initial non-equilibrium photoexcited electrons to form a hot thermalized distribution, initially implies that the electrons thermalize within the pulse duration of the pump. However, the analysis of the lineouts of TA features at 65.75 eV and 67.4 eV (Fig. 5.4(c) (dots)) shows that the duration of the growth of the TA features is significantly longer than the optical pump pulse. By fitting the lineouts with a modified Gaussian error function (Eq. (5.8)), TA signal rise times $\tau_{rise} = 15.1 \pm 0.4$ fs and 14 ± 2 fs for energies 65.75 eV and 67.4 eV are obtained, respectively (Fig. 5.4(c) (dashed lines)). The cross-correlation time between the optical and XUV pulses, whose upper limit is set by the cross-correlation between the pump pulse and the driving field for high-harmonic generation, is less than $\sqrt{4.3^2 + 3.6^2} \approx 5.6$ fs. The 15 fs rise time of the features at 65.75 eV and 67.4 eV (Fig. 5.4(c)), which is much longer than the <5.6 fs cross-correlation time between the pump and the probe, suggests that the electron thermalization time is longer than the pump pulse duration and the lengthened rise time is connected to non-thermal electron relaxation. We present experimental evidence to support this hypothesis, and a conjecture on the cause of the absence of spectral signatures of non-equilibrium electron distribution is discussed in Sec. 5.3.2.

To verify whether the electrons directly thermalize during photoexcitation, the XUV TA spectra (Fig. 5.1(c)) are fitted with Eq. (5.1), and the quality of the fitting and the relation between the fitted broadening $\sigma(t)$ and energy shift $\omega_s(t)$ are examined. Figure 5.4(a) shows the fitting results and the fitted broadening and energy shift as a function of time delay are plotted in Fig. 5.4(b). The good agreement between the fitting results (Fig. 5.4(a)) and experimental data (Fig. 5.1(c)) initially suggests that the electrons thermalize within the duration of the optical pulse. However, if the electrons already thermalize within the timescale of photoexcitation, the resulting spectral broadening σ and shift ω_s should follow the relation $\omega_s(t) \propto \sigma(t)^{1.5}$ as shown in Sec. 5.2.3. In Fig. 5.4(b), the changes in the broadening and the shift as a function of time delay are fitted to a modified Gaussian error function (Eq. (5.8)) and the obtained error function rise times for the broadening and the shift are $\tilde{\tau}_\sigma = 11.0 \pm 0.4$ fs and $\tilde{\tau}_s = 15.0 \pm 0.3$ fs, respectively. Given $\omega_s \propto \sigma^{1.5}$ for a thermalized electron distribution, the increase of magnitude in the spectral shift $\omega_s(t)$ should be steeper than the broadening $\sigma(t)$ ($\tilde{\tau}_\sigma > \tilde{\tau}_s$), which is opposite to the fitting results. This indicates that the electron thermalization time in nickel is either comparable or longer than the optical pulse (4.3 fs), and during the increase of magnitudes in the broadening and spectral red shift, the broadening σ cannot be directly related to an electron temperature.

In addition to the inconsistent behavior of the spectral shift and broadening compared to the results obtained at ≥ 40 fs time delay, we consider the fluence dependence of the TA signal rise time (Fig. 5.4(c)). Fermi liquid theory indicates that the electron collision rate is proportional to the square of electron temperature [272]. Using Boltzmann collision integrals, Mueller and Rethfeld predict that the electron thermalization time in nickel decreases by an order of magnitude as the "final" electron temperature, viz. the electron temperature after thermalization, increases from 2000

[4]Note that, however, because the core-level absorption spectrum at the Ni $M_{2,3}$ edge cannot be directly mapped on to the CB DOS, it is impossible to directly quantify the deviation of the carrier distribution from a hot Fermi-Dirac function with the core-level TA spectra.

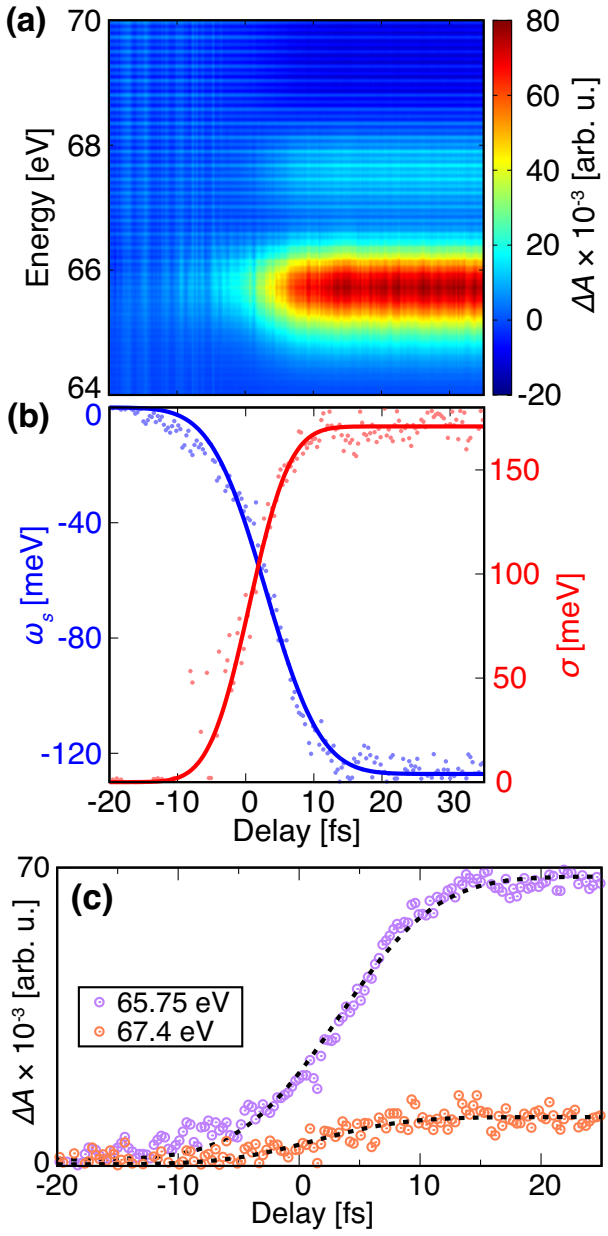

Figure 5.4: (a) Fitting results of Fig. 5.1(c) with Eq. (5.1). The fitted edge shift (ω_s) and broadening (σ) as a function of time delay are plotted in (b) as dots and the fitting of $\omega_s(t)$ and $\sigma(t)$ with Eq. (5.8) are depicted as blue and red lines, respectively. (c) shows the lineouts of ΔA, shown in circled dots, at 65.75 and 67.4 eV (Fig. 5.1(c), white dashed lines) and their fitting results (dashed black lines) with Eq. (5.8).

Table 5.1: Experimentally obtained TA signal rise time τ_{rise} and extracted electron thermalization time τ_{th} versus electron temperature T_e from fluence dependence measurements. The asymmetry in the uncertainty of τ_{rise} for entries with T_e =2129 K and 2552 K is due to the drift of time delay within the experiment which cannot be compensated, leading to a stretch in the rise time. Further explanation on the time delay drift is described in Sec. 5.A.

T_e [K]	τ_{rise} [fs]	τ_{th} [fs]
2129	35^{+10}_{-15}	34
2552	22^{+5}_{-10}	21
3060	15 ± 3	13

K to 8000 K [255]. The fluence dependence of electron thermalization has been experimentally observed by Obergfell and Demsar in Cu by optical pump-probe measurements [237]. Here we examine the connection between electron thermalization time and the rise time of the core-level TA signal (Fig. 5.4(c)) by a set of power dependence measurements at three different pump fluences. In Table 5.1, we list the final electron temperatures T_e and the rise times τ_{rise} of TA signal at 65.75 eV and a clear decrease in the rise time with respect to increasing electron temperature is observed. As the final electron temperature rises from approximately 2100 K to 3100 K, the measured rise time decreases from 35 fs to 15 fs. The observed behavior of the rise time as a function of final electron temperature is consistent with theoretical predictions of the electron thermalization time and we estimate this time τ_{th} by deconvolving the growth dynamics with the pump-probe cross-correlation ($\tau_{th} \approx \sqrt{\tau_{rise}^2 - 5.6^2}$). The electron thermalization times obtained by deconvolution are listed in Table 5.1, showing that the electron thermalization time decreases from 34 fs to 13 fs as the electron temperature rises from 2100 K to 3100 K. The obtained thermalization times are on the same order of the theoretically predicted thermalization time in nickel [255].

5.3 Discussion

Despite the success of fitting the TA profile with spectral shift and broadening (Eq. (5.1)), the physical origin of the spectral shift has yet to be clarified. In addition, while the electron thermalization time is extracted from the rise of TA signal (Fig. 5.4(c)), the absence of spectral signatures of the non-equilibrium electron distribution during photoexcitation has not been explained. Here we discuss the potential origin of the spectral shift and the absence of spectral features of non-thermalized electrons.

5.3.1 Origin of Spectral Shift

The spectral shift in the core-level absorption spectra can be interpreted as an overall change in the energy of the core-excited state in laser-heated nickel. This can be caused by electron-phonon interactions [9], and in particular, lattice displacement and heating due to optical excitations [76, 270]. However, as the experimental results suggest that the direct influence of phonon excitations on the TA profile is negligible, we restrict the discussion within the electronic domain. Electronically, the spectral red shift of core-level absorption after optical pump illumination can originate from the lowering of the chemical potential in the CB or stabilization of core-excited state due to many-body interactions [34]. The lowering of the chemical potential as a possible cause can be eliminated as Lin et al. showed that the chemical potential of the CB of nickel increases rather than decreases with rising electron temperature [273–275], in contrast to the experimental observations here. Due to the complexity in simulating the effect of many-body interactions in the core-excited state of nickel with hot, thermalized CB electrons, here we provide a subjective explanation for the nonlinear relationship between ω_s and ΔT based on related works by analogy and invite future theoretical works to verify the validity of the conjecture.

In attosecond TA studies of titanium, Volkov et al. showed that the optical excitation of electrons increases the occupation of the localized Ti $3d$ orbitals, which further causes a spectral blue shift due to the increase of electronic repulsion in the core-excited state [34]. In nickel, the increase of electron temperature causes the transfer of Ni $3d$ electrons to the higher-lying $4s$ and $4p$ bands [275], which would reduce the electronic repulsion in the localized $3d$ orbitals in contrast to the repulsion increase observed when heating an early transition metal such as Ti. The cause of the opposing behavior between Ni and Ti is theorized from the inversion in the orbital character with respect to band energies. In titanium, the occupied $4s$ bands are below the largely unoccupied $3d$ bands [34], whereas in nickel, the occupied bands are composed primarily of $3d$ orbitals and the unoccupied bands comprise an increased $4s$ and $4p$ character [276]. The reduction in electronic repulsion stabilizing the core-excited state of laser-heated nickel thus presents a plausible explanation to the spectral red shift observed in the XUV TA spectra. As the electron repulsion and reduction of population in the nickel $3d$ bands are not linearly proportional to electron temperature, the nonlinearity in the relation between ω_s and ΔT is also potentially clarified.

5.3.2 Non-Equilibrium Electron Relaxation

While the fluence dependent rise time of the TA signal (Fig. 5.4(c) and Table 5.1) indicate that the electron thermalization time is longer than the pump pulse duration, no energetically shifting spectral features are observed within the electron thermalization timescale in the TA spectra (Fig. 5.1(c)) to represent the thermalization of non-equilibrium carrier distribution. To understand this phenomenon, we simulated the dynamics of photoexcitation in nickel through a density matrix formalism based on the band structure of nickel calculated by density functional theory (DFT) (Sec. 5.F). Snapshots of electronic occupation near the Fermi-level (E_F) at different time delays with respect to the optical pulse are shown in Fig. 5.5. In the simulated electron distributions, occupation around 1.5 eV below the Fermi level decreases following photoexcitation. However, the

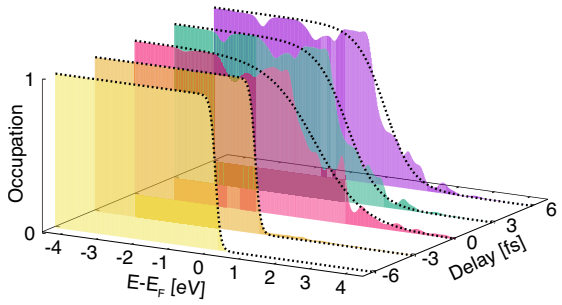

Figure 5.5: Electronic occupation as a function of energy during photoexcitation. The results of fitting each time slice to a Fermi-Dirac function are shown in black dashed lines.

photoexcited electron distribution at and above the Fermi energy still closely resembles a Fermi-Dirac function (Fig. 5.5, black dashed lines). This implies that because the initial photoexcited electronic occupation does not significantly deviate from a hot thermalized distribution, possible spectral signatures of a non-equilibrium CB electron distribution will not be easily distinguished. Note that in the density matrix formalism, the effects of scattering between the photoexcited electrons are not included. Therefore, it is expected that the true photoexcited carrier distribution will feature an even smaller deviation from the thermalized electron distribution than the simulated results (Fig. 5.5). This provides a potential explanation to the absence of spectral features of non-thermalized carriers.

5.4 Conclusion

In summary, it is observed that the transient absorption spectra of optically excited nickel at the nickel $M_{2,3}$ edge can be simulated with a spectral red shift and Gaussian broadening of the static spectrum. For a hot thermalized electron distribution, the Gaussian broadening is experimentally revealed and theoretically derived to be linearly related to the change of electron temperature and can be used to track the electron temperature. The increase of spectral red shift with rising electron temperature can be plausibly explained by the reduction of electron repulsion due to the repartitioning of localized $3d$ electrons to $4s$ and $4p$ bands through laser heating. For thermalized electrons, the red shift displays a power-law relationship with the electron temperature change by a power $\alpha \approx 1.5$. While probing the sub-40 fs dynamics of optically excited nickel, the relation between the spectral shift and electron temperature, and thus the broadening for thermalized carriers, is utilized to determine that the electrons do not thermalize instantaneously during the optical excitation, even though the core-level absorption lineshape at sub-15 fs timescale closely resembles the spectra with thermalized electrons. In the core-level transient absorption spectroscopy of nickel at Ni $M_{2,3}$ edge, the electron thermalization process is represented by a lengthened growth of spectral features for a thermalized electron distribution, indicating that electron scattering and thermalization accompany and follow the photoexcitation and finally create a hot thermalized carrier distribution. A fluence-dependent

electron thermalization timescale ranging between 34 fs and 13 fs is extracted by deconvolving the rise of the transient absorption signal from the instrument response.

The results in this work indicate that core-level absorption spectroscopy can be utilized to extract the electron temperature of metallic samples and to assess both the timescale of electron thermalization and the validity of using a multi-temperature model. As such, this work brings a unification of the observation of >30 fs dynamics of thermalized electrons, and the few-femtosecond dynamics of non-equilibrium electron relaxation. The former can be readily probed with time-resolved photoemission methods but has been difficult to extract and interpret from core-level absorption spectroscopy, while the latter can be interrogated with few-femtosecond core-level spectroscopy but is inaccessible through photoemission techniques. The methodology developed within this study facilitates the understanding of core-level absorption spectra of laser-heated metals with a simple and intuitive picture, and the approach can be readily extended to treat other metallic systems or to investigate photoinduced phase transitions in metallic films and multilayers.

5.A Experimental Apparatus

Details of the table-top XUV TA setup is described in Chapter 2. In brief, compressed broadband optical pulses spanning 500-1000 nm was split by a 1:9 broadband beam splitter into the pump and probe arm. The repetition rate of the laser was reduced to 100 Hz by a mechanical chopper so as to prevent sample damage from optical heating due to the poor heat conductivity in nanometer thick thin films. In addition, the sample is raster scanned during the measurement to prevent laser damage due to long time exposure and systematic error due to sample inhomogeneity. Static absorption measurements are taken before and after each transient absorption experiment to assess whether sample damage occurs during the experiment.

The fine tuning of dispersion in the pump and probe arm is achieved by a pair of glass wedges installed in each arm, and the pulse duration of the pump and probe pulses measured by dispersion scan [47] are 4.3±0.2 fs and 3.6±0.1 fs long, respectively. The duration of the pump pulse is slightly longer than the probe because of the limited bandwidth of the broadband beamsplitter. The typical spectrum and temporal profile of the pump pulse are shown in Fig. 5.6(a) and 5.6(b), respectively. The intensity of the pump beam is controlled by an iris and the beam is time-delayed, focused, and recombined collinearly into the probe arm with an annular mirror. For each individual experiment, the beam profile of the pump is measured by a CMOS camera directly at the sample position for the determination of the intensity and fluence of the pump pulse. The beam in the probe arm is focused into an Ar gas jet to generate broadband XUV pulses spectrally spanning 40-73 eV. After filtering the driving near-IR field with a 100 nm thick Al filter, the XUV beam is refocused by a gold coated toroidal mirror onto the measurement target. After passing through the measurement target, the XUV beam transmits through another 100 nm thick Al filter that blocks the pump light and the transmitted XUV is then dispersed by a flat-field grating onto an XUV CCD camera with 16-bit bit depth that provides a dynamic range of approximately 5 orders of magnitude. With the approximately 1 OD (optical density) edge jump at the nickel edge, the noise floor of the transient measurement is approximately 5 mOD, which is mainly contributed by the fluctuations of the XUV

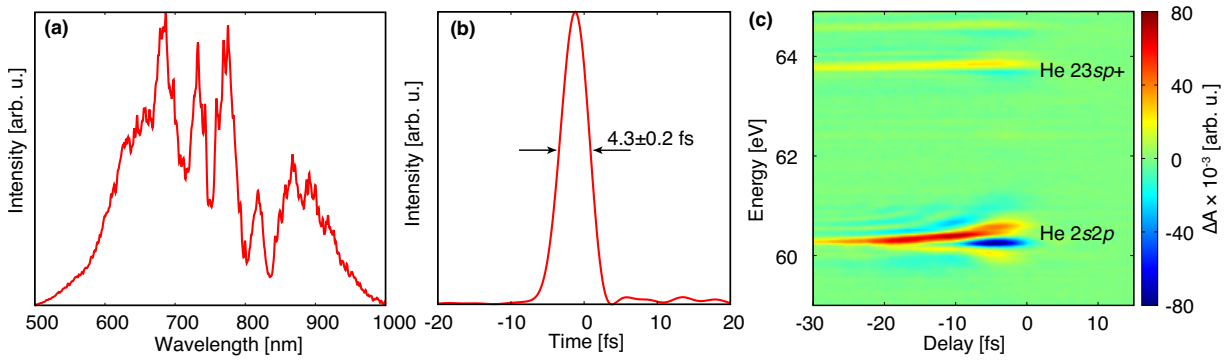

Figure 5.6: (a) The typical spectrum and (b) temporal profile of the pump pulses measured by dispersion scan [47]. (c) displays the typical transient absorption spectra of helium $2snp$ autoionization states taken subsequently after each scan through all time delay points on the nickel sample for time delay calibration.

light source. The spectral resolution of the apparatus at the photon energies of the experiment is approximately 60 meV. The measurement delay step sizes used in the results shown in Fig. 5.1(c) are 1.3 fs (0.2 μm) between -66.7 fs (-10 μm) to +133.3 fs (+20 μm) delay, 3.3 fs (0.5 μm) between +133.3 fs (+20 μm) and +560 fs (+84 μm) delay, and 20 fs (3 μm) between +560 fs (+84 μm) and +1.98 ps (+297 μm) delay. The measurement delay step size used in the results shown in Fig. 5.1(d) is 0.33 fs (0.05 μm) between -50 fs (-7.5 μm) and +50 fs (+7.5 μm) delay. Here the positions of the optical delay stage in micron are listed in parentheses. As the retroreflector folds the optical beam once, 1 μm change of the optical delay stage translates to approximately 6.6 fs delay.

To avoid the slow drift of time delays during the experiment, we ran one transient absorption measurement on the $2snp$ autoionizing states of helium after each scan through all time delay points on the nickel sample [24]. A typical transient absorption trace on the He $2snp$ autoionizing states is shown in Fig. 5.6(c). The transient absorption signal of the He $2s2p$ state near time zero was then fitted to an error function to determine the exact zero time overlap between the XUV and optical pulses. With the calibrated time zero of each scan, the changes of absorbance for each scan were then interpolated onto a gridline and averaged together [9]. A sample time zero drift trace over the course of an XUV TA measurement on nickel is shown in Fig. 5.7. Note that as the fluence dependence on the TA signal for the He autoionization lines is highly nonlinear [24], reliable TA measurements for time zero correction at fluences lower than 30 mJ/cm^2 have not been obtained. This leads to smearing and stretching of dynamics with respect to time delay for low fluence measurements. To estimate the amount of time-axis smearing in the observed dynamics (e.g. the rise of TA signal shown in Sec. 5.2.4) by the time zero drift, XUV TA measurements of He autoionization lines were conducted over the same amount of time as the acquisition time for the XUV TA experiments on nickel and we focus on the overall time delay drift over the entire measurement time. Specifically for the measurements displayed in Table 5.1, an overall time zero drift of 5 fs is obtained. This leads to an increase of negative uncertainty in the first two entries of

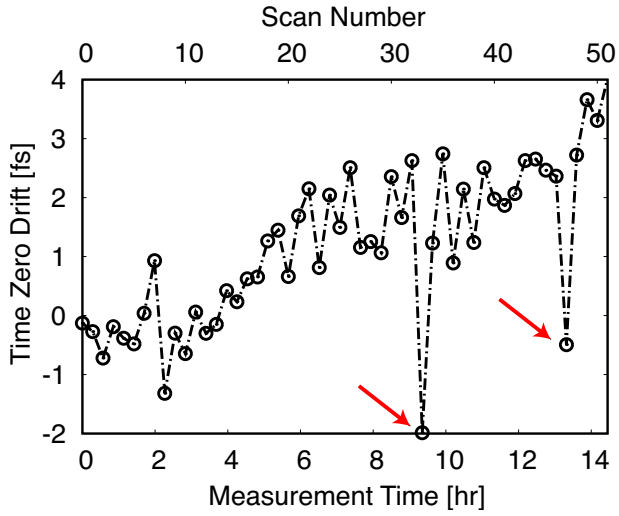

Figure 5.7: A sample time zero drift trace taken in an XUV TA experiment on nickel. The time zero is extracted from XUV TA measurements on He autoionization lines. The red arrows indicate the scans to be discarded from data analysis due to >3 fs drifts over a single scan.

τ_{rise} in Table 5.1.

5.B Sample Preparation

The nickel thin films used in this experiment were prepared by dual ion-beam deposition of 50 nm thick nickel onto 30 nm thick silicon nitride membranes with a free-standing window size of 3 mm × 3 mm [277], utilizing (neutralized) 600 eV krypton ions at a background pressure of 10^{-7} Pa. The layer thickness was controlled via the deposition time where typical sputter rates are below 0.1 nm per second and were calibrated using surface profilometry as well as *in situ* spectral ellipsometry. The sputter time calculations are based on a numerical model [277], to compensate both inter-diffusion losses and systematic deposition variations due to, for example, shutter response times. The substrate holder spun during deposition with a spinning frequency of 40 rpm and an R/θ shaper was used for shaping the particle flux laterally for a high lateral homogeneity film thickness growth. A film of 4 nm thick boron carbide was then deposited above the nickel thin film to prevent oxidation through exposure to ambient air.

5.C Estimating Electron Temperature Rise Due to Optical Absorption

The electron temperature rise after optical excitation of nickel at 40 fs time delay is calculated from the spectrum of the optical pulse (Fig. **??**(d)), the wavelength-dependent thin film absorbance, and

the electronic heat capacity of nickel. As the electron-phonon scattering time in nickel is a few hundred femtoseconds [251], the electronic cooling due to phonons is neglected in the following calculation. The energy absorbed by the nickel film at a specific wavelength λ can be described as $\mathcal{E}_{abs}(\lambda) = \frac{hc}{\lambda} N_{ph}(\lambda) f_{abs}(\lambda)$. Here $N_{ph}(\lambda)$ is the number of incident photons as a function of wavelength, which can be directly derived from the pump pulse spectrum. $f_{abs}(\lambda)$ is the fraction of light absorbed in the nickel film and is calculated using the transfer matrix method [198]. The value of wavelength-dependent complex refractive indices of nickel and silicon nitride are taken from Refs. [278] and [200], respectively. Denoting the electron heat capacity by $C_e(T)$, the estimated maximum electron temperature T_{est} is related to the total energy absorbed by the nickel film $\mathcal{E}$ as

$$\mathcal{E} = \int_{T_0=300K}^{T_{est}} C_e(T')dT',$$

where the temperature-dependent electron heat capacity of nickel is taken from Ref. [274]. The electron temperature rise ΔT_{est} is $T_{est} - T_0$.

5.D Expansion of $I'(t)$

The expression of the core-level absorption lineshape $I'(\omega)$ in Eq. (5.2) is the Fourier transform of its free-induction decay

$$I'(t) = \left(\frac{\pi T}{i \sinh(\pi T t)}\right)^{1-\zeta} = (-i\pi S(t,T))^{1-\zeta}. \tag{5.5}$$

To find $e^{g(t,\Delta T)}$ (cf. Eq. (5.4)), we first expand $S(t,T)$ with respect to temperature:

$$S(t, T+\Delta T) = S(t,T) + \partial_T S(t,T) \cdot \Delta T + \frac{1}{2}\partial_T^2 S(t,T) \cdot (\Delta T)^2 + \dots.$$

Letting $z = \pi t$, the derivatives of $S(t,T)$ are expressed

$$\begin{aligned}
\partial_T S(t,T) &= \frac{1}{\sinh(zT)} \left(1 - zT \coth(zT)\right) \\
\partial_T^2 S(t,T) &= \frac{T}{\sinh(zT)} \left(2\left(z^2 \coth^2(zT) - \frac{z\coth(zT)}{T}\right) - z^2\right).
\end{aligned}$$

Expressing the m^{th} Taylor expansion term of $S(t, T+\Delta T)$ as $\partial_T^m S(t,T)(\Delta T)^m/m! = s_m S(t,T)$, we can rewrite $S(t, T+\Delta T)$ as

$$S(t, T+\Delta T) = S(t,T) \exp\left(\ln\left(1 + \sum_{m=1}^{\infty} s_m\right)\right),$$

and by comparing the terms between the Taylor expansion of $S(t, T + \Delta T)$ and $\{s_m\}$, the second order expansion of $S(t, T + \Delta T)$ can be expressed as [279, 280]

$$S(t, T + \Delta T) \approx S(t, T) \exp\left(s_1 + s_2 - \frac{s_1^2}{2}\right). \tag{5.6}$$

Here we concentrate on the behavior of $S(t, T)$ when t is near zero because the denominator $\sinh(zt)$ in the integrand $I'(t)$ grows exponentially with t. This "short time" approximation can be further justified by comparing the temperature induced broadening and the natural linewidth of the core hole. While the temperature induced broadening is typically on the scale of tens to hundreds of meV (cf. Fig. 5.2(c)), the core hole lifetime broadening is typically larger by one order of magnitude [154, 256]. This indicates that the "true" free induction decay of the core-level transitions is far faster than the decay of $I'(t)$. Under such condition, we can approximate the term $\coth(zT)$ using the asymptotic relation $\coth x \approx 1/x + x/3 - x^3/45 + \ldots$ [281]. To first order with $\coth(zT) \approx 1/(zT)$, we obtain

$$\begin{aligned} s_1 &= \left(\frac{1}{T} - z\coth(zT)\right)\Delta T \approx 0 \\ s_2 &= \left(z^2\coth^2(zT) - \frac{z\coth(zT)}{T} - \frac{z^2}{2}\right)(\Delta T)^2 \\ &\approx -\frac{z^2}{2}(\Delta T)^2. \end{aligned}$$

Inserting the expansion terms back into Eq. (5.6), a preliminary expression for $S(t, T + \Delta T)$ is derived:

$$S(t, T + \Delta T) \approx S(t, T) \cdot \exp\left(-\frac{(\pi \Delta T t)^2}{2}\right),$$

and therefore

$$e^{g(t,\Delta T)} = \exp\left(-\frac{(\pi \Delta T t)^2}{2}\right).$$

To estimate the error of the approximated expression, we include the second and the third term of the asymptotic expansion ($\coth(zT) \approx 1/(zT) + zT/3 - (zT)^3/45$) and obtain

$$\begin{aligned} s_1 &= \left(\frac{1}{T} - z\coth(zT)\right)\Delta T \approx \left(-\frac{z^2T}{3} + \frac{z^4T^3}{45}\right)\Delta T \\ s_2 &= \left(z^2\coth^2(zT) - \frac{z\coth(zT)}{T} - \frac{z^2}{2}\right)(\Delta T)^2 \\ &\approx \left(-\frac{z^2}{2} + \frac{z^2}{3} + \frac{4z^4T^2}{45}\right)(\Delta T)^2. \end{aligned}$$

The expression $S(t, T + \Delta T)$ becomes

$$S(t, T + \Delta T) \approx S(t, T) \cdot \exp\left(-z^2\left(\frac{\Delta T^2 + 2T\Delta T}{6}\right)\right) \times \exp\left(z^4\left(\frac{T^3\Delta T}{45} + \frac{T^2(\Delta T)^2}{30}\right)\right).$$

Note that in the equations above, we only include the terms up to z^4 because in the region where $z = \pi t$ is near zero, the higher order terms can be neglected. The same reasoning also applies to leaving out the higher order terms in the asymptotic expansion of $\coth(zT)$ as higher order terms will lead to expressions of z^6 and above in $S(t, T + \Delta T)$. To explore the adequacy of the "short time" approximation, we compare the magnitude of the z^2 term to the z^4 term. Given the typical core hole lifetime broadening of ~1 eV [154], room temperature $T \approx 0.03$ eV, and an overestimated $\Delta T = 10000$ K ≈ 0.9 eV, the magnitude of the second order term is

$$\left(\frac{\pi\hbar}{1\text{ eV}}\right)^2 \frac{0.9^2 + 2 \cdot 0.9 \cdot 0.03}{6\hbar^2}(\text{eV})^2 \approx 1.42,$$

and the magnitude of the z^4 term is

$$\left(\frac{\pi\hbar}{1\text{ eV}}\right)^4 \left(\frac{0.9 \cdot 0.03^3}{45} + \frac{0.03^2 \cdot 0.9^2}{30}\right)(\frac{\text{eV}}{\hbar})^4 \approx 0.002.$$

The magnitude of the fourth order term is three orders of magnitude smaller than the second order term, indicating that the z^4 term can also be neglected, yielding

$$S(t, T + \Delta T) \approx S(t, T) \cdot \exp\left(-\frac{(\Delta T^2 + 2T\Delta T)(\pi t)^2}{6}\right). \tag{5.7}$$

Here we observe that the expression remains a Gaussian function with respect to t and there is no first order term with respect to t in the exponent. The Fourier transformed broadening factor in the spectral domain is proportional to $\sqrt{\Delta T^2 + 2T\Delta T}$. However, as the electron temperature change ΔT is at least 6 times larger than the temperature for the reference spectrum $T = T_0 = 300$ K in the measurements (Fig. 5.2(c)), the term $2T\Delta T$ is small compared to ΔT^2. This explains the linear relationship between the obtained spectral broadening and electron temperature. As a corollary on the comparison of terms with different orders of z, note that the terms in the expansion of $\{s_m\}$ always have the form $z^n T^k (\Delta T)^l$, with $n, k, l \geq 0$ and $k + l = n$. This indicates that the "short time" approximation, or the truncation at the second order holds as long as the electron temperature change ($k_B\Delta T$) and electron temperature ($k_B T$) are smaller than the core hole broadening.

Finally, we connect Eq. (5.7) with Eq. (5.4) and observe

$$\frac{\pi(T_0 + \Delta T)}{\sinh(\pi(T_0 + \Delta T)t)} \approx S(t, T_0) \times \exp\left(-\frac{\Delta T^2}{6}(\pi t)^2\right) \approx \frac{\pi T_0}{\sinh(\pi T_0 t)} \times e^{g(t,\Delta T)},$$

indicating $g(t,\Delta T) \approx \frac{(\pi\Delta T t)^2}{6}$. In the equation above, the term $2T\Delta T$ from Eq. (5.7) is ignored as $(\Delta T)^2 \gg 2T\Delta T$. The broadening function $f(\omega,\Delta T) = \frac{1}{2\pi}\int_{-\infty}^{\infty} e^{i\omega t} e^{(1-\zeta)g(t,\Delta T)} dt$ is thus

$$f(\omega,\Delta T) \approx \frac{1}{\sigma\sqrt{2\pi}} e^{-\frac{\omega^2}{2\sigma^2}},$$

with

$$\sigma = \pi\Delta T\sqrt{\frac{1-\zeta}{3}}.$$

Rewriting the equation in SI units, the broadening function reads

$$f(\hbar\omega,\Delta T) \approx \frac{1}{\sigma\sqrt{2\pi}} e^{-\frac{(\hbar\omega)^2}{2\sigma^2}},$$

and

$$\sigma = \pi k_B\Delta T\sqrt{\frac{1-\zeta}{3}} = a\Delta T.$$

Here $a = \pi k_B\sqrt{(1-\zeta)/3}$ and $\zeta < 1$ is a constant phase factor related to the electron scattering from the core hole potential (Eq. (5.2)).

5.E Fitting with Modified Gaussian Error Function

To fit the sub-20 femtosecond dynamics of $\sigma(t)$, $\omega_s(t)$, and the TA lineouts at 65.75 and 67.4 eV, a modified Gaussian error function

$$\mathcal{F}(t,\tau) = \frac{c_1}{2}\left(1 + \frac{2}{\sqrt{\pi}}\int_{t_0}^{t} e^{-\left(\frac{2\sqrt{\ln 2}(t'-t_0)}{\tilde{\tau}}\right)^2} dt'\right) + c_0 \tag{5.8}$$

is utilized, where t_0 marks the timing of the dynamics relative to zero time delay and $\tilde{\tau}$ the duration of the growth; c_0 and c_1 are fitting coefficients for offset and amplitude of the TA signal. The coefficient $2\sqrt{\ln 2}$ enables direct comparison between $\tilde{\tau}$ and the cross-correlation time between the pump and probe pulses. If the electronic response is instantaneous with respect to the excitation pulse, $\tilde{\tau}$ will be equal to the cross-correlation time.

5.F Simulation of Photoexcitation Dynamics

The dynamics of photoexcitation are simulated by the density matrix formalism based on the nickel band structure calculated by DFT, where the density matrix $\rho_{\mathbf{x}\mathbf{x}'}(t) = \langle c^\dagger_{\mathbf{x}}(t) c_{\mathbf{x}'}(t)\rangle$. c is the annihilation operator and $\mathbf{x} = \{\mathbf{k}, m, s\}$ denotes the combination of momentum $\mathbf{k}$, band index m, and spin index s. The Hamiltonian for the Liouville equation $\dot{\rho} = -i[H,\rho]/\hbar$ is

$$H = \sum_{\mathbf{x}} \mathcal{E}_{\mathbf{x}} c^\dagger_{\mathbf{x}} c_{\mathbf{x}} + \sum_{\mathbf{x},\mathbf{x}'} V_{\mathbf{x},\mathbf{x}'}(t) c^\dagger_{\mathbf{x}} c_{\mathbf{x}'},$$

where $\mathcal{E}$ denotes the band energy and

$$V_{\mathbf{x},\mathbf{x}'}(t) = -\mathbf{d}_{\mathbf{x},\mathbf{x}'} \cdot \mathbf{E}(t).$$

In the equation above, $\mathbf{d}$ is the dipole operator and the magnitude of the electric field $\mathbf{E}(t)$ is $E_0 \exp\left(-(2\sqrt{\ln 2}t/\tau_{pulse})^2\right)$. $E_0 = 2.5$ V/nm is derived from the peak intensity of the pulse and $\tau_{pulse} = 4.3$ fs. To obtain band energies $\mathcal{E}_\mathbf{x}$ and dipole operator $\mathbf{d}_{\mathbf{x},\mathbf{x}'}$, DFT calculations were performed using the Quantum ESPRESSO package with Perdew-Burke-Ernzerhof (PBE) exchange correlation functional and ultrasoft, scalar relativistic pseudopotential [130–132]. The simulation was conducted on a $15 \times 15 \times 15$ k-point meshgrid using the Monkhorst-Pack scheme [282], and converged with cutoff energy at 60 Ryd. The occupation number as a function of energy and time delay $O(\mathcal{E}, t)$ is calculated by summing the mapping of the diagonal terms of the density matrix onto an energy grid and subsequently dividing by the density of states:

$$O(\mathcal{E}, t) = \sum_\mathbf{x} w_\mathbf{x} \rho_{\mathbf{x}\mathbf{x}}(t) M(\mathcal{E}, \mathcal{E}_\mathbf{x}) / \sum_\mathbf{x} w_\mathbf{x} M(\mathcal{E}, \mathcal{E}_\mathbf{x}).$$

We use a Gaussian mapping function $M(\mathcal{E}, \mathcal{E}_\mathbf{x}) = \exp(-((\mathcal{E} - \mathcal{E}_\mathbf{x})/\delta\mathcal{E})^2)$ with width $\delta\mathcal{E} = 0.1$ eV. $w_\mathbf{x}$ is the weighting coefficient within the Monkhorst-Pack scheme at point $\mathbf{k}$.

Chapter 6

Perturbation of Core-Exciton States in NaCl by Optical Pulses

6.1 Introduction

Many-body interactions play an important role in the optical excitations of solids that have poor electronic screening. For example, in insulators and mono- or few-layer two-dimensional semiconductors [283, 284], the optical spectra can no longer be described by direct band-to-band transitions in the mean-field picture. Instead, the absorption onset is dominated by discrete transitions termed "excitons", which are formed due to the attraction of the excited electron in the conduction band (CB) and the valence band (VB). In core-level spectroscopy, electronic many-body interactions also contribute to the fine structure and the formation of core-excitons in the X-ray absorption spectra observed in various insulators [143–153]. It has been predicted that the electron-core-hole attraction of core-excitons can stabilize those transitions and grant them longer lifetimes compared to direct core-to-conduction band transitions [148], which has been experimentally observed in WS_2 as shown in Chapter 4. The population decay of core-level transitions in the <200 eV energy range is dominated by Auger processes [12]. Recently, Moulet et al. utilized attosecond transient absorption spectroscopy (ATAS) to observe the polarization decay of core-excitons in SiO_2 [31]. Géneaux et al. and Lucchini et al. measured the sub-5 fs decay of core-excitons in MgO and MgF_2, respectively [32, 33]. Despite their different composition, the decoherence of core-exciton transitions in the three materials is unanimously dominated by phonon-induced dephasing. The strong exciton-phonon coupling between the core-exciton and the longitudinal optical (LO) phonons in SiO_2, MgO, and MgF_2 enables the excitation of a large number of vibronic states in the core-level transition. Before the core-exciton transitions decay through Auger processes, destructive interference of the collectively excited vibrational wavefunctions causes the transition dipole of core-level excitations to diminish to zero [185] and imposes a Gaussian broadening on the core-exciton absorption spectra.

Strong coupling to the LO phonons is ubiquitous among the core-level excitations in alkali halides [285], leading to a 0.2-1 eV Gaussian broadening of their X-ray photoemission spectra,

which is much larger than the <0.1 eV intrinsic Auger linewidth of alkali metals [286]. The strong coupling to LO phonons originates from the highly polar chemical bonds between the alkali cation and the halide anion. When a core-electron is ejected by X-rays from the ionic solid, the core hole attracts the surrounding halide anions, leading to lattice deformation. By analogy, photoexcitation of core electrons to the conduction band has a similar effect, which was observed in the studies on SiO_2, MgO, and MgF_2. However, as the electron-phonon coupling originates from the change of electron density and its interaction with the lattice, the electron phonon coupling should strongly depend on the degree of localization of core-exciton wavefunctions. In addition, as the excitation energy increases from core-exciton transitions below the conduction band threshold to those states embedded within the CB, the intrinsic lifetime of the core-exciton states should vary with the different degree of coupling to the continuum states. In SiO_2, MgO, and MgF_2, observation of the variation of core-exciton lifetime with energy is difficult due to the relatively small energy window of the core-exciton states (5-10 eV) and the subfemtosecond lifetime of the core-excitons. Here, we report the observation of changes in core-exciton coherence lifetimes from >10 fs to <5 fs at the Na $L_{2,3}$edges (30-50 eV) in NaCl using attosecond transient absorption spectroscopy.

6.2 Experimental Scheme

The experimental apparatus is detailed in Chapter 2. In brief, 120 nm thick NaCl films on 50 nm thick silicon nitride windows (Norcada Inc.) were prepared with electron beam deposition (Lebow Company). Core electrons in the Na $2p$ shell were excited by a broadband XUV pulse produced by high harmonic generation in a Kr gas jet. The transition dipole of the core-level excitations was subsequently perturbed by a time-delayed broadband optical pulse (500-1000 nm) with nominal duration of 4 fs. The mechanical beam chopper was not used in this experiment as the sample is largely transparent to the optical beam. The change of absorbance $\Delta A(t)$ at time delay t is defined as $\Delta A(t) = A(t) - A(t = -30\text{ fs})$. Here the time delay t is defined as the difference between the arrival time of the optical pulse and the XUV pulse. In contrast to the previous chapters, here positive t indicates that the XUV pulse precedes the optical pulse.

6.3 Results and Discussion

The static absorption spectrum of the NaCl thin film at the Na $L_{2,3}$ edge is shown in Fig. 6.1(a). Instead of a smooth absorption edge as those observed in semiconductors such as 2H-$MoTe_2$ (Chapter 3), the absorption spectrum exhibits a series of discrete absorption peaks spanning 30-48 eV photon energies. Clearly, the core-level absorption profile cannot be described by direct core-level-to-CB transitions in the single particle picture, and electron-core-hole attraction, or the core-excitonic effect, must be taken into account. In addition to forming strong, discrete core-exciton absorption peaks at the low-energy end of the spectrum (~33 eV), many-body electron-hole interactions renormalize the whole absorption spectrum, which is observed at the W $N_{6,7}$ edge in WS_2 (Chapter 4). Instead of exhibiting a smooth rise of absorbance above the discrete core-

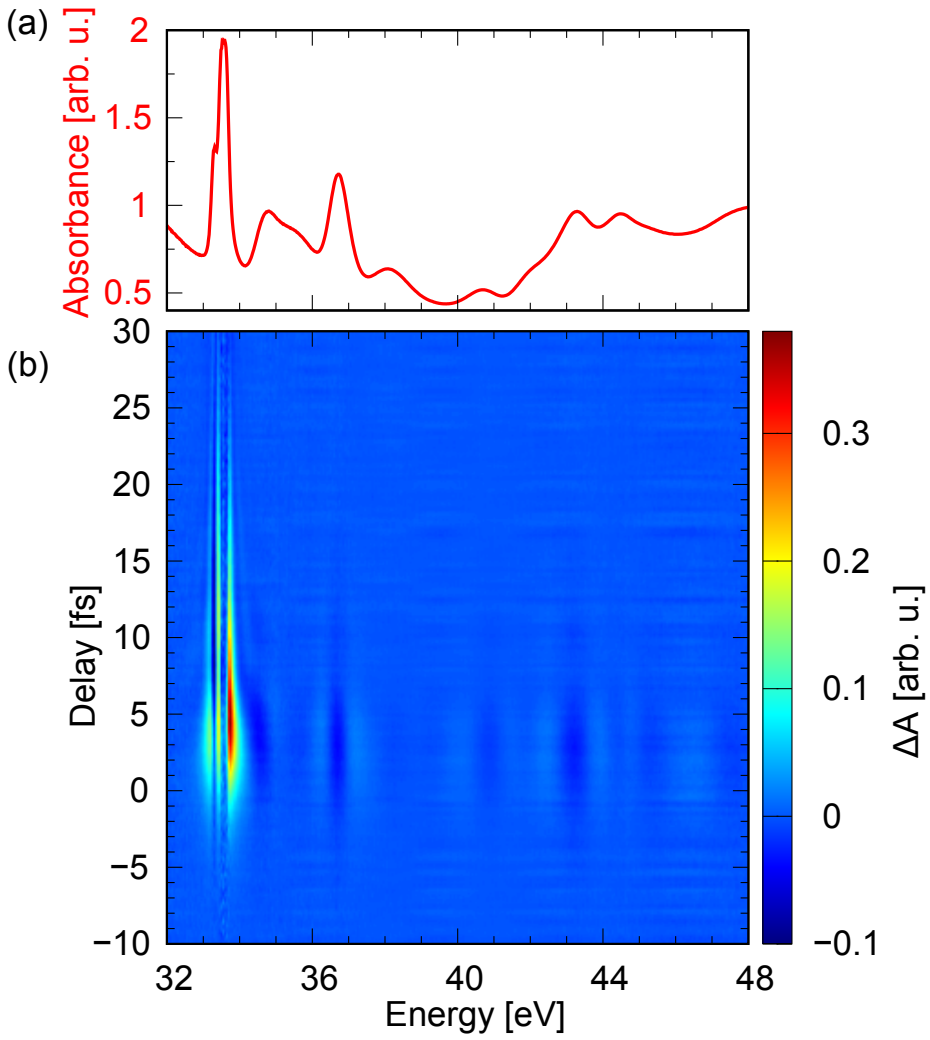

Figure 6.1: (a) Static absorption spectrum (b) XUV transient absorption spectra of the NaCl thin film at the Na $L_{2,3}$ edge.

exciton transitions at ~33 eV similar to the optical absorption spectrum of many semiconductors [284], discrete transitions are observed up to >10 eV above the lowest-energy core-exciton peak, indicating that many-body effects not only affect the transitions between the core-level and low-lying conduction bands but are also important for transitions well above the band edge.

The core-exciton transitions spanning across a >10 eV range and including states below and above the conduction band edge provide an excellent opportunity to investigate the relation between core-exciton lifetimes and the properties of their wavefunctions. XUV transient absorption spectra at the Na $L_{2,3}$ edge are shown in Fig. 6.1(b). Intense transient absorption features are observed at the low-energy core-exciton transitions at ~33 eV along with smaller absorption changes between

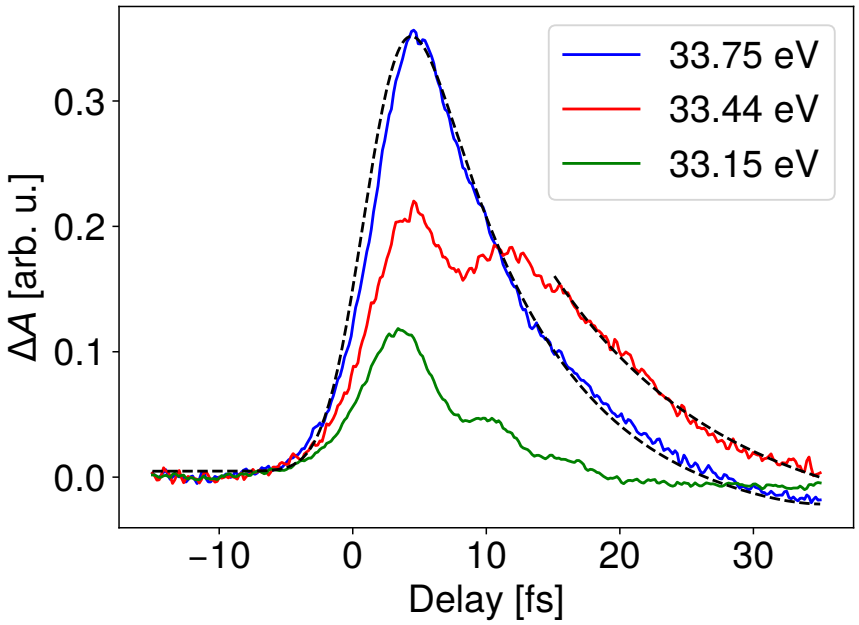

Figure 6.2: Lineouts of XUV transient absorption feature at 33.15 eV, 33.44 eV, and 33.75 eV. The fitting of the feature at 33.75 eV with an exponential decay convoluted by a Gaussian and the fitting of the feature at 33.44 eV with a single exponential decay are shown in black dashed lines.

36-48 eV near zero delay time. While transient absorption features can still be observed up to >20 fs delay at 33 eV, transient absorption signals at > 36 eV are close to zero at >10 fs time delays.

To further illustrate the difference between the decay of the transition dipole of the core-excitons, lineouts of transient absorption features at ~33 eV and ~37 eV are plotted in Figs. 6.2 and 6.3, respectively. In Fig. 6.2, the lineout at 33.75 eV can be fitted with a single exponential decay convoluted with a Gaussian instrument response function. The fitted exponential decay time is 8.9 ± 0.2 fs. The lineouts at 33.15 eV and 33.44 eV exhibit an oscillating profile between 0-15 fs delay. After 15 fs, the lineouts present a monotonic decay and the decay of the lineout at 33.44 eV can be fitted with a single exponential with a decay constant of 13.0 ± 0.6 fs. This indicates a coherence lifetime of core-exciton states at ~33 eV at approximately 10 fs and an estimated linewidth of the core-exciton absorption of approximately 0.06 eV. In addition, as phonon-induced dephasing typically leads to a Gaussian decay of the free induction decay (FID) profile [185, 287], the clear exponential decay of the lineouts suggest that phonon-induced dephasing is not the main contributor for the decoherence of core-exciton transitions at ~33 eV.

In contrast to the lineouts at ~33 eV, XUV transient absorption features at >36 eV decay within 10 fs time delay. In Fig. 6.3, the integrated region $|\Delta A(E,t)|$ between 37.1-37.6 eV (blue line) is fitted with an exponential decay (black solid line) and a Gaussian decay (black dashed line). Both decay functions are convoluted with a Gaussian instrument response function and the measured lineout (blue line) is fitted equally well with the exponential and Gaussian decay. The fitted time constant

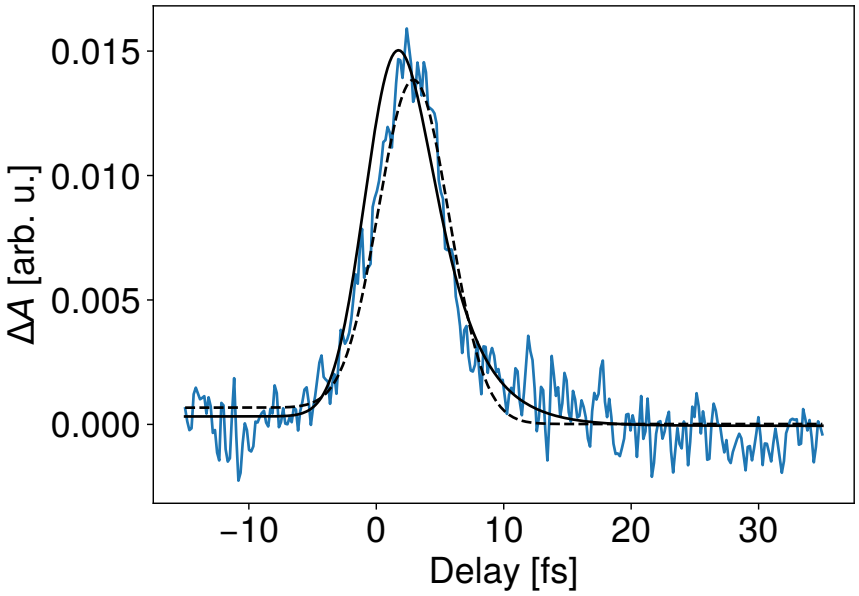

Figure 6.3: Averaged absolute value of XUV transient absorption feature between 37.1-37.6 eV (blue line). Fitting of the lineout with exponential and Gaussian decay convoluted with a Gaussian function are shown in a black and a black dashed line, respectively.

$(1/e)$ for the exponential and Gaussian decays are 3 fs and 1 fs, repectively. This suggests that the coherence lifetime of the core-exciton transition is well within the duration of the optical pulse and phonon dephasing may contribute to the decoherence of the core-exciton transition dipoles in this energy region. The XUV transient absorption profile at energies >37.6 eV exhibits similar behavior as the lineout shown in Fig. 6.3. The drastic difference between coherence lifetimes of transitions below and above 36 eV indicates a distinction between their electronic properties.

By comparing the Na $L_{2,3}$ edge absorption spectra with the optical absorption spectra of NaCl, Nakai and Sagawa assigned the onset of the core-to-conduction band edge transition at approximately 34 eV [176]. Further theoretical investigation by Pantelides suggested the onset of the core-to-conduction band edge transition at 36 eV [288–290], which is supported by Auger electron spectroscopy measurements conducted by Kamada et al. [291]. Despite the difference in their assignments, those studies unanimously indicate that the core-excitonic absorption features above 36 eV, which give rise to the transient absorption signal in Fig. 6.3, are embedded in the core-to-conduction band continuum transitions. The embedding within the core-to-conduction band continuum transitions may lead to additional decay channels that shorten the Auger lifetime of the core-excitonic transitions. In addition, the electronic wavefunctions of transitions above the core-to-conduction band onset may be more diffuse, which exposes the core hole on the Na atom and induces stronger electron-phonon coupling between the core-hole and the lattice.

Core-excitons below the core-to-conduction band edge onset

In this section, we focus on the core-excitons at ~33 eV below the core-to-conduction band onset. The oscillations shown in the lineouts of XUV transient absorption signal in this energy region suggest that the optical pulse may coherently couple the bright core-exciton states through a high-lying state or the continuum. To understand the observed transient absorption signal, we first identify the bright core-exciton states by fitting the static absorption spectrum in this energy region. The magnified static absorption spectrum and XUV transient absorption signal are shown in Fig. 6.4. To fit the static absorption spectrum, the absorption background from valence shell excitations is first subtracted by fitting the pre-edge absorption feature between 30-32 eV with a Gaussian function (Fig. 6.5). The transient absorption signal is concentrated within the 32.8-34 eV energy region, where the static spectrum exhibits two peaks labeled as A and B (Fig. 6.4(a)).

In a temperature-dependent XUV absorption experiment, Nakai et al. discovered that the spectral profile of transition A and B changes from Gaussian to Lorentzian when the temperature of the sample is lowered from room temperature to liquid nitrogen temperature [292]. The temperature dependent change in line profile indicates the presence of phonon broadening. When electron-phonon coupling is strong, the absorption lineshape becomes Gaussian and the Franck-Condon linewidth is proportional to the factor $\sqrt{\coth(\beta\omega/2)}$, where $\beta = 1/(k_B T)$ and ω is the phonon frequency. With the presence of phonon-induced broadening at room temperature, we fit the peaks A and B with two Voigt profiles expressed as

$$I(E) = \sum_{i=A,B} \int dE' \, \exp\left(-\frac{(E - E_i - E')^2}{2\Gamma_{G,i}^2}\right) \frac{\Gamma_{L,i}}{(E' - E_i)^2 + \Gamma_{L,i}^2}. \tag{6.1}$$

Here E_i is the energy of the i^{th} transition; Γ_G and Γ_L denotes the Gaussian and Lorentzian linewidth, respectively. The Gaussian linewidth is related to the phonon broadening and the Lorentzian linewidth is the natural linewidth due to Auger decay of the core-exciton.

The background-subtracted experimental spectrum and the fitted result are shown in Fig. 6.6(b). The necessity of including the Gaussian phonon broadening is illustrated by comparing against the fitting of the experimental data with two Lorentzian functions ($\Gamma_G = 0$, Fig. 6.6(a)). The fitting with two Lorentzian functions cannot fully reproduce the profile at peak B (~33.5 eV). The fitted transition energy (E_i) and linewidths (Γ_G and Γ_L) are listed in Table 6.1. For peak A, the Gaussian linewidth (0.08 eV) is much larger than the Lorentzian linewidth (0.02 eV). The 0.08 eV Gaussian width corresponds to a characteristic decay time of 8.2 fs. For peak B, the Lorentzian linewidth (0.1 eV) leads to a characteristic exponential decay time of 7 fs. The timescales of the decay of core-exciton transition dipoles derived from the fitted linewidths are shorter than the >10 fs decay dynamics observed through XUV transient absorption spectroscopy. This discrepancy indicates that there might be significant static disorder or more than two bright core-exciton transitions within the energy region. In addition, the fitted spectrum (Fig. 6.6(b)) has a visible discrepancy at the peak of transition B (~33.4 eV). As static disorder can typically be accounted for by a Gaussian broadening, which is already present in Eq. (6.1), this also points to the possibility of hidden bright states within peak A and B.

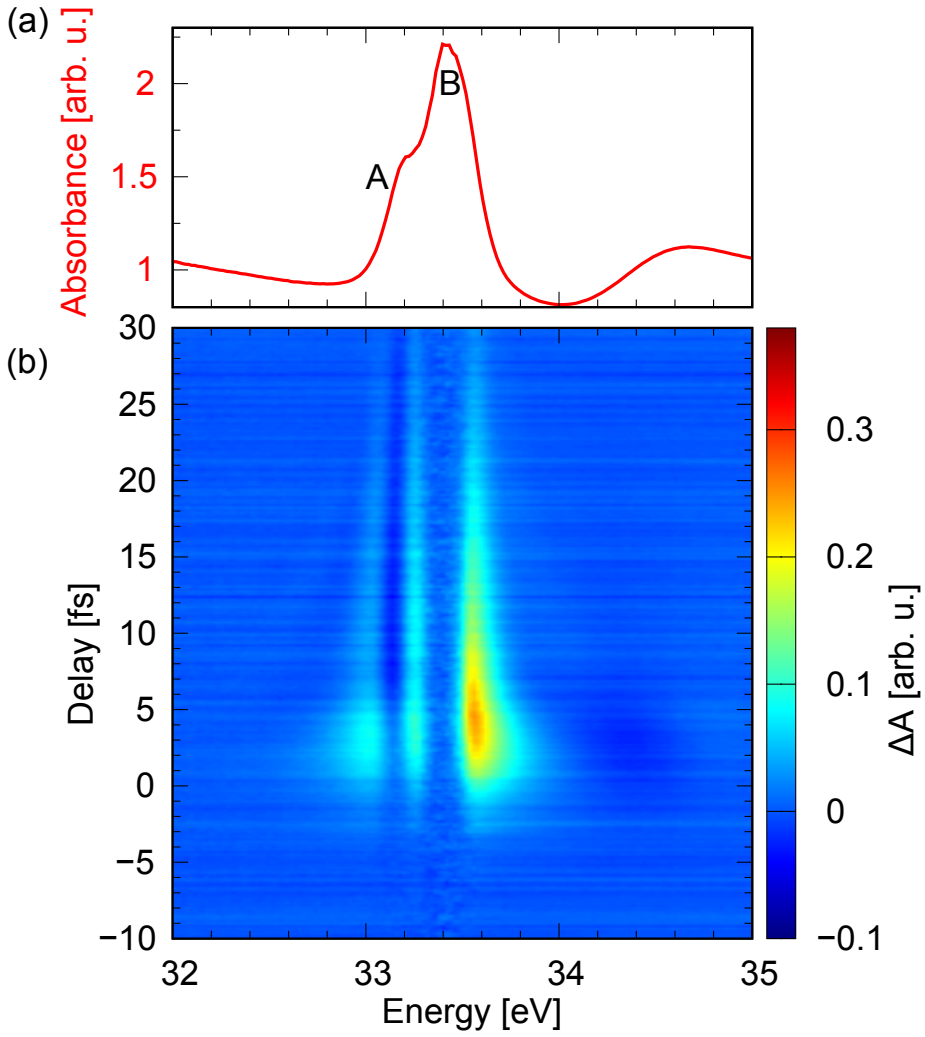

Figure 6.4: (a) Static absorption spectrum (b) XUV transient absorption spectra of the NaCl thin film at the Na $L_{2,3}$ edge below the core-to-conduction band onset.

Table 6.1: The fitted parameters of Eq. (6.1) (cf. Fig. 6.6(b)).

	E (eV)	Γ_L (eV)	Γ_G (eV)
A	33.18 ± 0.05	0.02 ± 0.01	0.08 ± 0.01
B	33.44 ± 0.05	0.10 ± 0.01	0.08 ± 0.01

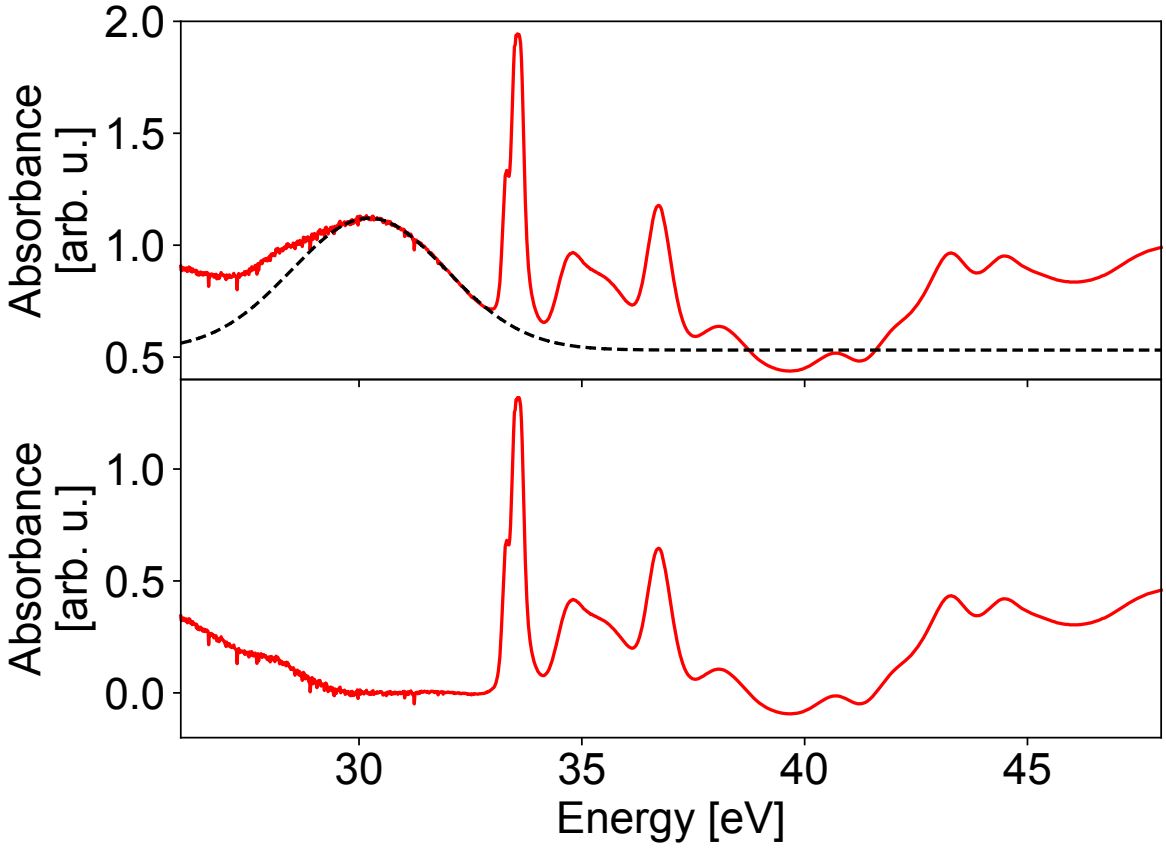

Figure 6.5: Measured (upper panel) and background subtracted (lower panel) static absorption spectrum. The fitted Gaussian function for the background is shown as a dashed black line.

The properties of core-exciton transitions in peaks A and B have been discussed in the studies by Overhauser, Nakai et al. and Tomita et al. [176, 293, 294]. Using the symmetry at the Γ point in the Brillouin zone at the conduction band minimum, Overhauser derived a 5-state multiplet Hamiltonian for the lowest lying optical excitons of NaCl. Extending the studies of optical excitons by Onodera and Toyozawa [295], Nakai and Sagawa concluded that the splitting between peaks A and B is due to spin-orbit coupling [176], which is corroborated by a first principles calculation conducted by Tomita et al. [294]. Recent attosecond four-wave mixing experiments on NaCl at the Na $L_{2,3}$ edges suggest that there are at least 5 bright states contributing to the absorption peak A and B [296]. Here we conduct Bethe-Salpeter equation (BSE) simulations [175] based on the wavefunctions of density functional theory (DFT) calculations using the linearized augmented plane-wave method (the Elk code [174]) to determine the number of states buried within peaks A and B. The DFT calculations were carried out on a $5 \times 5 \times 5$ k-point grid under the local spin density approximation [197]. Spin-orbit coupling effects are included. The BSE calculation includes 16 occupied and 16 unoccupied bands (spin-resolved) and 28 empty bands are included

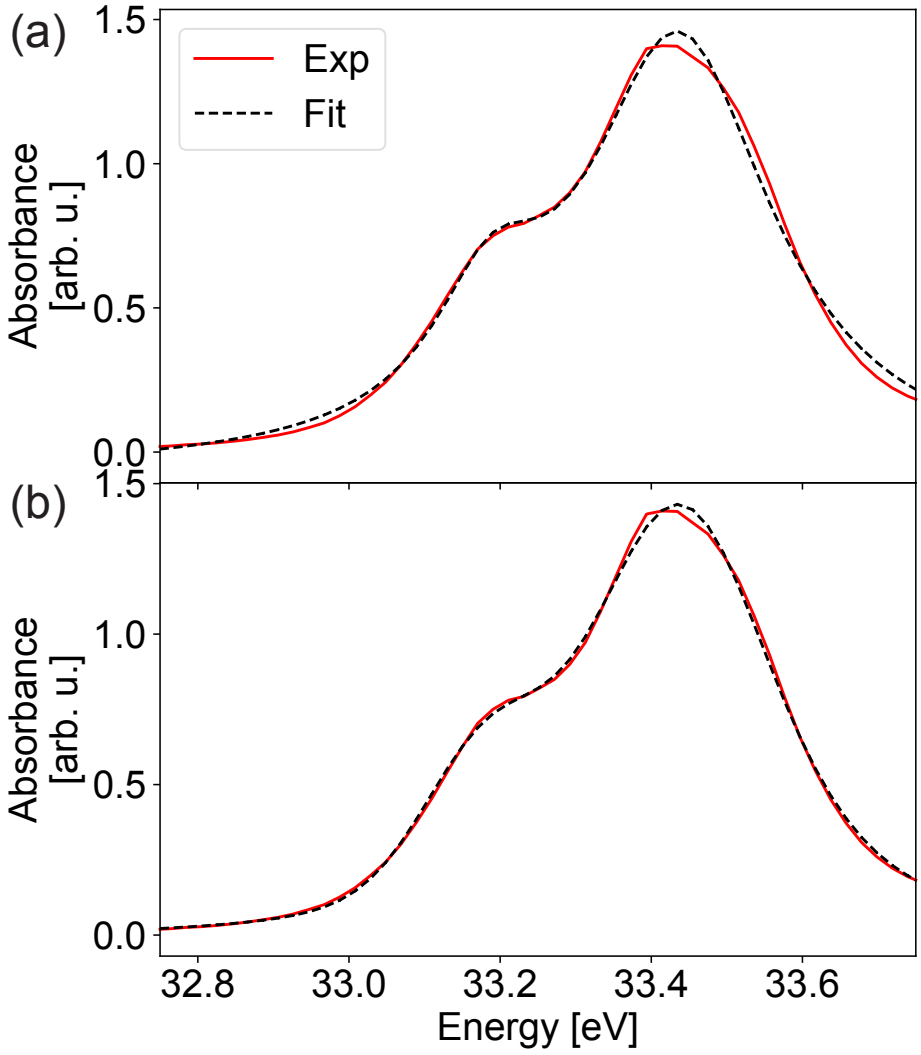

Figure 6.6: Fitting of measured static absorption spectrum of NaCl at the Na $L_{2,3}$ edge with (a) two Lorentzian functions and (b) two Voigt functions.

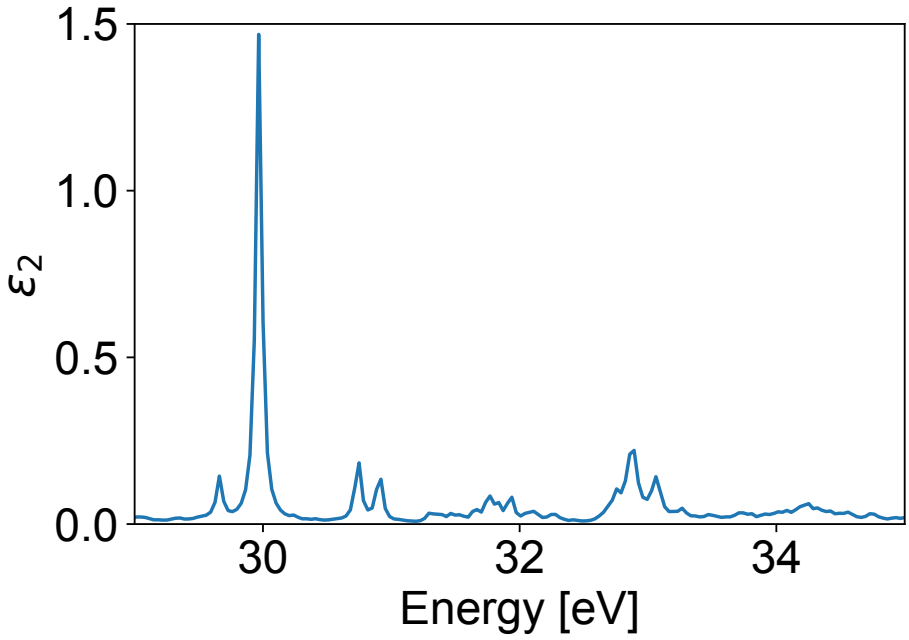

Figure 6.7: Absorption spectrum of NaCl at the Na $L_{2,3}$ edge with the BSE method. ϵ_2 denotes the imaginary part of the dielectric function including many-body interactions.

in the dielectric function calculation under the random phase approximation.

The simulated XUV absorption spectra of NaCl at the Na $L_{2,3}$ edge is plotted in Fig. 6.7. The simulated main absorption peak is located at 30 eV, 3 eV below the experimentally measured peak B. This is due to the underestimation of energy gap between the core-level and the conduction bands. The discrepancy can be remediated by introducing correction of band energies using the GW approximation [297, 298].[1] Despite the overall underestimation of transition energies, the spectral profile between 29-30.5 eV qualitatively reproduces the measured static absorption (peaks A and B, Fig. 6.4(a)). The simulated spectrum is also consistent with the calculation results obtained by Tomita et al. [294]. Although the low energy end of the simulated spectral lineshape agrees qualitatively with the measured spectrum, the high energy part of the spectrum (>30.5 eV) fails to reproduce the spectral features measured experimentally (Fig. 6.1). This can be due to an insufficient number of included empty bands[2] and the inaccuracy in the band energies, which can be corrected by GW approximation calculations. Below we list the states responsible for the low-lying core-exciton transitions near 30 eV.

Figure 6.8 depicts the averaged oscillator strength over all optical axes of the core-exciton states and their corresponding transition energies. The bright core-exciton states with nonzero oscillator strengths are clustered at 29.7 eV and 30 eV transition energy, corresponding to experimentally

[1] GW correction is not introduced in the calculation here due to the computational cost.

[2] The number of bands included is also limited by the computational capacity.

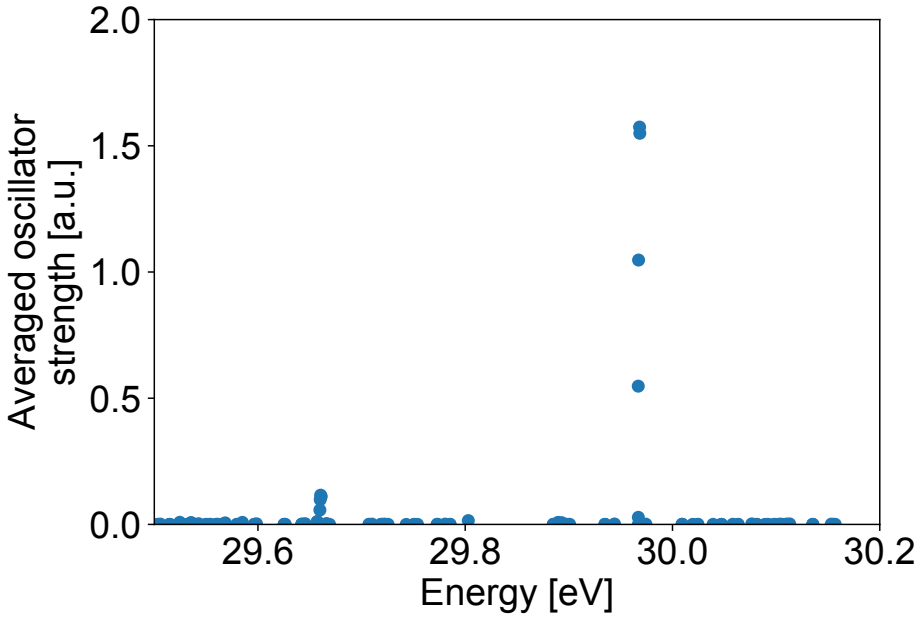

Figure 6.8: Energy and averaged oscillator strength over all optical axes of core-exciton states.

Table 6.2: Simulated bright core-exciton states in peak A and their averaged oscillator strengths in atomic units.

Energy [eV]	Oscillator strength [a.u.]
29.659762	0.056989
29.660107	0.098004
29.660501	0.115870
29.661047	0.110537

measured peaks A and B, respectively. Comparing the simulated oscillator strength of the core-exciton states and the experimentally measured spectrum, both peaks A and B consist of multiple core-exciton states. The energies and oscillator strengths of the core-exciton states corresponding to peaks A and B are listed in Table 6.2 and 6.3, respectively. The separation between the simulated transition energies for the bright core-exciton states within each peak is less than 0.01 eV, which prevents distinguishing the states in the fitting of the measured static spectrum.

6.4 Future Work

To understand the XUV transient absorption signal at peaks A and B (Fig. 6.4), time-dependent Schrödinger equation (TDSE) calculations including the bright core-exciton states and the dark core-

Table 6.3: Simulated bright core-exciton states in peak B and their averaged oscillator strengths in atomic units.

Energy [eV]	Oscillator strength [a.u.]
29.966965	0.547731
29.967267	1.047360
29.968231	1.574180
29.968459	1.549591

exciton states that can be optically coupled need to be conducted. The couplings between the bright and dark core-exciton states have to be obtained from the simulated core-exciton wavefunctions. In the appendix of this chapter, a pioneer study on the XUV transient absorption spectra of Na^+ containing MoS_2 sample is detailed, including the TDSE simulations of XUV transient absorption spectra.

6.A XUV Transient Absorption Study on Na^+ containing MoS_2

The study of core-exciton dynamics in NaCl is inspired from the XUV transient absorption results of a Na^+ containing MoS_2 samples. The samples were prepared by drop-casting diluted water solution of intercalated MoS_2 on a 30 nm thick silicon nitride membrane. The static absorption spectrum of the sample is shown in Fig. 6.9(b). Compared to the samples prepared by atomic layer deposition and drop-casting undiluted intercalated MoS_2 solution (Fig. 6.9(a)) and chemical vapor deposition (Fig. 6.9(c)), discrete peaks emerge around 33 eV and the smooth rise of the Mo $N_{2,3}$ edge absorption is absent. X-ray photoelectron spectroscopy measurement on the samples show a significantly enhanced Na L edge absorption for the sample prepared by drop-casting diluted water solution of intercalated MoS_2, indicating the presence of Na^+ ionic compounds in the solution. Comparison of the spectrum in Fig. 6.9(b) with the measured absorption spectra of sodium halides show that the spectrum is consistent with the Na $L_{2,3}$ edge absorption of NaI [176].

The main core-exciton peaks of the sample around 33 eV (Fig. 6.9(b)) can be fitted by a Lorentzian profile and 3 Fano profiles [173], labeled as A, B, C, and E, and shown in Fig. 6.10. The fitted energies, linewidths, and Fano q-factors of the transitions are listed in Table 6.4. The measured XUV transient absorption spectra for those transitions are displayed in Fig. 6.10(a). Lineouts of XUV transient absorption at 32.8 eV, 32.9 eV, 33.0 eV, and 33.3 eV are plotted in Fig. 6.10(d). Oscillatory features in the lineouts suggest the existence of a dark state that is mutually coupled to at least two of the bright core-exciton states. To understand the XUV transient absorption spectra, we simulate the optically induced dynamics of core-excitons with a time-dependent Schrödinger equation, which includes 7 states: the three major bright states A-C, a mutually coupled dark state M, and three dark states D_i ($i = A, B, C$) that are individually coupled to state i to represent the dissociation of the core-exciton induced by optical coupling to the ionization continuum (Fig. 6.11(c)).

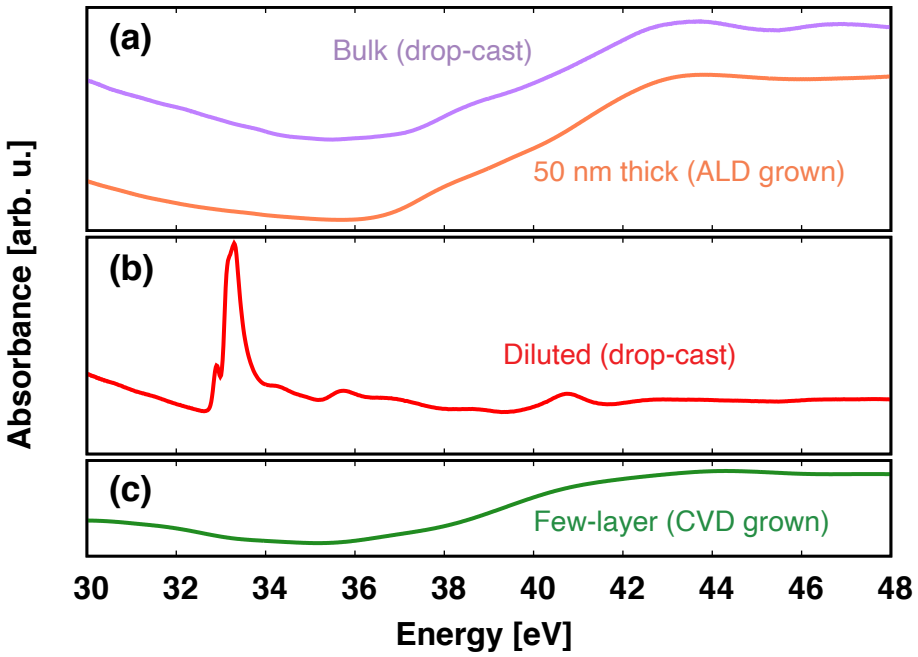

Figure 6.9: Static absorption spectrum of MoS_2 between 30-48 eV with different sample preparation methods (ALD: atomic layer deposition; CVD: chemical vapor deposition) and thickness. A smooth rise of the Mo $N_{2,3}$ edge absorption starting at 36 eV is observed in (a) and (c).

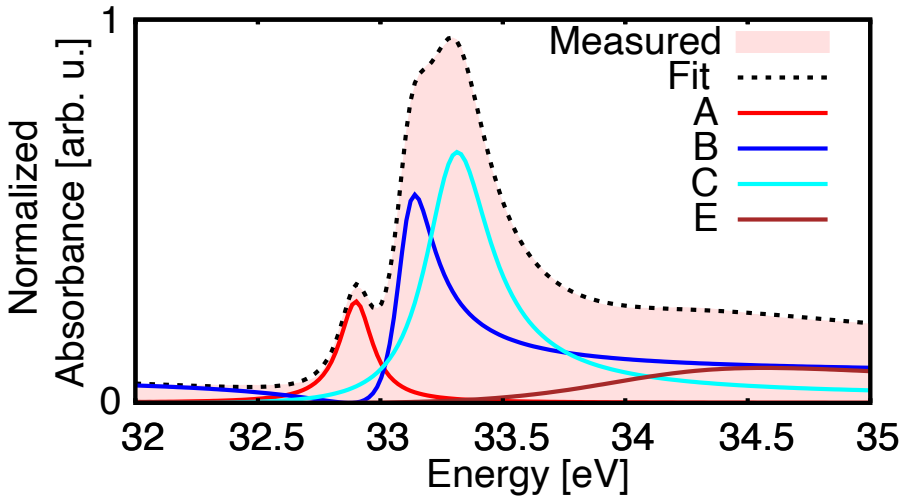

Figure 6.10: Fitting of the static absorption spectrum after background subtraction.

Table 6.4: Fitted transition energies, linewidths, and Fano q-factors of transitions A, B, C, and E.

Transition	A	B	C	E
Energy [eV]	32.90 ± 0.04	33.10 ± 0.04	33.29 ± 0.04	34.09 ± 0.06
Linewidth [eV]	0.16 ± 0.04	0.18 ± 0.04	0.32 ± 0.04	1.62 ± 0.08
Fano q-factor	N/A (Lorentzian)	2.53 ± 0.03	7.56 ± 0.01	1.68 ± 0.09

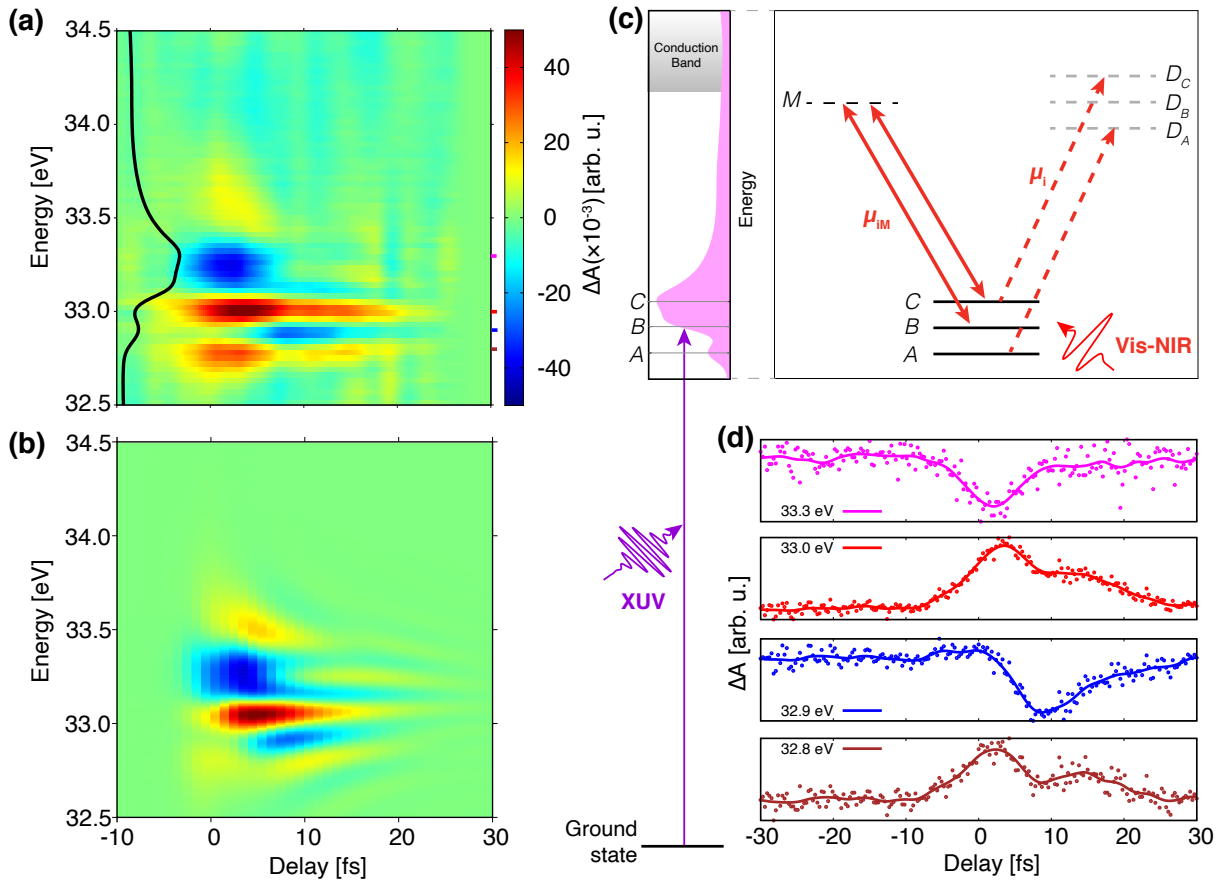

Figure 6.11: (a) Measured and (b) simulated XUV transient absorption spectra at the Na $L_{2,3}$ edge. The black line is the static absorption spectrum and ΔA denotes change of absorbance. (c) Model for simulating the dynamics of states A, B, and C induced by the optical pulse using a TDSE approach (see main text). (d) Lineouts of the change of absorbance (ΔA) at different XUV photon energies.

The Hamiltonian for the 7-state model for the TDSE simulation can be written as

$$H = E_M|M\rangle\langle M| + \sum_{i=A,B,C}\{|i\rangle H_0^i\langle i| + E_i^D|D_i\rangle\langle D_i| - [(\mu_i|i\rangle\langle D_i| + \mu_i M|i\rangle\langle M|) + h.c.]F_{opt}(\tau)$$
$$= H_0 + V(\tau),$$

where the optical laser field $F_{opt}(\tau) = A\exp(-((t-\tau)/\tau_0)^2)\cos(\omega(t-\tau))$, with τ denoting the time delay between the XUV and optical pulse. The pulse duration τ_0 and the field strength A are set to the experimental values. The central frequency of the pulse is set to 1.7 eV according to the spectrum of the optical pulse (Fig. S7A). H_0^i marks the Hamiltonian for the i^{th} isolated bright state and the energies of states $|D_i\rangle$ are set to be $E_i^D = \hbar\omega_i + 1.7$ eV. The state $|M\rangle$ is set to be resonantly coupled to the three bright states, covered within the bandwidth of the optical pulse, and here we set $E_M = \hbar\omega_B + 1.7$ eV. The energy of state $|M\rangle$, E_M, has been tested, ranging between $\hbar\omega_B + 1.4$ eV and $\hbar\omega_B + 2.0$ eV, during the fitting of dipole couplings μ_i's and μ_{iM}'s, and no qualitative difference in the fitting results was observed, implying that the laser-induced population transfer is only influenced by the energy difference between the bright states (A, B, C) as long as the high-energy state M can be resonantly coupled to the bright states. With the addition of the electronic ground state and the XUV excitation pulse, the total Hamiltonian is

$$H_{tot} = E_g|g\rangle\langle g| + H + \sum_{(i=A,B,C)}(\mu_{ig}|g\rangle\langle i| + h.c.)F_{XUV}(t)$$
$$= E_g|g\rangle\langle g| + H(\tau) - \mu_{XUV}F_{XUV}(t).$$

The lineshape of core-level excitations $S(\omega)$ can be calculated from the Fourier transformed dipole correlation function $\langle\mu_{XUV}(t)\mu_{XUV}\rangle$ [7]:

$$S(\omega) = Re[\int_0^\infty dt e^{i\omega t}\langle\mu_{XUV}(t)\mu_{XUV}\rangle],$$

and

$$\langle\mu_{XUV}(t)\mu_{XUV}\rangle = e^{((iE_g t)/\hbar)}\sum_{(i,j=A,B,C)}\langle i|e^{(-iH(\tau)t/\hbar)}|j\rangle\mu_i^*\mu_j.$$

To evaluate the dipole correlation function, we first consider the condition without the optical pulse that couples the bright states to the high energy states ($F_{opt} = 0$). Here, the dipole correlation function for state i can be written as [25]:

$$\langle i|e^{(-iH(F_{opt}=0)t/\hbar)}|i\rangle_0 = c_i^0\delta(t) + c_i\exp(-i(\omega_i t - \phi_i) - (\Gamma_i t)/2) = S_0^i(t),$$

where ω_i is the transition energy of the transition, c_i^0 marks the contribution from the continuum states and goes to zero when the lineshape is Lorentzian and 1 for Fano profile, c_i is also influenced by the degree of configuration interaction with the continuum and is unity for Lorentzian lines and becomes $1 + q_i^2$ for Fano lineshape. Γ_i is the population decay rate for the transition, and ϕ_i is the phase shift of the oscillator, which is related to the Fano q-factor by $q_i = -\cot(\phi_i/2)$. All

parameters in the zeroth order dipole correlation function above are obtained from nonlinear fitting of the static absorption spectrum (Fig. 6.10). With the application of the optical pulse, the dipole correlation function can be expanded in the interaction picture:

$$\langle i|e^{(-iH(\tau)t/\hbar)}|j\rangle = \langle i|e^{(-(iH_0t)/\hbar)}(1+\sum_{k=1}(-i)^k\int_0^t dt_1\int_0^{t_1}dt_2\ldots\int_0^{t_{k-1}}dt_k\prod_{n=1}^{k}V(\tau,t_n))|j\rangle,$$

with $V(\tau,t_n)=\exp((iH_0t_n)/\hbar)V(\tau)\exp(-(iH_0t_n)/\hbar)$.

The core-excited state wavefunction $|j(t)\rangle$ at a given time t cannot be directly calculated by propagating the time-dependent Schrödinger equation due to the contribution from continuum states implicitly taken into the Hamiltonian for the Fano profiles. However, the full dipole correlation function can be simplified via the analytical zeroth order expression. Taking one of the second order terms as an example:

$$\langle i|\exp(-(iH_0(t-t_1))/\hbar)|i\rangle\langle M|\exp(-(iH_0t_1)/\hbar))\exp((iH_0t_2)/\hbar)|M\rangle\times$$
$$\langle j|\exp(-(iH_0t_2)/\hbar)|j\rangle = S_0^i(t_1)S_0^j(t_2)e^{-i\omega_M(t_2-t_1)}.$$

After expanding the zeroth order dipole correlation functions, the full dipole correlation function can be solved by introducing an auxiliary time-dependent Schrödinger equation:

$$\langle\mu_{XUV}(t)\mu_{XUV}\rangle = e^{(iE_gt)/\hbar}\sum_{i,j=A,B,C}\langle i|\bar{j}(t)\rangle\mu_i^*\mu_j e^{i\phi_j},$$

and

$$\frac{d}{dt}|\bar{j}(t)\rangle = -\frac{i}{\hbar}H_{aux}(t)|\bar{j}(t)\rangle,$$

with

$$H_{aux}(t) = E_M|M\rangle\langle M| + \sum_{i=A,B,C}\{(\hbar\omega_i - i\Gamma_i)|i\rangle\langle i| + (E_i^D - i\Gamma_i^D)|D_i\rangle\langle D_i|\} + V_{aux}(t),$$

and

$$V_{aux}(t) = F_{opt}(t)\sum_{i=A,B,C}(\mu_i(e^{i\phi_i}|i\rangle\langle D_i| + |D_i\rangle\langle i|) + \mu_{iM}(e^{i\phi_i}|i\rangle\langle M| + |M\rangle\langle i|)).$$

Note that the auxiliary time-dependent Schrödinger equation is exact regardless of the optical field strength. By propagating the auxiliary time-dependent Schrödinger equation with a variable coefficient ODE solver [299], we obtain the full dipole correlation function for the excitonic transitions. To obtain the coupling strengths to the dark state M and the dissipative states D_i's (μ_i's and μ_{iM}'s), we computed the transient absorption spectra of the core-excited states between -10 fs to +30 fs with 1 fs time steps and fit them to experimental data using the Levenberg-Marquardt algorithm. In addition, because the linewidth of the static absorption spectrum (Fig. 6.10 and Table 6.4) only provides the lower bound for the lifetime of the transition [300], a nonlinear fit with varying population decay rate (Γ_i's) was carried out after obtaining the coupling strengths. The

Table 6.5: Fittted transition dipoles between the bright core-exciton states and the dark states.

Transition	A	B	C
μ_i [a.u.]	0.68 ± 0.03	0.73 ± 0.04	0.54 ± 0.02
μ_{iM} [a.u.]	0.72 ± 0.04	0.16 ± 0.05	0.20 ± 0.04

resulting lifetimes of the transitions with the fitting are within the uncertainty of the ones obtained from the static absorption spectrum, and we conclude that the contribution from inhomogeneous broadening to the measured linewidths is insignificant.

The result of the fitting of coupling strength μ_i's and μ_{iM}'s is plotted in Fig. 6.11(b) and the fitted parameters in Table 6.5. The simulated XUV transient absorption spectra exhibit qualitative agreement with the measured results. The TDSE formalism with an auxiliary Hamiltonian enables the simulation of coupled Fano transitions without the requirement of describing the discrete and continuum states separately (e.g. Ref. [301]) and can greatly reduce the mathematical complexity and computational cost in simulating the XUV transient absorption spectra.

Chapter 7

Generation of 400 nm Pump Pulses[1]

7.1 Introduction

Ultrashort few-cycle optical pulses are indispensable for attosecond optical spectroscopy, which is used to investigate electron dynamics in atoms, molecules, and solids [50, 303–309]. In a typical NIR-XUV attosecond pump-probe experiment, a compressed intense NIR pulse is split off and focused onto a noble gas to generate an XUV pulse through high-harmonic generation (HHG), while the remainder forms a NIR pump pulse. Attosecond NIR-XUV pump-probe spectroscopy is highly useful in investigating charge-carrier dynamics and strong field phenomena in semiconductors [27, 28, 307–312]. However, to investigate attosecond charge-carrier dynamics in wide band gap (>2.5 eV) semiconductors through one-photon excitation, it is valuable to develop a scheme to generate sub-5 fs 400 nm optical pulses at energies sufficient to perform pump-probe measurements in addition to the strong few-cycle pulse that is used to generate the attosecond probe pulse. Moreover, intense few-cycle 400 nm pulses will provide few-femtosecond or even sub-femtosecond time-resolution in many UV-Vis nonlinear optical spectroscopies in 350-500 nm region. Simultaneous generation of few-cycle 400 nm and 800 nm pulses further enables optical excitation within the whole visible range, which is extremely useful for studying excited-state dynamics in photovoltaic materials and photosynthetic light-harvesting systems [313, 314].

Generation of 400 nm laser pulses can be achieved by frequency-upconversion of an 800 nm Ti:Sapphire laser pulse. However, directly generating sub-5 fs 400 nm pulses through frequency-doubling of compressed 800 nm pulses requires extremely thin nonlinear crystals. For example, obtaining a 5 fs transform-limited 400 nm pulse in a BBO crystal requires <30 μm substrate thickness [315], which subsequently limits the output energy of the 400 nm pulse. Sub-10 fs 400 nm pulses with sufficient energy for pump-probe experiments have been reported using thick (>100 μm) BBO crystals. There, sufficient spectral bandwidth is obtained via broadband frequency-doubling [316–319], where the incoming beam is angularly dispersed and recollimated by a pair of gratings to achieve the desired phase-matching angle for different input wavelengths, or self-phase modulation in a hollow-core fiber with subsequent dispersion compensation [320–323].

[1]The content and figures of this chapter is adapted or reprinted with permission from Ref. [302]

Varillas et al. obtained 8 fs 400 nm pulses with ~40 nm spectral width using broadband sum-frequency generation [319]. With non-collinear broadband sum-frequency generation, Grün et al. successfully generated compressed, 400 nm pulses with pulse duration of 32 fs and pulse energy of 55 μJ using 800 nm pulses with 74 fs pulse duration [324]. Employing an Ar filled hollow-core fiber, Kobayashi and coworkers successfully broadened and compressed 400 nm laser pulses from second harmonic generation in a BBO crystal with 80 nm spectral width and 7.5 fs pulse duration [323]. However, compression of 400 nm pulses to below 5 fs duration requires even greater spectral bandwidth (>100 nm) in the output pulse. In broadband frequency doubling, this would require a broader spectral range of the input pulse and wider angular dispersion to achieve phase-matching of all input wavelengths, or a much thinner nonlinear medium. These constraints either pose challenges in compensating the high-order angular dispersion or preclude efficient energy conversion. The compression of pulses using a hollow-core fiber will require shorter input pulses to avoid fragmentation of the output pulses in the time domain, while the duration of the input pulse is restricted by the phase-matching bandwidth of the BBO crystal and the pulse duration from the Ti:Sapphire amplifier [323].

In pioneering work, Nisoli et al. showed that high-energy (>500 μJ) laser pulses can be spectrally broadened in a gas-filled hollow-core fiber to obtain pulses with 10 fs duration [43]. Goulielmakis and coworkers demonstrated that direct spectral broadening of an 800 nm laser pulse in a Ne-filled hollow-core fiber can yield pulses with an ultra-broadband spectrum ranging from 300 to 1100 nm [325–327]. Subsequent dichroic splitting of the supercontinuum into various spectral components from the ultra-broadband pulse yields 6-9 fs pulses across four separate wavelength components, which are successively recombined to generate optical attosecond pulses [327]. With 1 mJ, ~22 fs, 800 nm input pulses, the resulting pulse energy of the four wavelength components can reach ~320 μJ in total [327].

Here we report on the generation of 400 nm laser pulses with up to 5 μJ pulse energy with sub-5 fs pulse duration through dichroic beam splitting of a portion of the spectrally broadened pulse from a hollow-core fiber, while the spectrum and pulse energy around 800 nm necessary for attosecond XUV generation is fully preserved (>750 μJ). We also demonstrate long-term energy stability of the two pulses, making this pulse pair well-suited for ultrafast optical-XUV pump-probe experiments.

7.2 Results

To generate ultra-broadband pulses spanning 350-1100 nm spectral range, 1.5 mJ pulses with approximately 27 fs duration at 1 kHz repetition rate produced from a chirped pulse amplification (CPA) Ti:Sapphire amplifier (Femtolasers FemtoPower Compact PRO) are focused into a 1 m long, 320 μm diameter hollow-core fiber filled with 2-2.8 bar Ne (Fig. 7.1). A typical spectrum and autocorrelation trace of the pulse from the amplifier are shown in Fig. 2.4(a) and (b), respectively. The beam is spectrally broadened in the hollow-core fiber and subsequently separated by a 1 mm thick dichroic beam-splitter, with the front surface coated to reflect 350-500 nm, and the rear surface anti-reflection coated for 520 to 940 nm. The layers are optimized for low group-delay dispersion

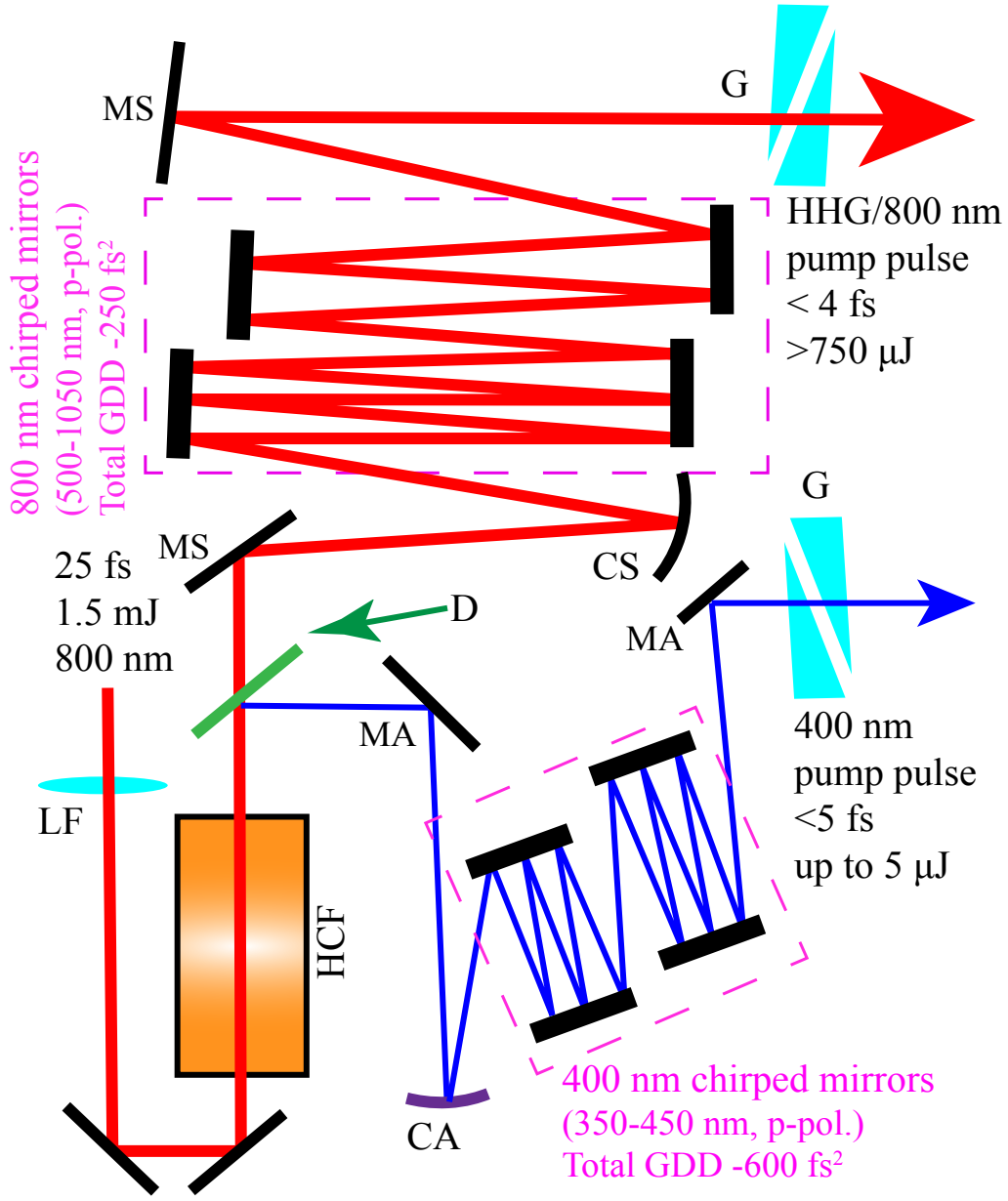

Figure 7.1: The experimental setup for broadening, separation, and compression of the pulses. (HCF: 1 m Ne-filled hollow-core fiber. D: 1 mm thick dichroic beam splitter. G: fused silica wedges. LF: convex lens (f=2m). CS: concave silver-coated mirror (f=1500 mm). CA: concave aluminum-coated mirror (f=750 mm) MA: planar aluminum-coated mirror. MS: planar silver-coated mirror.)

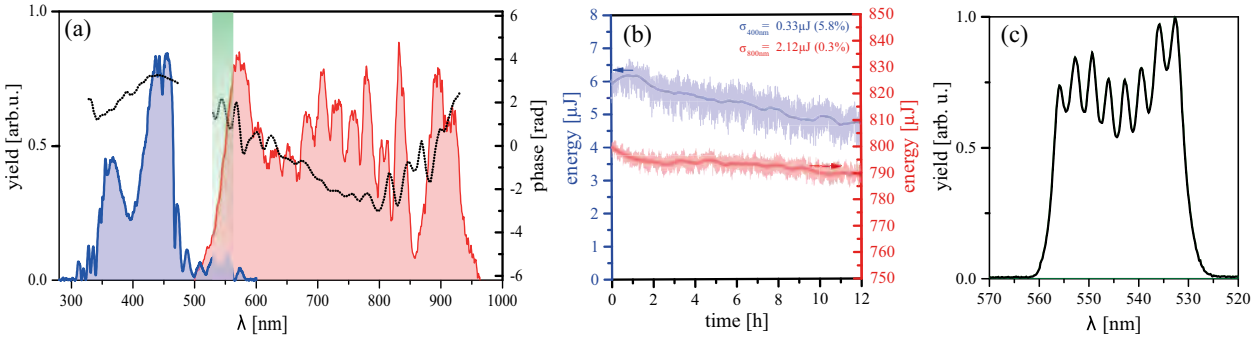

Figure 7.2: Properties of 800 nm and 400 nm pulses after compression. (a) Spectra of 400 nm (blue) and 800 nm (red) pulses and their retrieved spectral phase (dotted line). The green shade indicates the overlapping spectral region of the compressed 400 nm and 800 nm pulses. (b) Long-time stability of 400 nm (blue) and 800 nm (red) pulse energy over 12 hours with 2.8 bar Ne in the hollow-core fiber. (c) Measured spectra when the 400 nm and 800 nm pulses are overlapped in time with 525-560 nm band-pass filter.

(Layertec GmbH). In two separate arms, the transmitted and reflected beams are recollimated and separately compressed by two different sets of double-angle chirped mirrors (Ultrafast Innovations GmBH) and two pairs of fused silica wedges for fine dispersion compensation (Fig. 7.1). Because the 800 nm double-angle chirped mirrors for the transmitted beam only support wavelengths ranging from 500 to 1050 nm, separating the light with wavelength below 500 nm compromises neither the energy nor the spectral bandwidth of 800 nm pulses.

Spectra of the transmitted and reflected beams are shown in Fig. 7.2(a). The spectrum of the 400 nm pulses spans 350 nm to 500 nm, featuring ~150 nm bandwidth supporting <4 fs transform-limited pulses. Additionally, the 800 nm transmitted beam exhibits spectral bandwidth spanning 500-950 nm, which sets a transform limit of 3.2 fs to the pulse duration. By optimizing the Ne pressure in the hollow-core fiber, 400 nm and 800 nm pulses with pulse energies more than 5 μJ and 750 μJ, respectively, are readily obtainable. Figure 7.2(b) displays the evolution of pulse energy of both beams over 12 hours. With 2.8 bar Ne in the hollow-core fiber, the 400 nm beam yields >5 μJ pulse energy with ~6% variance while the 800 nm beam provides 780-800 μJ pulse energy with <0.5% variance. The strong dependence of the spectral broadening in the hollow-core fiber can also be observed in the long-time decrease in pulse energy. Over 12 hours, the pulse energy of the 400 nm beam decreases from ~6 μJ to ~5 μJ (<17%) due to leakage of high-pressure Ne from the hollow-core fiber chamber, while the energy of the 800 nm pulses decreases by less than 20 μJ (<3%).

The temporal structures of the 400 nm and 800 nm pulses are characterized by self-diffraction frequency-resolved optical gating (SD-FROG) [328, 329], and dispersion scan (D-Scan, Sphere Ultrafast Photonics) [47], respectively. The self-diffraction signal is obtained by wavefront-splitting of the 400 nm beam using two D-shaped mirrors on delay-scanning stages and subsequently focusing the two beams into a 100 μm thick sapphire crystal with a crossing angle of 50 mrad. The setup for

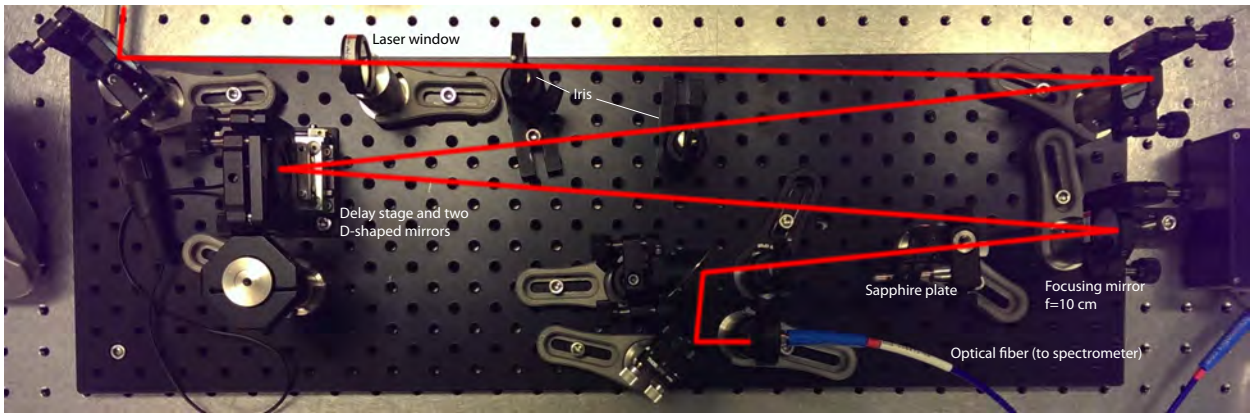

Figure 7.3: Photograph of the SD-FROG setup. Two irises are used to define the beam path of the 400 nm beam, which is subsequently split by the two D-shaped mirrors and focused onto a sapphire plate. The self-diffraction signal is focused into an optical fiber connected to the spectrometer.

SD-FROG measurements is shown in Fig. 7.3. Typical D-Scan and SD-FROG traces are shown in Fig. 7.4(a) and (b), respectively. The intensity profile (Fig. 7.4(c), blue line) and spectral phase (Fig. 7.2(a)) of the 400 nm pulse is retrieved using commercial software [330], yielding pulses with 4.4 ± 0.5 fs duration. On the other hand, the retrieval from the dispersion scan measurement shows that the pulse duration of the 800 nm beam is 3.8 ± 0.2 fs (Fig. 7.4(c), red line). The measurements clearly show that sub-5 fs pulses at the central wavelength for both 400 nm and 800 nm can be simultaneously obtained through spectral broadening of the output of a standard Ti:Sapphire amplifier in a hollow-core fiber and subsequent wavelength separation.

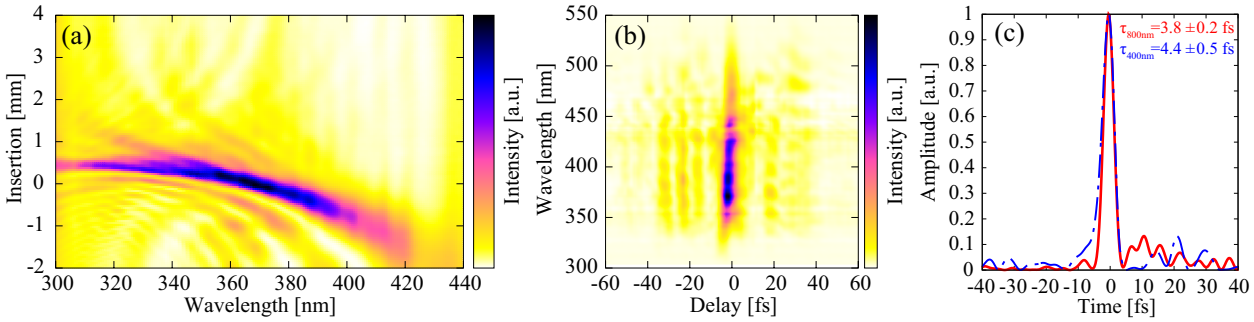

Figure 7.4: Temporal profiles of 800 nm and 400 nm pulses after compression. (a) The measured dispersion scan trace of the 800 nm pulse. (b) The measured two-dimensional SD-FROG trace of the 400 nm pulses. (c) The retrieved temporal profile of the 400 nm (blue, dash-dotted) and 800 nm (red) pulses. The hollow-core fiber is filled with 2.2 bar Ne. The pulse energy of the 400 nm and 800 nm beam are 1.6 and 800 μJ, respectively.

In a pump-probe experiment, the pump and probe pulses must overlap in both space and time. Within the presented setup, we demonstrate that the overlap of two pulses in time can be directly performed by observing the spectral interference of the two pulses in the 525-560 nm spectral region. Figure 7.2(a) shows that the 400 nm and 800 nm pulses share a common spectral region between 500 nm and 600 nm. Focusing the two beams into a spectrometer (HR4000, Ocean Optics) and with a band-pass filter (525-560 nm) to block the non-overlapping spectral region, clear spectral interference between the two beams is observed (Fig. 7.2(c)). The interferometric stability of the pump and probe arm can be inferred from the stability of the interferogram (Fig. 7.2(c)). However, the interferometric stability highly depends on the path length and optical elements between compression and recollimation. Here we only show the interferogram that is used to find the time overlap of the 400 nm and 800 nm beam, and no estimate of the jitter between the 400 nm and 800 nm beam was made. The ease of determining the time-overlap in this experimental setup makes it feasible for pump-probe and multidimensional spectroscopic experiments.

7.3 Summary

In summary, we demonstrate simultaneous generation of sub-5 fs pulses in both the 800 nm and 400 nm spectral region through wavelength separation of a supercontinuum produced in a Ne-filled hollow-core fiber. To the best of our knowledge, the reported pulse duration of 4.4 fs, comprising only three optical cycles, is the shortest value achieved thus far for blue light pulses. The intensity of the 400 nm pulses strongly depends on the self-phase modulation determined by the Ne pressure in the hollow-core fiber and thus it is possible to tune the energy of the 400 nm pulse by changing the pressure in the hollow-core fiber. Up to 5 μJ pulse energy in 400 nm pulses can be obtained by focusing the 1.5 mJ, 27 fs laser pulses into the hollow-core fiber, while maintaining more than 750 μJ pulse energy around 800 nm for generating attosecond pulses via high harmonic generation. It is worth noting that although changing the gas pressure affects the spectrum of the 400 nm pulses, it is possible to adjust the energy from 1 μJ to 5 μJ while maintaining sub-5 fs pulse duration. This setup enables direct optical excitation across the whole visible range with sub-5 fs time resolution for pump-probe and multi-dimensional spectroscopic experiments. Focusing the 400 nm beam to 10 μm focal diameter will result in an intensity of $\sim 10^{14}$ W/cm^2, which is sufficient for studying strong-field phenomena. Furthermore, nonlinear crystals are absent in this setup and thus it is not prone to optical damage. This method provides further energy scalability by increasing the energy of the input pulse. The use of a gas-filled hollow-core fiber as the broadening medium also allows changing the energy ratio between the blue and the red portion by altering the input wavelength. Our setup extends the spectral region of the optical pump in attosecond pump-probe experiments down to 350 nm. The demonstrated approach can be easily implemented in any regular few-cycle compression setup and opens up new experimental possibilities. In existing NIR-XUV pump-probe setups, an additional pump channel can be created without compromising the capabilities of the original beamline and this further paves the way for multi-dimensional UV-Vis-XUV spectroscopy on the attosecond time scale.

Chapter 8

Conclusion and Outlook

This work summarizes my graduate study on electronic and structural dynamics in solids with attosecond core-level transient absorption spectroscopy. In the studies of 2H-$MoTe_2$ and nickel presented here, the core-level transient absorption spectra can generally be described by a shift and a broadening of the static absorption spectrum in addition to the carrier-induced change in state filling in the valence shell. Where many-body effects in core-level absorption are minimized by electronic screening, such as in 2H-$MoTe_2$, the energy distribution of holes can be directly extracted from core-level transient absorption signal below the absorption edge. While, theoretically, electron distribution in the conduction band can also be extracted from core-level transient absorption signal above the edge, the signal of the electron distribution is usually buried beneath the transient absorption signal due to the carrier- and phonon-induced shift of the absorption edge, and the overlapping transient absorption signal of holes from the spin-orbit split core-levels [1]. The problem of overlapping signal from the spin-orbit split core-level can be eliminated by performing core-level transient absorption spectroscopy with deeper core-levels. For example, compared to the Te $N_{4,5}$ edge probed in this study, which has a splitting of 1.5 eV, the spin-orbit splitting at the Te $M_{4,5}$ edge is about 10 eV, which is well above the band gap of a semiconductor [141].

In the study of electron thermalization and relaxation dynamics in nickel, it is observed that although the core-level absorption spectrum can no longer be described by single-particle core-to-band transitions, the core-level transient absorption signal can be described by a Gaussian broadening and a shift of the static absorption spectrum. For thermalized carriers, the broadening can be utilized to extract carrier temperatures. The independent derivation of the relation between the Gaussian broadening and the carrier temperature without material-specific parameters indicates that this relation may be general among the core-level absorption of metals. This simple approach of extracting physical parameters directly from experimental data without the use of *ab initio* simulations is highly useful for time-critical experiments, for example, at free electron laser facilities.

The study of core-exciton decay in WS_2 and NaCl presents two different pathways of perturbing the core-exciton by an optical pulse. Whereas in NaCl the core-excitons are solely perturbed by

[1] Also see Ref. [9].

couplings of different core-exciton states and the continuum by the electric field of the optical pulse, in WS_2 the dominant contribution to the modification of core-exciton transitions is the photoexcted carriers. The observation of discrete core-excitons at the W $N_{6,7}$ edge in bulk WS_2 also defies the usual concept that core-excitons mainly occur in poorly screened insulators. The core-exciton transitions at the W $N_{6,7}$ edge and the core-to-band transitions at the W O_3 edge in the same energy region suggests that the properties of the core wavefunction plays a significant role in the core-exciton formation.

The methodology developed in this work can be readily extended to study electronic and structural dynamics in multi-component systems such as alloys, multilayers, heterostructures, and superlattices, where the element specificity of core-level absorption enables domain-specific probe of photoinduced dynamics, which is important to the understanding of phenomena such as demagnetization and optical induced magnetic state switching [36, 234, 239]. The data analysis methods developed here can also benefit the studies of photoinduced dynamics with deep core excitations as a probe, for example, at free electron laser facilities where high-brightness X-ray with tunable polarizations is available.

Bibliography

[1]M. Chergui and J. M. Thomas, "From structure to structural dynamics: Ahmed Zewail's legacy", Struct Dyn **4**, 043802 (2017).

[2]A. H. Zewail, "Femtochemistry: Atomic-Scale Dynamics of the Chemical Bond", J. Phys. Chem. A **104**, 5660–5694 (2000).

[3]B. Kok, B. Forbush, and M. McGloin, "Cooperation of charges in photosynthetic O_2 evolution-I. A linear four step mechanism", Photochem Photobiol **11**, 457–475 (1970).

[4]U. Keller, "Recent developments in compact ultrafast lasers", Nature **424**, 831–838 (2003).

[5]K. F. Wall and A. Sanchez, "Titanium sapphire lasers", Linc. Lab. J. USA **3** (1990).

[6]B. E. A. Saleh, *Fundamentals of photonics*, Third edition, Wiley Series in Pure and Applied Optics (Wiley, Hoboken, NJ, 2019).

[7]S. Mukamel, *Principles of Nonlinear Optics and Spectroscopy* (Oxford University Press, 1995).

[8]P. M. Kraus, M. Zürch, S. K. Cushing, D. M. Neumark, and S. R. Leone, "The ultrafast X-ray spectroscopic revolution in chemical dynamics", Nat. Rev. Chem. **2**, 82–94 (2018).

[9]M. Zürch, H.-T. Chang, L. J. Borja, P. M. Kraus, S. K. Cushing, A. Gandman, C. J. Kaplan, M. H. Oh, J. S. Prell, D. Prendergast, C. D. Pemmaraju, D. M. Neumark, and S. R. Leone, "Direct and simultaneous observation of ultrafast electron and hole dynamics in germanium", Nat. Commun. **8**, 15734 (2017).

[10]H. Wang, M. Chini, S. Chen, C.-H. Zhang, F. He, Y. Cheng, Y. Wu, U. Thumm, and Z. Chang, "Attosecond Time-Resolved Autoionization of Argon", Phys. Rev. Lett. **105**, 143002 (2010).

[11]A. E. Sandström, "Experimental Methods of X-ray Spectroscopy: Ordinary Wavelengths", in *Röntgenstrahlen / X-Rays*, edited by W. Schaaffs, A. E. Sandström, D. H. Tomboulian, P. Kirkpatrick, H. H. Pattee, and S. T. Stephenson, Handbuch Der Physik / Encyclopedia of Physics (Springer, Berlin, Heidelberg, 1957), pp. 78–245.

[12]D. T. Attwood and A. Sakdinawat, *X-rays and extreme ultraviolet radiation: principles andapplications*, Second edition (Cambridge University Press, Cambridge, United Kingdom ; New York, NY, 2016).

[13]P. Willmott, *An introduction to synchrotron radiation: techniques and applications*, Second edition (John Wiley & Sons, Inc, Hoboken, NJ, 2019).

[14]R. W. Schoenlein, W. P. Leemans, A. H. Chin, P. Volfbeyn, T. E. Glover, P. Balling, M. Zolotorev, K.-J. Kim, S. Chattopadhyay, and C. V. Shank, "Femtosecond X-ray Pulses at 0.4 Å Generated by 90° Thomson Scattering: A Tool for Probing the Structural Dynamics of Materials", Science **274**, 236–238 (1996).

[15]C. Pellegrini, "X-ray free-electron lasers: from dreams to reality", Phys. Scr. **T169**, 014004 (2016).

[16]H.-S. Kang, C.-K. Min, H. Heo, C. Kim, H. Yang, G. Kim, I. Nam, S. Y. Baek, H.-J. Choi, G. Mun, B. R. Park, Y. J. Suh, D. C. Shin, J. Hu, J. Hong, S. Jung, S.-H. Kim, K. Kim, D. Na, S. S. Park, Y. J. Park, J.-H. Han, Y. G. Jung, S. H. Jeong, H. G. Lee, S. Lee, S. Lee, W.-W. Lee, B. Oh, H. S. Suh, Y. W. Parc, S.-J. Park, M. H. Kim, N.-S. Jung, Y.-C. Kim, M.-S. Lee, B.-H. Lee, C.-W. Sung, I.-S. Mok, J.-M. Yang, C.-S. Lee, H. Shin, J. H. Kim, Y. Kim, J. H. Lee, S.-Y. Park, J. Kim, J. Park, I. Eom, S. Rah, S. Kim, K. H. Nam, J. Park, J. Park, S. Kim, S. Kwon, S. H. Park, K. S. Kim, H. Hyun, S. N. Kim, S. Kim, S.-m. Hwang, M. J. Kim, C.-y. Lim, C.-J. Yu, B.-S. Kim, T.-H. Kang, K.-W. Kim, S.-H. Kim, H.-S. Lee, H.-S. Lee, K.-H. Park, T.-Y. Koo, D.-E. Kim, and I. S. Ko, "Hard X-ray free-electron laser with femtosecond-scale timing jitter", Nat. Photonics **11**, 708–713 (2017).

[17]D. Strickland and G. Mourou, "Compression of amplified chirped optical pulses", Optics Communications **56**, 219–221 (1985).

[18]A. L'Huillier, K. J. Schafer, and K. C. Kulander, "Theoretical aspects of intense field harmonic generation", J. Phys. B: At. Mol. Opt. Phys. **24**, 3315–3341 (1991).

[19]C. J. Joachain, N. J. Kylstra, and R. M. Potvliege, *Atoms in intense laser fields* (Cambridge University Press, Cambridge ; New York, 2012).

[20]H. Timmers, M. Sabbar, J. Hellwagner, Y. Kobayashi, D. M. Neumark, and S. R. Leone, "Polarization-assisted amplitude gating as a route to tunable, high-contrast attosecond pulses", Optica **3**, 707 (2016).

[21]J. Li, X. Ren, Y. Yin, K. Zhao, A. Chew, Y. Cheng, E. Cunningham, Y. Wang, S. Hu, Y. Wu, M. Chini, and Z. Chang, "53-attosecond X-ray pulses reach the carbon K-edge", Nat. Commun. **8**, 186 (2017).

[22]E. Goulielmakis, Z.-H. Loh, A. Wirth, R. Santra, N. Rohringer, V. S. Yakovlev, S. Zherebtsov, T. Pfeifer, A. M. Azzeer, M. F. Kling, S. R. Leone, and F. Krausz, "Real-time observation of valence electron motion.", Nature **466**, 739–43 (2010).

[23]A. R. Beck, B. Bernhardt, E. R. Warrick, M. Wu, S. Chen, M. B. Gaarde, K. J. Schafer, D. M. Neumark, and S. R. Leone, "Attosecond transient absorption probing of electronic superpositions of bound states in neon: detection of quantum beats", New J. Phys. **16**, 113016 (2014).

[24]A. Kaldun, A. Blättermann, V. Stooß, S. Donsa, H. Wei, R. Pazourek, S. Nagele, C. Ott, C. D. Lin, J. Burgdörfer, and T. Pfeifer, "Observing the ultrafast buildup of a Fano resonance in the time domain", Science **354**, 738–741 (2016).

[25]C. Ott, A. Kaldun, P. Raith, K. Meyer, M. Laux, J. Evers, C. H. Keitel, C. H. Greene, and T. Pfeifer, "Lorentz meets Fano in spectral line shapes: a universal phase and its laser control.", Science **340**, 716 (2013).

[26]E. R. Warrick, J. E. Bækhøj, W. Cao, A. P. Fidler, F. Jensen, L. B. Madsen, S. R. Leone, and D. M. Neumark, "Attosecond transient absorption spectroscopy of molecular nitrogen: Vibrational coherences in the b′ 1Σ+u state", Chem. Phys. Lett. **683**, 408–415 (2017).

[27]M. Schultze, E. M. Bothschafter, A. Sommer, S. Holzner, W. Schweinberger, M. Fiess, M. Hofstetter, R. Kienberger, V. Apalkov, V. S. Yakovlev, M. I. Stockman, and F. Krausz, "Controlling dielectrics with the electric field of light", Nature **493**, 75–78 (2012).

[28]M. Schultze, K. Ramasesha, C. D. Pemmaraju, S. A. Sato, D. Whitmore, A. Gandman, J. S. Prell, L. J. Borja, D. Prendergast, K. Yabana, D. M. Neumark, and S. R. Leone, "Attosecond band-gap dynamics in silicon", Science **346**, 1348–1352 (2014).

[29]F. Schlaepfer, M. Lucchini, S. A. Sato, M. Volkov, L. Kasmi, N. Hartmann, A. Rubio, L. Gallmann, and U. Keller, "Attosecond optical-field-enhanced carrier injection into the GaAs conduction band", Nat. Phys. **14**, 560–564 (2018).

[30]M. Zürch, H.-T. Chang, P. M. Kraus, S. K. Cushing, L. J. Borja, A. Gandman, C. J. Kaplan, M. H. Oh, J. S. Prell, D. Prendergast, C. D. Pemmaraju, D. M. Neumark, and S. R. Leone, "Ultrafast carrier thermalization and trapping in silicon-germanium alloy probed by extreme ultraviolet transient absorption spectroscopy", Struct. Dyn. **4**, 044029 (2017).

[31]A. Moulet, J. B. Bertrand, T. Klostermann, A. Guggenmos, N. Karpowicz, and E. Goulielmakis, "Soft x-ray excitonics", Science **357**, 1134–1138 (2017).

[32]R. Géneaux, C. J. Kaplan, L. Yue, A. D. Ross, J. E. Bækhøj, P. M. Kraus, H.-T. Chang, A. Guggenmos, M.-Y. Huang, M. Zürch, K. J. Schafer, D. M. Neumark, M. B. Gaarde, and S. R. Leone, "Attosecond Time-Domain Measurement of Core-Level-Exciton Decay in Magnesium Oxide", Phys. Rev. Lett. **124**, 207401 (2020).

[33]M. Lucchini, S. A. Sato, G. D. Lucarelli, B. Moio, G. Inzani, R. Borrego-Varillas, F. Frassetto, L. Poletto, H. Hübener, U. De Giovannini, A. Rubio, and M. Nisoli, "Unravelling the intertwined atomic and bulk nature of localised excitons by attosecond spectroscopy", Nat. Commun. **12**, 1021 (2020).

[34]M. Volkov, S. A. Sato, F. Schlaepfer, L. Kasmi, N. Hartmann, M. Lucchini, L. Gallmann, A. Rubio, and U. Keller, "Attosecond screening dynamics mediated by electron localization in transition metals", Nat. Phys. **15**, 1145–1149 (2019).

[35]M. Lucchini, S. A. Sato, A. Ludwig, J. Herrmann, M. Volkov, L. Kasmi, Y. Shinohara, K. Yabana, L. Gallmann, and U. Keller, "Attosecond dynamical Franz-Keldysh effect in polycrystalline diamond", Science **353**, 916–919 (2016).

[36]F. Siegrist, J. A. Gessner, M. Ossiander, C. Denker, Y.-P. Chang, M. C. Schröder, A. Guggenmos, Y. Cui, J. Walowski, U. Martens, J. K. Dewhurst, U. Kleineberg, M. Münzenberg, S. Sharma, and M. Schultze, "Light-wave dynamic control of magnetism", Nature **571**, 240–244 (2019).

[37]G. D. Mahan, *Many-Particle Physics* (Springer US, Boston, MA, 2000).

[38]A. Apolonski, A. Poppe, G. Tempea, C. Spielmann, T. Udem, R. Holzwarth, T. W. Hänsch, and F. Krausz, "Controlling the Phase Evolution of Few-Cycle Light Pulses", Phys. Rev. Lett. **85**, 740–743 (2000).

[39]M. Zimmermann, C. Gohle, R. Holzwarth, T. Udem, and T. W. Hänsch, "Optical clockwork with an offset-free difference-frequency comb:accuracy of sum- and difference-frequency generation", Opt. Lett. **29**, 310 (2004).

[40]T. Fuji, A. Apolonski, and F. Krausz, "Self-stabilization of carrier-envelope offset phase by use of difference-frequency generation", Opt. Lett. **29**, 632 (2004).

[41]T. Fuji, J. Rauschenberger, A. Apolonski, V. S. Yakovlev, G. Tempea, T. Udem, C. Gohle, T. W. Hänsch, W. Lehnert, M. Scherer, and F. Krausz, "Monolithic carrier-envelope phase-stabilization scheme", Opt. Lett. **30**, 332 (2005).

[42]J. Rauschenberger, T. Fuji, M. Hentschel, A.-J. Verhoef, T. Udem, C. Gohle, T. W. Hänsch, and F. Krausz, "Carrier-envelope phase-stabilized amplifier system", Laser Phys. Lett. **3**, 37 (2005).

[43]M. Nisoli, S. De Silvestri, and O. Svelto, "Generation of high energy 10 fs pulses by a new pulse compression technique", Appl. Phys. Lett. **68**, 2793–2795 (1996).

[44]M. Nisoli, S. De Silvestri, O. Svelto, R. Szipöcs, K. Ferencz, C. Spielmann, S. Sartania, and F. Krausz, "Compression of high-energy laser pulses below 5 fs", Opt. Lett. **22**, 522 (1997).

[45]V. Pervak, I. Ahmad, M. K. Trubetskov, A. V. Tikhonravov, and F. Krausz, "Double-angle multilayer mirrors with smooth dispersion characteristics", Opt. Express **17**, 7943–7951 (2009).

[46]H. Timmers, Y. Kobayashi, K. F. Chang, M. Reduzzi, D. M. Neumark, and S. R. Leone, "Generating high-contrast, near single-cycle waveforms with third-order dispersion compensation", Opt. Lett. **42**, 811 (2017).

[47]F. Silva, M. Miranda, B. Alonso, J. Rauschenberger, V. Pervak, and H. Crespo, "Simultaneous compression, characterization and phase stabilization of GW-level 14 cycle VIS-NIR femtosecond pulses using a single dispersion-scan setup", Opt. Express **22**, 10181 (2014).

[48]J. A. Nelder and R. Mead, "A Simplex Method for Function Minimization", The Computer Journal **7**, 308–313 (1965).

[49]M. Miranda, C. L. Arnold, T. Fordell, F. Silva, B. Alonso, R. Weigand, A. L'Huillier, and H. Crespo, "Characterization of broadband few-cycle laser pulses with the d-scan technique", Opt. Express **20**, 18732–18743 (2012).

[50]F. Krausz and M. Ivanov, "Attosecond physics", Rev. Mod. Phys. **81**, 163–234 (2009).

[51]K. J. Schafer, B. Yang, L. F. DiMauro, and K. C. Kulander, "Above threshold ionization beyond the high harmonic cutoff", Phys. Rev. Lett. **70**, 1599–1602 (1993).

[52]P. B. Corkum, "Plasma perspective on strong field multiphoton ionization", Phys. Rev. Lett. **71**, 1994–1997 (1993).

[53]E. Goulielmakis, M. Schultze, M. Hofstetter, V. S. Yakovlev, J. Gagnon, M. Uiberacker, A. L. Aquila, E. M. Gullikson, D. T. Attwood, R. Kienberger, F. Krausz, and U. Kleineberg, "Single-Cycle Nonlinear Optics", Science **320**, 1614–1617 (2008).

[54]P. B. Corkum, N. H. Burnett, and M. Y. Ivanov, "Subfemtosecond pulses", Opt. Lett. **19**, 1870 (1994).

[55]P. Dietrich, N. H. Burnett, M. Ivanov, and P. B. Corkum, "High-harmonic generation and correlated two-electron multiphoton ionization with elliptically polarized light", Phys. Rev. A **50**, R3585–R3588 (1994).

[56]I. J. Sola, E. Mével, L. Elouga, E. Constant, V. Strelkov, L. Poletto, P. Villoresi, E. Benedetti, J.-P. Caumes, S. Stagira, C. Vozzi, G. Sansone, and M. Nisoli, "Controlling attosecond electron dynamics by phase-stabilized polarization gating", Nat. Phys. **2**, 319–322 (2006).

[57]G. Sansone, E. Benedetti, F. Calegari, C. Vozzi, L. Avaldi, R. Flammini, L. Poletto, P. Villoresi, C. Altucci, R. Velotta, S. Stagira, S. D. Silvestri, and M. Nisoli, "Isolated Single-Cycle Attosecond Pulses", Science **314**, 443–446 (2006).

[58]S. Gilbertson, H. Mashiko, C. Li, S. D. Khan, M. M. Shakya, E. Moon, and Z. Chang, "A low-loss, robust setup for double optical gating of high harmonic generation", Appl. Phys. Lett. **92**, 071109 (2008).

[59]F. Ferrari, F. Calegari, M. Lucchini, C. Vozzi, S. Stagira, G. Sansone, and M. Nisoli, "High-energy isolated attosecond pulses generated by above-saturation few-cycle fields", Nat. Photonics **4**, 875–879 (2010).

[60]M. J. Abel, T. Pfeifer, P. M. Nagel, W. Boutu, M. J. Bell, C. P. Steiner, D. M. Neumark, and S. R. Leone, "Isolated attosecond pulses from ionization gating of high-harmonic emission", Chemical Physics, Attosecond Molecular Dynamics **366**, 9–14 (2009).

[61]A. Paul, E. A. Gibson, Xiaoshi Zhang, A. Lytle, T. Popmintchev, Xibin Zhou, M. M. Murnane, I. P. Christov, and H. C. Kapteyn, "Phase-matching techniques for coherent soft X-ray generation", IEEE J. Quantum Electron. **42**, 14–26 (2006).

[62]Z. Chang, *Fundamentals of attosecond optics* (CRC Press, Boca Raton, Fla, 2011).

[63]M. Lewenstein, P. Balcou, M. Y. Ivanov, A. L'Huillier, and P. B. Corkum, "Theory of high-harmonic generation by low-frequency laser fields", Phys. Rev. A **49**, 2117–2132 (1994).

[64]M. V. Ammosov, N. B. Delone, and V. P. Krainov, "Tunnel ionization of complex atoms and of atomic ions in an alternating electromagnetic field", Sov. Phys. JETP **64**, 1191 (1986).

[65]M. V. Ammosov, P. A. Golovinsky, I. Y. Kiyan, V. P. Krainov, and V. M. Ristic, "Tunneling ionization of atoms and atomic ions in an intense laser field with a nonhomogeneous space–time distribution", J. Opt. Soc. Am. B **9**, 1225–1230 (1992).

[66]C. Z. Bisgaard and L. B. Madsen, "Tunneling ionization of atoms", American Journal of Physics **72**, 249–254 (2004).

[67]J. L. Krause, K. J. Schafer, and K. C. Kulander, "High-order harmonic generation from atoms and ions in the high intensity regime", Phys. Rev. Lett. **68**, 3535–3538 (1992).

[68]P. Antoine, A. L'Huillier, and M. Lewenstein, "Attosecond Pulse Trains Using High–Order Harmonics", Phys. Rev. Lett. **77**, 1234–1237 (1996).

[69]L. Lipsky and A. Russek, "Auto-ionizing states in helium", Phys. Rev. **142**, 59–71 (1966).

[70]R. P. Madden and K. Codling, "Two-Electron Excitation States in Helium.", Astrophys. J. **141**, 364 (1965).

[71]K. Codling, R. P. Madden, and D. L. Ederer, "Resonances in the photo-ionization continuum of Ne I (20-150 eV)", Phys. Rev. **155**, 26–37 (1967).

[72]R. P. Madden, D. L. Ederer, and K. Codling, "Resonances in the photo-ionization continuum of Ar i (20-150 eV)", Phys. Rev. **177**, 136–151 (1969).

[73]G. C. King, M. Tronc, F. H. Read, and R. C. Bradford, "An investigation of the structure near the L2,3 edges of argon, the M4,5 edges of krypton and the N4,5 edges of xenon, using electron impact with high resolution", J. Phys. B **10**, 3357–3357 (1977).

[74]J. A. Bearden and A. F. Burr, "Reevaluation of X-Ray Atomic Energy Levels", Rev. Mod. Phys. **39**, 125–142 (1967).

[75]M. Born, E. Wolf, and A. B. Bhatia, *Principles of optics: electromagnetic theory of propagation, interference and diffraction of light*, 7th (expanded) ed., repr. with corrections (Cambridge University Press, Cambridge, UK ; New York, 2002).

[76]A. R. Attar, H.-T. Chang, A. Britz, X. Zhang, M.-F. Lin, A. Krishnamoorthy, T. Linker, D. Fritz, D. M. Neumark, R. K. Kalia, A. Nakano, P. Ajayan, P. Vashishta, U. Bergmann, and S. R. Leone, "Simultaneous Observation of Carrier-Specific Redistribution and Coherent Lattice Dynamics in 2H-$MoTe_2$ with Femtosecond Core-Level Spectroscopy", ACS Nano **14**, 15829–15840 (2020).

[77]S. Manzeli, D. Ovchinnikov, D. Pasquier, O. V. Yazyev, and A. Kis, "2D transition metal dichalcogenides", Nat. Rev. Mater. **2**, 17033 (2017).

[78]T. A. Empante, Y. Zhou, V. Klee, A. E. Nguyen, I.-H. Lu, M. D. Valentin, S. A. Naghibi Alvillar, E. Preciado, A. J. Berges, C. S. Merida, M. Gomez, S. Bobek, M. Isarraraz, E. J. Reed, and L. Bartels, "Chemical Vapor Deposition Growth of Few-Layer $MoTe_2$ in the 2H, 1T′, and 1T Phases: Tunable Properties of MoTe2 Films", ACS Nano **11**, 900–905 (2017).

[79]X. Zhang, Z. Jin, L. Wang, J. A. Hachtel, E. Villarreal, Z. Wang, T. Ha, Y. Nakanishi, C. S. Tiwary, J. Lai, L. Dong, J. Yang, R. Vajtai, E. Ringe, J. C. Idrobo, B. I. Yakobson, J. Lou, V. Gambin, R. Koltun, and P. M. Ajayan, "Low Contact Barrier in 2H/1T′ $MoTe_2$ In-Plane Heterostructure Synthesized by Chemical Vapor Deposition", ACS Appl. Mater. Interfaces **11**, 12777–12785 (2019).

[80]C. Ruppert, O. B. Aslan, and T. F. Heinz, "Optical Properties and Band Gap of Single- and Few-Layer $MoTe_2$ Crystals", Nano Lett. **14**, 6231–6236 (2014).

[81]S. Cho, S. Kim, J. H. Kim, J. Zhao, J. Seok, D. H. Keum, J. Baik, D.-H. Choe, K. J. Chang, K. Suenaga, S. W. Kim, Y. H. Lee, and H. Yang, "Phase patterning for ohmic homojunction contact in $MoTe_2$", Science **349**, 625–628 (2015).

[82]W. Choi, M. Y. Cho, A. Konar, J. H. Lee, G.-B. Cha, S. C. Hong, S. Kim, J. Kim, D. Jena, J. Joo, and S. Kim, "High-Detectivity Multilayer MoS_2 Phototransistors with Spectral Response from Ultraviolet to Infrared", Adv. Mater. **24**, 5832–5836 (2012).

[83]T. Roy, M. Tosun, J. S. Kang, A. B. Sachid, S. B. Desai, M. Hettick, C. C. Hu, and A. Javey, "Field-Effect Transistors Built from All Two-Dimensional Material Components", ACS Nano **8**, 6259–6264 (2014).

[84]N. T. Duong, J. Lee, S. Bang, C. Park, S. C. Lim, and M. S. Jeong, "Modulating the Functions of MoS_2/$MoTe_2$ van der Waals Heterostructure via Thickness Variation", ACS Nano **13**, 4478–4485 (2019).

[85]G. A. Saenz, G. Karapetrov, J. Curtis, and A. B. Kaul, "Ultra-high Photoresponsivity in Suspended Metal-Semiconductor-Metal Mesoscopic Multilayer MoS 2 Broadband Detector from UV-to-IR with Low Schottky Barrier Contacts", Sci. Rep. **8**, 1276 (2018).

[86]S. Bertolazzi, D. Krasnozhon, and A. Kis, "Nonvolatile Memory Cells Based on MoS2/Graphene Heterostructures", ACS Nano **7**, 3246–3252 (2013).

[87]H.-P. Komsa and A. V. Krasheninnikov, "Electronic structures and optical properties of realistic transition metal dichalcogenide heterostructures from first principles", Phys. Rev. B **88**, 085318 (2013).

[88]D. Yadav, M. Trushin, and F. Pauly, "Thermalization of photoexcited carriers in two-dimensional transition metal dichalcogenides and internal quantum efficiency of van der Waals heterostructures", Phys. Rev. Research **2**, 043051 (2020).

[89]H. Ji, G. Lee, M.-K. Joo, Y. Yun, H. Yi, J.-H. Park, D. Suh, and S. C. Lim, "Thickness-dependent carrier mobility of ambipolar $MoTe_2$: Interplay between interface trap and Coulomb scattering", Appl. Phys. Lett. **110**, 183501 (2017).

[90]E. J. Sie, C. M. Nyby, C. D. Pemmaraju, S. J. Park, X. Shen, J. Yang, M. C. Hoffmann, B. K. Ofori-Okai, R. Li, A. H. Reid, S. Weathersby, E. Mannebach, N. Finney, D. Rhodes, D. Chenet, A. Antony, L. Balicas, J. Hone, T. P. Devereaux, T. F. Heinz, X. Wang, and A. M. Lindenberg, "An ultrafast symmetry switch in a Weyl semimetal", Nature **565**, 61–66 (2019).

[91]M. Y. Zhang, Z. X. Wang, Y. N. Li, L. Y. Shi, D. Wu, T. Lin, S. J. Zhang, Y. Q. Liu, Q. M. Liu, J. Wang, T. Dong, and N. L. Wang, "Light-Induced Subpicosecond Lattice Symmetry Switch in $MoTe_2$", Phys. Rev. X **9**, 021036 (2019).

[92]A. Krishnamoorthy, L. Bassman, R. K. Kalia, A. Nakano, F. Shimojo, and P. Vashishta, "Semiconductor–metal structural phase transformation in MoTe2 monolayers by electronic excitation", Nanoscale **10**, 2742–2747 (2018).

[93]L. Li, M.-F. Lin, X. Zhang, A. Britz, A. Krishnamoorthy, R. Ma, R. K. Kalia, A. Nakano, P. Vashishta, P. Ajayan, M. C. Hoffmann, D. M. Fritz, U. Bergmann, and O. V. Prezhdo, "Phonon-Suppressed Auger Scattering of Charge Carriers in Defective Two-Dimensional Transition Metal Dichalcogenides", Nano Lett. **19**, 6078–6086 (2019).

[94]Z. Chi, H. Chen, Q. Zhao, and Y.-X. Weng, "Ultrafast carrier and phonon dynamics in few-layer 2H–MoTe2", J. Chem. Phys. **151**, 114704 (2019).

[95]A. Krishnamoorthy, M.-F. Lin, X. Zhang, C. Weninger, R. Ma, A. Britz, C. S. Tiwary, V. Kochat, A. Apte, J. Yang, S. Park, R. Li, X. Shen, X. Wang, R. Kalia, A. Nakano, F. Shimojo, D. Fritz, U. Bergmann, P. Ajayan, and P. Vashishta, "Optical Control of Non-Equilibrium Phonon Dynamics", Nano Lett. **19**, 4981–4989 (2019).

[96]V. A. Jhalani, J.-J. Zhou, and M. Bernardi, "Ultrafast Hot Carrier Dynamics in GaN and Its Impact on the Efficiency Droop", Nano Lett. **17**, 5012–5019 (2017).

[97]G. Pace, I. Bargigia, Y.-Y. Noh, C. Silva, and M. Caironi, "Intrinsically distinct hole and electron transport in conjugated polymers controlled by intra and intermolecular interactions", Nat. Commun. **10**, 5226 (2019).

[98]M. F. Lin, M. A. Verkamp, J. Leveillee, E. S. Ryland, K. Benke, K. Zhang, C. Weninger, X. Shen, R. Li, D. Fritz, U. Bergmann, X. Wang, A. Schleife, and J. Vura-Weis, "Carrier-Specific Femtosecond XUV Transient Absorption of PbI2Reveals Ultrafast Nonradiative Recombination", J. Phys. Chem. C **121**, 27886–27893 (2017).

[99]M. A. Verkamp, J. Leveillee, A. Sharma, A. Schleife, and J. Vura-Weis, "Bottleneck-Free Hot Hole Cooling in CH3NH3PbI3 Revealed by Femtosecond XUV Absorption", ChemRxiv, `10.26434/chemrxiv.8323289.v1` (2019).

[100]J. E. Hamann-Borrero, S. Macke, B. Gray, M. Kareev, E. Schierle, S. Partzsch, M. Zwiebler, U. Treske, A. Koitzsch, B. Büchner, J. W. Freeland, J. Chakhalian, and J. Geck, "Site-selective spectroscopy with depth resolution using resonant x-ray reflectometry", Sci. Rep. **7**, 13792 (2017).

[101]S. K. Cushing, I. J. Porter, B. R. de Roulet, A. Lee, B. M. Marsh, S. Szoke, M. E. Vaida, and S. R. Leone, "Layer-resolved ultrafast extreme ultraviolet measurement of hole transport in a Ni-TiO2-Si photoanode", Sci. Adv. **6**, eaay6650 (2020).

[102]E. R. Hosler and S. R. Leone, "Characterization of vibrational wave packets by core-level high-harmonic transient absorption spectroscopy", Phys. Rev. A **88**, 023420 (2013).

[103]S. K. Cushing, M. Zürch, P. M. Kraus, L. M. Carneiro, A. Lee, H.-T. Chang, C. J. Kaplan, and S. R. Leone, "Hot phonon and carrier relaxation in Si(100) determined by transient extreme ultraviolet spectroscopy", Struct. Dyn. **5**, 054302 (2018).

[104]N. A. Miller, A. Deb, R. Alonso-Mori, B. D. Garabato, J. M. Glownia, L. M. Kiefer, J. Koralek, M. Sikorski, K. G. Spears, T. E. Wiley, D. Zhu, P. M. Kozlowski, K. J. Kubarych, J. E. Penner-Hahn, and R. J. Sension, "Polarized XANES Monitors Femtosecond Structural Evolution of Photoexcited Vitamin B12", J. Am. Chem. Soc. **139**, 1894–1899 (2017).

[105]M. Levantino, G. Schirò, H. T. Lemke, G. Cottone, J. M. Glownia, D. Zhu, M. Chollet, H. Ihee, A. Cupane, and M. Cammarata, "Ultrafast myoglobin structural dynamics observed with an X-ray free-electron laser", Nat. Commun. **6**, 6772 (2015).

[106]M. Cammarata, R. Bertoni, M. Lorenc, H. Cailleau, S. Di Matteo, C. Mauriac, S. F. Matar, H. Lemke, M. Chollet, S. Ravy, C. Laulhé, J.-F. Létard, and E. Collet, "Sequential Activation of Molecular Breathing and Bending during Spin-Crossover Photoswitching Revealed by Femtosecond Optical and X-Ray Absorption Spectroscopy", Phys. Rev. Lett. **113**, 227402 (2014).

[107]Y. Obara, H. Ito, T. Ito, N. Kurahashi, S. Thürmer, H. Tanaka, T. Katayama, T. Togashi, S. Owada, Y.-i. Yamamoto, S. Karashima, J. Nishitani, M. Yabashi, T. Suzuki, and K. Misawa, "Femtosecond time-resolved X-ray absorption spectroscopy of anatase TiO2 nanoparticles using XFEL", Struct. Dyn. **4**, 044033 (2017).

[108]J. Shah, *Ultrafast spectroscopy of semiconductors and semiconductornanostructures*, Springer Series in Solid-State Sciences 115 (Springer, Berlin ; New York, 1996).

[109]J. M. Richter, F. Branchi, F. Valduga de Almeida Camargo, B. Zhao, R. H. Friend, G. Cerullo, and F. Deschler, "Ultrafast carrier thermalization in lead iodide perovskite probed with two-dimensional electronic spectroscopy", Nat. Commun. **8**, 376 (2017).

[110]Z. Nie, R. Long, L. Sun, C.-c. Huang, J. Zhang, Q. Xiong, D. W. Hewak, Z. Shen, O. V. Prezhdo, and Z.-H. Loh, "Ultrafast Carrier Thermalization and Cooling Dynamics in Few-Layer MoS 2", ACS Nano **8**, 10931–10940 (2014).

[111]L. Rota, P. Lugli, T. Elsaesser, and J. Shah, "Ultrafast thermalization of photoexcited carriers in polar semiconductors", Phys. Rev. B **47**, 4226–4237 (1993).

[112]B. Peng, H. Zhang, W. Chen, B. Hou, Z.-J. Qiu, H. Shao, H. Zhu, B. Monserrat, D. Fu, H. Weng, and C. M. Soukoulis, "Sub-picosecond photo-induced displacive phase transition in two-dimensional MoTe 2", Npj 2D Mater. Appl. **4**, 1–8 (2020).

[113]G. Rohde, A. Stange, A. Müller, M. Behrendt, L.-P. Oloff, K. Hanff, T. J. Albert, P. Hein, K. Rossnagel, and M. Bauer, "Ultrafast Formation of a Fermi-Dirac Distributed Electron Gas", Phys. Rev. Lett. **121**, 256401 (2018).

[114]R. Bertoni, C. W. Nicholson, L. Waldecker, H. Hübener, C. Monney, U. De Giovannini, M. Puppin, M. Hoesch, E. Springate, R. T. Chapman, C. Cacho, M. Wolf, A. Rubio, and R. Ernstorfer, "Generation and Evolution of Spin-, Valley-, and Layer-Polarized Excited Carriers in Inversion-Symmetric WSe_2", Phys. Rev. Lett. **117**, 277201 (2016).

[115]S. K. Cushing, A. Lee, I. J. Porter, L. M. Carneiro, H.-T. Chang, M. Zürch, and S. R. Leone, "Differentiating Photoexcited Carrier and Phonon Dynamics in the Δ, L , and Γ Valleys of Si(100) with Transient Extreme Ultraviolet Spectroscopy", J. Phys. Chem. C **123**, 3343–3352 (2019).

[116]G. Froehlicher, E. Lorchat, F. Fernique, C. Joshi, A. Molina-Sánchez, L. Wirtz, and S. Berciaud, "Unified Description of the Optical Phonon Modes in N-Layer $MoTe_2$", Nano Lett. **15**, 6481–6489 (2015).

[117]T. Y. Jeong, B. M. Jin, S. H. Rhim, L. Debbichi, J. Park, Y. D. Jang, H. R. Lee, D.-H. Chae, D. Lee, Y.-H. Kim, S. Jung, and K. J. Yee, "Coherent Lattice Vibrations in Mono- and Few-Layer WSe_2", ACS Nano **10**, 5560–5566 (2016).

[118]H. J. Zeiger, J. Vidal, T. K. Cheng, E. P. Ippen, G. Dresselhaus, and M. S. Dresselhaus, "Theory for displacive excitation of coherent phonons", Phys. Rev. B **45**, 768–778 (1992).

[119]A. V. Kuznetsov and C. J. Stanton, "Theory of Coherent Phonon Oscillations in Semiconductors", Phys. Rev. Lett. **73**, 3243–3246 (1994).

[120]R. Merlin, "Generating coherent THz phonons with light pulses", Solid State Communications, Highlights in Condensed Matter Physics and Materials Science **102**, 207–220 (1997).

[121]C. Trovatello, H. P. C. Miranda, A. Molina-Sánchez, R. Borrego-Varillas, C. Manzoni, L. Moretti, L. Ganzer, M. Maiuri, J. Wang, D. Dumcenco, A. Kis, L. Wirtz, A. Marini, G. Soavi, A. C. Ferrari, G. Cerullo, D. Sangalli, and S. D. Conte, "Strongly Coupled Coherent Phonons in Single-Layer MoS2", ACS Nano **14**, 5700–5710 (2020).

[122]D. M. Fritz, D. A. Reis, B. Adams, R. A. Akre, J. Arthur, C. Blome, P. H. Bucksbaum, A. L. Cavalieri, S. Engemann, S. Fahy, R. W. Falcone, P. H. Fuoss, K. J. Gaffney, M. J. George, J. Hajdu, M. P. Hertlein, P. B. Hillyard, M. H.-v. Hoegen, M. Kammler, J. Kaspar, R. Kienberger, P. Krejcik, S. H. Lee, A. M. Lindenberg, B. McFarland, D. Meyer, T. Montagne, É. D. Murray, A. J. Nelson, M. Nicoul, R. Pahl, J. Rudati, H. Schlarb, D. P. Siddons, K. Sokolowski-Tinten, T. Tschentscher, D. von der Linde, and J. B. Hastings, "Ultrafast Bond Softening in Bismuth: Mapping a Solid's Interatomic Potential with X-rays", Science **315**, 633–636 (2007).

[123]K. Ishioka, M. Kitajima, and O. V. Misochko, "Temperature dependence of coherent A1g and Eg phonons of bismuth", Journal of Applied Physics **100**, 093501 (2006).

[124]M.-C. Lee, C. H. Kim, I. Kwak, C. W. Seo, C. Sohn, F. Nakamura, C. Sow, Y. Maeno, E.-A. Kim, T. W. Noh, and K. W. Kim, "Strong spin-phonon coupling unveiled by coherent phonon oscillations in Ca_2RuO_4", Phys. Rev. B **99**, 144306 (2019).

[125]J. Vinson, J. J. Rehr, J. J. Kas, and E. L. Shirley, "Bethe-Salpeter equation calculations of core excitation spectra", Phys. Rev. B **83**, 115106 (2011).

[126]K. Gilmore, J. Vinson, E. L. Shirley, D. Prendergast, C. D. Pemmaraju, J. J. Kas, F. D. Vila, and J. J. Rehr, "Efficient implementation of core-excitation Bethe–Salpeter equation calculations", Computer Physics Communications **197**, 109–117 (2015).

[127]P. E. Blöchl, "Projector augmented-wave method", Phys. Rev. B **50**, 17953–17979 (1994).

[128]G. Kresse and J. Furthmüller, "Efficient iterative schemes for ab initio total-energy calculations using a plane-wave basis set", Phys. Rev. B **54**, 11169–11186 (1996).

[129]G. Kresse and J. Furthmüller, "Efficiency of ab-initio total energy calculations for metals and semiconductors using a plane-wave basis set", Computational Materials Science **6**, 15–50 (1996).

[130]J. P. Perdew, K. Burke, and M. Ernzerhof, "Generalized Gradient Approximation Made Simple", Phys. Rev. Lett. **77**, 3865–3868 (1996).

[131]P. Giannozzi, S. Baroni, N. Bonini, M. Calandra, R. Car, C. Cavazzoni, D. Ceresoli, G. L. Chiarotti, M. Cococcioni, I. Dabo, A. Dal Corso, S. de Gironcoli, S. Fabris, G. Fratesi, R. Gebauer, U. Gerstmann, C. Gougoussis, A. Kokalj, M. Lazzeri, L. Martin-Samos, N. Marzari, F. Mauri, R. Mazzarello, S. Paolini, A. Pasquarello, L. Paulatto, C. Sbraccia, S. Scandolo, G. Sclauzero, A. P. Seitsonen, A. Smogunov, P. Umari, and R. M. Wentzcovitch, "QUANTUM ESPRESSO: a modular and open-source software project for quantum simulations of materials", J. Phys. Condens. Matter **21**, 395502 (2009).

[132]P. Giannozzi, O. Andreussi, T. Brumme, O. Bunau, M. Buongiorno Nardelli, M. Calandra, R. Car, C. Cavazzoni, D. Ceresoli, M. Cococcioni, N. Colonna, I. Carnimeo, A. Dal Corso, S. de Gironcoli, P. Delugas, R. A. DiStasio, A. Ferretti, A. Floris, G. Fratesi, G. Fugallo, R. Gebauer, U. Gerstmann, F. Giustino, T. Gorni, J. Jia, M. Kawamura, H.-Y. Ko, A. Kokalj, E. Küçükbenli, M. Lazzeri, M. Marsili, N. Marzari, F. Mauri, N. L. Nguyen, H.-V. Nguyen, A. Otero-de-la-Roza, L. Paulatto, S. Poncé, D. Rocca, R. Sabatini, B. Santra, M. Schlipf, A. P. Seitsonen, A. Smogunov, I. Timrov, T. Thonhauser, P. Umari, N. Vast, X. Wu, and S. Baroni, "Advanced capabilities for materials modelling with Quantum ESPRESSO", J. Phys. Condens. Matter **29**, 465901 (2017).

[133]N. Troullier and J. L. Martins, "Efficient pseudopotentials for plane-wave calculations", Phys. Rev. B **43**, 1993–2006 (1991).

[134]S. G. Louie, S. Froyen, and M. L. Cohen, "Nonlinear ionic pseudopotentials in spin-density-functional calculations", Phys. Rev. B **26**, 1738–1742 (1982).

[135]I. Grinberg, N. J. Ramer, and A. M. Rappe, "Transferable relativistic Dirac-Slater pseudopotentials", Phys. Rev. B **62**, 2311–2314 (2000).

[136]O. S. Heavens, *Optical properties of thin solid films* (Academic Press, New York, 1955).

[137]K. Wang, Y. Feng, C. Chang, J. Zhan, C. Wang, Q. Zhao, J. N. Coleman, L. Zhang, W. J. Blau, and J. Wang, "Broadband ultrafast nonlinear absorption and nonlinear refraction of layered molybdenum dichalcogenide semiconductors", Nanoscale **6**, 10530–10535 (2014).

[138]H.-T. Chang, A. Guggenmos, C. T. Chen, J. Oh, R. Géneaux, Y.-D. Chuang, A. M. Schwartzberg, S. Aloni, D. M. Neumark, and S. R. Leone, "Coupled Valence Carrier and Core-Exciton Dynamics in WS_2 Probed by Attosecond Transient Absorption Spectroscopy", ArXiv Prepr., 2103.09965 (2021).

[139]S. W. Koch, M. Kira, G. Khitrova, and H. M. Gibbs, "Semiconductor excitons in new light", Nat. Mater. **5**, 523–531 (2006).

[140]B. Buades, A. Picon, E. Berger, I. Leon, N. Di Palo, S. L. Cousin, C. Cocchi, E. Pellegrin, J. H. Martin, S. Mañas-Valero, E. Coronado, T. Danz, C. Draxl, M. Uemoto, K. Yabana, M. Schultze, S. Wall, M. Zürch, and J. Biegert, "Attosecond state-resolved carrier motion in quantum materials probed by soft X-ray XANES", ArXiv180806493 Cond-Mat (2020).

[141] A. Britz, A. R. Attar, X. Zhang, H.-T. Chang, C. Nyby, A. Krishnamoorthy, S. H. Park, S. Kwon, M. Kim, D. Nordlund, S. Sainio, T. F. Heinz, S. R. Leone, A. M. Lindenberg, A. Nakano, P. Ajayan, P. Vashishta, D. Fritz, M.-F. Lin, and U. Bergmann, "Carrier-specific dynamics in 2H-MoTe2 observed by femtosecond soft x-ray absorption spectroscopy using an x-ray free-electron laser", Structural Dynamics **8**, 014501 (2021).

[142] J. J. Rehr, "Failure of the quasiparticle picture of x-ray absorption?", Found. Phys. **33**, 1735–1742 (2003).

[143] W. Gudat, C. Kunz, and H. Petersen, "Core Exciton and Band Structure in LiF", Phys. Rev. Lett. **32**, 1370–1373 (1974).

[144] C. Kunz, "Electron hole interaction in deep level spectra", J. Phys. Colloq. **39**, C4-112-C4–119 (1978).

[145] F. Bassani, "Core excitons in solids", Appl. Opt. **19**, 4093 (1980).

[146] M. Altarelli, "Substitutional Donors and Core Excitons in Many-Valley Semiconductors", Phys. Rev. Lett. **46**, 205–208 (1981).

[147] H. P. Hjalmarson, H. Büttner, and J. D. Dow, "Theory of core excitons", Phys. Rev. B **24**, 6010–6019 (1981).

[148] G. Strinati, "Dynamical Shift and Broadening of Core Excitons in Semiconductors", Phys. Rev. Lett. **49**, 1519–1522 (1982).

[149] G. Iadonisi and F. Bassani, "Core excitons in the electronic polaron model", Il Nuovo Cimento D **3**, 408–420 (1984).

[150] J. F. Morar, F. J. Himpsel, G. Hollinger, G. Hughes, and J. L. Jordan, "Observation of a C-$1s$ Core Exciton in Diamond", Phys. Rev. Lett. **54**, 1960–1963 (1985).

[151] A. Balzarotti and M. Piacentini, "Optical Properties in the High Energy Range", in *Electronic Structure and Electronic Transitions in Layered Materials*, edited by V. Grasso (Springer Netherlands, Dordrecht, 1986), pp. 289–398.

[152] C. Sugiura, W. Konishi, S. Shoji, and S. Kojima, "Fluorine Kα X-Ray Emission Spectra of MgF2, CaF2, SrF2 and BaF2", J. Phys. Soc. Jpn. **59**, 4049–4053 (1990).

[153] W. L. O'Brien, J. Jia, Q.-Y. Dong, T. A. Callcott, J.-E. Rubensson, D. L. Mueller, and D. L. Ederer, "Intermediate coupling in L_2-L_3 core excitons of MgO, Al_2O_3, and SiO_2", Phys. Rev. B **44**, 1013–1018 (1991).

[154] F. de Groot and A. Kotani, *Core level spectroscopy of solids*, Advances in Condensed Matter Science v. 6 (CRC Press, Boca Raton, 2008).

[155] H. Jiang, "Electronic band structures of molybdenum and tungsten dichalcogenides by the GW approach", J. Phys. Chem. C **116**, 7664–7671 (2012).

[156] A. Berkdemir, H. R. Gutiérrez, A. R. Botello-Méndez, N. Perea-López, A. L. Elías, C.-I. Chia, B. Wang, V. H. Crespi, F. López-Urías, J.-C. Charlier, H. Terrones, and M. Terrones, "Identification of individual and few layers of WS2 using Raman Spectroscopy", Sci. Rep. **3**, 1755 (2013).

[157]H. R. Gutiérrez, N. Perea-López, A. L. Elías, A. Berkdemir, B. Wang, R. Lv, F. López-Urías, V. H. Crespi, H. Terrones, and M. Terrones, "Extraordinary room-temperature photoluminescence in triangular WS2monolayers", Nano Lett. **13**, 3447–3454 (2013).

[158]A. Chernikov, T. C. Berkelbach, H. M. Hill, A. Rigosi, Y. Li, O. B. Aslan, D. R. Reichman, M. S. Hybertsen, and T. F. Heinz, "Exciton Binding Energy and Nonhydrogenic Rydberg Series in Monolayer WS 2", Phys. Rev. Lett. **113**, 076802 (2014).

[159]Z. Ye, T. Cao, K. O'Brien, H. Zhu, X. Yin, Y. Wang, S. G. Louie, and X. Zhang, "Probing excitonic dark states in single-layer tungsten disulphide", Nature **513**, 214–218 (2014).

[160]E. J. Sie, J. W. McIver, Y.-H. Lee, L. Fu, J. Kong, and N. Gedik, "Valley-selective optical Stark effect in monolayer WS2", Nat. Mater. **14**, 290–294 (2014).

[161]A. Chernikov, C. Ruppert, H. M. Hill, A. F. Rigosi, and T. F. Heinz, "Population inversion and giant bandgap renormalization in atomically thin WS2 layers", Nat. Photonics **9**, 466–470 (2015).

[162]A. Chernikov, A. M. Van Der Zande, H. M. Hill, A. F. Rigosi, A. Velauthapillai, J. Hone, and T. F. Heinz, "Electrical Tuning of Exciton Binding Energies in Monolayer WS2", Phys. Rev. Lett. **115**, 1–6 (2015).

[163]A. Raja, A. Chaves, J. Yu, G. Arefe, H. M. Hill, A. F. Rigosi, T. C. Berkelbach, P. Nagler, C. Schüller, T. Korn, C. Nuckolls, J. Hone, L. E. Brus, T. F. Heinz, D. R. Reichman, and A. Chernikov, "Coulomb engineering of the bandgap and excitons in two-dimensional materials", Nat. Commun. **8**, 15251 (2017).

[164]P. Nagler, M. V. Ballottin, A. A. Mitioglu, M. V. Durnev, T. Taniguchi, K. Watanabe, A. Chernikov, C. Schüller, M. M. Glazov, P. C. M. Christianen, and T. Korn, "Zeeman Splitting and Inverted Polarization of Biexciton Emission in Monolayer WS_2", Phys. Rev. Lett. **121**, 057402 (2018).

[165]A. Raja, M. Selig, G. Berghäuser, J. Yu, H. M. Hill, A. F. Rigosi, L. E. Brus, A. Knorr, T. F. Heinz, E. Malic, and A. Chernikov, "Enhancement of Exciton–Phonon Scattering from Monolayer to Bilayer WS_2", Nano Lett. **18**, 6135–6143 (2018).

[166]H. Su, A. Deng, Z. Zhen, and J.-F. Dai, "Gamma-valley assisted intervalley scattering in monolayer and bilayer WS_2 revealed by time-resolved Kerr rotation spectroscopy", Phys. Rev. B **97**, 115426 (2018).

[167]J. Gu, B. Chakraborty, M. Khatoniar, and V. M. Menon, "A room-temperature polariton light-emitting diode based on monolayer WS_2", Nat. Nanotechnol., 1–5 (2019).

[168]C. Jin, J. Kim, M. Iqbal Bakti Utama, E. C. Regan, H. Kleemann, H. Cai, Y. Shen, M. J. Shinner, A. Sengupta, K. Watanabe, T. Taniguchi, S. Tongay, A. Zettl, and F. Wang, "Imaging of pure spin-valley diffusion current in WS2-WSe2 heterostructures", Science **360**, 893–896 (2018).

[169]L. Yuan, T.-F. Chung, A. Kuc, Y. Wan, Y. Xu, Y. P. Chen, T. Heine, and L. Huang, "Photocarrier generation from interlayer charge-transfer transitions in WS_2 -graphene heterostructures", Sci. Adv. **4**, e1700324 (2018).

[170]C. Jin, E. C. Regan, A. Yan, M. Iqbal Bakti Utama, D. Wang, S. Zhao, Y. Qin, S. Yang, Z. Zheng, S. Shi, K. Watanabe, T. Taniguchi, S. Tongay, A. Zettl, and F. Wang, "Observation of moiré excitons in WSe_2/WS_2 heterostructure superlattices", Nature **567**, 76–80 (2019).

[171]H. Li, S. Li, M. H. Naik, J. Xie, X. Li, J. Wang, E. Regan, D. Wang, W. Zhao, S. Zhao, S. Kahn, K. Yumigeta, M. Blei, T. Taniguchi, K. Watanabe, S. Tongay, A. Zettl, S. G. Louie, F. Wang, and M. F. Crommie, "Imaging moiré flat bands in three-dimensional reconstructed WSe_2/WS_2 superlattices", Nat. Mater., 1–6 (2021).

[172]C. Kastl, C. T. Chen, T. Kuykendall, B. Shevitski, T. P. Darlington, N. J. Borys, A. Krayev, P. J. Schuck, S. Aloni, and A. M. Schwartzberg, "The important role of water in growth of monolayer transition metal dichalcogenides", 2D Mater. **4**, 021024 (2017).

[173]U. Fano, "Effects of Configuration Interaction on Intensities and Phase Shifts", Phys. Rev. **124**, 1866–1878 (1961).

[174]*The Elk code*, http://elk.sourceforge.net/.

[175]G. Onida, L. Reining, and A. Rubio, "Electronic excitations: density-functional versus many-body Green's-function approaches", Rev. Mod. Phys. **74**, 601–659 (2002).

[176]S.-i. Nakai and T. Sagawa, "Na^+ $L_{2,3}$ Absorption Spectra of Sodium Halides", J. Phys. Soc. Jpn. **26**, 1427–1434 (1969).

[177]P. B. Allen and M. Cardona, "Temperature dependence of the direct gap of Si and Ge", Phys. Rev. B **27**, 4760–4769 (1983).

[178]Y. H. Lee, A. Chavez-Pirson, S. W. Koch, H. M. Gibbs, S. H. Park, J. Morhange, A. Jeffery, N. Peyghambarian, L. Banyai, A. C. Gossard, and W. Wiegmann, "Room-Temperature Optical Nonlinearities in GaAs", Phys. Rev. Lett. **57**, 2446–2449 (1986).

[179]H. Haug and S. Schmitt-Rink, "Electron theory of the optical properties of laser-excited semiconductors", Progress in Quantum Electronics **9**, 3–100 (1984).

[180]Y. Li, W. Liu, Y. Wang, Z. Xue, Y.-C. Leng, A. Hu, H. Yang, P.-H. Tan, Y. Liu, H. Misawa, Q. Sun, Y. Gao, X. Hu, and Q. Gong, "Ultrafast Electron Cooling and Decay in Monolayer WS2 Revealed by Time- and Energy-Resolved Photoemission Electron Microscopy", Nano Lett. **20**, 3747–3753 (2020).

[181]L. Waldecker, R. Bertoni, H. Hübener, T. Brumme, T. Vasileiadis, D. Zahn, A. Rubio, and R. Ernstorfer, "Momentum-Resolved View of Electron-Phonon Coupling in Multilayer WSe_2", Phys. Rev. Lett. **119**, 036803 (2017).

[182]A. Kaldun, C. Ott, A. Blättermann, M. Laux, K. Meyer, T. Ding, A. Fischer, and T. Pfeifer, "Extracting Phase and Amplitude Modifications of Laser-Coupled Fano Resonances", Phys. Rev. Lett. **112**, 103001 (2014).

[183]A. R. Beck, D. M. Neumark, and S. R. Leone, "Probing ultrafast dynamics with attosecond transient absorption", Chem. Phys. Lett. **624**, 119–130 (2015).

[184]T. Ding, C. Ott, A. Kaldun, A. Blättermann, K. Meyer, V. Stooss, M. Rebholz, P. Birk, M. Hartmann, A. Brown, H. V. D. Hart, and T. Pfeifer, "Time-resolved four-wave-mixing spectroscopy for inner-valence transitions", Opt. Lett. **41**, 709–712 (2016).

[185]K. Huang, A. Rhys, and N. F. Mott, "Theory of light absorption and non-radiative transitions in F-centres", Proc. R. Soc. Lond. Ser. Math. Phys. Sci. **204**, 406–423 (1950).

[186]P. H. Citrin, P. Eisenberger, and D. R. Hamann, "Phonon Broadening of X-Ray Photoemission Linewidths", Phys. Rev. Lett. **33**, 965–969 (1974).

[187]R. J. Elliott, "Intensity of Optical Absorption by Excitons", Phys. Rev. **108**, 1384–1389 (1957).

[188]L. Bányai and S. W. Koch, "A simple theory for the effects of plasma screening on the optical spectra of highly excited semiconductors", Z. Phys. B **63**, 283–291 (1986).

[189]S. W. Koch, N. Peyghambarian, and H. M. Gibbs, "Band-edge nonlinearities in direct-gap semiconductors and their application to optical bistability and optical computing", J. Appl. Phys. **63**, R1–R12 (1988).

[190]H. Haug and D. B. T. Thoai, "Dynamical screening of excitons by free carriers", Phys. Status Solidi B **85**, 561–568 (1978).

[191]R. Zimmermann, K. Kilimann, W. D. Kraeft, D. Kremp, and G. Röpke, "Dynamical screening and self-energy of excitons in the electron–hole plasma", Phys. Status Solidi B **90**, 175–187 (1978).

[192]S. Schmitt-Rink, C. Ell, and H. Haug, "Many-body effects in the absorption, gain, and luminescence spectra of semiconductor quantum-well structures", Phys. Rev. B **33**, 1183–1189 (1986).

[193]R. Doering and Y. Nishi, eds., *Handbook of semiconductor manufacturing technology*, 2nd ed (CRC Press, Boca Raton, 2008).

[194]C. J. Kaplan, P. M. Kraus, A. D. Ross, M. Zürch, S. K. Cushing, M. F. Jager, H.-T. Chang, E. M. Gullikson, D. M. Neumark, and S. R. Leone, "Femtosecond tracking of carrier relaxation in germanium with extreme ultraviolet transient reflectivity", Phys. Rev. B **97**, 205202 (2018).

[195]R. Géneaux, H.-T. Chang, A. M. Schwartzberg, and H. J. B. Marroux, "Source noise suppression in attosecond transient absorption spectroscopy by edge-pixel referencing", Opt. Express **29**, 951 (2021).

[196]D. J. Singh and L. Nordström, *Planewaves, pseudopotentials, and the LAPW method*, 2nd ed (Springer, New York, NY, 2006).

[197]J. P. Perdew and Y. Wang, "Accurate and simple analytic representation of the electron-gas correlation energy", Phys. Rev. B **45**, 13244–13249 (1992).

[198]G. F. Burkhard, E. T. Hoke, and M. D. McGehee, "Accounting for Interference, Scattering, and Electrode Absorption to Make Accurate Internal Quantum Efficiency Measurements in Organic and Other Thin Solar Cells", Adv. Mater. **22**, 3293–3297 (2010).

[199]C. Hsu, R. Frisenda, R. Schmidt, A. Arora, S. M. de Vasconcellos, R. Bratschitsch, H. S. J. van der Zant, and A. Castellanos-Gomez, "Thickness-Dependent Refractive Index of 1L, 2L, and 3L MoS2, MoSe2, WS2, and WSe2", Adv. Opt. Mater. **7**, 1900239 (2019).

[200]M. R. Vogt, "Development of physical models for the simulation of optical properties of solar cell modules", PhD thesis (Dissertation, Gottfried Wilhelm Leibniz Universität Hannover, 2015).

[201]A. Mondal, J. R. Aswin, R. K. Yadav, and K. V. Adarsh, "Ultrafast nonlinear optical response in tungsten sulfide (WS2) nanospheres", AIP Conference Proceedings **2082**, 030003 (2019).

[202]*WS2 crystal structure: Datasheet from "PAULING FILE multinaries edition – 2012" in SpringerMaterials*, Springer-Verlag Berlin Heidelberg & Material Phases Data System (MPDS), Switzerland & National Institute for Materials Science (NIMS), Japan.

[203]H.-T. Chang, A. Guggenmos, S. K. Cushing, Y. Cui, N. U. Din, S. R. Acharya, I. J. Porter, U. Kleineberg, V. Turkowski, T. S. Rahman, D. M. Neumark, and S. R. Leone, "Electron thermalization and relaxation in laser-heated nickel by few-femtosecond core-level transient absorption spectroscopy", Phys. Rev. B **103**, 064305 (2021).

[204]R. T. Ross and A. J. Nozik, "Efficiency of hot-carrier solar energy converters", J. Appl. Phys. **53**, 3813–3818 (1982).

[205]P. Würfel, "Solar energy conversion with hot electrons from impact ionisation", Solar Energy Materials and Solar Cells **46**, 43–52 (1997).

[206]A. Luque and A. Martí, "Electron–phonon energy transfer in hot-carrier solar cells", Solar Energy Materials and Solar Cells **94**, 287–296 (2010).

[207]A. E. Jailaubekov, A. P. Willard, J. R. Tritsch, W.-L. Chan, N. Sai, R. Gearba, L. G. Kaake, K. J. Williams, K. Leung, P. J. Rossky, and X.-Y. Zhu, "Hot charge-transfer excitons set the time limit for charge separation at donor/acceptor interfaces in organic photovoltaics", Nat. Mater. **12**, 66–73 (2013).

[208]K. Kamide, T. Mochizuki, H. Akiyama, and H. Takato, "Nonequilibrium Theory of the Conversion Efficiency Limit of Solar Cells Including Thermalization and Extraction of Carriers", Phys. Rev. Applied **10**, 044069 (2018).

[209]Y. Zhang, S. He, W. Guo, Y. Hu, J. Huang, J. R. Mulcahy, and W. D. Wei, "Surface-Plasmon-Driven Hot Electron Photochemistry", Chem. Rev. **118**, 2927–2954 (2018).

[210]Z. Zhang, C. Zhang, H. Zheng, and H. Xu, "Plasmon-Driven Catalysis on Molecules and Nanomaterials", Acc. Chem. Res. **52**, 2506–2515 (2019).

[211]E. Beaurepaire, J.-C. Merle, A. Daunois, and J.-Y. Bigot, "Ultrafast Spin Dynamics in Ferromagnetic Nickel", Phys. Rev. Lett. **76**, 4250–4253 (1996).

[212]M. Imada, A. Fujimori, and Y. Tokura, "Metal-insulator transitions", Rev. Mod. Phys. **70**, 1039–1263 (1998).

[213]A. Kirilyuk, A. V. Kimel, and T. Rasing, "Ultrafast optical manipulation of magnetic order", Rev. Mod. Phys. **82**, 2731–2784 (2010).

[214]S. L. Johnson, M. Savoini, P. Beaud, G. Ingold, U. Staub, F. Carbone, L. Castiglioni, M. Hengsberger, and J. Osterwalder, "Watching ultrafast responses of structure and magnetism in condensed matter with momentum-resolved probes", Struct. Dyn. **4**, 061506 (2017).

[215]S. I. Anisimov, B. L. Kapeliovich, and T. L. Perelman, "Electron emission from metal surfaces exposed to ultrashort laser pulses", Soviet JETP **39**, 375–377 (1974).

[216]P. B. Allen, "Theory of thermal relaxation of electrons in metals", Phys. Rev. Lett. **59**, 1460–1463 (1987).

[217]N. Singh, "Two-temperature model of nonequilibrium electron relaxation: a review", Int. J. Mod. Phys. B **24**, 1141–1158 (2010).

[218]T. Vasileiadis, L. Waldecker, D. Foster, A. Da Silva, D. Zahn, R. Bertoni, R. E. Palmer, and R. Ernstorfer, "Ultrafast heat flow in heterostructures of Au nanoclusters on thin films: Atomic disorder induced by hot electrons", ACS Nano **12**, 7710–7720 (2018).

[219]T. Kampfrath, L. Perfetti, F. Schapper, C. Frischkorn, and M. Wolf, "Strongly Coupled Optical Phonons in the Ultrafast Dynamics of the Electronic Energy and Current Relaxation in Graphite", Phys. Rev. Lett. **95**, 187403 (2005).

[220]B. Mansart, M. J. G. Cottet, G. F. Mancini, T. Jarlborg, S. B. Dugdale, S. L. Johnson, S. O. Mariager, C. J. Milne, P. Beaud, S. Grübel, J. A. Johnson, T. Kubacka, G. Ingold, K. Prsa, H. M. Rønnow, K. Conder, E. Pomjakushina, M. Chergui, and F. Carbone, "Temperature-dependent electron-phonon coupling in $La_{2-x}Sr_xCuO_4$ probed by femtosecond x-ray diffraction", Phys. Rev. B **88**, 054507 (2013).

[221]H.-S. Rhie, H. A. Dürr, and W. Eberhardt, "Femtosecond Electron and Spin Dynamics in $\mathrm{N}\mathrm{i}/\mathrm{W}(110)$ Films", Phys. Rev. Lett. **90**, 247201 (2003).

[222]A. V. Kimel, A. Kirilyuk, A. Tsvetkov, R. V. Pisarev, and T. Rasing, "Laser-induced ultrafast spin reorientation in the antiferromagnet TmFeO3", Nature **429**, 850–853 (2004).

[223]C. Stamm, T. Kachel, N. Pontius, R. Mitzner, T. Quast, K. Holldack, S. Khan, C. Lupulescu, E. F. Aziz, M. Wietstruk, H. A. Dürr, and W. Eberhardt, "Femtosecond modification of electron localization and transfer of angular momentum in nickel", Nat. Mater. **6**, 740–743 (2007).

[224]T. Kachel, N. Pontius, C. Stamm, M. Wietstruk, E. F. Aziz, H. A. Dürr, W. Eberhardt, and F. M. F. de Groot, "Transient electronic and magnetic structures of nickel heated by ultrafast laser pulses", Phys. Rev. B **80**, 092404 (2009).

[225]C. Boeglin, E. Beaurepaire, V. Halté, V. López-Flores, C. Stamm, N. Pontius, H. A. Dürr, and J.-Y. Bigot, "Distinguishing the ultrafast dynamics of spin and orbital moments in solids", Nature **465**, 458–461 (2010).

[226]C. La-O-Vorakiat, E. Turgut, C. A. Teale, H. C. Kapteyn, M. M. Murnane, S. Mathias, M. Aeschlimann, C. M. Schneider, J. M. Shaw, H. T. Nembach, and T. J. Silva, "Ultrafast Demagnetization Measurements Using Extreme Ultraviolet Light: Comparison of Electronic and Magnetic Contributions", Phys. Rev. X **2**, 011005 (2012).

[227]I. Radu, K. Vahaplar, C. Stamm, T. Kachel, N. Pontius, H. A. Dürr, T. A. Ostler, J. Barker, R. F. L. Evans, R. W. Chantrell, A. Tsukamoto, A. Itoh, A. Kirilyuk, T. Rasing, and A. V. Kimel, "Transient ferromagnetic-like state mediating ultrafast reversal of antiferromagnetically coupled spins", Nature **472**, 205–208 (2011).

[228]U. Staub, R. A. de Souza, P. Beaud, E. Möhr-Vorobeva, G. Ingold, A. Caviezel, V. Scagnoli, B. Delley, W. F. Schlotter, J. J. Turner, O. Krupin, W.-S. Lee, Y.-D. Chuang, L. Patthey, R. G. Moore, D. Lu, M. Yi, P. S. Kirchmann, M. Trigo, P. Denes, D. Doering, Z. Hussain, Z. X. Shen, D. Prabhakaran, A. T. Boothroyd, and S. L. Johnson, "Persistence of magnetic order in a highly excited Cu^{2+} state in CuO", Phys. Rev. B **89**, 220401 (2014).

[229]J. A. Johnson, T. Kubacka, M. C. Hoffmann, C. Vicario, S. de Jong, P. Beaud, S. Grübel, S.-W. Huang, L. Huber, Y. W. Windsor, E. M. Bothschafter, L. Rettig, M. Ramakrishnan, A. Alberca, L. Patthey, Y.-D. Chuang, J. J. Turner, G. L. Dakovski, W.-S. Lee, M. P. Minitti, W. Schlotter, R. G. Moore, C. P. Hauri, S. M. Koohpayeh, V. Scagnoli, G. Ingold, S. L. Johnson, and U. Staub, "Magnetic order dynamics in optically excited multiferroic $TbMnO_3$", Phys. Rev. B **92**, 184429 (2015).

[230]M. Naseska, A. Pogrebna, G. Cao, Z. A. Xu, D. Mihailovic, and T. Mertelj, "Ultrafast destruction and recovery of the spin density wave order in iron-based pnictides: A multipulse optical study", Phys. Rev. B **98**, 035148 (2018).

[231]A. V. Kimel, A. Kirilyuk, P. A. Usachev, R. V. Pisarev, A. M. Balbashov, and T. Rasing, "Ultrafast non-thermal control of magnetization by instantaneous photomagnetic pulses", Nature **435**, 655–657 (2005).

[232]J.-Y. Bigot, M. Vomir, and E. Beaurepaire, "Coherent ultrafast magnetism induced by femtosecond laser pulses", Nat. Phys. **5**, 515–520 (2009).

[233]C. E. Graves, A. H. Reid, T. Wang, B. Wu, S. de Jong, K. Vahaplar, I. Radu, D. P. Bernstein, M. Messerschmidt, L. Müller, R. Coffee, M. Bionta, S. W. Epp, R. Hartmann, N. Kimmel, G. Hauser, A. Hartmann, P. Holl, H. Gorke, J. H. Mentink, A. Tsukamoto, A. Fognini, J. J. Turner, W. F. Schlotter, D. Rolles, H. Soltau, L. Strüder, Y. Acremann, A. V. Kimel, A. Kirilyuk, T. Rasing, J. Stöhr, A. O. Scherz, and H. A. Dürr, "Nanoscale spin reversal by non-local angular momentum transfer following ultrafast laser excitation in ferrimagnetic GdFeCo", Nat. Mater. **12**, 293–298 (2013).

[234]A. Eschenlohr, M. Battiato, P. Maldonado, N. Pontius, T. Kachel, K. Holldack, R. Mitzner, A. Föhlisch, P. M. Oppeneer, and C. Stamm, "Ultrafast spin transport as key to femtosecond demagnetization", Nat. Mater. **12**, 332–336 (2013).

[235]G. Batignani, D. Bossini, N. Di Palo, C. Ferrante, E. Pontecorvo, G. Cerullo, A. Kimel, and T. Scopigno, "Probing ultrafast photo-induced dynamics of the exchange energy in a Heisenberg antiferromagnet", Nat. Photonics **9**, 506–510 (2015).

[236]D. Bossini, S. Dal Conte, Y. Hashimoto, A. Secchi, R. V. Pisarev, T. Rasing, G. Cerullo, and A. V. Kimel, "Macrospin dynamics in antiferromagnets triggered by sub-20 femtosecond injection of nanomagnons.", Nat. Commun. **7**, 10645 (2016).

[237]M. Obergfell and J. Demsar, "Tracking the Time Evolution of the Electron Distribution Function in Copper by Femtosecond Broadband Optical Spectroscopy", Phys. Rev. Lett. **124**, 037401 (2020).

[238]A. El-Ghazaly, B. Tran, A. Ceballos, C.-H. Lambert, A. Pattabi, S. Salahuddin, F. Hellman, and J. Bokor, "Ultrafast magnetization switching in nanoscale magnetic dots", Appl. Phys. Lett. **114**, 232407 (2019).

[239]M. Hofherr, S. Häuser, J. K. Dewhurst, P. Tengdin, S. Sakshath, H. T. Nembach, S. T. Weber, J. M. Shaw, T. J. Silva, H. C. Kapteyn, M. Cinchetti, B. Rethfeld, M. M. Murnane, D. Steil, B. Stadtmüller, S. Sharma, M. Aeschlimann, and S. Mathias, "Ultrafast optically induced spin transfer in ferromagnetic alloys", Sci. Adv. **6**, eaay8717 (2020).

[240]L. M. Carneiro, S. K. Cushing, C. Liu, Y. Su, P. Yang, A. P. Alivisatos, and S. R. Leone, "Excitation-wavelength-dependent small polaron trapping of photoexcited carriers in α-Fe_2O_3", Nat. Mater. **16**, 819–825 (2017).

[241]I. J. Porter, S. K. Cushing, L. M. Carneiro, A. Lee, J. C. Ondry, J. C. Dahl, H.-T. Chang, A. P. Alivisatos, and S. R. Leone, "Photoexcited Small Polaron Formation in Goethite (α-FeOOH) Nanorods Probed by Transient Extreme Ultraviolet Spectroscopy", J. Phys. Chem. Lett. **9**, 4120–4124 (2018).

[242]G. D. Mahan, "Excitons in Metals: Infinite Hole Mass", Phys. Rev. **163**, 612–617 (1967).

[243]B. Roulet, J. Gavoret, and P. Nozières, "Singularities in the X-Ray Absorption and Emission of Metals. I. First-Order Parquet Calculation", Phys. Rev. **178**, 1072–1083 (1969).

[244]P. Nozières and C. T. De Dominicis, "Singularities in the X-Ray Absorption and Emission of Metals. III. One-Body Theory Exact Solution", Phys. Rev. **178**, 1097–1107 (1969).

[245]G. D. Mahan, "Collective excitations in x-ray spectra of metals", Phys. Rev. B **11**, 4814–4824 (1975).

[246]K. Ohtaka and Y. Tanabe, "Theory of the soft-x-ray edge problem in simple metals: historical survey and recent developments", Rev. Mod. Phys. **62**, 929–991 (1990).

[247]J. Hohlfeld, E. Matthias, R. Knorren, and K. H. Bennemann, "Nonequilibrium Magnetization Dynamics of Nickel", Phys. Rev. Lett. **78**, 4861–4864 (1997).

[248]U. Conrad, J. Güdde, V. Jähnke, and E. Matthias, "Ultrafast electron and magnetization dynamics of thin Ni and Co films on Cu(001) observed by time-resolved SHG", Appl Phys B **68**, 511–517 (1999).

[249]H. Regensburger, R. Vollmer, and J. Kirschner, "Time-resolved magnetization-induced second-harmonic generation from the Ni(110) surface", Phys. Rev. B **61**, 14716–14722 (2000).

[250]A. Melnikov, J. Güdde, and E. Matthias, "Demagnetization following optical excitation in nickel and permalloy films", Appl Phys B **74**, 735–740 (2002).

[251]M. van Kampen, J. T. Kohlhepp, W. J. M. de Jonge, B. Koopmans, and R. Coehoorn, "Sub-picosecond electron and phonon dynamics in nickel", J. Phys. Condens. Matter **17**, 6823–6834 (2005).

[252]W. You, P. Tengdin, C. Chen, X. Shi, D. Zusin, Y. Zhang, C. Gentry, A. Blonsky, M. Keller, P. M. Oppeneer, H. Kapteyn, Z. Tao, and M. Murnane, "Revealing the Nature of the Ultrafast Magnetic Phase Transition in Ni by Correlating Extreme Ultraviolet Magneto-Optic and Photoemission Spectroscopies", Phys. Rev. Lett. **121**, 077204 (2018).

[253]P. Tengdin, W. You, C. Chen, X. Shi, D. Zusin, Y. Zhang, C. Gentry, A. Blonsky, M. Keller, P. M. Oppeneer, H. C. Kapteyn, Z. Tao, and M. M. Murnane, "Critical behavior within 20 fs drives the out-of-equilibrium laser-induced magnetic phase transition in nickel", Sci. Adv. **4**, eaap9744 (2018).

[254]P. Maldonado, T. Chase, A. H. Reid, X. Shen, R. K. Li, K. Carva, T. Payer, M. Horn von Hoegen, K. Sokolowski-Tinten, X. J. Wang, P. M. Oppeneer, and H. A. Dürr, "Tracking the ultrafast nonequilibrium energy flow between electronic and lattice degrees of freedom in crystalline nickel", Phys. Rev. B **101**, 100302 (2020).

[255]B. Y. Mueller and B. Rethfeld, "Relaxation dynamics in laser-excited metals under nonequilibrium conditions", Phys. Rev. B **87**, 035139 (2013).

[256]R. E. Dietz, E. G. McRae, and J. H. Weaver, "Core-electron excitation edges in metallic Ni, Cu, Pt, and Au", Phys. Rev. B **21**, 2229–2247 (1980).

[257]K. Carva, D. Legut, and P. M. Oppeneer, "Influence of laser-excited electron distributions on the X-ray magnetic circular dichroism spectra: Implications for femtosecond demagnetization in Ni", Europhys. Lett. **86**, 57002 (2009).

[258]L. C. Davis and L. A. Feldkamp, "Interpretation of 3p-core-excitation spectra in Cr, Mn, Fe, Co, and Ni", Solid State Commun. **19**, 413–416 (1976).

[259]S. Valencia, A. Kleibert, A. Gaupp, J. Rusz, D. Legut, J. Bansmann, W. Gudat, and P. M. Oppeneer, "Quadratic X-Ray Magneto-Optical Effect upon Reflection in a Near-Normal-Incidence Configuration at the M Edges of 3d-Transition Metals", Phys. Rev. Lett. **104**, 187401 (2010).

[260]C.-O. Almbladh and P. Minnhagen, "On the thermal broadening of core levels in metals due to many-electron effects", Phys. Status Solidi B **85**, 135–143 (1978).

[261]K. Ohtaka and Y. Tanabe, "Golden-rule approach to the soft-x-ray-absorption problem", Phys. Rev. B **28**, 6833–6846 (1983).

[262]Y. Tanabe and K. Ohtaka, "Golden-rule approach to the soft-x-ray-absorption problem. II. The effect of a bound state", Phys. Rev. B **29**, 1653–1664 (1984).

[263]K. Ohtaka and Y. Tanabe, "Golden-rule approach to the soft-x-ray-absorption problem. III. The temperature dependence", Phys. Rev. B **30**, 4235–4258 (1984).

[264]V. M. Adamjan, J. Ortner, A. G. Salistra, and I. M. Tkachenko, "X-ray-absorption problem in metals within the one-electron approximation", Phys. Rev. B **52**, 13827–13837 (1995).

[265]J. Ortner, "X-ray-absorption problem in metals within the one-electron approximation: Extension to finite temperature", Phys. Rev. B **54**, 4401–4404 (1996).

[266]J. Ortner, "X-ray absorption problem in metals within the one-electron approximation: The temperature dependence", Phys. B Condens. Matter **239**, 328–336 (1997).

[267]B. Johansson and N. Mårtensson, "Core-level binding-energy shifts for the metallic elements", Phys. Rev. B **21**, 4427–4457 (1980).

[268]C. G. Olson and D. W. Lynch, "Thermomodulated exafs of soft x-ray absorption edges", Solid State Commun. **36**, 513–517 (1980).

[269]C. G. Olson and D. W. Lynch, "Temperature dependence of the M2,3 edge in nickel", Solid State Commun. **33**, 849–850 (1980).

[270]N. Rothenbach, M. E. Gruner, K. Ollefs, C. Schmitz-Antoniak, S. Salamon, P. Zhou, R. Li, M. Mo, S. Park, X. Shen, S. Weathersby, J. Yang, X. J. Wang, R. Pentcheva, H. Wende, U. Bovensiepen, K. Sokolowski-Tinten, and A. Eschenlohr, "Microscopic nonequilibrium energy transfer dynamics in a photoexcited metal/insulator heterostructure", Phys. Rev. B **100**, 174301 (2019).

[271]L. Waldecker, R. Bertoni, R. Ernstorfer, and J. Vorberger, "Electron-Phonon Coupling and Energy Flow in a Simple Metal beyond the Two-Temperature Approximation", Phys. Rev. X **6**, 021003 (2016).

[272]D. Pines and P. Nozières, *The theory of quantum liquids*, Advanced Book Classics Series (Addison-Wesley Pub. Co., Advanced Book Program, Redwood City, Calif, 1989).

[273]Z. Lin and L. V. Zhigilei, "Temperature dependences of the electron-phonon coupling, electron heat capacity and thermal conductivity in Ni under femtosecond laser irradiation", Appl. Surf. Sci. **253**, 6295–6300 (2007).

[274]Z. Lin, L. V. Zhigilei, and V. Celli, "Electron-phonon coupling and electron heat capacity of metals under conditions of strong electron-phonon nonequilibrium", Phys. Rev. B **77**, 075133 (2008).

[275]E. Bévillon, J. P. Colombier, V. Recoules, and R. Stoian, "Free-electron properties of metals under ultrafast laser-induced electron-phonon nonequilibrium: A first-principles study", Phys. Rev. B **89**, 115117 (2014).

[276]S. Kasap and P. Capper, eds., *Springer handbook of electronic and photonic materials*, 2nd edition, Springer Handbooks (Springer, Cham, Switzerland, 2017).

[277]A. Guggenmos, R. Rauhut, M. Hofstetter, S. Hertrich, B. Nickel, J. Schmidt, E. M. Gullikson, M. Seibald, W. Schnick, and U. Kleineberg, "Aperiodic CrSc multilayer mirrors for attosecond water window pulses", Opt. Express **21**, 21728–21740 (2013).

[278]P. Johnson and R. Christy, "Optical constants of transition metals: Ti, V, Cr, Mn, Fe, Co, Ni, and Pd", Phys. Rev. B **9**, 5056–5070 (1974).

[279]M. Lax, "The Franck-Condon Principle and Its Application to Crystals", J. Chem. Phys. **20**, 1752–1760 (1952).

[280]R. Kubo, "Generalized Cumulant Expansion Method", J. Phys. Soc. Jpn. **17**, 1100–1120 (1962).

[281]M. Abramowitz and I. A. Stegun, eds., *Handbook of mathematical functions: with formulas, graphs, and mathematical tables*, Dover Books on Advanced Mathematics (Dover Publications, New York, 1970).

[282]H. J. Monkhorst and J. D. Pack, "Special points for Brillouin-zone integrations", Phys. Rev. B **13**, 5188–5192 (1976).

[283]V. Grasso, ed., *Electronic Structure and Electronic Transitions in Layered Materials* (Springer Netherlands, Dordrecht, 1986).

[284]G. Wang, A. Chernikov, M. M. Glazov, T. F. Heinz, X. Marie, T. Amand, and B. Urbaszek, "Colloquium : Excitons in atomically thin transition metal dichalcogenides", Rev. Mod. Phys. **90**, 021001 (2018).

[285]G. D. Mahan, "Photoemission from alkali halides: Energies and line shapes", Phys. Rev. B **21**, 4791–4803 (1980).

[286]P. H. Citrin, G. K. Wertheim, and Y. Baer, "Many-body processes in x-ray photoemission line shapes from Li, Na, Mg, and Al metals", Phys. Rev. B **16**, 4256–4282 (1977).

[287]P. H. Citrin and D. R. Hamann, "Phonon broadening of x-ray photoemission line shapes in solids and its independence of hole state lifetimes", Phys. Rev. B **15**, 2923–2928 (1977).

[288]S. T. Pantelides, "Electronic excitation energies and the soft-x-ray absorption spectra of alkali halides", Phys. Rev. B **11**, 2391–2411 (1975).

[289]S. Pantelides, "On the interpretation of the $Na^{+}L_{2,3}$ soft-X-ray absorption spectra of the sodium halides", Physics Letters A **48**, 433–434 (1974).

[290]S. T. Pantelides and F. C. Brown, "New Interpretation of the Soft-X-Ray Absorption Spectra of Several Alkali Halides", Phys. Rev. Lett. **33**, 298–301 (1974).

[291]M. Kamada, O. Aita, K. Ichikawa, and K. Tsutsumi, "Decay of the Na 2p core exciton in sodium halides studied by photoelectron spectroscopy", Phys. Rev. B **36**, 4962–4972 (1987).

[292]S.-i. Nakai, T. Ishii, and T. Sagawa, "Core Exciton Absorption in Sodium Halides", J. Phys. Soc. Jpn. **30**, 428–439 (1971).

[293]A. W. Overhauser, "Multiplet Structure of Excitons in Ionic Crystals", Phys. Rev. **101**, 1702–1712 (1956).

[294]K. Tomita, T. Miyata, W. Olovsson, and T. Mizoguchi, "Core–Exciton Interaction in Sodium L2,3 edge Structure Investigated Using the Bethe–Salpeter Equation", J. Phys. Chem. C **120**, 9036–9042 (2016).

[295]Y. Onodera and Y. Toyozawa, "Excitons in Alkali Halides", J. Phys. Soc. Jpn. **22**, 833–844 (1967).

[296]J. D. Gaynor, A. P. Fidler, Y.-C. Lin, H.-T. Chang, M. Zuerch, D. M. Neumark, and S. R. Leone, "Solid-state core-exciton dynamics in NaCl observed by tabletop attosecond four-wave mixing spectroscopy", ArXiv210314590 Cond-Mat (2021).

[297]M. S. Hybertsen and S. G. Louie, "Electron correlation in semiconductors and insulators: Band gaps and quasiparticle energies", Phys. Rev. B **34**, 5390–5413 (1986).

[298]S. G. Louie and M. S. Hybertsen, "Theory of quasiparticle energies: Band gaps and excitation spectra in solids", Int. J. Quantum Chem. **32**, 31–44 (1987).

[299]P. N. Brown, G. D. Byrne, and A. C. Hindmarsh, "VODE: A Variable-Coefficient ODE Solver", SIAM J. Sci. Stat. Comput. **10**, 1038–1051 (1989).

[300]X. Li, B. Bernhardt, A. R. Beck, E. R. Warrick, A. N. Pfeiffer, M. Justine Bell, D. J. Haxton, C. William McCurdy, D. M. Neumark, and S. R. Leone, "Investigation of coupling mechanisms in attosecond transient absorption of autoionizing states: Comparison of theory and experiment in xenon", J. Phys. B At. Mol. Opt. Phys. **48**, 1–10 (2015).

[301]V. Stooß, S. M. Cavaletto, S. Donsa, A. Blättermann, P. Birk, C. H. Keitel, I. Březinová, J. Burgdörfer, C. Ott, and T. Pfeifer, "Real-Time Reconstruction of the Strong-Field-Driven Dipole Response", Phys. Rev. Lett. **121**, 173005 (2018).

[302]H.-T. Chang, M. Zürch, P. M. Kraus, L. J. Borja, D. M. Neumark, and S. R. Leone, "Simultaneous generation of sub-5-femtosecond 400 nm and 800 nm pulses for attosecond extreme ultraviolet pump–probe spectroscopy", Opt. Lett. **41**, 5365 (2016).

[303]M. Hentschel, R. Kienberger, C. Spielmann, G. A. Reider, N. Milosevic, T. Brabec, P. Corkum, U. Heinzmann, M. Drescher, and F. Krausz, "Attosecond metrology.", Nature **414**, 509–513 (2001).

[304]M. F. Kling and M. J. J. Vrakking, "Attosecond electron dynamics", in *Annual Review of Physical Chemistry*, Vol. 59 (2008), pp. 463–492.

[305]L. Gallmann, C. Cirelli, and U. Keller, "Attosecond Science: Recent Highlights and Future Trends", Annu. Rev. Phys. Chem. **63**, 447–469 (2012).

[306]F. Krausz and M. I. Stockman, "Attosecond metrology: from electron capture to future signal processing", Nat. Photonics **8**, 205–213 (2014).

[307]Z. Chang, P. B. Corkum, and S. R. Leone, "Attosecond optics and technology: progress to date and future prospects [Invited]", J. Opt. Soc. Am. B **33**, 1081 (2016).

[308]L. J. Borja, M. Zürch, C. D. Pemmaraju, M. Schultze, K. Ramasesha, A. Gandman, J. S. Prell, D. Prendergast, D. M. Neumark, and S. R. Leone, "Extreme ultraviolet transient absorption of solids from femtosecond to attosecond timescales", J. Opt. Soc. Am. B **33**, C57 (2016).

[309]K. Ramasesha, S. R. Leone, and D. M. Neumark, "Real-Time Probing of Electron Dynamics Using Attosecond Time-Resolved Spectroscopy", Annu. Rev. Phys. Chem. **67**, 41–63 (2016).

[310]T. T. Luu, M. Garg, S. Y. Kruchinin, A. Moulet, M. T. Hassan, and E. Goulielmakis, "Extreme ultraviolet high-harmonic spectroscopy of solids", Nature **521**, 498–502 (2015).

[311]W. A. Okell, T. Witting, D. Fabris, C. A. Arrell, J. Hengster, S. Ibrahimkutty, A. Seiler, M. Barthelmess, S. Stankov, D. Y. Lei, Y. Sonnefraud, M. Rahmani, T. Uphues, S. A. Maier, J. P. Marangos, and J. W. G. Tisch, "Temporal broadening of attosecond photoelectron wavepackets from solid surfaces", Optica **2**, 383–387 (2015).

[312]H. Mashiko, K. Oguri, T. Yamaguchi, A. Suda, and H. Gotoh, "Petahertz optical drive with wide-bandgap semiconductor", Nat. Phys., 1–6 (2016).

[313]C. Brabec, V. Dyakonov, J. Parisi, and N. Sariciftci, *Organic photovoltaics: Concepts and realization*, Springer Series in Materials Science (Springer Berlin Heidelberg, 2003).

[314]R. Blankenship, *Molecular mechanisms of photosynthesis* (Wiley, 2002).

[315]W. J. Alford and A. V. Smith, "Frequency-doubling broadband light in multiple crystals", J. Opt. Soc. Am. B **18**, 515 (2001).

[316]T. Kanai, X. Zhou, T. Sekikawa, S. Watanabe, and T. Togashi, "Generation of subterawatt sub-10-fs blue pulses at 1–5kHz by broadband frequency doubling", Opt. Lett. **28**, 1484 (2003).

[317]T. Kanai, X. Zhou, T. Liu, A. Kosuge, T. Sekikawa, and S. Watanabe, "Generation of terawatt 10-fs blue pulses by compensation for pulse-front distortion in broadband frequency doubling", Opt. Lett. **29**, 2929 (2004).

[318]X. Zhou, T. Kanai, D. Yoshitomi, T. Sekikawa, and S. Watanabe, "Generation of high average power, 7.5-fs blue pulses at 5 kHz by adaptive phase control", Appl. Phys. B **81**, 13–17 (2005).

[319]R. B. Varillas, A. Candeo, D. Viola, M. Garavelli, S. De Silvestri, G. Cerullo, and C. Manzoni, "Microjoule-level, tunable sub-10 fs UV pulses by broadband sum-frequency generation.", Opt. Lett. **39**, 3849–52 (2014).

[320]O. Dühr, E. T. J. Nibbering, G. Korn, G. Tempea, and F. Krausz, "Generation of intense 8-fs pulses at 400 nm", Opt. Lett. **24**, 34–36 (1999).

[321]A. Fürbach, T. Le, C. Spielmann, and F. Krausz, "Generation of 8-fs pulses at 390 nm", Appl. Phys. B **70**, S37–S40 (2000).

[322]K.-l. Liu, S.-J. Lee, I.-c. Chen, C.-P. Hsu, M.-Y. Yeh, and T.-Y. Luh, "Ultrafast Energy Transfer in a Regioregular Silylene-Spaced Copolymer", J. Phys. Chem. C **114**, 13909–13916 (2010).

[323]J. Liu, K. Okamura, Y. Kida, T. Teramoto, and T. Kobayashi, "Clean sub-8-fs pulses at 400 nm generated by a hollow fiber compressor for ultraviolet ultrafast pump-probe spectroscopy.", Opt. Express **18**, 20645–50 (2010).

[324]A. Grün, D. R. Austin, S. L. Cousin, and J. Biegert, "Three-wave mixing mediated femtosecond pulse compression in β-barium borate", Opt. Lett. **40**, 4679 (2015).

[325]A. Wirth, M. T. Hassan, I. Grguras, J. Gagnon, A. Moulet, T. T. Luu, S. Pabst, R. Santra, Z. A. Alahmed, A. M. Azzeer, V. S. Yakovlev, V. Pervak, F. Krausz, and E. Goulielmakis, "Synthesized Light Transients", Science **334**, 195–200 (2011).

[326]M. T. Hassan, A. Wirth, I. Grguraš, A. Moulet, T. T. Luu, J. Gagnon, V. Pervak, and E. Goulielmakis, "Invited article: attosecond photonics: synthesis and control of light transients.", Rev. Sci. Instrum. **83**, 111301 (2012).

[327]M. T. Hassan, T. T. Luu, A. Moulet, O. Raskazovskaya, P. Zhokhov, M. Garg, N. Karpowicz, A. M. Zheltikov, V. Pervak, F. Krausz, and E. Goulielmakis, "Optical attosecond pulses and tracking the nonlinear response of bound electrons", Nature **530**, 66–70 (2016).

[328]R. Trebino, K. W. DeLong, D. N. Fittinghoff, J. N. Sweetser, M. A. Krumbugel, B. A. Richman, D. J. Kane, M. A. Krumbügel, B. A. Richman, and D. J. Kane, "Measuring ultrashort laser pulses in the time-frequency domain using frequency-resolved optical gating", Rev. Sci. Instrum. **68**, 3277–3295 (1997).

[329]R. Trebino, *Frequency-resolved optical gating: The measurement of ultrashort laser pulses* (Springer US, 2012).

[330]Femtosoft Technologies, *FROG ver. 3.2.4*, Oct. 2014.